ABSTRACT

VOLLMER, DAVID RUSSELL. The Interaction of Jet/Front Systems and Mountain Waves: Implications for Lower Stratospheric Aviation Turbulence. (Under the direction of S. Pal Arya and Michael L. Kaplan.)

The role of jet streaks and their associated upper-level structures (fronts, troughs, thermal fields, etc.) in enhancing orographically-induced aviation turbulence near and above the tropopause is investigated. The primary hypothesis for this research suggests that there is an optimal configuration for the positioning of upper-level circulations leading to vertically confluent flow and differential thermal advection, forming an intense inversion. Such a configuration may be associated with vertically-intersecting ageostrophic jet circulations or trough-induced differential vertical motions leading to cold air undercutting a warm layer aloft, and compression of the warm layer in the presence of jet-induced shear. This structure is then perturbed by mountain waves, leading to a downscale cascade of kinetic energy, eventually leading to potential aviation turbulence. Two cases of clear-air turbulence (CAT) are examined using mesoscale numerical simulations. The first case involved a DC-8 attempting to cross the Colorado Front Range when it encountered extreme CAT resulting in loss of part of one wing and an engine. In this case the superposition of two distinct jet features was hypothesized to have established an unusually strong inversion just above the tropopause which allowed strong buoyancy-driven motions to enhance the horizontal shear and turbulent eddies, eventually leading to the turbulent downburst hypothesized to have played a role in damaging the aircraft. The second study used data from the Terrain-Induced Rotor Experiment (T-REX) and examined a turbulent wave-breaking event recorded by a research aircraft in the lower stratosphere. A different jet regime was found in this case, with a strong upstream trough and decreasing cyclonic curvature with height above the tropopause

Report Documentation Page

Public reporting burden for the collection of information is estimated to average 1 hour per response, including the time for reviewing instructions, searching existing data sources, gathering and maintaining the data needed, and completing and reviewing the collection of information. Send comments regarding this burden estimate or any other aspect of this collection of information, including suggestions for reducing this burden, to Washington Headquarters Services, Directorate for Information Operations and Reports, 1215 Jefferson Davis Highway, Suite 1204, Arlington VA 22202-4302. Respondents should be aware that notwithstanding any other provision of law, no person shall be subject to a penalty for failing to comply with a collection of information if it does not display a currently valid OMB control number.

1. REPORT DATE **01 JUL 2008**	2. REPORT TYPE **N/A**	3. DATES COVERED **-**

4. TITLE AND SUBTITLE	5a. CONTRACT NUMBER
The Interaction of Jet/Front Systems and Mountain Waves: Implications for Lower Stratospheric Aviation Turbulence	5b. GRANT NUMBER
	5c. PROGRAM ELEMENT NUMBER

6. AUTHOR(S)	5d. PROJECT NUMBER
	5e. TASK NUMBER
	5f. WORK UNIT NUMBER

7. PERFORMING ORGANIZATION NAME(S) AND ADDRESS(ES) **North Carolina State University**	8. PERFORMING ORGANIZATION REPORT NUMBER

9. SPONSORING/MONITORING AGENCY NAME(S) AND ADDRESS(ES) **AFIT/ENEL Wright-Patterson AFB OH 45433-7765**	10. SPONSOR/MONITOR'S ACRONYM(S)
	11. SPONSOR/MONITOR'S REPORT NUMBER(S) **Cl09-0007**

12. DISTRIBUTION/AVAILABILITY STATEMENT
Approved for public release, distribution unlimited

13. SUPPLEMENTARY NOTES

14. ABSTRACT

15. SUBJECT TERMS

16. SECURITY CLASSIFICATION OF:			17. LIMITATION OF ABSTRACT	18. NUMBER OF PAGES	19a. NAME OF RESPONSIBLE PERSON
a. REPORT **unclassified**	b. ABSTRACT **unclassified**	c. THIS PAGE **unclassified**	**UU**	**216**	

Standard Form 298 (Rev. 8-98)
Prescribed by ANSI Std Z39-18

and a strong lower stratospheric inversion. The vertical variation of static stability in the lower stratosphere was found to create a favorable environment for amplification and breaking of the mountain wave in this case. Lastly, a series of two-dimensional idealized experiments were conducted to further examine the role of static stability and jet structure on the potential for stratospheric turbulence over complex terrain. Vertical static stability gradients in the lower stratosphere were found to play a significant role in the potential for aviation turbulence, as were the angle of incidence of the winds and the strength of the flow.

The Interaction of Jet/Front Systems and Mountain Waves: Implications for Lower
Stratospheric Aviation Turbulence

by
David Russell Vollmer

A dissertation submitted to the Graduate Faculty of
North Carolina State University
in partial fulfillment of the
requirements for the Degree of
Doctor of Philosophy

Marine, Earth, and Atmospheric Sciences

Raleigh, North Carolina

2008

APPROVED BY:

_____   _____
Gerald S. Janowitz   Gary M. Lackmann

_____   _____
S. Pal Arya   Michael L. Kaplan
Co-chair of Advisory Committee   Co-chair of Advisory Committee

BIOGRAPHY

Major David R. Vollmer, USAF, was born on Long Island, and graduated in 1992 from Harborfields High School in Greenlawn, NY. He graduated in January 1996 with a Bachelor of Science degree in meteorology from the Pennsylvania State University. In June 1996, he was commissioned as a Second Lieutenant in the United States Air Force at the USAF Officer Training School at Maxwell Air Force Base (AFB), AL. His first duty assignment was as a staff weather officer with the 21st Air Support Operations Squadron, Fort Polk, LA, from which he deployed as a peacekeeper during Operation JOINT GUARD in Bosnia-Herzegovina in 1997. In 1998 he was transferred to the 607th Weather Squadron, Yongsan, South Korea, where he served as a plans officer and later as a combat weather team leader in support of US Army aviation operations. In 2002, he graduated from the Air Force Institute of Technology (AFIT) at Wright-Patterson AFB, OH, with a Master of Science in Military Meteorology. After graduation, he was assigned to the Air Force Technical Applications Center (AFTAC) at Patrick AFB, FL. In 2003, he deployed with the US Army 2d Armored Cavalry Regiment to Baghdad, Iraq, during Operation IRAQI FREEDOM. Upon return from Iraq, he was selected to be the Chief, Commander's Action Group for AFTAC. In 2005 he was selected by AFIT to enter the doctoral program in atmospheric science at the North Carolina State University.

Major Vollmer is married with two wonderful sons. Upon graduation he and his family will be moving to Offutt AFB, NE, where Major Vollmer will be assigned to Headquarters, Air Force Weather Agency.

ACKNOWLEDGMENTS

TABLE OF CONTENTS

LIST OF TABLES

LIST OF FIGURES

Chapter 1

Chapter 2

Chapter 3

Chapter 4

Chapter 5

Appendix A

CHAPTER 1

INTRODUCTION

1.1. Introduction

Clear-air turbulence (CAT) in the upper troposphere and lower stratosphere is a major

hazard facing both commercial and government aviation interests. According to Federal

Aviation Administration (FAA) statistics (available at http://www.faa.gov), US commercial

air carriers reported 198 turbulence incidents involving damage or injury between 1980 and

June 2004, of which approximately two-thirds occurred above 30,000 feet (9 km). These

incidents resulted in 266 injuries and three deaths. Two primary sources of this upper-level

CAT are shear zones in the vicinity of jet streaks and where flow crosses a topographic

barrier. It follows that interactions between jet streak circulations and orographically-

induced gravity waves can be especially conducive to aviation turbulence. For example, on

20-21 February, 1973, a series of gravity waves triggered by jet flow over the Continental

Divide west of Denver resulted in numerous reports of moderate to severe CAT by aircrews

over a two-day period (Bedard et al. 1986). Rawinsonde and microbarograph data confirmed

the presence of gravity waves aloft and at the surface, and the aircraft turbulence reports

came from a layer corresponding to the level of the jet stream, in which the Richardson

number decreased to near zero. Additionally, Kaplan et al. (2005a,b) studied 44 cases of

aircraft turbulence encounters between 1990 and 1996. Three of these cases involved

mountain waves, and all of those included significant vertical wind shear and immediate

upstream jet curvature.

Motivation for this study comes from the primary sponsor of the research, the US Air Force Research Laboratory. Since so many of the US Air Force's assets operate at altitudes near or above the tropopause, the Air Force as a whole is keenly interested in being able to better predict and avoid severe turbulence which can cause damage to its aircraft. Turbulence may also interfere with procedures such as aerial refueling or with the operation of certain weapon systems. Many of the US Air Force's operations occur in regions with significant topography, where orographic turbulence may be present. It is therefore most productive to explore cases in which severe turbulence resulted from interactions between mountain waves and upper-level jet/front systems.

The first case took place on 9 December 1992 over the Front Range of the Colorado Rockies, in which a DC-8 lost 19 feet of wing and an engine during an encounter with severe turbulence caused by jet streak/mountain wave interaction. This case study includes discussion of the pre-turbulent jet environment and downscale energy cascade, as well as model simulations across the scales of motion. The second case study comes from Intensive Observing Period (IOP) 6 during the Terrain-induced Rotor Experiment (T-REX). This case involved interaction between mountain waves and a polar jet at the base of a strong trough in the lee of the Sierra Nevada, and was characterized by strong gravity waves above the tropopause. Extreme turbulence associated with gravity-wave breaking was reported by a high-altitude research aircraft during IOP 6. In addition, two other IOPs from T-REX which involved stratospheric gravity waves were compared to IOP 6.

The third major section of this research consists of idealized simulations involving aspects of the first two real-data cases. Two-dimensional simulations of the 9 December 1992 Colorado case and six of the T-REX IOPs were conducted using idealized terrain

2

profiles which approximated the Colorado Front Range and California's Owens Valley, respectively. The upstream sounding data for these simulations were derived from real data, and in the case of the Colorado simulations, were modified to find an optimal configuration of winds and temperatures which would maximize the potential for lower stratospheric turbulence. For the T-REX cases, simulations of three IOPs characterized by stratospheric gravity wave observations were compared to simulations of three IOPs not observed to have significant wave activity above tropopause.

1.2. Literature Review

1.2.1. Flow over a terrain barrier

It has long been known that topographical features such as mountains can have a significant impact on the flow characteristics of the air above them. Both theoretical studies of stably-stratified fluid flows over complex orography and direct observations and simulations of real data cases show that gravity waves are very often excited by such flows, and depending on conditions, can influence the thermal and momentum fields both up- and downstream of the barrier. Depending upon the flow characteristics relative to the mountain height, these waves can either decay with height (evanescent case) or propagate vertically. In order to determine the response of the flow to the barrier, several parameters may be used. The most common non-dimensional flow parameter from theoretical fluid mechanics used to describe the behavior of stably-stratified fluid passing over a barrier is the Froude number, often given by:

$$F = \frac{U}{NH} \qquad\qquad (1.1)$$

where U is the mean wind, N is the static stability parameter (Brunt-Väisäla frequency), given by:

$$N = \sqrt{\frac{g}{\theta}\frac{\partial \theta}{\partial z}} \qquad (1.2)$$

and H is the height of the topographic barrier. Huppert and Miles (1969) determined the critical Froude number to be approximately 1.18 for a bell-shaped mountain in continuously-stratified hydrostatic flow. Flow at Froude values greater than 1.18 may be considered supercritical (i.e., flow is linear and tends to be evanescent), and at values of F below 1.18 will be subcritical, meaning the parcel oscillation period exceeds the advection period, allowing the generation of vertically-propagating gravity waves. The Froude number is also a measure of the linearity of the flow; the smaller the Froude number, the more non-linear becomes the flow response as verified by numerical simulations (Lin and Wang 1996). Figure 1.1 shows the relationship between F and the response, with the flow completely nonlinear at F=0.5.

Another useful parameter used to describe the nature of flow over a mountain is the Scorer parameter (Scorer 1949) given by:

$$l^2 = \frac{N^2}{U^2} - \frac{\left(\partial^2 U / \partial z^2\right)}{U} \qquad (1.3)$$

Fig. 1.2 relates a vertically-uniform l to k, where k is the wave number of the mountain (inverse of the wavelength), indicating that as l gets large relative to k, the mountain waves propagate vertically and eventually become fully hydrostatic (Lin 2007). Fig. 1.3 shows the extreme cases from Fig. 1.2., with irrotational flow depicted in Fig.1.3a and hydrostatic gravity waves in Fig.1.3a. Based on linear theory (Queney 1948), one would

expect a vertical wavelength for a stable, vertically-propagating hydrostatic wave to be

$\lambda_z = 2\pi U / N$.

A phenomenon confined to the lower tropopsphere which sometimes results from flow over a mountain is the rotor, which is a strong, horizontal vortex occurring in the lee of and parallel to the mountain (Kuettner 1959). These circulations pose a very significant hazard to aircraft (Carney et al. 1988) due to their extremely violent and compact nature, yet have only recently been studied in depth. The Terrain-Induced Rotor Experiment (T-REX) was conducted to study rotors and mountain waves in the Owens Valley of California (Grubišić et al. 2004) and yielded significant amounts of data, providing further insight into rotor generation and structure. An example of a rotor circulation and its relation to other phenomena is given in Fig. 1.4. Of relevance to this study is that even in the presence of rotors in the lower troposphere, a turbulent layer is indicated near the tropopause. Rotors are formed as a result of boundary layer separation in the lee, and are associated with lee waves that become trapped, as happens when l^2 decreases over a short vertical distance above the mountain (Doyle and Durran 2002). Rotors are often made visible by the appearance of a roll cloud.

Another well-known response to non-linear flow over a mountain is the generation of severe downslope winds on the lee side. Such an event along the Colorado Front Range on 11 January 1972 produced surface gusts in excess of 50 ms^{-1} at Boulder, CO, causing significant damage and resulting in reports of aviation turbulence as high as 12 km (Lilly 1978). Several theories have been put forward to explain the behavior of the flow on the lee slope during a downslope wind event. Klemp and Lilly (1975) suggested that the presence of an upstream inversion near the level of the mountain top along with an unstable tropospheric

lapse rate, capped by the stable stratosphere, could lead to the generation of an intense lee-side standing wave that would be associated with strong downslope winds. They theorized that if the vertical momentum and thermal profiles were such that the tropopause occurred at ½ the wavelength, amplification could occur as upward propagating large-amplitude wave energy is partially reflected downward by the vertical variation of the static stability as manifested by a sudden decrease in the Scorer parameter. In this manner, the downslope wind is amplified by the superposition of upward and downward propagating wave energy, hence "reflection amplification." This essentially linear model compared well with observations of downslope wind events in the Boulder, CO area. The density profile for this optimum configuration is shown in Fig. 1.5.

A theory advanced by Smith (1985) is known as hydraulic theory (Fig. 1.6), and describes a "high drag" state in which the flow is separated into smooth stratified flow and highly turbulent, mixed flow known as the "dead region." This dead region forms above the strong, laminar downslope wind flow by a "dividing streamline." The dividing streamline is the notional boundary between the turbulent flow and stratified laminar flow, and it descends considerably from its upstream position (H_0 in Fig. 1.6) to downstream of the peak (H_1), with subcritical flow on the windward side transitioning to supercritical flow on the lee side. The pressure drag is proportional to the cube of the difference between the upper and lower dividing streamlines. The dead region, well above the lee slope, is an area preferred for turbulence.

Another theory describing the downslope wind formation is that of resonant amplification. This involves the breaking of a mountain wave as well as the transition (as in Smith's theory) from subcritical flow upstream to supercritical flow downstream of the

mountain peak. Scinocca and Peltier (1993) proposed a three-stage hypothesis for the formation of severe downslope winds. In the first stage, the standing mountain wave begins to overturn and break aloft due to static instability (Fig. 1.7a-b). This generates a stationary hydraulic jump in the lee of the mountain during the second stage as Kelvin-Helmholtz shear instability overtakes the buoyant instability as the primary means of mixing (Fig. 1.7c). The hydraulic jump is characterized by near-vertical streamlines above the downslope wind. In the third stage, the downslope wind structure extends downstream (Fig. 1.7d). The resonant amplification occurs as the breaking wave aloft creates a critical level (due to wind reversal), which serves to overreflect the upward-directed waves and duct them downstream. In this manner, the downslope wind flow is reinforced by both upward- and downward-directed waves in resonance. The turbulent mixed layer extends throughout a deep layer of the troposphere.

1.2.2. Frontogenesis and jet streak dynamics

Traditionally, the term "front" has meant the interface between two airmasses of differing density or a first-order discontinuity in temperature. Although fronts are most often associated with a locally tight horizontal gradient of temperature, they are often also associated with differences in humidity and a wind shift. Miller (1948) extended the concept of frontogenesis from a two-dimensional concept confined to the earth's surface to a fully three-dimensional process, noting the role of vertical motions in establishing and maintaining a frontal boundary through the depth of the troposphere. A version of his frontogenesis equation is given by:

$$F = \frac{1}{|\nabla \theta|} \left[\frac{\partial \theta}{\partial x} \left(-\frac{\partial u}{\partial x}\frac{\partial \theta}{\partial x} - \frac{\partial v}{\partial x}\frac{\partial \theta}{\partial y} \right) + \frac{\partial \theta}{\partial y} \left(-\frac{\partial u}{\partial y}\frac{\partial \theta}{\partial x} - \frac{\partial v}{\partial y}\frac{\partial \theta}{\partial y} \right) + \frac{\partial \theta}{\partial p} \left(-\frac{\partial \theta}{\partial x}\frac{\partial \omega}{\partial x} - \frac{\partial \theta}{\partial y}\frac{\partial \omega}{\partial y} \right) \right] \quad (1.4)$$

In this equation, $\nabla \theta$ represents the 3-dimensional gradient of potential temperature, u and v are the horizontal x and y components of the wind, respectively, p is pressure, and ω is the vertical motion in pressure coordinates. The terms represent contributions to frontogenesis by shearing and stretching deformation of the isentropic field, differential diabatic heating, and tilting of the isentropic surfaces. It should be clear from Eq. 1.4 that compression of isentropes through convergence, as well as tilting of isentropes into the vertical, are frontogenetical processes.

Jet streams (hereafter called simply "jets") are narrow bands of locally maximum winds. A jet forms in response to the thermal wind relation, given by:

$$-\frac{\partial \vec{V}_g}{\partial p} = \frac{R}{pf}\hat{k} \times \nabla_p T \qquad (1.5)$$

where $\vec{V}_g$ is the geostrophic wind, R is the gas constant for dry air, f is the Coriolis parameter, and $\nabla_p T$ is the horizontal temperature gradient on a constant pressure surface. Because of this relation to horizontal temperature gradient, the jet is found along the maximum temperature gradient. The large scale-jets (i.e., the polar and subtropical jets) occur at the tropopause, where the temperature gradient (and thus thermal wind) reverses. In the sense that thermal wind is maximum where the temperature gradient is a maximum, the region of the jet is associated with the upper-level front. In that respect, it is useful to consider the jet/front system as an integrated whole. The upper front associated with the jet is an enhanced gradient of temperature which typically slopes toward the cold air from the surface to the tropopause. In addition, the tropopause, representing the troposphere/stratosphere interface, slopes downward toward the cold side of the front (Keyser and Shapiro 1986). The jet is found near the intersection of the frontal boundary and the tropopause (Fig.1.8). The

polar jet is typically found along the boundary between the polar airmass and the subtropical airmass. The subtropical jet, however, typically occurs at the poleward-most extent of the Hadley cell. The subtropical jet is generally higher and weaker than the polar jet, yet is still a significant part of the global circulation even during winter months (Krishnamurti 1961).

Jet streaks are simply local maxima within the wind maximum that is the jet stream. Jet streaks are accompanied by ageostrophic motions which develop to maintain thermal wind balance, which would otherwise be destroyed through advection of the geostrophic wind *by* the geostrophic wind (Namias and Clapp 1949). One may consider the region where the flow is accelerating into the jet streak to be the "entrance region," and where it is decelerating downstream as the "exit region." Considering first a linear, uniform jet streak (Fig. 1.9a), a four-cell pattern of divergence is noted, with divergence in the right entrance and left exit regions, and convergence in the left entrance and right exit regions. Therefore at the level of the jet, one finds ageostrophic flow directed poleward at the entrance region, and equatorward at the exit region. This creates a solenoidal ageostrophic circulation which is thermally direct in the entrance region (cold air sinking and warm air rising) as seen in Fig.(1.10a) and thermally indirect (with cold air rising and warm air sinking) in the exit region (Bosart 1970; Shapiro 1970; Uccellini and Johnson 1979). These vertical motions will tend to tilt isentropes into the vertical, leading to frontogenesis (Reed and Sanders 1953). Since vertical motions are associated with adiabatic warming and cooling, they also tend to increase the thermal gradient in the exit region and decrease the thermal gradient in the entrance region.

For a cyclonically curved jet, one finds a two-cell, rather than a four-cell model (Fig. 1.9b). Here, convergence at the entrance results in a strong upstream-directed ageostrophic

component at the base of the trough, with a strongly divergent region downstream of the trough axis. Through mass compensation one finds a region of subsidence below the convergence in the entrance and of upward vertical motion beneath the divergence in the exit region (Moore and Vanknowe 1992) as seen in Fig. 1.10b. Likewise, the situation is reversed in the case of an anticyclonically curved jet streak, with rising air below the entrance region and sinking air below the exit (Fig. 1.10c). A cyclonically curved jet streak is associated with an upper-level trough. Through a quasigeostrophic (QG) framework one expects upward vertical motion ahead of the trough below the region of maximum curvature and subsiding flow above, as the differential advection of vorticity drives vertical motion. The QG-omega equation relates vertical motion to vertically differential vorticity advection and thickness advection. The traditional form of the QG-omega equation is given by (Holton 2004):

$$\left(\nabla^2 + \frac{f_0^2}{\sigma}\frac{\partial^2}{\partial p^2}\right)\omega = \frac{f_0}{\sigma}\frac{\partial}{\partial p}\left[\vec{V}_g \bullet \nabla\left(\frac{1}{f_0}\nabla^2\Phi + f\right)\right] + \frac{1}{\sigma}\nabla^2\left[\vec{V}_g \bullet \nabla\left(\frac{\partial \Phi}{\partial P}\right)\right] - \frac{\kappa}{\sigma p}\nabla^2 J$$

(1.6)

where the left hand side represents the three-dimensional Laplacian of the vertical motion (ω) and the right hand terms represent vertically differential advection of absolute vorticity by the geostrophic wind, the Laplacian of geostrophic thickness advection, and the diabatic heating term. The first two terms on the right-hand side often involve some degree of cancellation; however, one may interpret Eq. (1.6) to mean that increasing cyclonic vorticity advection with height leads to upward vertical motion, and decreasing cyclonic vorticity advection with height leads to subsidence. This is a critical point with regard to the vertical motion expected upstream of an upper trough.

As stated previously, the role of the ageostrophic circulations within the jet streak is to maintain approximate geostrophic balance by transporting mass and momentum (Namias and Clapp 1949; Sawyer 1956). The ageostrophic wind can be expressed as follows (Uccellini and Johnson 1979):

$$\vec{V}_{ag} = \frac{1}{f}\left[\hat{k} \times \frac{\partial \vec{V}_g}{\partial t_\theta} + \vec{V} \bullet \nabla_\theta \left(\hat{k} \times \vec{V}_g \right) \right] \qquad (1.7)$$

The first term represents the isallobaric wind, and the second term represents interial/advective processes. The isallobaric wind is primarily responsible for mass redistribution and adjustment. Uccellini and Johnson (1979) found that the isallobaric component of the indirect entrance region circulation is often associated with the formation of a low-level jet. The inertial/advective term is responsible for transporting momentum along isentropic surfaces. The isallobaric component tends to be the dominant one at lower levels, with the inertial/advective term dominating in the middle and upper troposphere. Keyser and Johnson (1984) also considered a third component to the ageostrophic wind, the inertial diabatic term, which is related to the vertical advection of momentum through isentropic surfaces in the geostrophic momentum form of the equations of motion.

The ageostrophic motions associated with jet streaks have a significant impact on frontogenesis in the upper troposphere as noted by many researchers (Reed and Sanders 1953; Reed 1955; Shapiro 1981; Mattocks and Bleck 1986). One important feature of upper-frontogenesis is the tropopause fold, i.e., when the ageostrophic circulation draws stratospheric air down into the troposphere, effectively folding the tropopause over itself. Verification of the stratospheric origin of the air in the fold can be made through ozone observations, as the stratospheric air contains relative high concentrations of ozone relative to

the troposphere. The stratosphere is also characterized by higher potential vorticity (Reed 1955; Shapiro 1978) and potential vorticity is often tracked as a conserved quantity, so potential vorticity analysis is also used to determine the stratospheric origin of air in the fold (Fig. 1.11). Reed (1955) found stratospheric air having descended as low as 700-800 hPa in the direct circulation of the jet entrance region. Lackmann et al. (1997) found a strong tropopause fold associated with a strengthening mid-tropospheric jet which led to rapid cyclogenesis. The tropopause fold was attributed to the transverse ageostrophic circulation of the jet/front system. For clarity, the tropopause is often represented by a concept known as the "dynamic tropopause," which is a somewhat arbitrary value of potential vorticity chosen to represent the boundary between stratospheric and tropospheric air. The value chosen to represent the dynamic tropopause is typically 1.5 to 2 potential vorticity units (PVU, where 1 PVU equals 1.0×10^{-6} $Km^2kg^{-1}s^{-1}$) in the literature (Conaty et al. 2001; Swanson 2001).

1.2.3. Dynamical turbulence

This project examines turbulence as the end result of a downscale cascade of kinetic energy from the synoptic-scale flow and mesoscale gravity waves down to the aircraft response scale. As such, it is useful to define what is meant by turbulence. Fluid mechanics deals with turbulence as irregular, chaotic flow distinguished from laminar flow by unpredictability. Aviators, likewise, will report turbulence when the aircraft is buffeted by significantly erratic winds causing temporary fluctuations in the lift characteristics of the aircraft. This second definition is broader and will be discussed in section 1.2.4.

The importance of inertial forces relative to viscosity effects in a viscous flow may be determined by the Reynolds number, given by $\mathrm{Re} = UL/\upsilon$, where U and L are characteristic velocity and length scales, respectively, and υ is the kinematic viscosity (Arya 2001). Turbulence occurs at large Re, larger than some critical Re which is dependent on the type of flow. Large Re flow is typically found above values of 10^5 to 10^6 for the atmosphere. For large Re flow, molecular viscosity may be ignored, and the flow may be considered Reynolds number-independent (Glickman 2000). A similar ratio describes the relative importance of buoyancy to shear effects, known as the Richardson number, given by $\mathrm{Ri} = N^2/(\partial U/\partial z)^2$, where U represents the total horizontal wind. For turbulent flows, the mechanical shear will dominate the buoyant suppression in a stably-stratified fluid, thus resulting in a small Ri. A necessary condition for turbulence to occur and be maintained is for Ri to be less than a critical value $\mathrm{Ri_c}$, which is estimated to lie between 0.2 and 1 (Stull 1988; Arya 2001). A more definite value of $\mathrm{Ri_c} = 0.25$ has been determined for the dynamic instability of stably stratified flow (Miles 1961; Howard 1961).

There are several key hypotheses and theories relating to turbulence that will aid in the analysis of the model results in the following chapters. Taylor's (1938) frozen turbulence hypothesis states, in part, that if the velocity of the mean flow is much greater than that of the turbulent eddies, one may then assume that the velocity fluctuations at a fixed point in space are due simply to a pattern of unchanging turbulence passing that point. This then allows one to interchange time and spatial correlations of turbulence statistics. Kolmogorov's (1941) local similarity theory (local isotropy) is based upon Richardson's famous energy cascade hypothesis and asserts that the small-scale structure of turbulence becomes locally isotropic regardless of the large-scale flow, inferring that the smallest eddies have no "memory" of the

large-scale structure from which they draw their energy. Kolmogorov suggested that at

sufficiently large Reynolds number, there exists a range of large wave numbers where the

structure of turbulence is in statistical equilibrium (i.e., the equilibrium range) and is

uniquely determined by the dissipation and the viscosity appropriate for that range. He

further hypothesized that at sufficiently high Re, there exists an inertial subrange of wave

numbers at which energy is neither produced nor dissipated. Within the inertial subrange, the

statistical structure of the turbulence is uniquely determined by the rate of energy transfer,

which is equal to the rate of dissipation, and is independent of viscosity. The energy

spectrum in the inertial subrange is given by (Obukhov 1941):

$$E(\kappa) = \alpha \varepsilon^{2/3} \kappa^{-5/3} \tag{1.8}$$

where κ represents the wave number, α is the Kolmogorov constant (approximately 0.5 for

the atmosphere), and ε is the rate of dissipation. Fig. 1.12a shows the portions of the

Kolmogorov energy spectrum while Fig. 1.12b gives an example of such a spectrum. Of

note is that the maximum energy is contained in the larger eddies and the spectrum has a -5/3

slope in the inertial subrange. Kolmogorov also introduced the so-called microscales, which

are the smallest length, time, and velocity scales in turbulence, which are all functions only

of the viscosity and dissipation rate.

The turbulence kinetic energy (TKE) tendency equation, with the assumption of

horizontal homogeneity, is given by Stull (1988) and Arya (2001) as:

$$\frac{\partial E}{\partial t} = \frac{g}{\overline{\theta_v}} \overline{(w'\theta_v')} - \overline{(u'w')}\frac{\partial U}{\partial z} - \overline{(v'w')}\frac{\partial V}{\partial z} - \frac{\partial}{\partial z}\overline{(w'e')} - \frac{1}{\rho}\frac{\partial}{\partial z}\overline{(w'p')} - \varepsilon \tag{1.9}$$

The left-hand side of (1.8) represents the TKE tendency (or storage) term. The terms

on the right are in Reynolds-averaged flux form and are, in order, the buoyancy production or

destruction term, the U and V mechanical shear production terms, turbulent transport term, the pressure correlation term, and viscous dissipation. The buoyancy term is typically positive in the daytime convective boundary layer, because heat flux is generally directed upward from the surface, but is typically negative in the stably stratified atmosphere. The mechanical shear terms most often represent shear production, because the momentum flux is typically directed opposite the mean shear, which, when multiplied by the negative sign, becomes positive. Turbulent transport deals with the vertical trasnport of TKE and the pressure correlation term is a function of pressure perturbations, typically very small for turbulence, but often associated with waves. Dissipation, also known as the eddy dissipation rate (EDR), is proportional to TKE production, and is driven by small-scale turbulence. Fig.1.13 shows the relationship between the production, transport, and dissipation terms.

Numerical models often parameterize TKE because even the energy containing eddies are typically of a length scale smaller than the distance between model grid points. Moreover, turbulence closure becomes a problem because the addition of the turbulent flux divergence terms adds unknown variables without adding additional equations to close the set. Numerical models typically use a closure "scheme" in which the variances and covariances are parameterized. The two used in this study include a first-order Smagorinsky closure scheme and a 1.5-order TKE closure scheme. First order closure models represent fluxes with an eddy viscosity (diffusivity) coefficient, which is in turn often based on a mixing length. Separate eddy viscosities of momentum and heat (K_m and K_h) represent the momentum flux and heat flux, respectively (Arya 2001). A typical 1.5-order closure scheme maintains the eddy viscosity parameterization, but adds a modified version of the TKE

equation to the set of governing equations, as well as TKE diffusivity (proportional to the

diffusivity of momentum). For example:

$$\frac{\partial E}{\partial t} = K_m\left[\left(\frac{\partial U}{\partial z}\right)^2 + \left(\frac{\partial V}{\partial z}\right)^2\right] - K_h N^2 + \frac{\partial}{\partial z}\left(K_E \frac{\partial E}{\partial z}\right) - \varepsilon \qquad (1.10)$$

In Eq. 1.9, the familiar mechanical shear production, buoyancy production or destruction,

TKE transport, and dissipation terms are included, parameterized by eddy diffusivity

coefficients. Second- and third-order closure models exist, but are not often used in

operational forecasting. Additional options to model turbulent flow in the atmosphere

include large eddy simulation (LES) such as Deardorff (1970; 1972). These models typically

include a sub-grid scale (SGS) model such as the Smagorinsky (1963). Direct numerical

simulation (DNS), on the other hand, solves the full Navier-Stokes equations without

parameterizing the turbulence, so must directly solve for motions even at the Kolmogorov

microscales. Due to the extreme computation expense involved, DNS is confined primarily

to research endeavors (Moin and Mahesh 1998).

1.2.4. Aviation turbulence

Aviation turbulence, clear air turbulence (CAT), or aircraft turbulence are much more

subjective terms and do not imply a strict dynamic paradigm. The Glossary of Meteorology

defines aircraft turbulence as "irregular motion of an aircraft in flight, especially when

characterized by rapid up-and-down motion, caused by a rapid variation of atmospheric wind

velocities (Glickman 2000)." Lane et al. (2003) made an important point about aviation

turbulence which will have considerable bearing on this study. They mention that the flow

encountered by an aircraft may, in fact, be laminar in a dynamic sense but still be

experienced as "turbulence" because it is of a scale capable of affecting the aircraft's flight

characteristics (i.e., scales of 50 m to 1 km for a Boeing 747). For that reason this study will

distinguish between "aviation turbulence" and dynamically turbulent flow.

Aviation turbulence, when reported as part of a Pilot Report (PIREP), is further

subdivided into four categories by the FAA based on somewhat subjective criteria:

1. Light. Loose objects in aircraft remain at rest.

2. Moderate. Unsecured objects are dislodged. Occupants feel definite strains against
seat belts and shoulder straps.

3. Severe. Occupants thrown violently against seat belts. Momentary loss of aircraft
control. Unsecured objects tossed about.

4. Extreme. Aircraft is tossed violently about, impossible to control. May cause
structural damage.

The 9 December 1992 Colorado DC-8 case is a good example of the extreme case.

Significant damage did occur (including the loss of an engine and part of a wing) as seen in

Fig. 1.14. Interestingly, the NTSB report brief from that incident (available at

http://www8.landings.com) found that the cause was an "encounter with severe clear air

turbulence," yet it mentions both the structural damage and multiple "departures from

controlled flight," indicating that the "major fluctuations in speed and oscillations in both

pitch and roll" could probably be categorized as extreme turbulence. Regardless of the

terminology, the motivation to study the environments which lead to aircraft-damaging

turbulence is clear.

Aircrews may expect upper-level CAT in a number of situations. Shapiro (1976)

showed that turbulence may be expected immediately above and below the jet core and along

the upper frontal surface (Fig. 1.15). Kaplan et al. (2005a,b) found that jet entrance regions

with upstream curvature are preferred regions for CAT. Situations in which the subtropical

jet is superposed over the polar jet have also been shown in the literature to produce turbulence. Reiter and Nania (1964) examined a case of severe CAT near the tropopause over the Allegheny Mountains and found that the polar jet was undercutting the subtropical jet in that region at the time of the aircraft CAT reports. They concluded that the CAT generation mechanism was related to the thermally-stable layer between the jets. This layer was also characterized by direction shear through the depth of the layer, and a gravity wave mechanism was suspected as having generated the perturbations which eventually led to CAT. Other studies found similar undercutting jet structures such as Uccellini et al. (1986). At finer scales, perturbations to the jet, either through jet streak interactions or gravity waves (such as orographic waves) can lead to the formation of horizontal vortex tubes. Kaplan and Karyampudi (1992b) studied terrain-induced horizontal vortex tubes which were enhanced by frontogenetical tilting of the isentropes through along-stream jet circulations. Clarke et al. (2000) found along-stream horizontal vortex tubes at jet level in their simulations of the 9 December 1992 Colorado turbulence case, formed as the result of the mountain wave perturbing the jet streak. They hypothesized that the scale of these vortex tubes was such that an aircraft entering at an oblique angle would experience sufficient roll to cause the aircraft to depart from controlled flight.

In order to effectively predict regions in which aviation turbulence is likely, a number of parameters are available with which to analyze model output. Sharman et al. (2006) examined 10 turbulence algorithms and parameters for flight levels above 20,000 ft to determine their skill at predicting yes or no PIREPs of moderate or greater turbulence. The 6-hour forecast NCSU1 parameter displayed a skill of 0.832, with 1.0 being perfect skill. NCSU1 (Kaplan et al. 2006) is given by:

$$NCSU1 = \left[\vec{U} \bullet \nabla \vec{U} \right] \frac{|\nabla \zeta|}{|Ri|} \qquad (1.11)$$

This index was particularly useful in the testing of an automatic model grid nesting algorithm separately from this study while using the same real-data cases. The NCSU1 index is primarily designed to diagnose the mesoscale structures which are most likely to organize smaller-scale eddies which may lead to turbulence, or at the very least, violent motions that may affect aircraft flight characteristics. To that end, NCSU1 considers momentum advection and vorticity gradients as well as vertical shear and static stability. Relative maxima and minima of these parameters correlated well with observed turbulence in these and other cases (Kaplan et al. 2006, Lin et al 2006).

1.3. Methodology and Organization

This research project uses both observations and fine-resolution numerical weather prediction (NWP) models to examine the characteristics and evolution of fine-scale lower-stratospheric turbulent flow from the prospective of the pre-turbulent environment, .i.e., how the large-scale thermal and momentum fields facilitate the downscale organization of kinetic energy into violent eddies on the aircraft scale. This study relies heavily on two NWP models: the Stratospheric Non-Hydrostatic Mesoscale Atmospheric Simulation System (STRATONHMASS, hereafter abbreviated as NHMASS) version 6.4, and the Weather Research and Forecasting Model Advanced Research WRF (WRF/ARW) version 2.2. Initial and boundary conditions for these simulations came from the NCEP/NCAR Global Reanalysis dataset for the NHMASS simulations of the Colorado case, the Global Forecast System (GFS) model 00-hour analyses for the WRF real-data simulations of T-REX IOP 6, and from rawinsonde sounding data for the idealized two-dimensional WRF simulations.

Several other datasets were utilized for this study. The NCAR North American Regional Reanalysis (NARR) data were used as a proxy for observational data in the lower stratosphere due to the paucity of direct observations from that region. Use of NARR data as surrogate observational data does introduce some error in verification of the model simulations, but absent other datasets, is adequate. Rawinsonde and radiosonde soundings were used, as were direct aircraft observations of turbulent motions.

Two primary visualization packages were used to post-process the model output and to display the NARR data. For the two real-data case studies, GEMPAK was used to plot the model output (Koch et al. 1983). In addition to having a wealth of pre-programmed scalar and vector parameters available to the user, GEMPAK allows the user to perform further mathematical operations on the model variables prior to plotting. To convert the NHMASS and WRF output to GEMPAK format for plotting, two protocols developed by Meso, Inc., were employed. The NHMASS output "plot" files were converted using plot2gem, and the WRF netCDF output was converted using model2plot, followed by plot2gem. The idealized simulations, on the other hand, used GrADS for visualization, since it is readily compatible with two-dimensional idealized WRF output.

Chapter 2 discusses the 9 December 1992 Colorado Front Range turbulence case in depth, including both observations and NHMASS simulations. Chapter 3 describes the results of WRF simulations of T-REX IOP 6, and compares them to observations, as well as comparing IOP 6 to two other IOPs involving stratospheric gravity waves. Chapter 4 describes a series of two-dimensional idealized experiments using both previous case studies as the starting point, exploring the effects of thermal and wind profile changes and topographic changes on the upper tropospheric and lower stratospheric response to flow over

idealized terrain. Appendix A compares a series of smoothed-terrain NHMASS simulations of the Colorado case to the full-terrain simulations. Appendices B and C describe the numerical models used in this project.

1.4. Overview

The very nature of CAT (i.e., transient and nearly impossible to detect until too late) makes it a very difficult subject to research, hence it is a subject of which relatively little is understood even today. Evidence from multiple studies confirms that jet streak/mountain wave interactions can trigger severe turbulence. However, based upon the existing literature, additional research is needed in the establishment of climatological paradigms for severe stratospheric turbulence and the "connective tissue" between the synoptic-scale conditions and the aircraft-scale turbulent eddies. For example, Clark et al. (2000) briefly examined the synoptic conditions prior to a severe turbulence event but focused primarily on the meso-γ and mircroscale structure of the environment at the aircraft incident site. Other CAT studies (Uccellini et al. 1986, Kaplan et al. 2005a,b) have also focused on the large-scale environment with less discussion of the process by which it organized motions on the smaller scale. This dissertation seeks to examine the specific case of multiple jet flows over complex terrain. The questions it seeks to answer are: What configurations of upper-level circulations are optimal for mountain-wave induced turbulence? How do upper-level disturbances affect the vertical thermal and momentum profiles? How does a mountain wave perturb a jet streak? How does the kinetic energy cascade downscale from the synoptic scale to turbulent eddies at the aircraft scale? This dissertation addresses these questions through numerical simulations of two real-world cases involving direct aircraft observations of severe

to extreme CAT and a series of idealized simulations in which thermal and wind profiles are modified to examine the response in the turbulent kinetic energy fields.

The main hypothesis of this dissertation is that there exists an optimal configuration of upper-level circulations which can lead to extreme mountain wave-induced turbulence in the lower stratosphere when a strong cold layer develops below warm advection or subsidence, creating a very strong inversion directly above or associated with the tropopause. This configuration is characterized by vertically convergent flow, driven either by vertically intersecting ageostrophic jet circulations or by a strong trough and associated differential subsidence forced by differential vorticity advection. The vertical gradients of stability and jet-induced shear "prime" the environment for a downscale cascade of kinetic energy when strongly perturbed by a mountain wave. This kinetic energy is then transferred to violent turbulent eddies of a scale capable of damaging an aircraft.
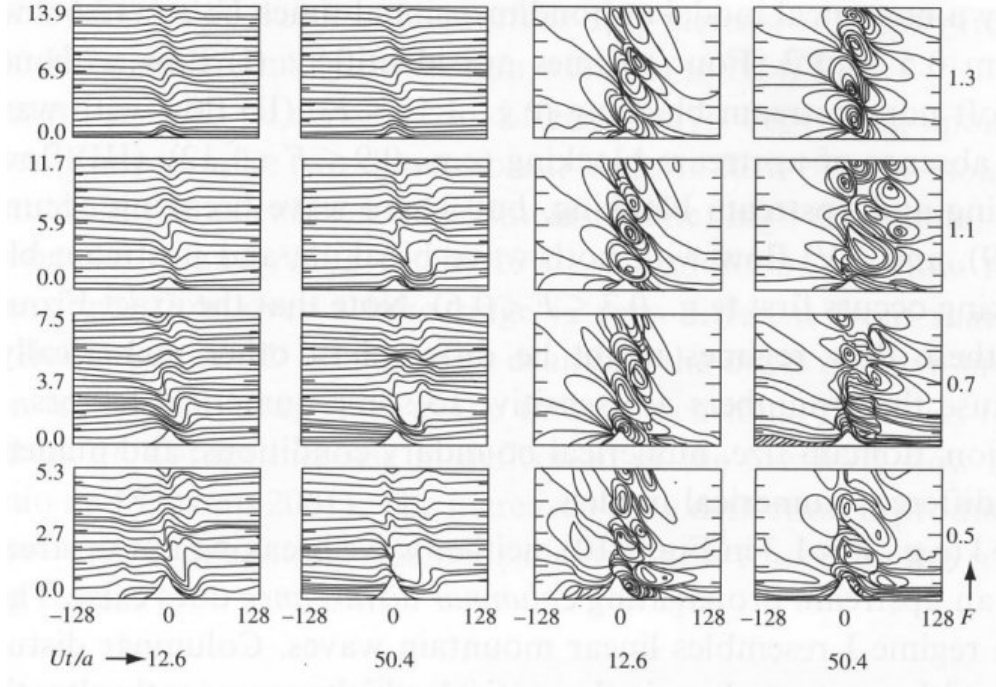
Figure 1.1: Two-dimensional numerical simulations of nonlinear responses to uniform, hydrostatic flow over a 1 km-tall bell-shaped mountain. Contours are potential temperature (left two columns) and perturbation u-wind (right two columns) for non-dimensional times Ut/a=12.6 and 50.4, where U is the base-state mean wind and a is the mountain half-width (in this case 10 km). N=0.01 s^{-1} in all cases, with U values of 5, 7, 11, and 13 ms^{-1} corresponding to F=0.5, 0.7, 1.1, and 1.3. From Lin (2007).
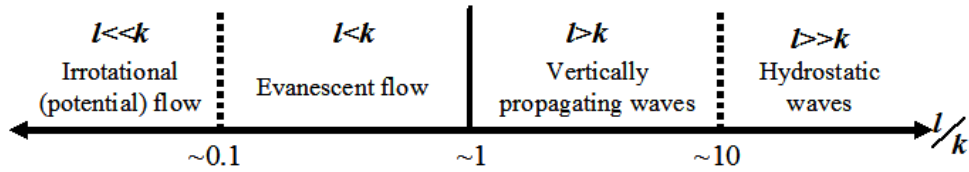
Figure 1.2: Spectrum of mountain wave regimes as a function of the ratio of Scorer parameter to wave number. Adapted from Lin (2007).
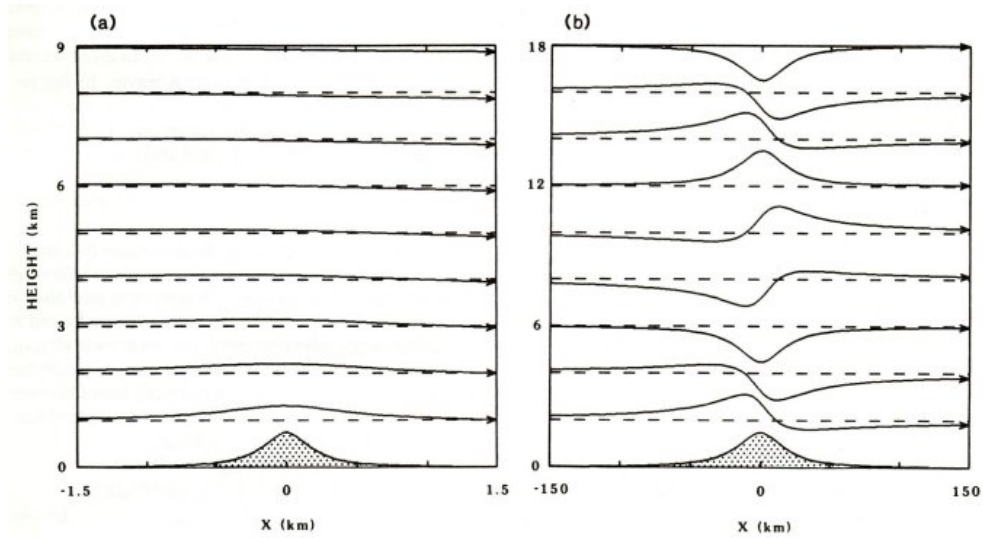
Figure 1.3: Streamlines of uniform airflow over a mountain for the (a) irrotational case where $l<<k$ and for the (b) fully hydrostatic case where $l>>k$. From Durran (1990).
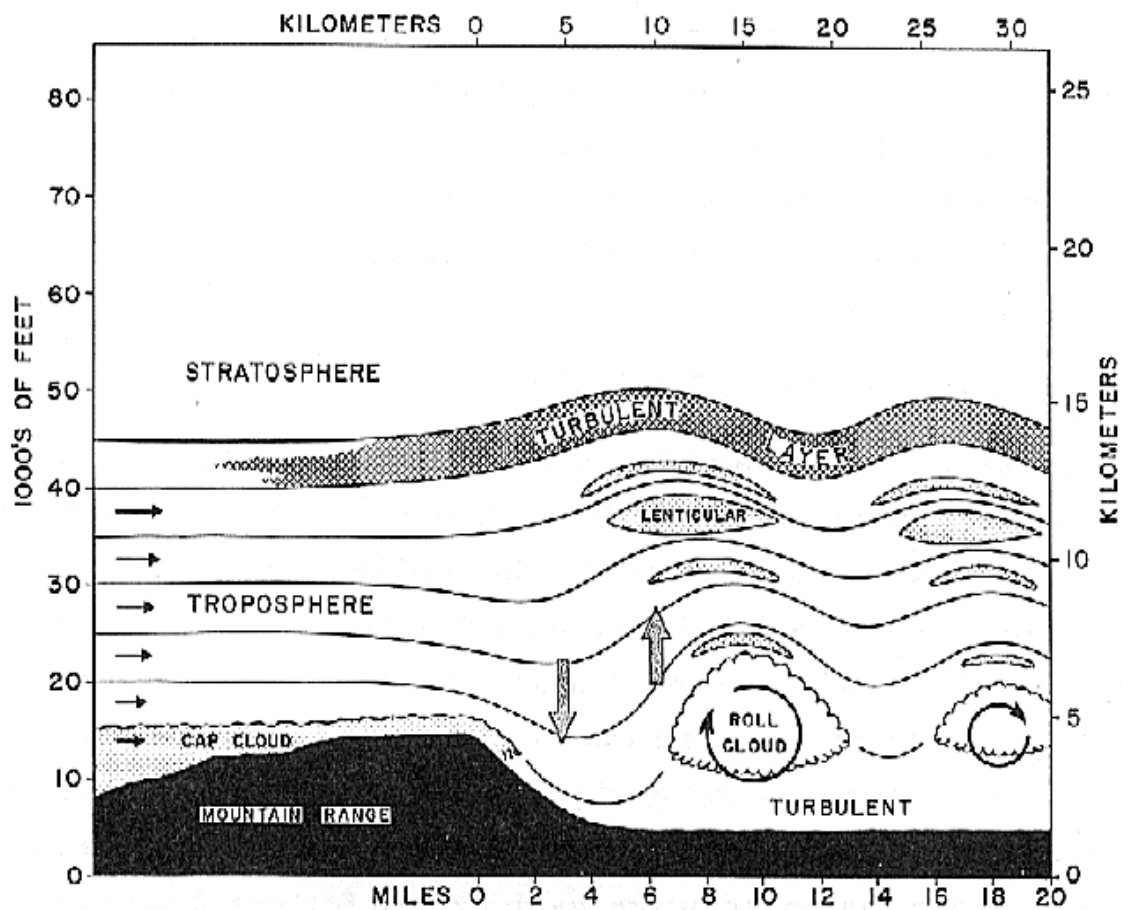
Figure 1.4: Schematic of flow over a mountain with a rotor and roll cloud (from Kuettner 1959).
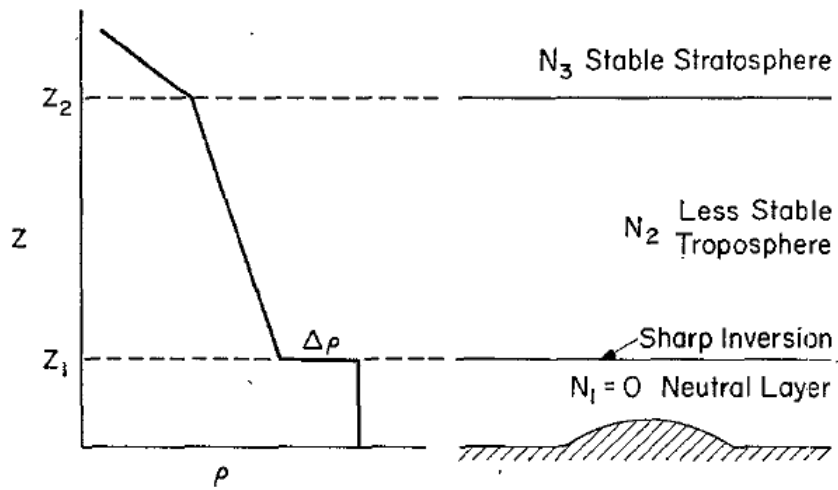
Figure 1.5: Density profile for a three-layer incompressible atmosphere from reflection amplification theory. Z_1 represents a strong inversion and Z_2 represents the tropopause (from Klemp and Lilly 1975).
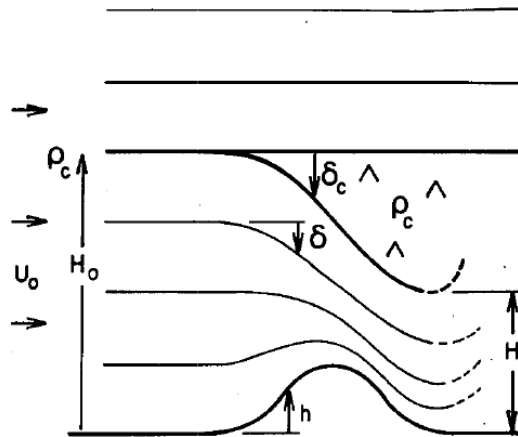
Figure 1.6: Hydraulic theory for idealized high-drag flow over a mountain. The upper contour in H_0 and H_1 denotes the dividing streamline, above the downstream side of which is the "dead region," indicated by (^). From Smith (1985).

Height (km)

Range (km)
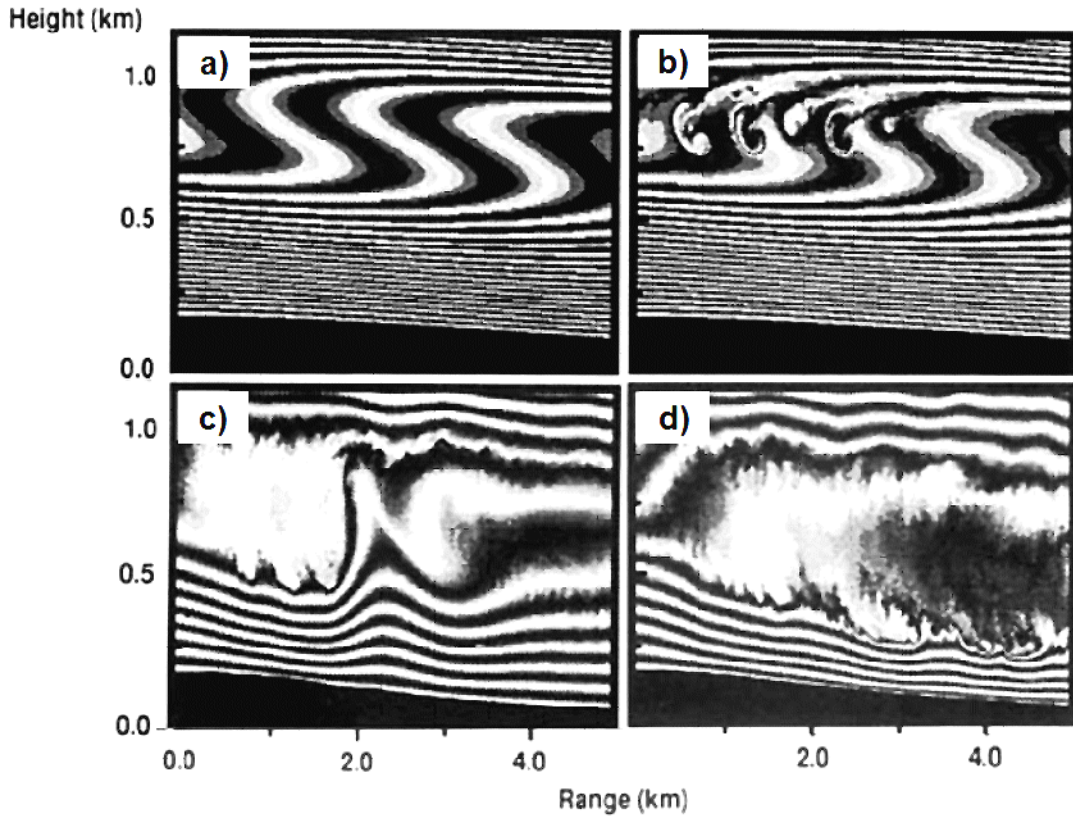
Figure 1.7:   Potential temperature fields characterizing the three stages of resonant amplification theory from a triple-nested numerical model (500 m, 50 m, and 16.667 m grid lengths). The figure depicts the lee side of a bell-shaped mountain with a height of 165 m and a 3 km half-width. The Froude number in this case is 1. Stages shown are (a) initial model time, stage 1 at (b) 20 min, stage 2 at (c) 66 min, and stage 3 at (d) 166 min. Adapted from Scinooca and Peltier (1993).
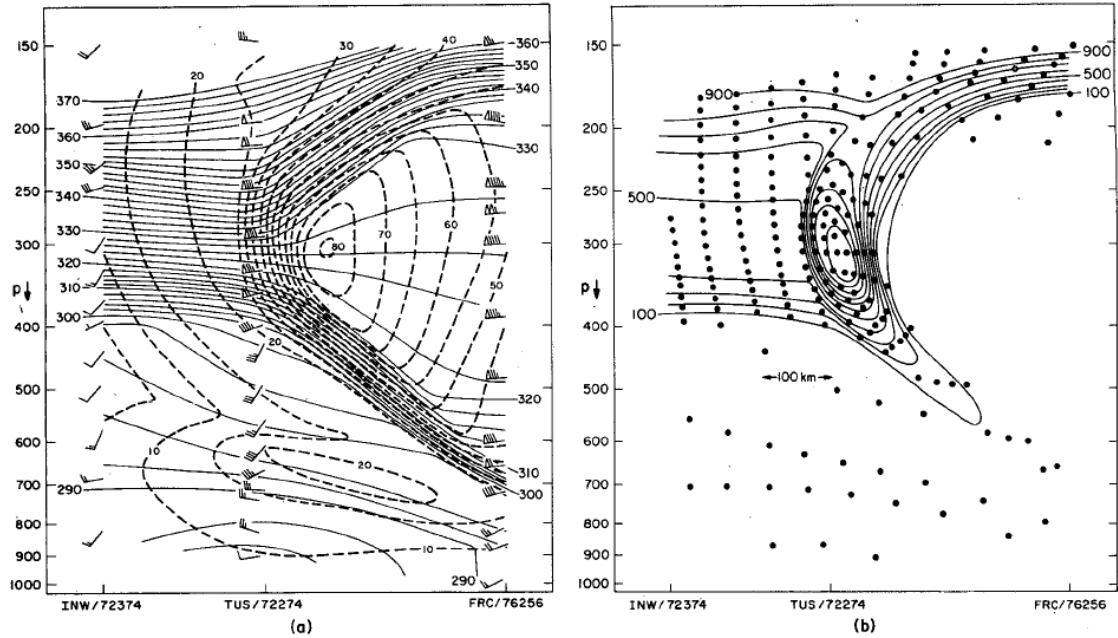
Figure 1.8: Cross-section of (a) potential temperature (solid, K), wind speed (dashed, ms^{-1}), and wind barbs (ms^{-1}) and (b) potential vorticity (10^{-7} Kmb^{-1}s^{-1}) valid 0000 UTC 17 April 1976. Vertical coordinate is pressure in mb, and data from rawinsonde soundings launched from Winslow, AZ (INW), Tucson, AZ, and Fraccionamiento, Mexico (FRC). From Shapiro (1981).

27
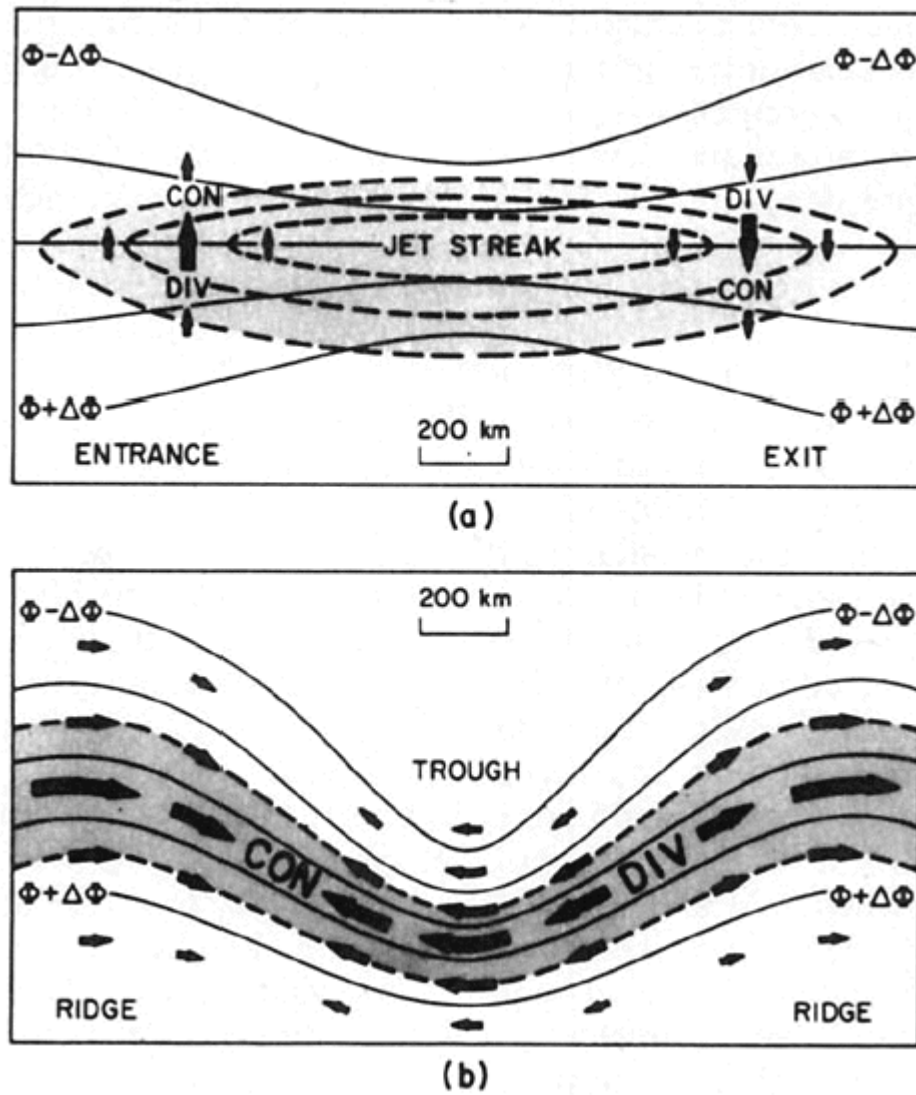
Figure 1.9: Schematic of a (a) linear jet streak and (b) cyclonically curved jet streak with notional geopotential contours (solid) and isotachs (dashed). The ageostrophic flow at jet level is shown by the vectors, with areas of convergence and divergence noted. From Shapiro and Kennedy (1981).
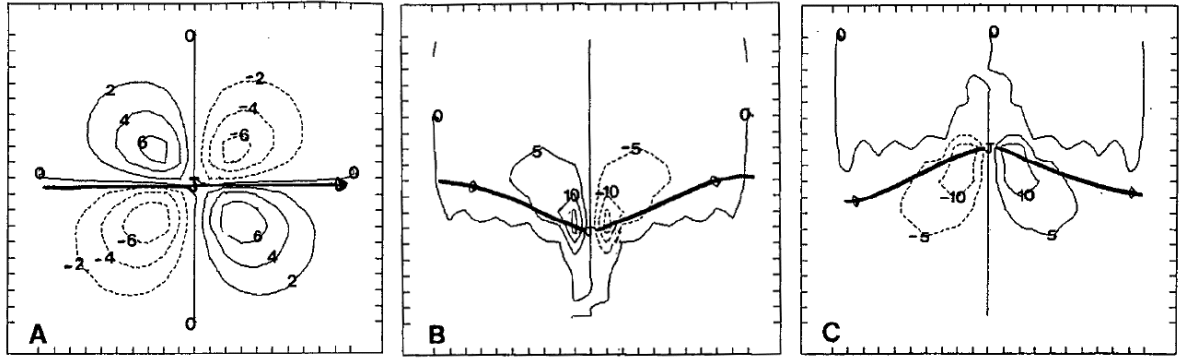
Figure 1.10: Vertical motion (10^{-1} μbs^{-1}) at 600 mb associated with (a) a linear jet streak, (b) a cyclonically curved jet streak, and (c) an anticyclonically curved jet streak, with the jet axis indicated by the heavy line. Data from initial time in a two-layer primitive equation model (From Moore and Vanknowe 1992).
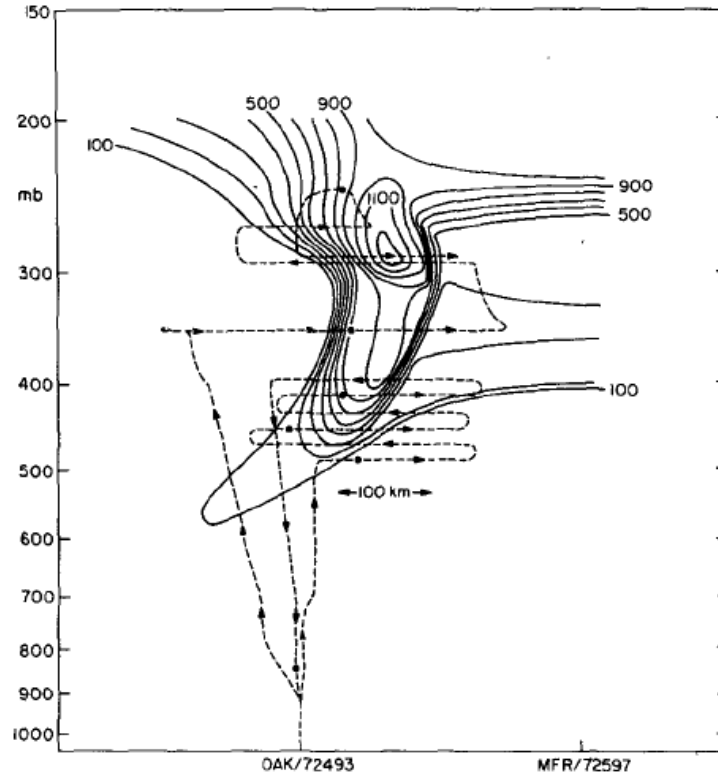
Figure 1.11: Cross-section of potential vorticity (10^{-7} Kmb^{-1}s^{-1}) valid 0000 UTC 6 April 1976 along a line from Oakland, CA (OAK) and Medford, OR (MFR). Vertical coordinate is pressure in mb, and data from NCAR research aircraft (flight track denoted by dashed line). From Shapiro (1978).
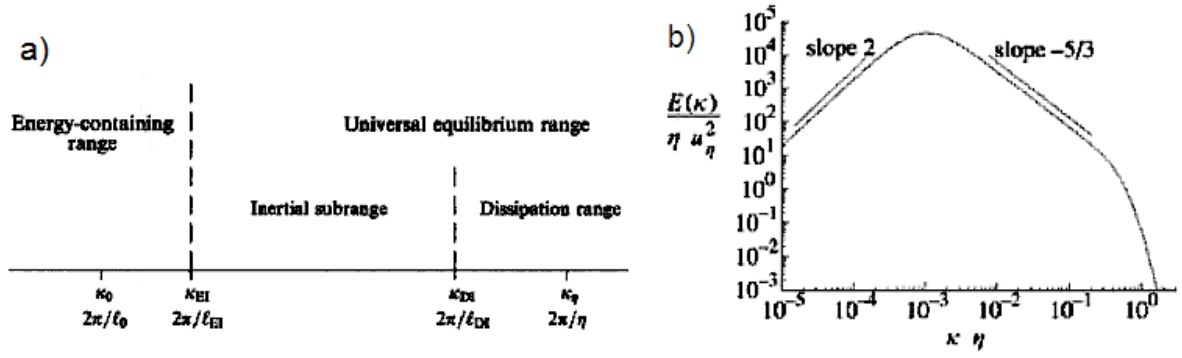
Figure 1.12: (a) Portions of the Kolmogorov spectrum as a function of wavenumber and (b) normalized spectrum at $R_\lambda = 500$ (from Pope 2000).
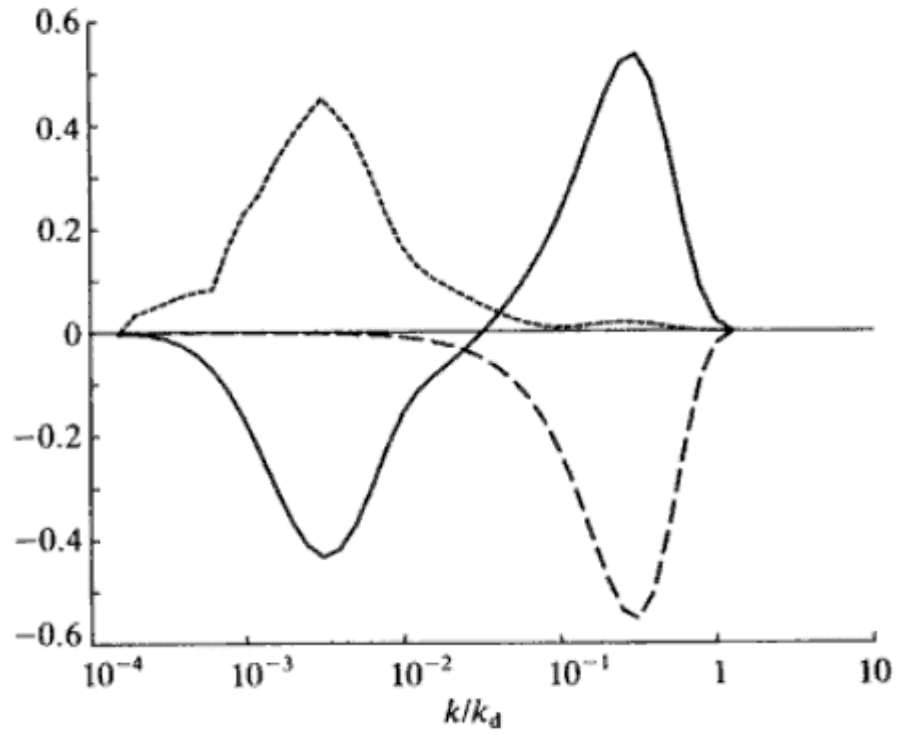
Figure 1.13: Three-dimensional spectra of the energy (short dash), dissipation (long dash), and transfer (solid), scaled by $k/k_d \upsilon^3$ where k_d is the Kolmogorov dissipation wavenumber and υ is the velocity scale (McComb 1990).

Figure 1.14: DC-8 damaged by encounter with turbulence near the tropopause along the Front Range of the Colorado Rockies at 1507 UTC 9 December 1992. The circle denotes where one engine pod and 19 feet of wind were lost.
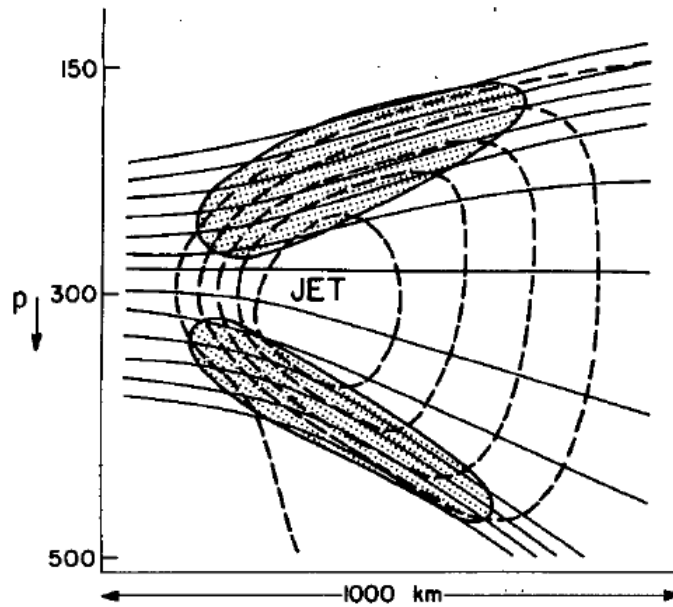
Figure 1.15: Notional schematic of the jet/front system with preferred areas of clear air turbulence shaded. Solid contours denote isentropes and dashed contours are isotachs. From Shapiro (1976).

CHAPTER 2

VERTICALLY INTERSECTING JET FRONTAL SYSTEMS AND MOUNTAIN WAVE INTERACTIONS LEADING TO THE 9 DECEMBER 1992 COLORADO SEVERE TURBULENCE EVENT.

2.1. Introduction

On 9 December 1992, interactions between a transiting jet streak and a vertically propagating mountain wave on the lee of the Colorado Rockies likely led to widespread turbulence from near the surface to the lower stratosphere. It has been shown by Clark et al. (2000) that the jet streak and mountain waves were co-located when and where severe aviation turbulence occurred. At 1507 UTC a DC-8 cargo aircraft flying at approximately 9.7 km MSL encountered severe turbulence which severed a section of wing and one of the engines (Ralph et al. 1997). Although a spectacular example of turbulence, the DC-8 incident was one of dozens of pilot reports (PIREPS) of turbulence in the area throughout the day. Clark et al. (2000) examined the case in detail, describing the general synoptic conditions of the day and then focusing on the fine-scale turbulent motions, which they theorize led to the aircraft incident. They presented observational data confirming the presence of turbulence and wave breaking, such as lidar imagery depicting a flow reversal region in the vicinity of the tropopause and figures depicting PIREPS of turbulence. They then used the Clark-Hall numerical model (Clark and Hall 1991) run at four successively finer grid spacings (25.6 km, 6.4 km, 1.6 km, and 200 m) to simulate the case using data from the National Centers for Environmental Prediction (NCEP) as initial and boundary conditions. Their simulations reproduced wave breaking, which appeared to be physically reasonable. Additionally, they found wave-like undulations associated with the jet streak

which, they hypothesized, were caused by the mountain-induced gravity waves. These wave-like undulations were further hypothesized to have produced the turbulence via the generation of horizontal vortex tubes (HVTs). Their model produced flow-aligned HVTs, which remained aloft and propagated downstream near the flight level of the incident DC-8. They concluded that an encounter between the aircraft and one of these HVTs was directly responsible for the damage to the airframe.

This case was chosen for further examination because it was known to have caused aircraft-damaging turbulence and so could be used to verify the location and timing of turbulence in model simulations. Moreover, the Clark et al. (2000) study included high-resolution model simulations and so could offer an additional means of "verification" for the structures and circulations generated by the model in the current study, since the smallest scale of motions in stratospheric aviation turbulence cases are otherwise impossible to verify with the synoptic-scale observational set. Although the 9 December 1992 is a particularly violent example of jet/mountain wave aviation turbulence, other investigators have also shown compelling proof of the importance of intersecting or complex jet structures in the environment preceding aviation turbulence. For example, in summarizing the upper-level winds at the time of the 28 January 1986 Space Shuttle Challenger explosion, Uccellini et al. (1986) documented a very similar thermal structure. Although the jet streak in their case was highly cyclonic, it was associated with a tropopause fold and a 200 hPa warm layer being undercut by a 250 hPa cold layer. Vertical cross-sections showed a distinct 150 hPa subtropical jet feature above and equatorward of the 300 hPa polar jet. In their study they hypothesized that severe turbulence was possible throughout the upper troposphere and the lower stratosphere, indicated by Ri values derived from rawinsonde data as low as 0.08

between the jets at 250 and 240 hPa. Mesoscale modeling confirmed strong isentropic perturbations and low Ri in this layer. In addition, Kaplan et al. (2005b) found that vertically-aligned jet entrance regions on 28 January 1997 led to isentropic overturning and strong vertical frontogenesis contributing to extreme aviation turbulence reported over Cape Girardeau, Missouri (CGI). In this case as well, the jet circulations resulted in a relative θ minimum extending down from Iowa at 250 hPa, capped by a high-θ ridge at 200 hPa at 1200 UTC, less than 3 hours prior to the turbulence report at 400 hPa. The stacked jet and complex thermal structures in these cases are consistent with many other case studies such as those analyzed in Kaplan et al. (2005a and 2006). Koch et al. (2005) examined an aviation turbulence event during the Severe Clear-Air Turbulence Colliding with Aircraft Traffic (SCATCAT) experiment, during which a tropopause fold associated with an upper jet/front system led to a wide spectrum of gravity waves and turbulence. Multiple tropopause structures are evident in the SCATCAT case study and two distinct upper fronts were found. Moreover, they found that the gravity wave genesis region was highly unbalanced and frontogenetical, suggesting that the largest gravity waves were generated by geostrophic adjustment associated with streamwise ageostrophic frontogenesis. The existence of two distinct, superposed jet structures associated with a complex thermal profile appears to be a relatively common thread among the published cases of extreme stratospheric turbulence, including some cases with no obvious terrain influence.

The question of the role of the larger scale environment was not addressed in detail by Clark et al. (2000); in particular, not discussed is how the synoptic and meso-α scale features established a favorable environment for and were connected to the microscale HVT's, i.e., how the flow evolved from the jet streak and mountain wave at the larger scale

to the HVTs at the aircraft scale. The intent, therefore, is to re-examine the case from a multi-scale perspective, following the evolution of the flow across a spectrum of length scales, using numerical simulations on six successfully finer nested grids ranging from 18 km to 71 m grid spacing. The hypothesis for this study is that superposition of a departing 150 hPa subtropical jet streak over an arriving 250 hPa polar jet streak established a favorable shear and stability environment for aviation turbulence, and that the mountain wave acted as a significant buoyant perturbation to this environment, thus triggering that aviation turbulence. This study differs from Clark et al. (2000) primarily in that the current study emphasizes the mesoscale "connective tissue" between the synoptic-scale flow and the microscale turbulent processes rather than on the various turbulent instability theories proposed in Clark et al. (2000) as the source for the HVTs, none of which are disputed here. In this respect, the current study compliments Clark et al (2000) by examining the scale contraction in detail.

2.2. Observational Analysis

Observations from this case were analyzed in depth by both Ralph et al. (1997) and Clark et al. (2000), so they will not be discussed in detail here. However, there are some very important observational data points that bear repeating because of their obvious relevance to the hypothesis and model results. Fig. 2.1 shows a vertical east-west cross-section of the Front Range of the Colorado Rockies in the vicinity of the aircraft incident, showing areas where turbulence was reported by aircrews on 9 December. As can be seen from this image there were numerous reports of moderate or greater turbulence at and below the lidar-indicated tropopause level (roughly 10-11 km), especially in the lee of the Front Range. Those turbulence reports closer to the tropopause and, in particular, the DC-8

involved in the incident, were likely the result of several converging factors. Fortunately there were several lidar observations taken that day from a point 10 miles north of Boulder, CO. Fig. 2.2 is a contoured summary of the lidar RHI displayed radial velocity from 1605 UTC 9 December. The "noisiness" of these observations alone indicated a turbulent, chaotic flow. However, Fig. 2.2 actually shows a flow reversal, where the local flow was directed in the opposite sense (from the east) relative to the mean flow (from the west). Flow reversal regions are often associated with wave amplification and can establish critical levels, which can serve to over-reflect and amplify waves such as those generated by mountainous topography (Clark and Peltier 1984). These waves may then extract energy from the environment and amplify, finally transferring that energy to violent turbulent eddies.

Indications of the potential for turbulent flow near the tropopause were evident in the 1200 UTC sounding from Denver (DEN) on 9 December (Fig. 2.3). There was a minor inversion found at 250 hPa. However, the tropopause was likely located within the extreme inversion at 200 hPa. As will be shown later, an unstable layer developed immediately below this level in the numerical simulations, and it is this layer that is the main focus of this study and the suspected reasons for the amplification of the turbulence which eventually damaged the DC-8. Evidence of the decrease in static stability in this layer can be seen in the temperature profile, where from 250 to 200 hPa the profile between the tropopause and 200 hPa inversion began to approach moist neutral stability. In addition to a significant vertical gradient of static stability in this layer, there also existed directional and velocity shear in the vertical which could serve to generate shearing instability. This signal reflects jet-induced perturbations likely considerably larger than the scale of the Colorado Front Range. This concept is supported by the 1200 UTC Grand Junction, CO (GJT) sounding (Fig. 2.4), which

also displays an intense inversion immediately above the tropopause, however well upstream of the aircraft incident and free of any influence of lee-side mountain wave activity.

The synoptic conditions over the Front Range on 0300 UTC 9 December (roughly 12 hours prior to the aircraft incident) were dominated by the approaching 250 hPa polar jet streak exit region and its associated upper-level front. In Fig. 2.5 from the North American Regional Reanaylsis (NARR) data, one can see evidence of a tropopause fold, as a maximum of stratospheric potential vorticity (greater than the 2 PVU value chosen as the dynamic tropopause, where 1 PVU $= 10^{-6}\,Km^2s^{-1}kg^{-1}$) was being extruded below 250 hPa consistent with a complex baroclinic structure. In this case it is clear that the tropopause fold is a region of vertically varying thermal advection consistent with complex baroclinic zones. At this time the Front Range was at the base of a deep trough between the polar jet streak approaching from the west and the subtropical jet to the southeast. As can be seen depicted in Fig. 2.5, the 250 hPa winds were veering, as the flow was transitioning between southwesterly and northwesterly flow as the trough axis passed the aircraft incident location. As one ascended to 150 hPa, the flow backed to become more westerly, as that layer was strongly influenced by the subtropical jet. By 1500 UTC, however, the aircraft incident location was in an area of strong northwesterly flow along the 250 hPa polar jet axis, but winds were considerably weaker and westerly at 150 hPa.

The vertical relationship between the jets and their associated circulations are shown in Fig. 2.6. At 0300 UTC 9 December (Fig. 2.6a) the dominant feature was the departing subtropical jet feature to the south. At that time the dynamic tropopause had been folded below 500 hPa to the south of the aircraft incident location in response to the thermally direct ageostrophic circulation in the left entrance region of the jet. Directly over the Front Range

(denoted by the lightly shaded oval) was a broad region of subsidence between 200 and 100

hPa associated with the backing winds in that layer and the departing subtropical jet. By

1500 UTC (Fig. 2.6b), the subtropical jet feature was still evident, however the core of the

250 hPa polar jet streak was arriving below and just to the north of the subtropical jet. The

aircraft incident occurred in the core of the polar jet streak in an area of strong inertial-

advective forcing within the jet exit region which was trapped below the persistent area of

subsidence above 200 hPa. From Fig. 2.6, one may infer that the vertical relationship

between the jets and their associated ageostrophic circulations, though influenced by terrain-

inducted wave motions, likely served to reinforce the shear that would be critical in the

generation of aviation turbulence. Additionally, the broad region of subsidence above 150

hPa associated with the left entrance circulation of the subtropical jet is likely to have

supported the formation the unusually strong tropopause inversion at 200 hPa seen in Fig.

2.3.

These differing flow regimes in the layer ascending from 250 to 150 hPa were

accompanied by consistently differing thermal structures in the horizontal and vertical as can

be diagnosed in the analyses of potential temperature (Fig. 2.7) and temperature advection

(Fig. 2.8). Evident is a cold layer at 250 hPa and cyclonic thermal geometry consistent with

the polar jet left exit region and weak cold air advection, which was undercutting the relative

maxima of potential temperature at 200 and 150 hPa between 0300 and 1500 UTC. At 200

hPa, a θ-ridge upstream of the accident location at 0300 UTC had settled over the Front

Range by 1500 UTC. Ascending to 150 hPa, the warm ridge was still evident upstream at

0300 UTC. By 1500 UTC, however, this ridge had passed downstream of the incident

location and weak cold air advection, consistent with the backing wind structure in this layer,

was occurring. This produced a scenario where the warm air advection in the left entrance region of the upper level subtropical jet was outdistancing the cold air advection in the lower level left exit region of the polar jet as can be inferred from Figures 2.5-2.8. The thermal structure by 1500 UTC was therefore characterized by a warm layer above a cold layer below 200 hPa and additional cold air advection above 150 hPa, forming a complex baroclinic zone that sloped northwestward with height.

Above the incident location at 150 hPa one sees a transition from neutral advection to cold air advection (-2×10^{-4} Ks^{-1}) over the period from 0300 to 1500 UTC (Fig. 2.8a-b), while at 200 hPa an area of warm air advection ($+2 \times 10^{-4}$ Ks^{-1}) propagated through the region above the incident location ahead of an area of very strong cold air advection which had reached the western Colorado Rockies by 1500 UTC. The cold air advection in the region exceeded -6×10^{-4} Ks^{-1} and was most likely the main area of along-flow cold air advection behind the upper-level front. Just 50 hPa lower, slight cold air advection (-2×10^{-4} Ks^{-1}) was occurring at the incident site at 0300 UTC and decreasing to (-1×10^{-4} Ks^{-1}) at 1500 UTC. In the 250-200 hPa layer, there was warm air advection at the top and cold air advection at the bottom, creating an extremely sharp vertical temperature gradient. The result of this differential temperature advection becomes apparent in Fig. 2.7. At 150 hPa, a high-θ ridge extended southward from Wyoming across the incident site, advecting downstream during the 12-hour period (Fig. 2.7a-b). The large-scale effect of the tropopause sinking along the north side of the jet is evident. At 200 hPa, a cold trough extended from California across the incident location to the Northern Plains, while two warm pockets associated with lower tropopause levels were apparent over Montana/Alberta and another toward the southeast over New Mexico/Texas. The tropopause fold was being advected

downstream and its static stability variation was amplified by the superposed warm air aloft and cold air below. At 0300 UTC 9 December (Fig. 2.7c) the 200 hPa surface above the incident site had a potential temperature of 348 K, however by 1500 UTC the same location had cooled to slightly 344 K, although it was now on the downstream edge of a relative maximum of θ extending down from the warm layer to the north of the jet. At 250 hPa (Fig.2.7e-f), on the other hand, a relative cold layer persisted over Colorado through 1500 UTC, advecting across the Colorado Rockies through the period. This cold advection served to destabilize the layer below the 200 hPa inversion, which in turn was being reinforced both by warm advection and by subsidence as seen in Fig. 2.6.

Based on the temperature advection (Fig. 2.8), the horizontal upper fronts were aligned in the vertical. This led to the strong vertical gradient of temperature evident in the 1200 UTC DEN sounding with a substantial vertical variation of static stability (Fig. 2.3). In this way the horizontal fronts associated with the jet streaks at different levels helped create the discontinuity that would lead to the unstable layer between 250 and 200 hPa. The importance of this structure in the 9 December case is that warm air was being advected over the region experiencing cold air advection within the left exit region of the lower polar jet resulting in a very stable layer and distinct tropopause, with the cold air advection reinforcing the static destabilization below the 200 hPa inversion. The vertical variation of the buoyancy frequency became very large when these wind and thermal advection regimes overlapped, thus creating a favorable environment for wave-induced energy reflection and vertical buoyancy gradients just above the vertical location of the lidar-observed HVTs and aircraft incident.

2.3. Numerical Simulation Experiments

The present study uses the Stratospheric Non-Hydrostatic Mesoscale Analysis Simulation System (Strato-NHMASS) Version 6.4 developed by MESO, Inc. An earlier hydrostatic version of the model was described in detail by Kaplan et al. (2000). NHMASS numerics are fourth-order accurate finite differencing for the primitive equations in terrain-following (σ) vertical coordinate. Initialization data for the control simulation's outer grid were obtained from the NCEP Global Reanalysis dataset, available at 6-hourly intervals. The outer grid was employed for 24 hours with a grid length of 18 km , and was initialized at 0000 UTC 9 December. Each inner grid then used the next outer grid information for initial and boundary conditions with one-way nesting, at grid lengths of 6 km, 2 km, 667 m, 222 m, and 71 m. The nesting strategy was chosen to ensure no scale of motion was missed between the synoptic scale and the overturning eddies as well as to maximize the influence of each parent domain on its child domain, with the intention of emulating the real scale contraction process. The smallest grid sizes were chosen so that they could resolve features of a scale capable of significantly impacting the control characteristics of the aircraft. Simulations from 18 km to 222 m were centered near the aircraft incident location (39.64 N 105.58 W) and the 71 m simulation was centered slightly west to capture the finer upstream structure. The nesting hierarchy is shown in Fig. 2.9.

The model top was set at 10 hPa. The model was run with 90 vertical (sigma) levels placing emphasis on the lower stratosphere, with $\Delta\sigma$ in the top 12 layers chosen to be 10^{-3} to optimize resolution of stratospheric turbulence features. The outermost domain had a horizontal grid of 100 x 100 cells, and the remaining domains used 162 x 162 grid cells. The two largest grid lengths employed the Kain-Fritsch cumulus parameterization with a 30-

minute call interval. No convective parameterizations were used below 6 km grid length.

All simulations used a two-dimensional Turbulence Kinetic Energy (TKE) diffusion scheme

with 1.5-degree closure (Therry and LaCarrerre 1983). A 1 km global terrain dataset was

used. In addition, a series of smoothed-terrain simulations were conducted as discussed in

Appendix A.

2.4. Simulated Perturbations of Jet/Front Systems by a Large-Amplitude Mountain Wave

As stated in Section 2.2, the region of interest for the generation of turbulence was the

unstable layer, which developed between 250 hPa and the strong 200 hPa inversion.

Therefore, it is most useful to examine the simulated evolution of the pre-turbulence

environment by focusing on how the unique temperature structure in this 250 to 200 hPa

layer 1) developed prior to and 2) was subsequently influenced by the mountain wave.

Comparing the 18 km NHMASS model output (Fig. 2.10) to the NARR data in Fig. 2.6, the

model matched the observed thermal structures quite well, although the model output

included some additional fine structure most likely associated with the terrain-induced waves

not captured by the coarser-resolution NARR data. At 150 hPa (Fig. 2.10a) a relative θ

maximum was present over the incident location, however by 1500 UTC the θ field had

become complex, most likely in response to the mountain wave. The warm ridge extending

southward from the Canadian border, however, is still evident in the data. At 250 hPa (Fig.

2.10e-f) the cold layer was still seen to undercut the warm ridge at 200 hPa, although thermal

structure was influenced by the terrain gradients and associated gravity waves. Evidence of

horizontal frontogenesis can also be seen at 200 hPa at 1200 UTC (Fig. 2.10d) associated

with a narrow horizontal wind maximum. While it is probable that this feature was related to

the standing mountain wave, the gradient of the isentropes below it at 250 hPa was considerably weaker, making it likely that the 200 hPa feature was at least partially an indication of the upper front at that level as well. This assertion has been confirmed by sensitivity simulations in which the Front Range was smoothed, which indicated the existence of a similar feature in the presence of very weak terrain forcing (see Appendix A). The jet streak placement by the NHMASS model was also quite similar to the NARR-depicted jet location. One difference of note is that the NHMASS placement of the two 150 hPa jet features was slightly south of the NARR depiction. The 250 hPa polar jet feature matched the NARR placement quite well both in magnitude and location. The primary difference between the two data sets, however, is the appearance of a series of along-flow maxima in horizontal wind speed at 1500 UTC at all levels in the NHMASS output (Fig. 2.10b,d,f). This is hypothesized to be caused by mountain wave action as will be discussed later.

Now that similarity has been established between the observed and simulated jet/front-induced meso-α scale thermal structure, the next step is to move downscale providing simulated fields which show that the mountain wave further acted to significantly perturb the polar jet streak and its baroclinic zone. Fig. 2.11a-c shows a vertical cross-section of the along-flow wind speed, potential temperature, and dynamic tropopause from the 6 km NHMASS simulation valid at 1000, 1500, and 2000 UTC. In the wind fields, meso-γ wave-like structures are apparent. These wavy perturbations were equally apparent in the cross-flow direction. Notice that the dynamic tropopause was extremely perturbed and folded, roughly following the horizontal wavelength of the mountain. The along-flow terrain wavelength from the 6 km simulation in Fig. 2.11 varied between approximately 33 and 48

km, while the horizontal wavelength of the perturbations in the jet streak were more regular and averaged roughly 45 km. The jet core propagation velocity in this case was approximately 17 ms^{-1} between 1000 and 1500 UTC, and closer to 20 ms^{-1} between 1500 and 2000 UTC. Fig. 2.12 shows the same along-flow vertical cross-section as Fig. 2.11, however it now depicts the vertical profile of stability (N^2 and Ri) and velocity divergence at 1000 and 1500 UTC (near incident time). Of note is the increase in N^2 with height as well as the vertical discontinuity in N^2 near the tropopause. It was here, in the 200 to 250 hPa layer, where signals of the most reduction in scale of the circulations near the mountain wave occurred. The velocity divergence fields showed a strong wave-like structure even upstream of the Front Range, likely generated by upstream mountain crests. The horizontal wavelength roughly matched that of the horizontal velocity field, as expected.

Viewing the west-east vertical cross-section through the incident location (Fig. 2.13), again from the 6 km simulation at 1500 UTC, one gets a sense of the accelerations in the jet streak associated with the mountain wave. Model-relative u velocity maxima in excess of 60 ms^{-1} occurred approximately 90 degrees out-of-phase from the vertical velocity maxima (Fig. 2.14), indicating the likely influence of gravity waves. The vertical wavelength of the large-amplitude standing wave when viewed in height coordinates (not shown) was roughly 2350 m. Based on linear theory (Queney 1948), one would expect a vertical wavelength for a stable, vertically-propagating hydrostatic wave to be $\lambda_z = 2\pi U / N$. In this case, the upstream conditions yielded an expected vertical wavelength of roughly 2.9 km, so it can be said to first approximation that this wave was hydrostatic. The effect of the mountain wave on the jet streak seems to be two-fold. The first was to cause both along- and cross-stream wavelike perturbations in the isotachs in the vertical cross-section. A series of local along-

flow accelerations in the horizontal wind (the 50 ms^{-1} contours in Fig. 2.13) was associated with the velocity divergence of the gravity wave (not shown for the west-east cross-section, but similar to Fig. 2.12c-d). The second effect was to bend the jet core downward from 250 hPa upstream to 300 hPa in the lee of the Front Range. Most likely, the jet core was following the downward bending isentropes associated with the downslope portion of the mountain wave configuration.

The dynamic tropopause again became highly distorted by the wave action, overturning in several places. Perhaps more significant is the cross-flow (jet-normal) vertical cross section (Fig. 2.15). The extremely chaotic vertical velocity profile is not consistent with the classic jet-streak circulation model. The meso-γ perturbation of the tropopause and the complex vertical circulations are what set the stage for the scale contraction down to microscale buoyancy perturbations and HVTs as will be described shortly. Appendix A contains comparisons between the full-terrain and smoothed-terrain simulations, supporting the hypothesis that the majority of the vertical motions associated with the full-terrain case were generated by the mountain waves, and that the mountain waves severely perturbed the jet/front environment.

2.5. Vertical Convergence/Divergence Causing HVT Formation within Strong Downdrafts

The complex vertical velocity field depicted in Fig. 2.15 clearly shows several significant vertical circulations. These intense circulations were forced at the mesoscale by the significant variations in horizontal velocity divergence associated with the mountain wave, i.e., the mountain wave distorted the larger scale vertically varying isentropes causing local accelerations that induced finer scale velocity convergence/divergence maxima and

minima. The vertical cross-sections from the 2 km NHMASS simulation (Fig. 2.16) show

the horizontal velocity divergence fields at 1000 UTC and 1500 UTC. While the structure

remained relatively consistent over the five-hour period (as expected with a nearly steady-

state standing mountain wave), the main feature of note is the broad area of divergence above

the incident level (approximately 278 hPa) and convergence below. Several features from

the NHMASS simulations indicated the existence of vertical circulations (about the along-

flow axis) at multiple wavelengths.

As the mountain wave perturbed the pressure gradient force associated with the large-

scale sloping baroclinic zone at the tropopause, the result was the generation of vertical

variations in the velocity divergence fields, which in turn served to intensify the vertical

circulations by modifying the differential vertical advection of momentum. The role of the

mountain wave was to provide a continuous and meso-β scale source of pressure

perturbations, velocity divergence perturbations, and non-uniform upward vertical motion

resulting in non-uniform vertical advection of momentum. This forcing served to displace

and intensify the stable layer above 200 hPa from below, which was trapped from above by

the descent and convergence associated with the departing 150 hPa subtropical jet feature.

Between 1000 UTC and 1500 UTC the 340 K to 380 K layer became trapped and

compressed between the upward vertical motion from the mountain wave (Fig. 2.14) and

growing subsidence above the polar jet. Fig. 2.17 shows the change in height for the 340K

and 380K surfaces and the resultant reduction in layer thickness due to this vertical

convergence. The values for the isentropic surfaces' heights were calculated as a simple

mean of the height values between a point one degree longitude west of the incident location

and a point one degree east, in order to remove the oscillatory effect of transient waves

through these surfaces. As expected from mass continuity, the aforementioned expansion

and compression of the isentropes strengthening the inversion layer is analogous to

vertically-directed confluence at the meso-γ scale of atmospheric motion. This vertically

varying mass flux convergence and divergence and its resulting vertical perturbation of the

potential temperature fields led to the modified vertical temperature gradient by intensifying

the stable layer above 200 hPa while continuing to de-stabilize the layer below. The 340 K

isentrope can be taken to represent the lower boundary of this stable layer, whose stability

increased through time due to the compression by the vertical motions induced by the vertical

variation of velocity divergence.

The resultant vertical convergence (stretching and compression) from the 667 m

NHMASS simulation is indicated in Fig. 2.18. The intensity of this vertical convergence

increased over time, such that localized regions at 1506 UTC indicated *dw/dz* in excess of -

$5 \times 10^{-3} s^{-1}$, showing significant layer compression at small scales. Fig. 2.19 shows the

perturbation vertical velocity calculated as a departure from spatial mean values of model

output fields following Lane et al. (2003). Fig. 2.19a shows larger values of w' (in excess of

$\pm 5 \ ms^{-1}$) at a height of 9.75 km (approximately the altitude of the aircraft incident) than at 11

km (Fig. 2.19b, within the stable layer). This differential vertical motion, forced by the

smaller-scale terrain perturbation of the pressure gradient, was directly responsible for the

fine scale vertical convergence field depicted in Fig. 2.18.

The result of these vertical motions and the contraction of the stable layer above 200

hPa was the continued amplification and stretching of the aforementioned unstable layer

between 250 hPa and 200 hPa (primarily below 340 K) in which the Brunt-Väisäla frequency

and the Richardson number both decreased relative to the layers above and below it, as a

response to the decrease in stability and increase in shear through the layer. At approximately 1507 UTC, values of N^2 in the unstable layer approached zero just above and upstream of the aircraft incident, indicating static instability (Fig. 2.20). Also within this layer, Ri dropped below 1, with isolated pockets of Ri below the critical value of 0.25, satisfying a necessary condition for shear instability (Miles 1961; Howard 1961). At this point waves began to amplify and achieve near breaking due to shearing instability, as indicated by the overturning 342 K isentrope in Fig. 2.20.

The horizontal gradient of vertical motion near vertically varying horizontal wind shear layers simulated with multiple wavelengths (Figs. 2.15 and 2.19) clearly provided a potent source of horizontal vorticity where shearing instability was occurring. Fig. 2.21 shows the x axis $(\partial w/\partial y - \partial v/\partial z)$ and y axis $(\partial u/\partial z - \partial w/\partial x)$ components of relative horizontal vorticity with the viewer looking east and north, respectively at 1507 UTC from the 222 m simulation. Since the flow was west-northwesterly, the x axis component (Fig. 2.21a) was closest to being flow-aligned, and shows the maxima of negative horizontal vorticity that are the predecessors to possible HVTs, i.e., the environment was primed for horizontal rotation and might rotate violently if additional vertical velocity gradients were organized at near turbulent length scales. The core of these features showed relative vorticity maxima of -1×10^{-2} s^{-1} at approximately $10 - 11$ km. Notice also the significant gradient of horizontal vorticity at the aircraft flight level, with positive values below and negative values above.

As was mentioned previously, the differential vertical advection of momentum was critical in the establishment of the highly-perturbed environment into which the DC-8 flew on 9 December 1992. Fig. 2.22 is the 222 m NHMASS depiction of the vertical momentum

and heat flux divergence in the layer between the aircraft incident level (9.75 km) and 11 km

MSL. The perturbations were calculated as the local model grid point departure from a

domain-area average as before. These fields show both positive and negative values in close

proximity, most likely due to the influence of high-frequency gravity waves. When averaged

over the domain, both the u and v components of the vertical momentum flux divergence

(Figures 2.22a and 2.22b) had net negative values (-4.3 × 10^{-6} ms^{-2} and -4.9 × 10^{-6} ms^{-2},

respectively), indicating vertical momentum flux convergence into this layer. The 9.75 km

$\overline{u'w'}$ had a net upward directed flux (2.8 × 10^{-3} m^{-2}s^{-2}) while at 11 km it had a net downward

flux (-2.6 × 10^{-3} m^{-2}s^{-2}). This is consistent with a highly perturbed environment and is

indicative of the compression and deformation hypothesized to be present within this layer.

Fig. 2.22c depicts a strong up-ward directed vertical heat flux in the vicinity of the aircraft

incident. However, averaged over the domain, the net heat flux (1.0 × 10^{-7} Ks^{-1}) was

divergent and downward-directed, consistent with the presence of the strong thermal

gradient.

Parcels ascending or descending as a result of the horizontal vorticity would be

subjected to considerable changes in buoyancy. This vertical gradient of buoyancy near the

interface of the unstable and stable layers is crucial to understanding how the HVTs may

result. It can be expected that a parcels displaced upward by the ascending branch of an

HVT along the extreme inversion at 200 hPa would develop significant negative buoyancy.

Figure 2.23 depicts a model-derived sounding from the 222 m NHMASS simulation at the

location and time of the aircraft incident. While the model did not depict as abrupt an

inversion as was visible from the DEN sounding (Fig. 2.3), the model did still capture the

overall complexity of the thermal structure. The coarse vertical resolution of the

initialization data (50 hPa separate the vertical layers near 200 hPa) prevented the model

from capturing the extreme discontinuity at 200 hPa. An interesting feature of the sounding

in Fig. 2.23 is a super-saturated layer centered at 175 hPa. Examination of the NHMASS

222 m simulation's microphysical fields (not shown) indicated a cloud layer centered at 175

hPa. This is consistent with satellite imagery from 1506 UTC 9 December 1992, which

indicated the presence of some high cloudiness in the vicinity of the tropopause over the

incident location (Clark et al. 2000). However, the model appears to have been producing

precipitation, suggesting that sublimational cooling below the 175 hPa cloud layer may have

contributed to further static destabilization of the cold air at and below 200 hPa in the model.

Moreover, the larger layer from 250 hPa to 175 hPa in Fig. 2.22 forms almost an "inverted

V" sounding of the type often associated with micorbursts (Wakimoto 1985).

This microburst-like mechanism may have served to reinforce the vertical circulations

associated with the horizontal vorticity. Clarke et al. (2000) found a turbulent downburst in

their simulations of this case, which they attributed to wave-breaking. Similar downburst-

like phenomena were found in the current study. Such an intense inversion as seen in Fig.

2.3 has been shown to reflect gravity waves (Lindzen and Tung 1976). The large-scale

waves can grow in the presence of this downward-reflected energy (Klemp and Lilly 1975),

and should they break (as seen in Fig 2.20), over-reflection becomes possible (Clark &

Peltier 1984) allowing the small-scale waves to extract energy from the base state. Growth

of these smaller waves is likely responsible for what the aircraft feels as "turbulence." The

inversion capped this wave-breaking layer, and while one should expect through mass

continuity that the column of air directly above a parcel oscillating in wave motion would

also be vertically displaced and should oscillate, the parcels above the inversion in this case

would be subject to far more negative buoyancy than below, given the rapid increase with height of N^2. This downward-directed force could have reinforced the normal descent associated with the downward component of the oscillation, but could also have served to reinforce downward components of the horizontal shear-generated vortices at the interface found both the NHMASS output and the Clark et al. (2000) simulations. It is also possible, though difficult to prove, that the NHMASS model was also generating downbursts through sublimational cooling as noted above. Phasing between the descending branch of the HVT circulations and the downward-directed energy from an over-reflected wave would cause the appearance of such a downburst phenomenon as well. The vertical cross-section of circulation in the east-west plane in Fig. 2.20 shows substantial simulated descent consistent with a downburst just above and upstream of the aircraft incident location. Note that the "downburst" was located between the low N^2 and Ri region in which wave breaking was occurring. The hypothesis is that the turbulent downburst which caused the damage to the DC-8 was caused by a transient turbulent "downburst" caused by wave-breaking above the aircraft flight level, reinforced by the strong static stability gradient and perhaps enhanced by sublimational cooling beneath the cloud.

Koch et al. (2005) described the horizontal scale of eddy overturning for CAT as 100-300 m. The 71 m simulation begins to approach large eddy simulation, and it produced eddies with a horizontal scale on the order of a few kilometers. A horizontal depiction of the 275 hPa (incident pressure level) vertical motion field from the 71 m simulation (Fig. 2.24) shows a band of negative vertical velocity just upstream of the incident location with a maximum value in excess of -7.5 ms^{-1} to the southwest. The 222 m NHMASS simulation showed that while these individual intense negative vertical velocity features were

themselves transient (lasting between one and three minutes), their magnitude continued to reach -5 to -10 ms^{-1} 30 minutes either side of the incident time, indicating the presence of turbulent downbursts throughout that period. Such a downburst, in the presence of vertical wind shear and in an environment already exhibiting horizontal rotation, may be an effective mechanism for forcing a deviation from controlled flight at the scale of an aircraft, i.e., tipping a wing thus resulting in a brief loss of pilot control. Given a typical cruise speed for a DC-8 of 222 ms^{-1} (roughly 500 mph), the aircraft would have transitioned between these updrafts and extremely intense downdrafts every 9 seconds. One could hypothesize that such extreme changes in lift over such a short period of time would be more than adequate to prevent the aircrew from making the necessary adjustments in the flight controls to avoid damage to the airframe. That Clark et al. (2000) also described the presence of similar turbulent downbursts in their simulations serves to verify that these features are not an artifact of the model or analyses.

2.6. Conclusions

Observations and numerical simulations provide evidence that the interactions among vertically stacked jet/front systems and a standing mountain wave generated the environment favorable for extreme turbulence affecting a DC-8 on 9 December 1992. The downscale structure of these circulations was examined, starting with the complex temperature structure associated with the jet circulations in the 250 to 150 hPa layer and the 3-dimensional perturbation of both the jet streak and the tropopause by the mountain wave. This process occurred in the larger scale environment where the vertical static stability variation in the stratosphere was pre-existent as a result of the polar and subtropical jet/front systems. The mountain drag induced wave-like perturbations and accelerations within the jet streak. The

vertical circulations associated with this mountain-wave-perturbed jet environment amplified the non-uniform vertical temperature and shear structure including the pre-existing unstable layer below 200 hPa capped by an intense inversion above 200 hPa. This supported the generation of higher-frequency gravity waves. A wave-breaking level developed immediately below the inversion at 200 hPa, resulting in enhanced local increases in horizontal vorticity within the shear layer resulting in a feature analogous to Clark's hypothesized HVT circulation. These horizontal vortices interacted with breaking waves to generate a downburst-like phenomenon which may have been reinforced by sublimational cooling due to precipitation in the NHMASS simulation. Thus the mountain wave and dual jet streaks are hypothesized to have acted to generate the pre-turbulence environment which led to the formation of a turbulent downburst. The precursor signal that this could happen would be the vertically intersecting jet/front systems in proximity to strong flow across complex terrain.
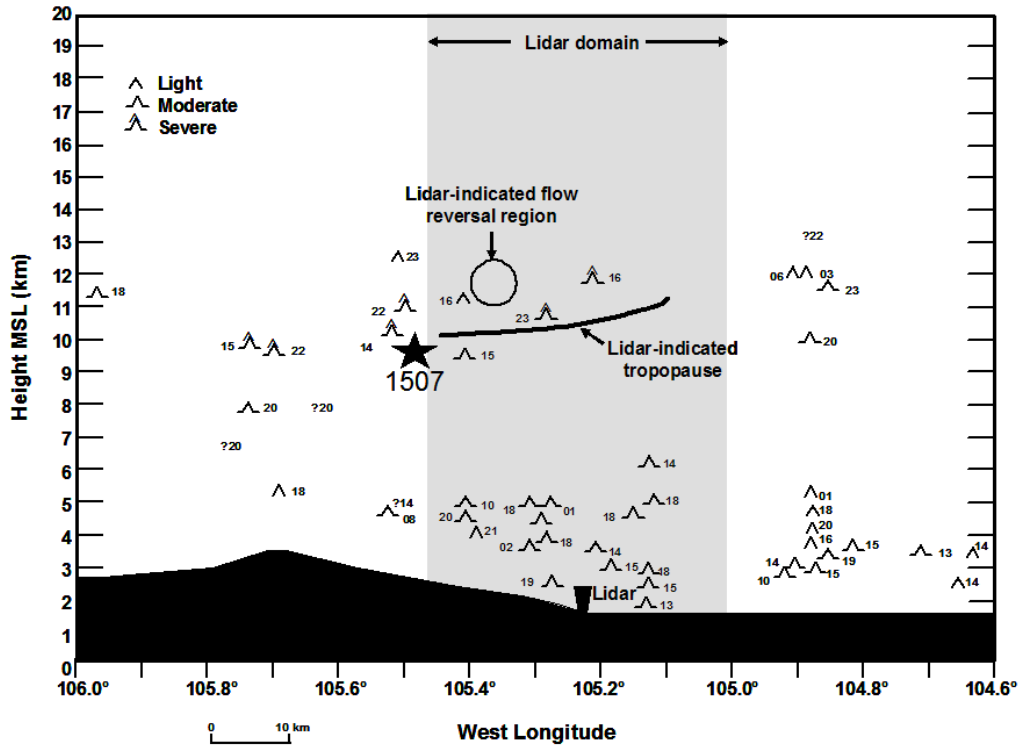
Figure 2.1: Cross-section through accident location (marked with a star) showing location and times (to nearest hour UTC) of pilot reports of turbulence between 39.5° N and 40.3° N latitude (by intensity, where available), lidar position and domain, and lidar-indicated flow reversal region and tropopause for 9 December 1992. Adapted from Clark et al. (2000).
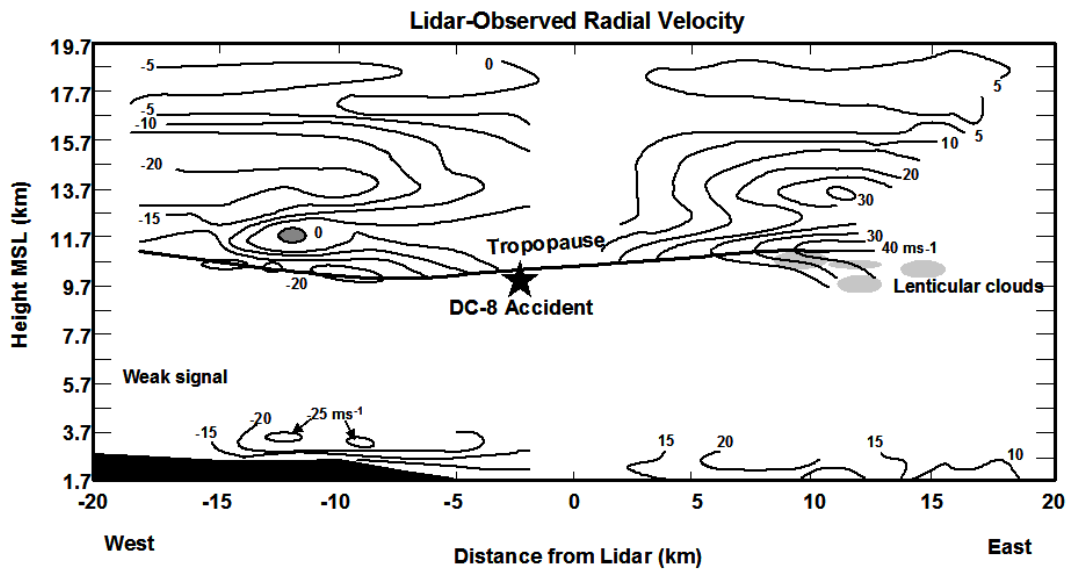
Figure 2.2: Contours of Doppler lidar-observed radial velocity (ms^{-1}) in east-west RHI scan from 1605 UTC 9 December 1992. From 10-μm CO_2 NOAA/ERL/ETL lidar located 10 miles north of Boulder. Scan was 60 seconds long at $3°s^{-1}$. Flow reversal region indicated by shading inside 0 ms^{-1} contour. Adapted from Clark et al. (2000).
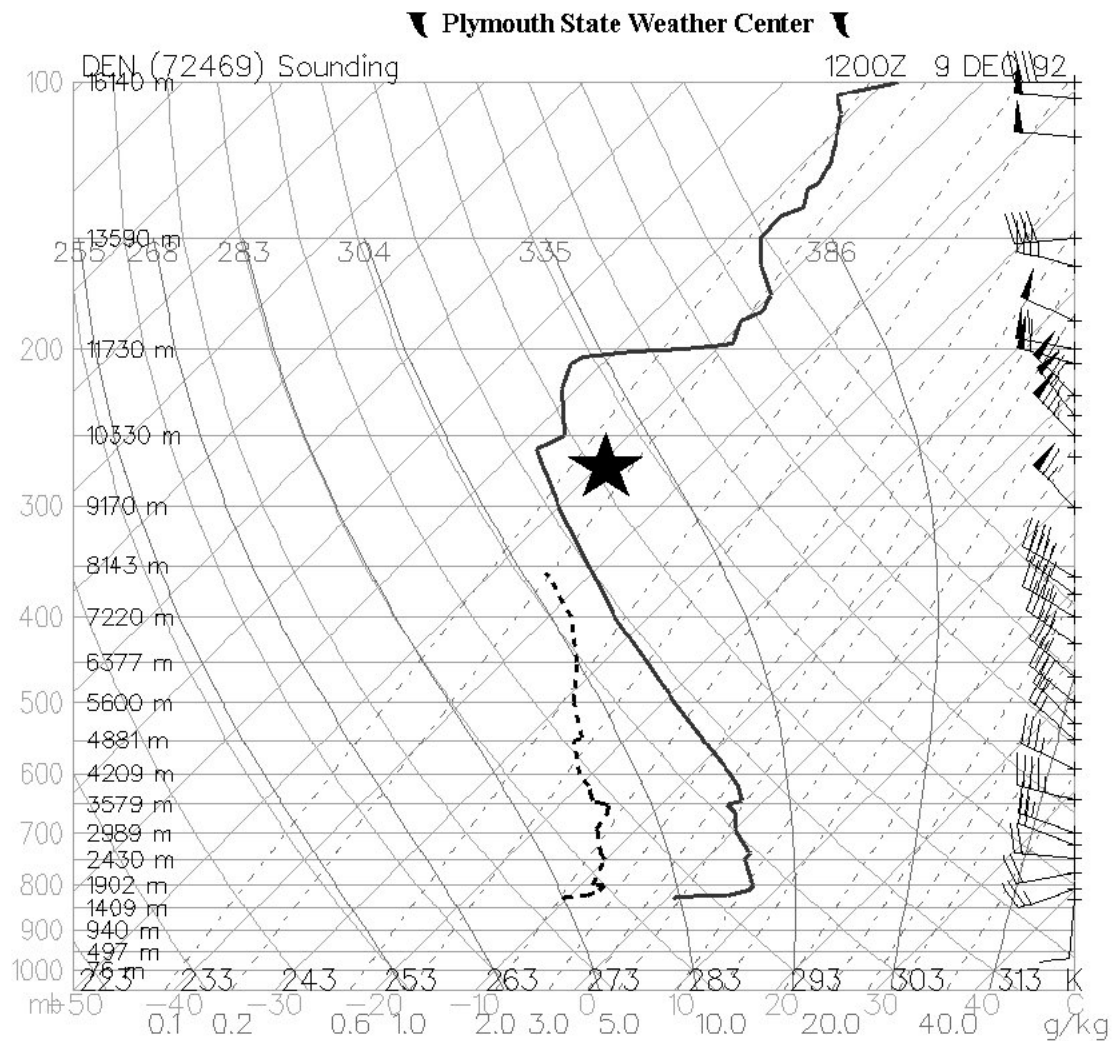
Figure 2.3: Skew-T, Log-P diagram from the 1200 UTC 9 December 1992 Denver, CO rawinsonde sounding. The star marks the aircraft level. From Plymouth State Weather Center.
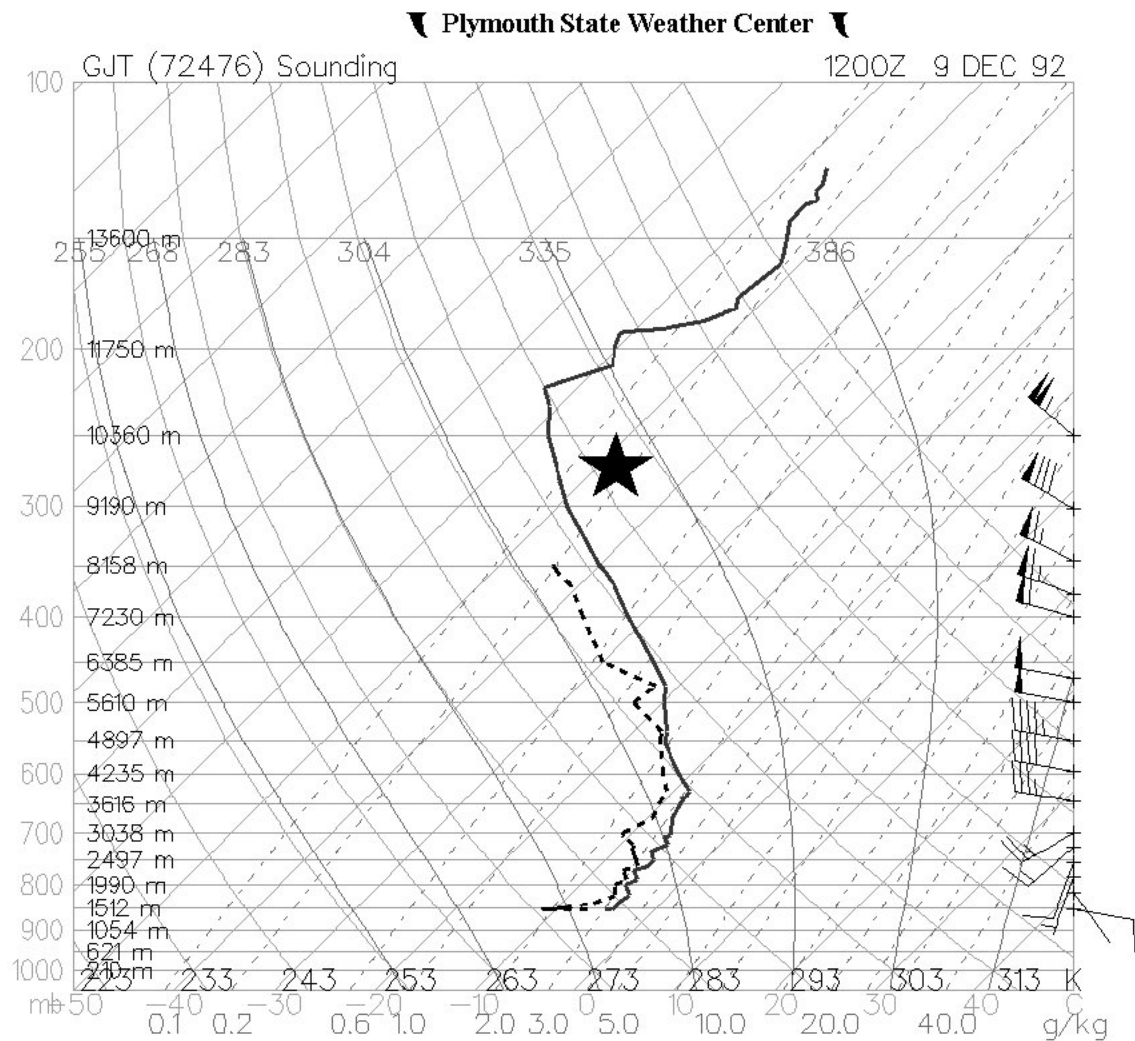
Figure 2.4: Skew-T, Log-P diagram from the 1200 UTC 9 December 1992 Grand Junction, CO rawinsonde sounding. The star marks the aircraft level. From Plymouth State Weather Center.
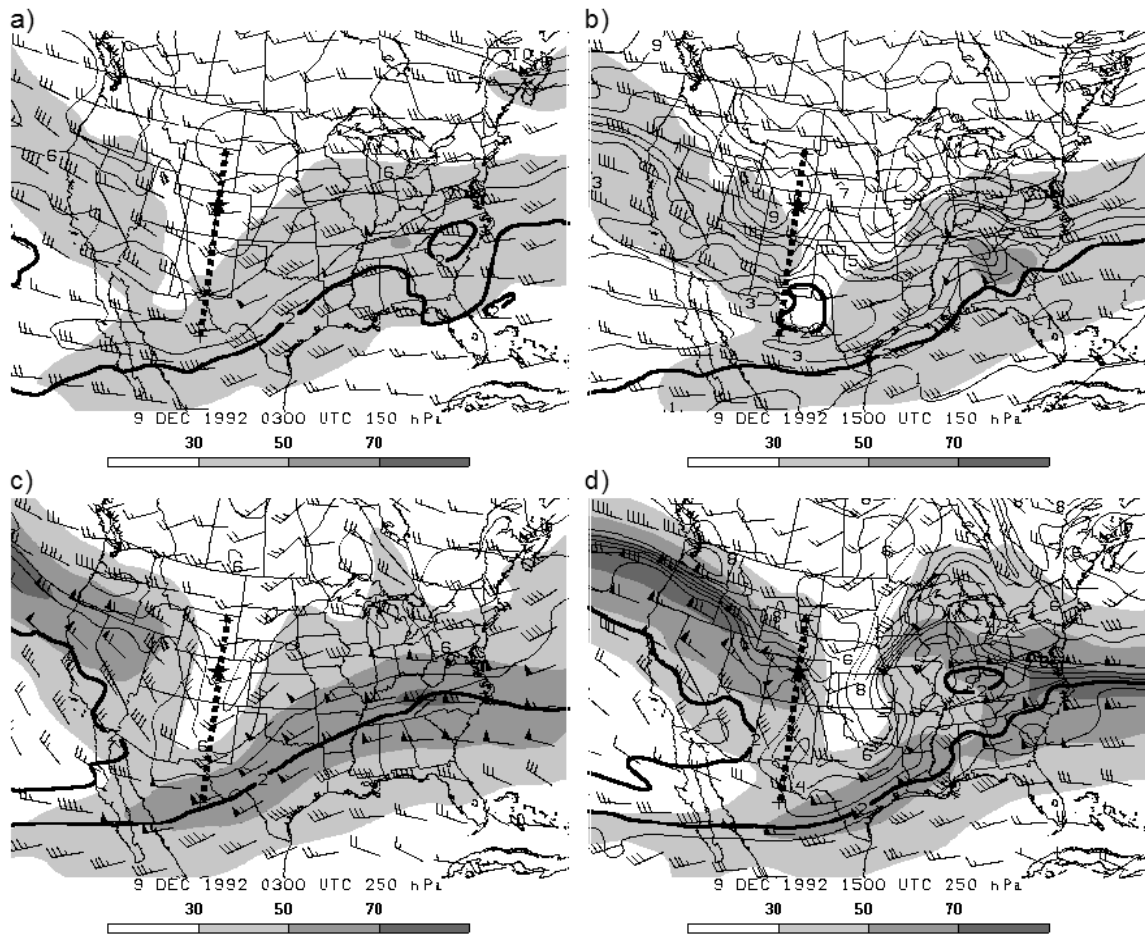
Figure 2.5: Wind speed (ms^{-1}, shaded) and potential vorticity (PVU, or 10^{-6} Km^{2}s^{-1}kg^{-1}) at (a-b) 150 hPa and (c-d) 250 hPa at 0300 UTC (left column) and 1500 UTC 9 December 1992 (right column). Data from NCEP/NCAR North American Regional Reanalysis. Dynamic tropopause (2 PVU) depicted by bold contour. Data was smoothed with six passes of a Gaussian filter to eliminate noise after winds were corrected from model-relative to true. Cross-section for Fig. 2.6 denoted by dotted line. Aircraft incident location denoted by star.
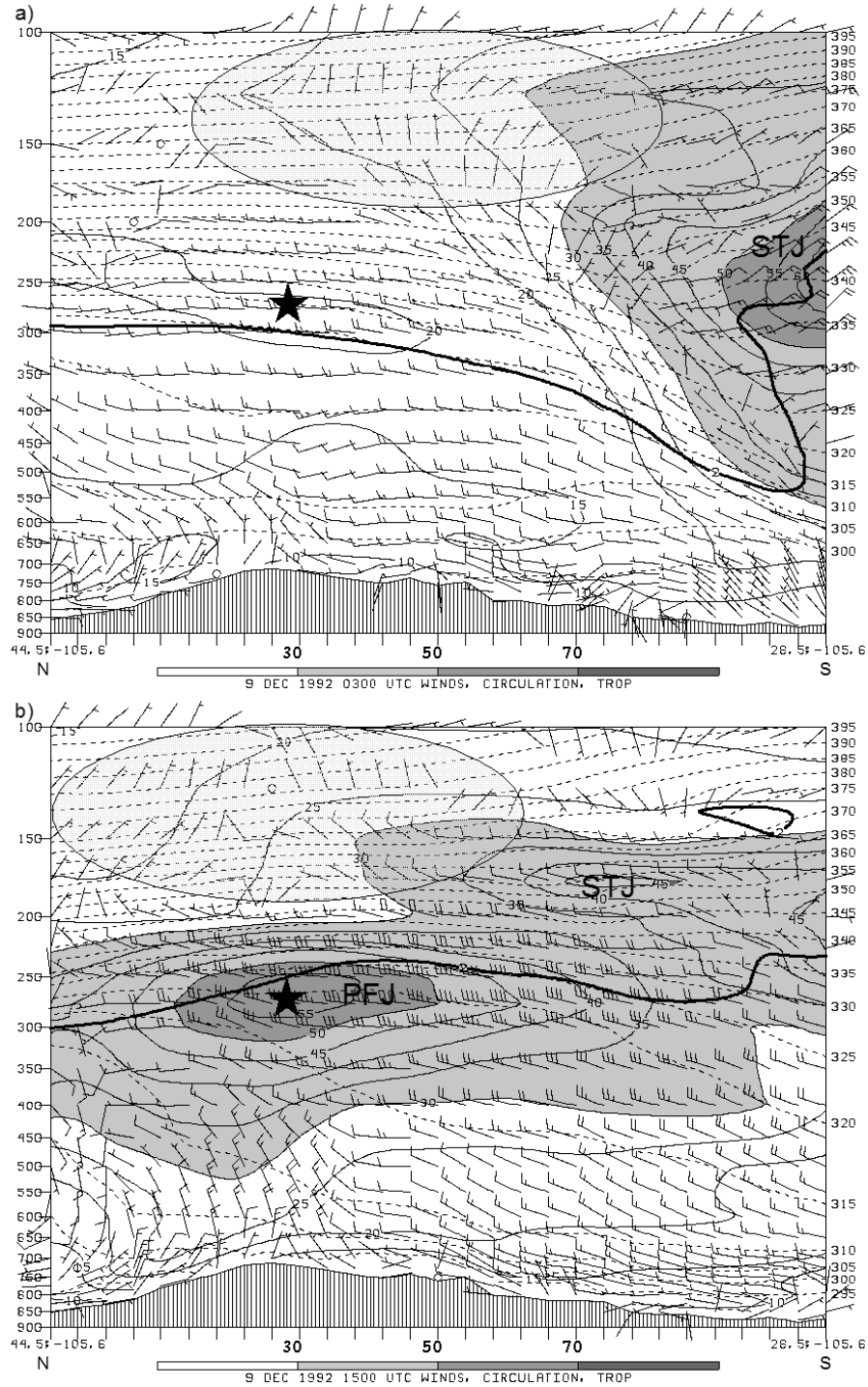
Figure 2.6: North-south vertical cross section of wind speed (ms^{-1}, shaded and solid contours), potential temperature (K, dashed), and circulation (ms^{-1}, wind barbs) at (a) 0300 and (b) 1500 UTC 9 December 1992 along dashed line shown in Fig. 2.5. Subsidence region denoted by shaded oval. Dynamic tropopause (2 PVU) depicted by bold contour. Data from NCEP/NCAR North American Regional Reanalysis. Data was smoothed with six passes of a Gaussian filter to eliminate noise after winds were corrected from model-relative to true. Aircraft incident location denoted by star. Horizontal scale is 64 km per tick.
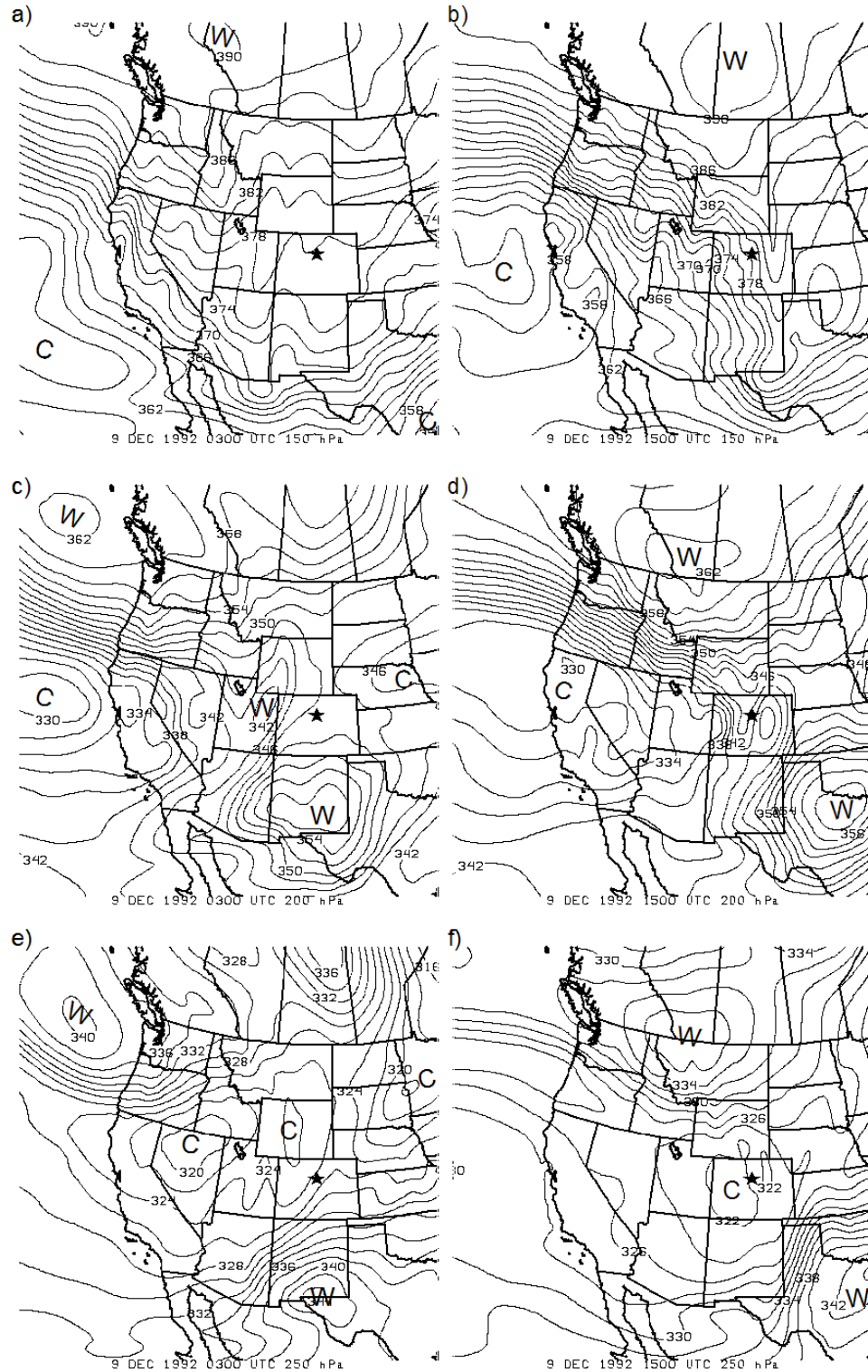
Figure 2.7: Potential temperature (K) at (a-b) 150 hPa, (c-d) 200 hPa, and (e-f) 250 hPa at 0300 UTC (left column) and 1500 UTC 9 December 1992 (right column). Warm maxima and cold minima dnoted by "W" and "C," respectively. Data from NCEP/NCAR North American Regional Reanalysis. Aircraft incident location denoted by star.
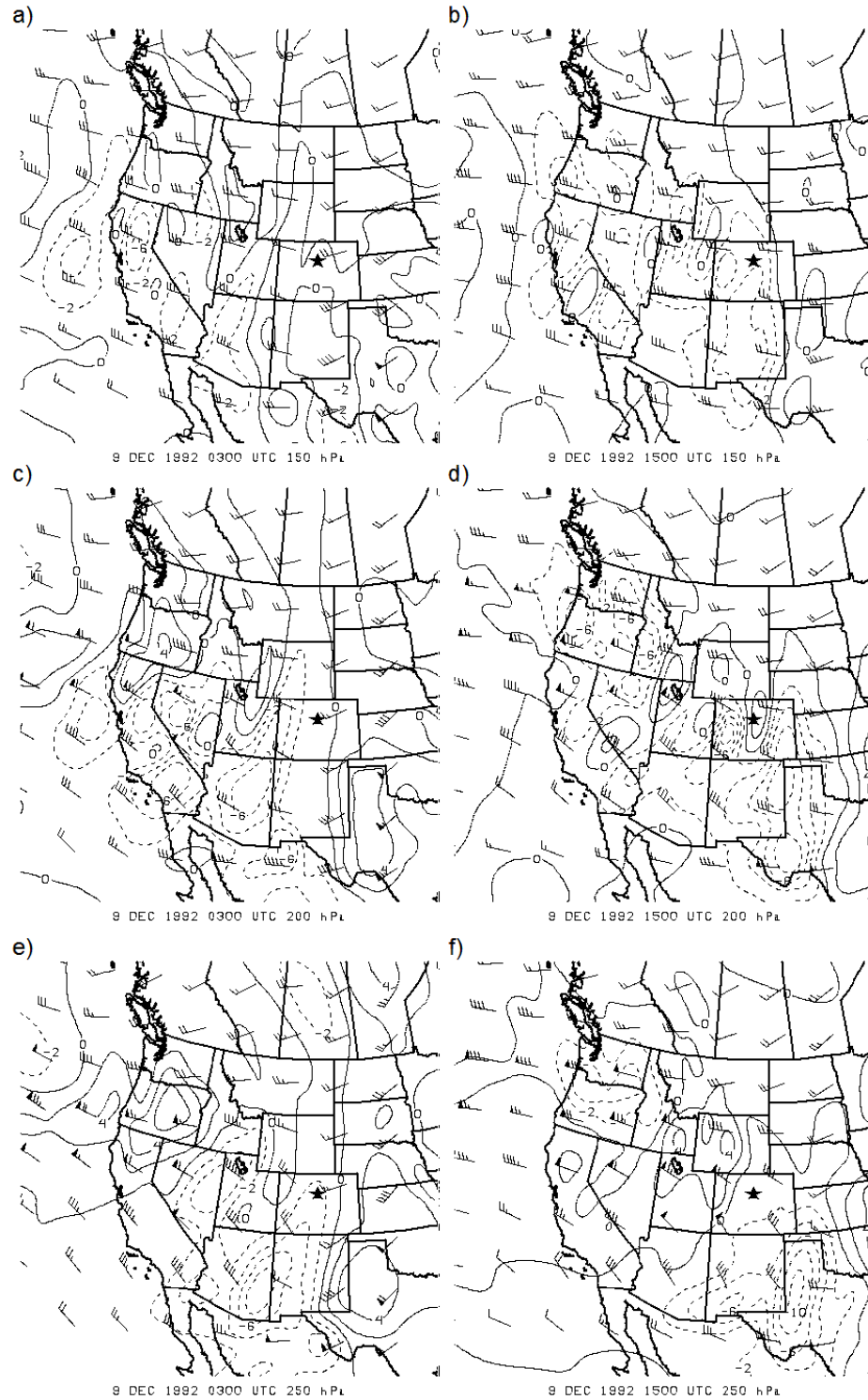
Figure 2.8: Temperature advection (Ks^{-1} × 10^{-4}) and winds (ms^{-1}) at (a-b) 150 hPa, (c-d) 200 hPa, and (e-f) 250 hPa at 0300 UTC (left column) and 1500 UTC 9 December 1992 (right column). Dashed contour indicates cold advection, and solid warm. Data from NCEP/NCAR North American Regional Reanalysis. Aircraft incident location denoted by star.

60
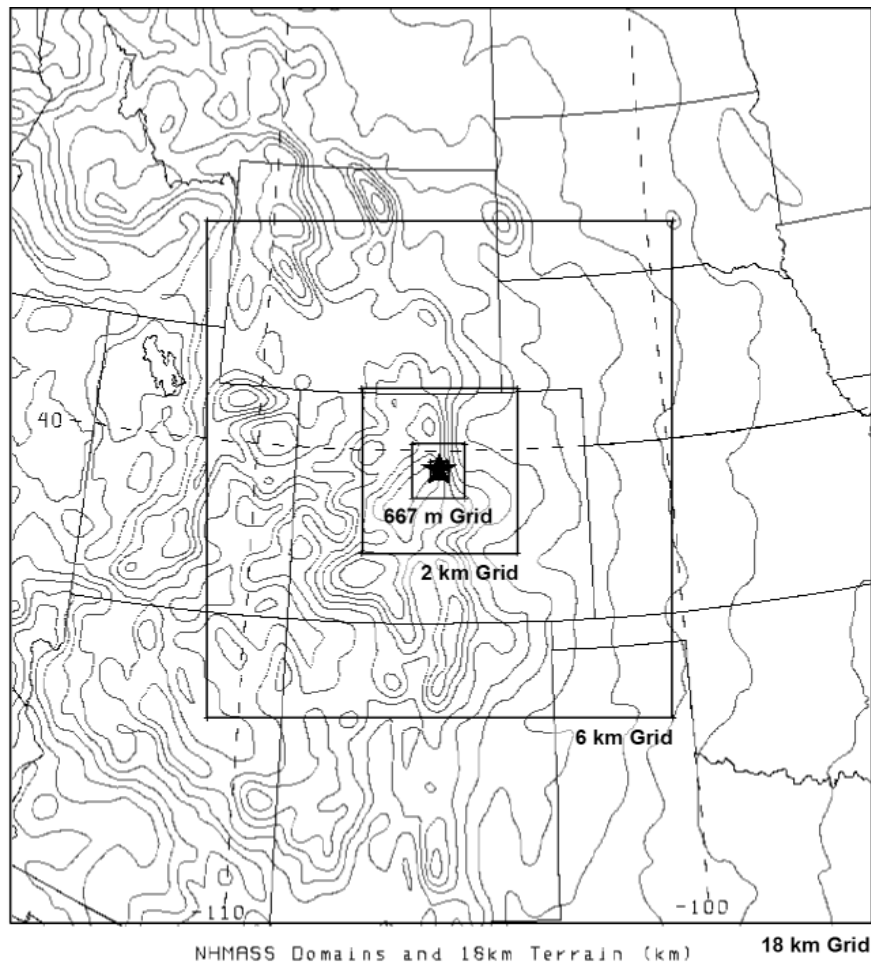
Figure 2.9: NHMASS model domains and terrain from 18 km NHMASS simulation (contoured every 0.25 km). The aircraft incident location is denoted by the star. The 222 m and 71 m domains are obscured by the star.
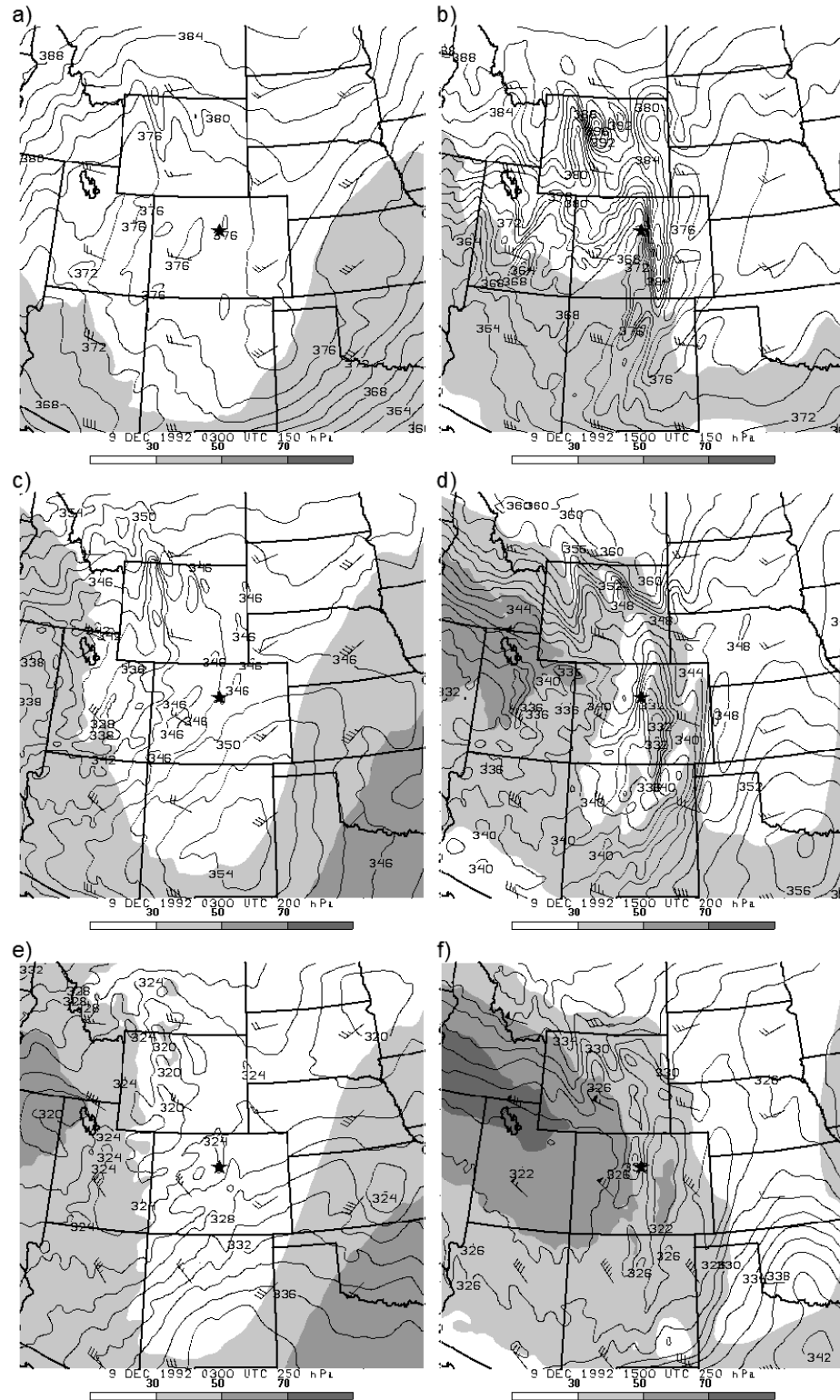
Figure 2.10: Wind speed (ms^{-1}, shaded) and potential temperature (K) at (a-b) 150 hPa, (c-d) 200 hPa, and (e-f) 250 hPa at 0300 UTC (left column) and 1500 UTC 9 December 1992 (right column). Aircraft incident location denoted by star. From 18 km NHMASS simulation.
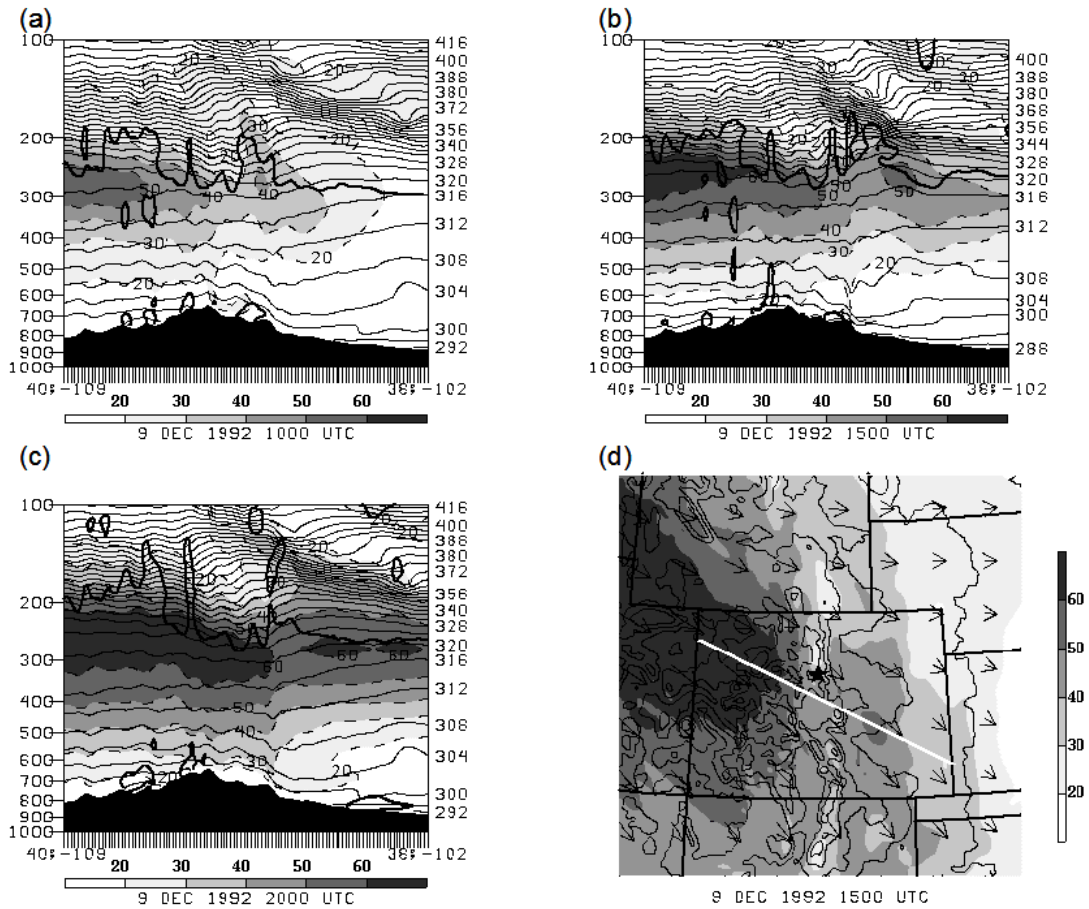
Figure 2.11: Along-flow vertical cross-section of wind speed (ms^{-1}, shaded and dashed), isentropes (K, thin contours), and dynamic tropopause (2 PVU, heavy contour) at (a) 1000 UTC, (b) 1500 UTC, and (c) 2000 UTC 9 December 1992 and (d) 250 hPa winds (ms^{-1}, shaded and vectors) and terrain (500 m contour) at 1500 UTC. Heavy line indicates cross-section for a-c. Aircraft incident location denoted by star in (d). Horizontal length of cross-section is 445 km. From 6 km NHMASS simulation.
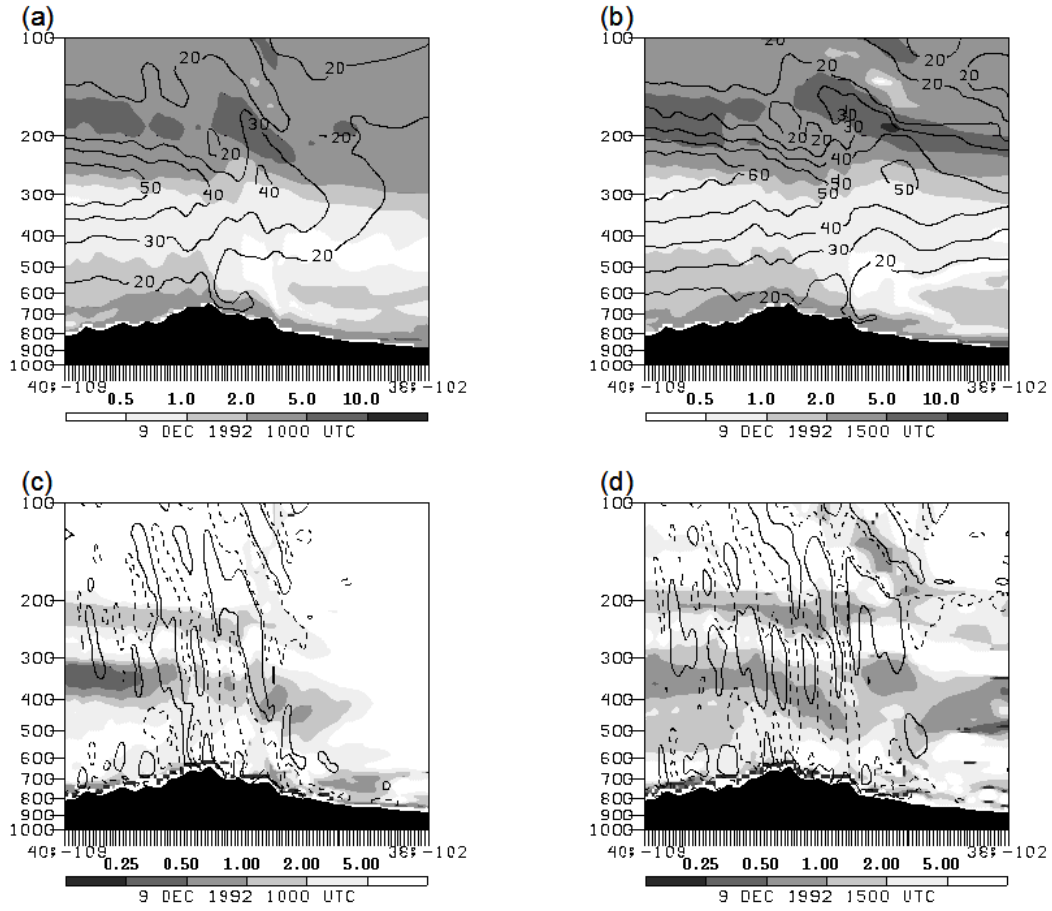
Figure 2.12: Along-flow vertical cross-section (same section as in Fig. 2.10d) of N^2 ($\times\ 10^{-4}$ s^{-2}, shaded) and wind speed (ms^{-1}, contours) at (a) 1000 UTC and (b) 1500 UTC 9 December 1992 as well as Ri (shaded) and velocity divergence (solid contour = 10^{-4} s^{-1} and dashed contour = -10^{-4} s^{-1}) at (c) 1000 UTC and (d) 1500 UTC 9 December 1992. From 6 km NHMASS simulation.
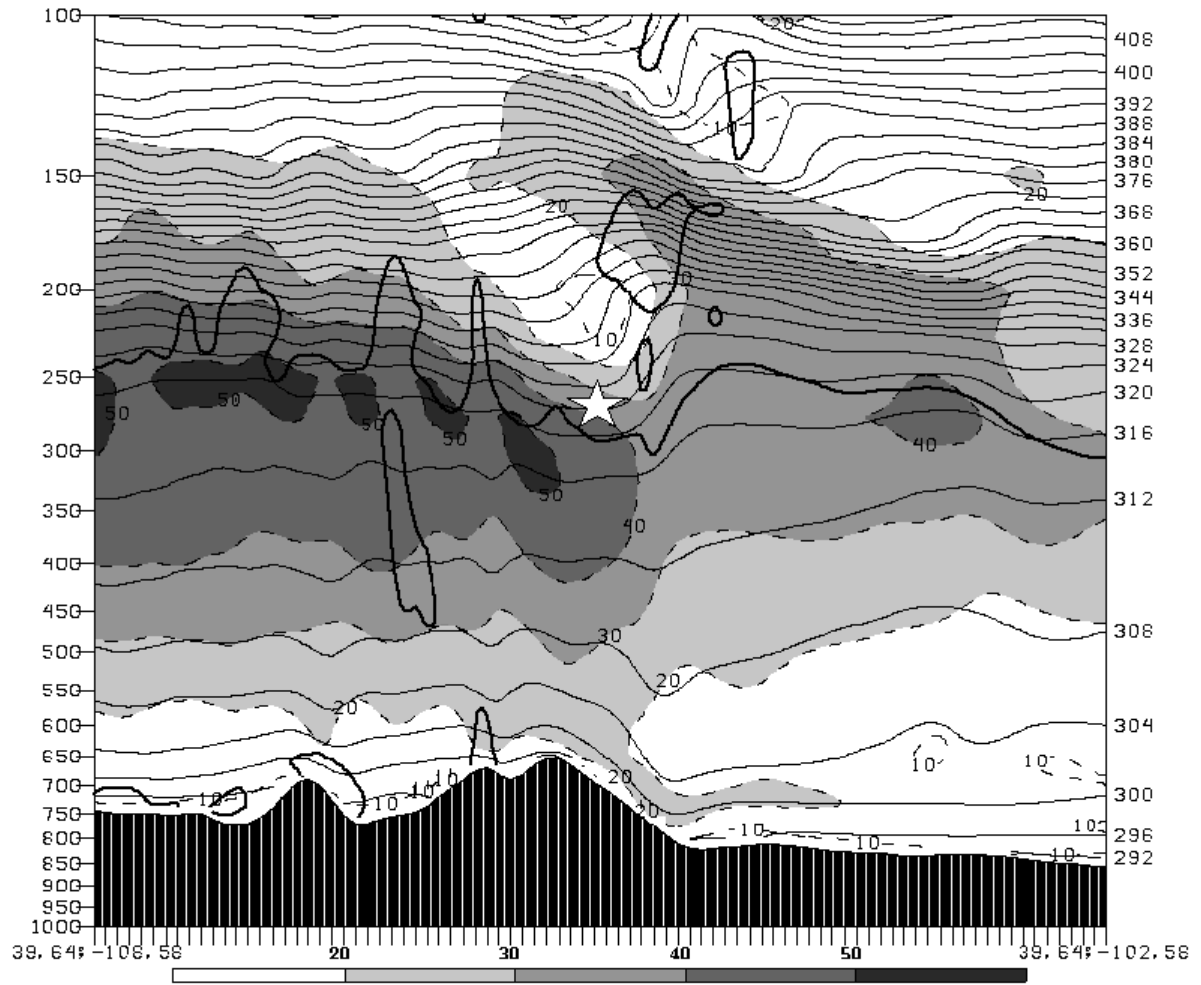
Figure 2.13: West-east vertical cross-section through aircraft incident location showing wind speed (ms^{-1}, shaded and dashed), isentropes (K, thin contours), and dynamic tropopause (2 PVU, heavy contour) at 1500 UTC. Each tick mark on the horizontal scale represents one grid length. From 6 km NHMASS simulation.
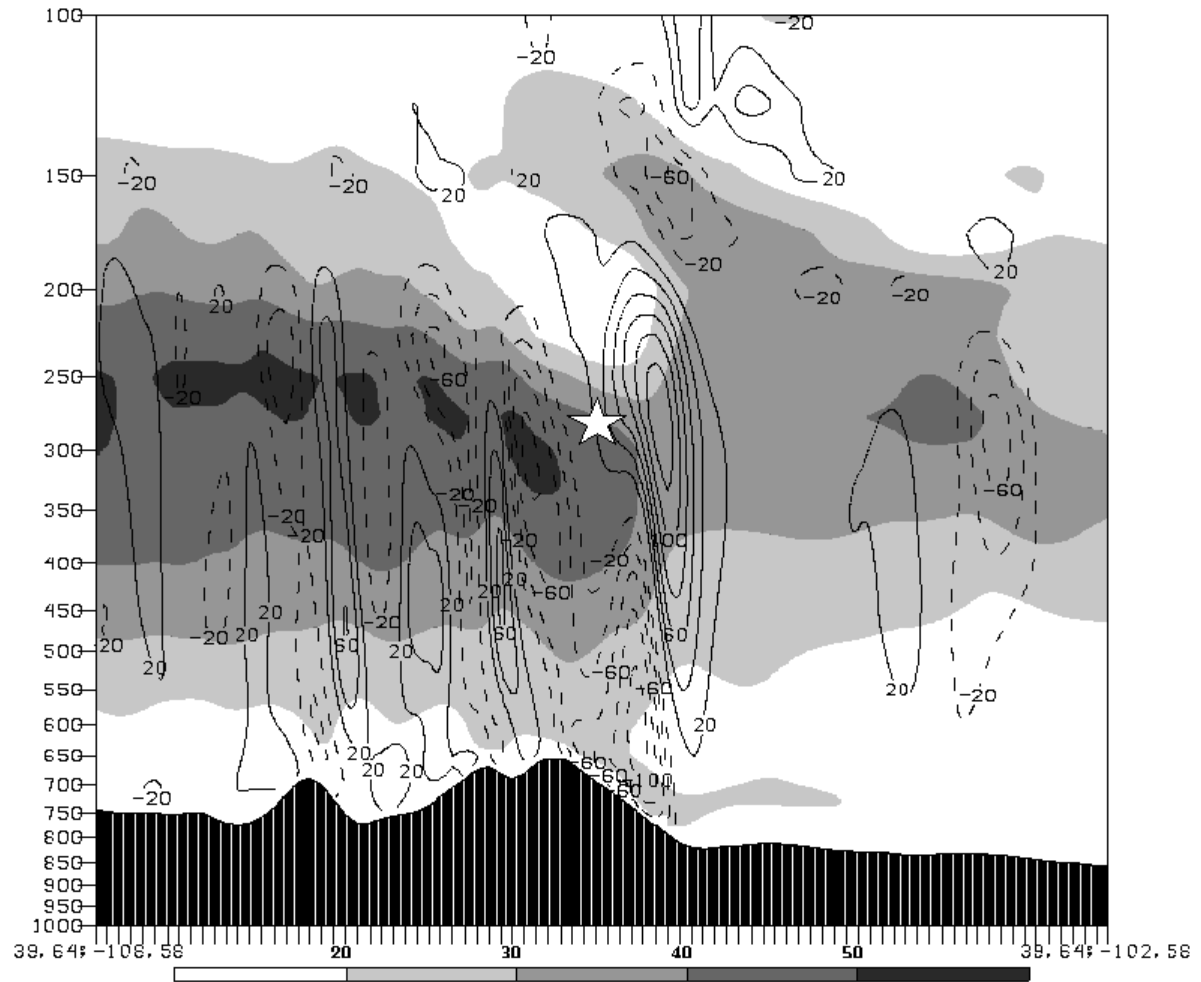
Figure 2.14: West-east vertical cross-section through aircraft incident location showing wind speed (ms^{-1}, shaded) and vertical velocity (cms^{-1}) at 1500 UTC. Each tick mark on the horizontal scale represents one grid length. Aircraft incident location marked by star. From 6 km NHMASS simulation.
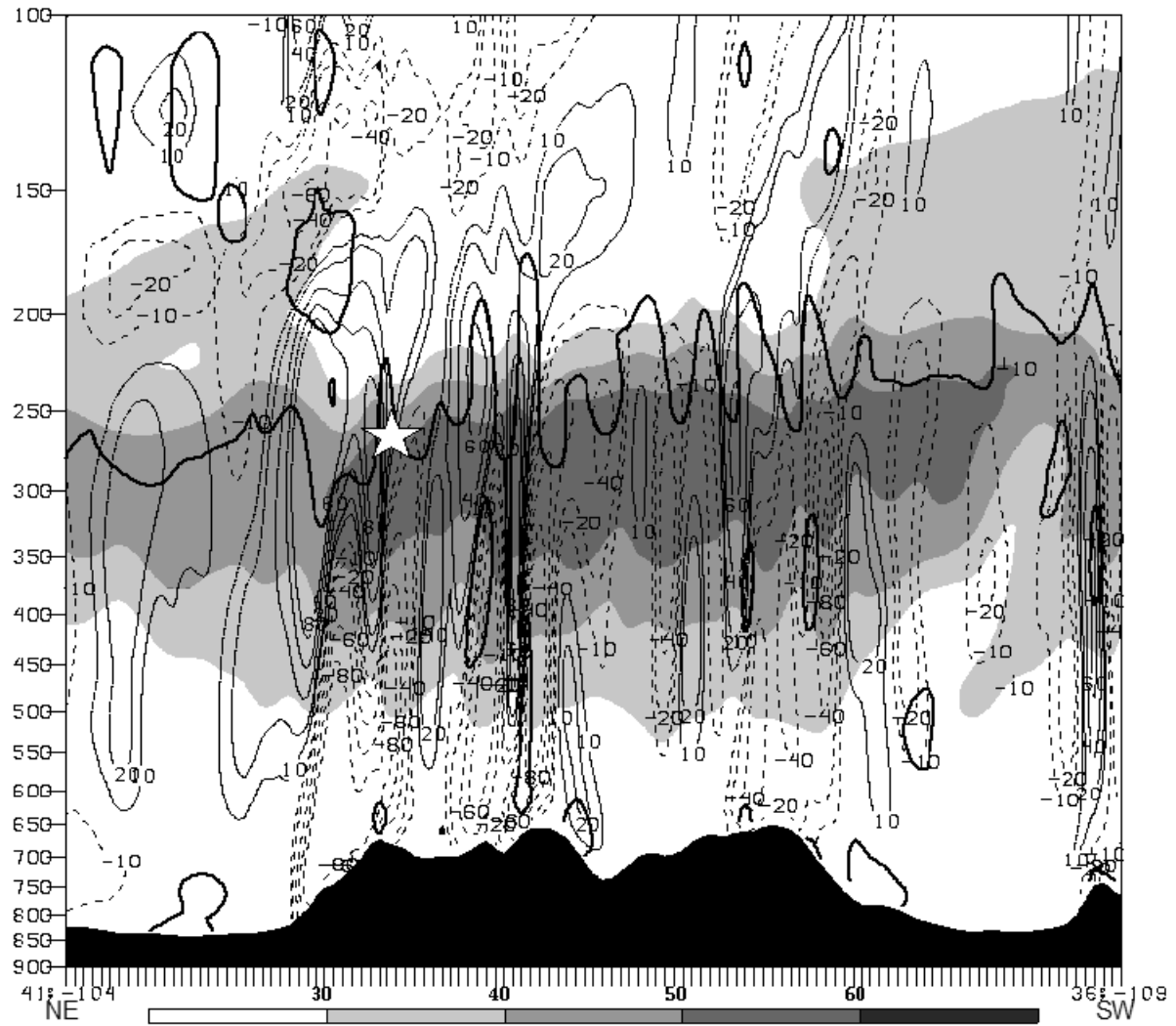
Figure 2.15: Cross-flow NE to SW vertical cross-section through aircraft incident location (normal to cross section in Fig. 2.10d) showing wind speed (ms^{-1}, shaded), vertical velocity (cms^{-1}), and dynamic tropopause (2 PVU, bold contour) at 1500 UTC. Tick marks on horizontal axis are equal to one grid length. View is downstream; the jet is directed into the page. Aircraft incident location marked by star. From 6 km NHMASS simulation.
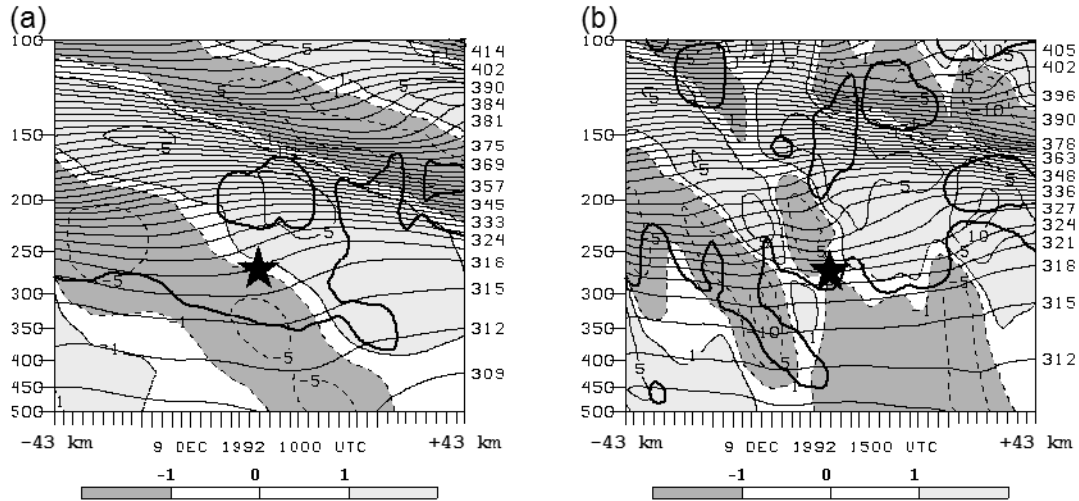
Figure 2.16: East-west vertical cross-section through aircraft incident location showing horizontal velocity divergence (s^{-1} × 10^{-4}, shaded), potential temperature (K, thin contours), and dynamic tropopause (2 PVU, bold contour) at (a) 1000 UTC and (b) 1500 UTC 9 December 1992. Aircraft incident denoted by star. Horizontal axis units equal to one grid length, vertical axis in hPa. From 2 km NHMASS simulation.
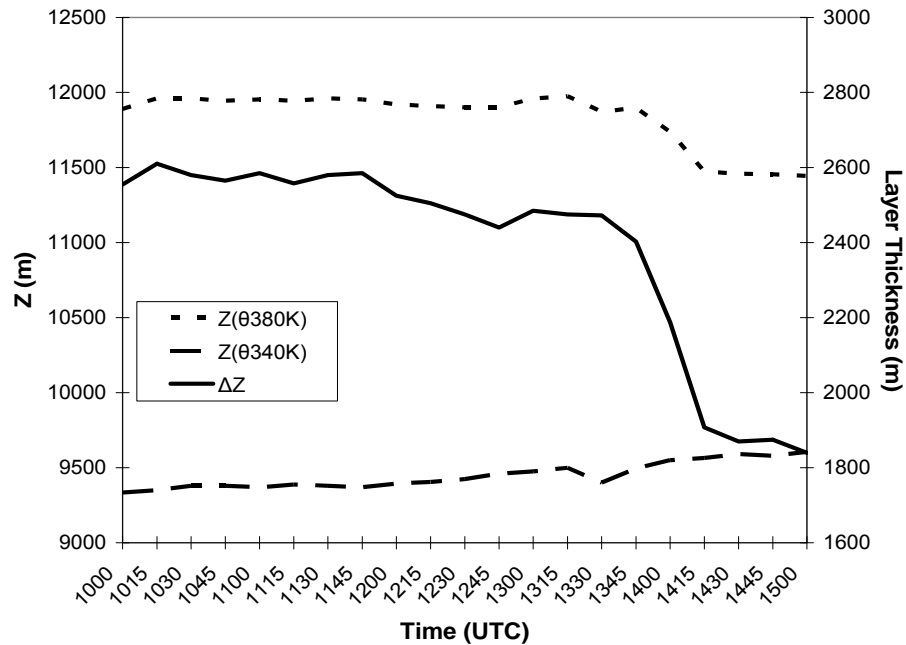
Figure 2.17: Mean height z (m, left ordinate) of the 340K and 380K θ surfaces (dashed lines) as a function of time and the resultant layer thickness Δz (m, right ordinate, solid line) for 9 December 1992 from 2 km NHMASS model output.
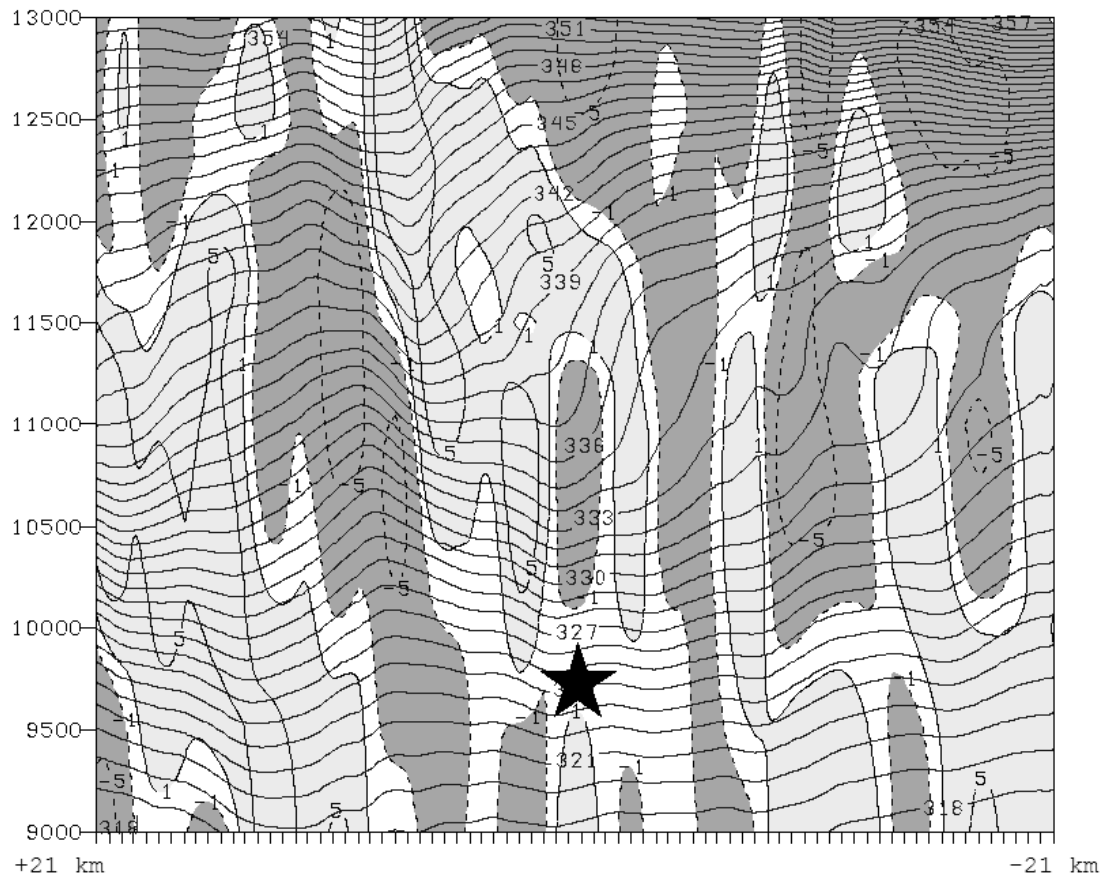
Figure 2.18: East-west vertical cross-section near aircraft incident location showing vertical divergence (dw/dz, s^{-1} × 10^{-4}, shaded, dashed outline is vertical convergence, solid outline is vertical divergence) and virtual potential temperature (K, contours) at 1506 UTC 9 December 1992. Vertical coordinate is height above MSL in meters. Incident location marked by star. From 667 m NHMASS simulation.
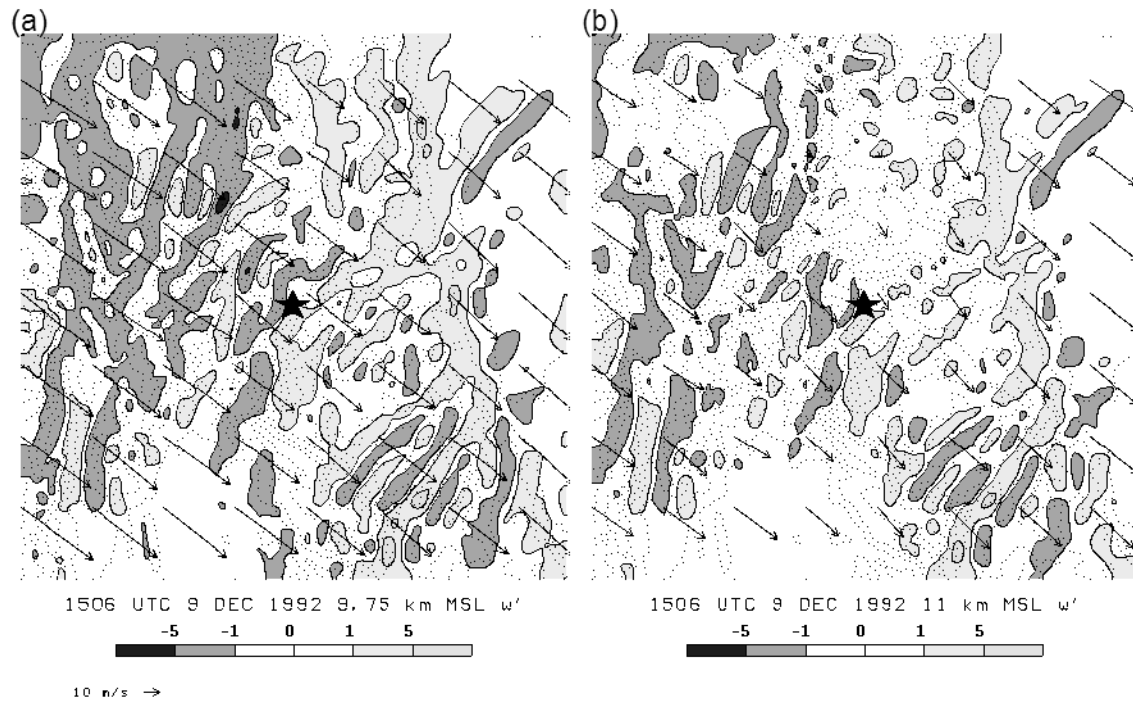
Figure 2.19: NHMASS-simulated perturbation vertical velocity (w', ms^{-1}), shaded, terrain (dotted, 250 m interval), and horizontal wind (vector) valid 1506 UTC 9 December 1992 at (a) 9.75 km above mean sea level (incident level) and (b) 11 km above mean sea level (within the stable layer). Incident location marked by star. From 667 m NHMASS simulation.
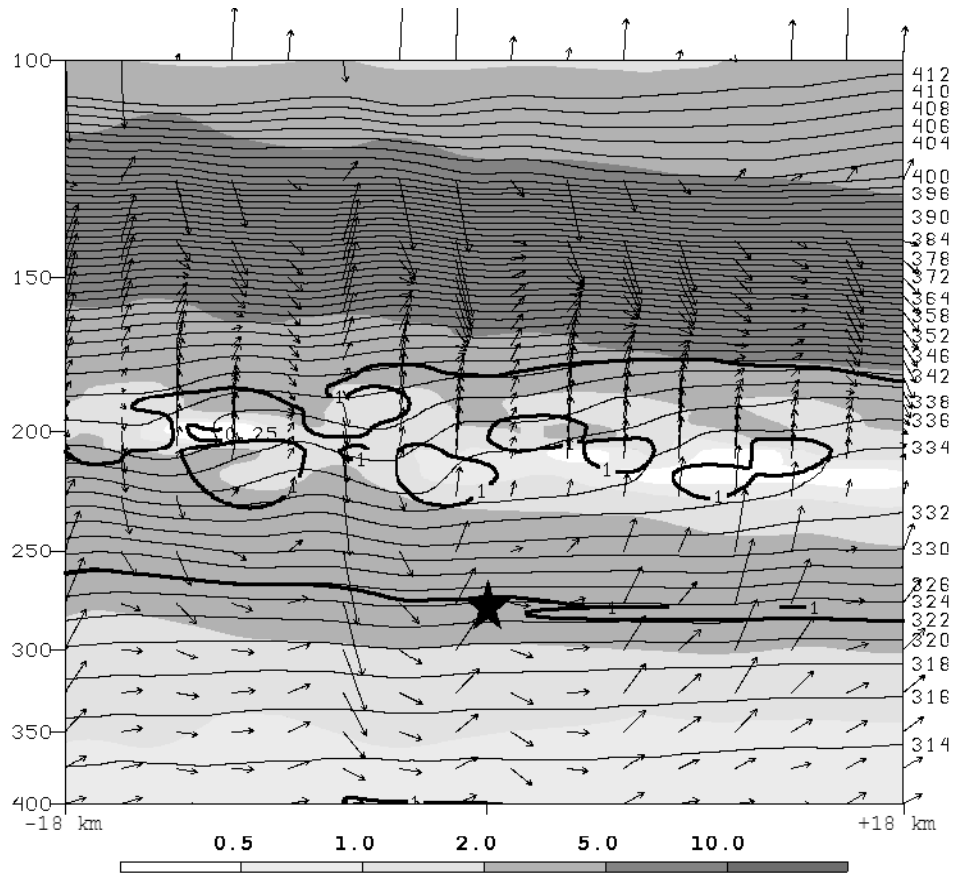
Figure 2.20: Vertical east-west cross-section of N^2 ($\times 10^{-4}$ s^{-2}, shading), Richardson number (bold contours), x-P circulation (ms^{-1}), and potential temperature (K, thin contours) at 1507 UTC 9 December 1992 from 222 m NHMASS model output. Vertical scale is pressure in hPa. Incident location is denoted by star.
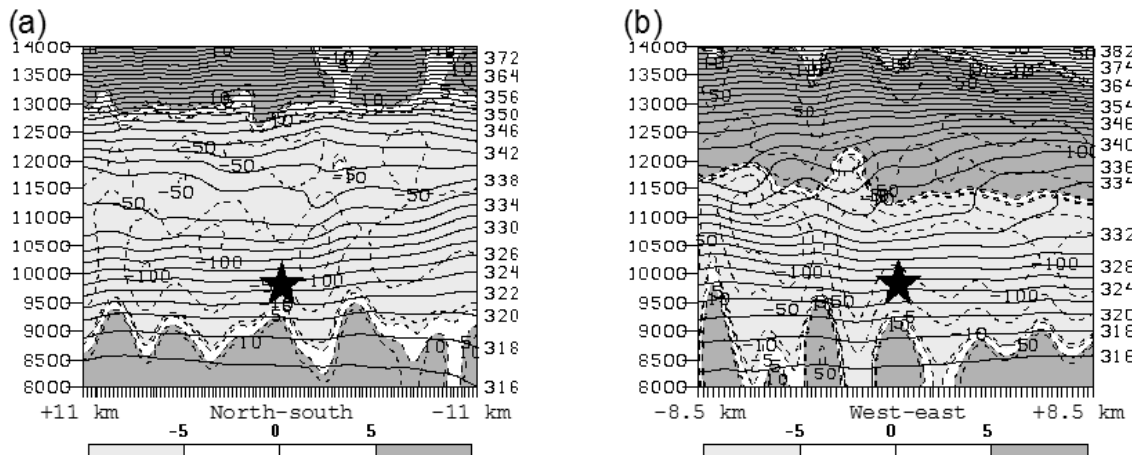
Figure 2.21: Vertical cross-section of NHMASS-simulated y-z plane (a, north is left) and x-z plane (b, west is left) horizontal relative vorticity (s^{-1} $\times 10^{-4}$) and virtual potential temperature (bold contours, K) from 222 m NHMASS run valid 1507 UTC 9 December 1992. Height in meters. Aircraft incident location marked with star.

71
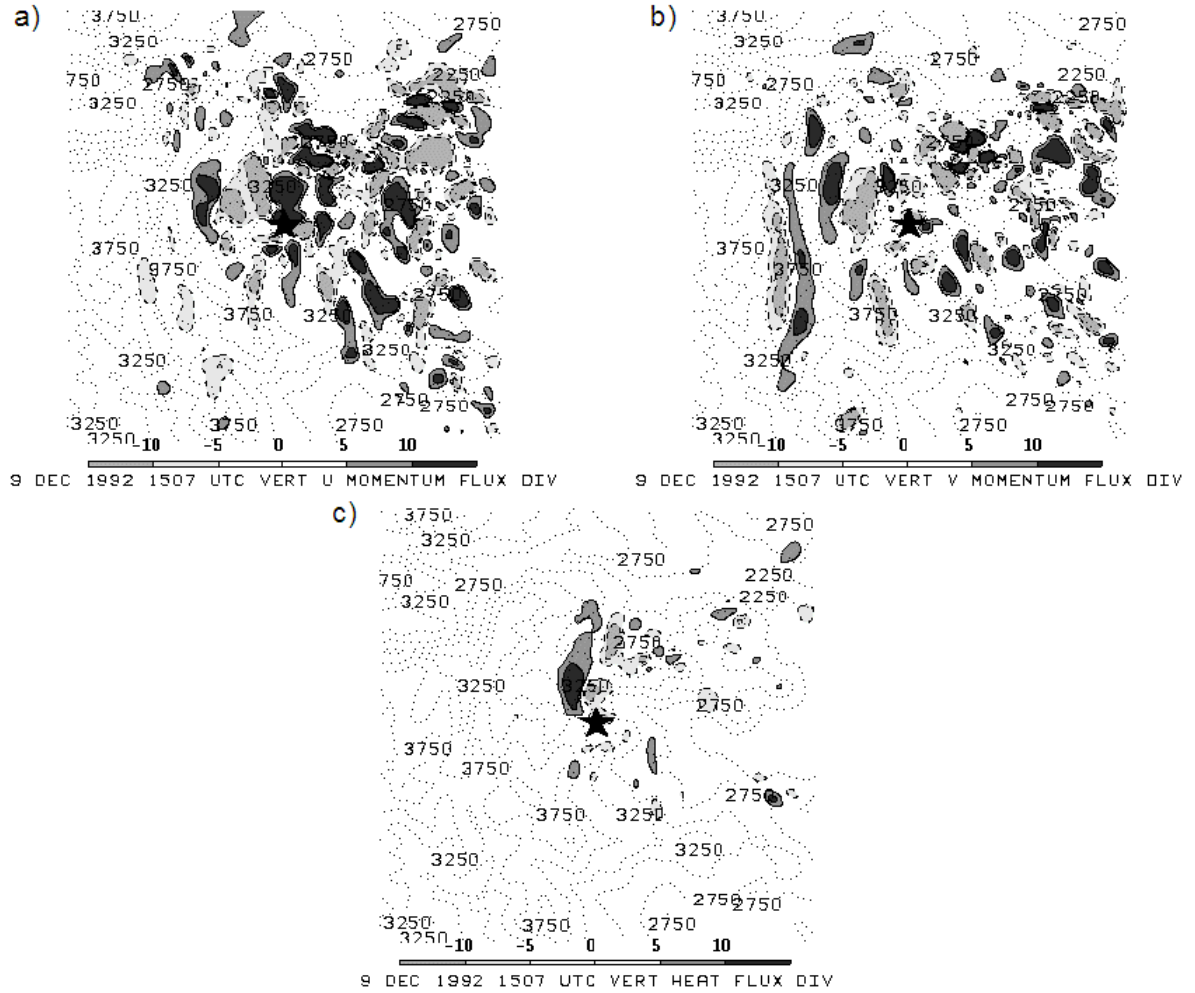
Figure 2.22: 1500 UTC 9 December 1992 spatial Reynolds-averaged (a) vertical u momentum flux divergence ($\partial\overline{(u'w')}/\partial z$, shaded and contoured, ms^{-2} × 10^{-5}), (b) vertical v momentum flux divergence ($\partial\overline{(v'w')}/\partial z$, shaded and contoured, ms^{-2} × 10^{-5}) and (c) vertical heat flux divergence ($\partial\overline{(\theta'w')}/\partial z$, Ks^{-1} × 10^{-5}) in the 9.75 to 11 km MSL layer. From 222 m NHMASS simulation. Aircraft incident location marked with star.
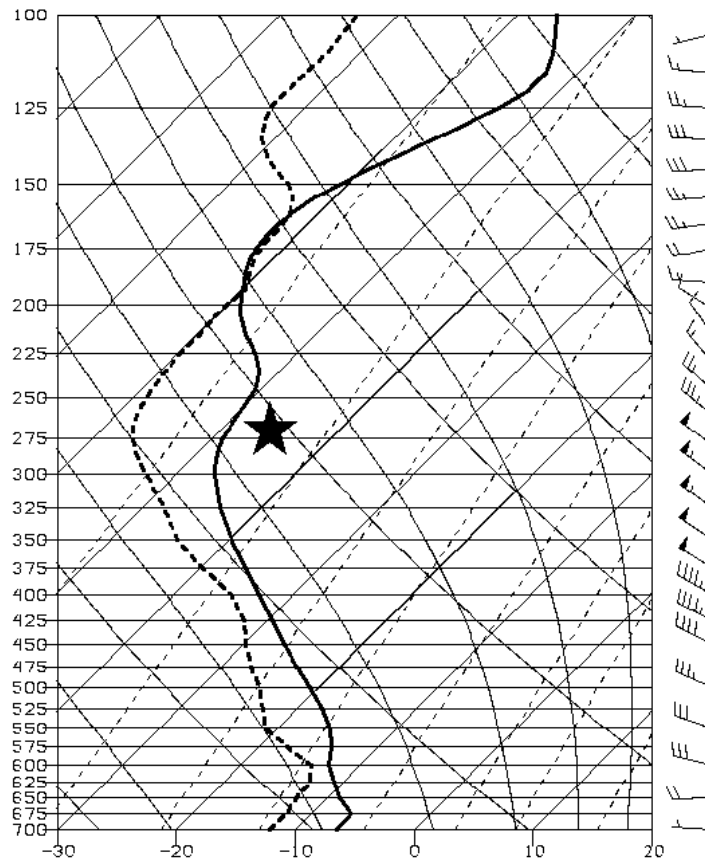
Figure 2.23: NHMASS-simulated Skew-T, Log-P diagram from 1507 UTC 9 December 1992 at the aircraft incident location (39.65N, 105.58W). The star marks the aircraft level. From 222 m NHMASS simulation.
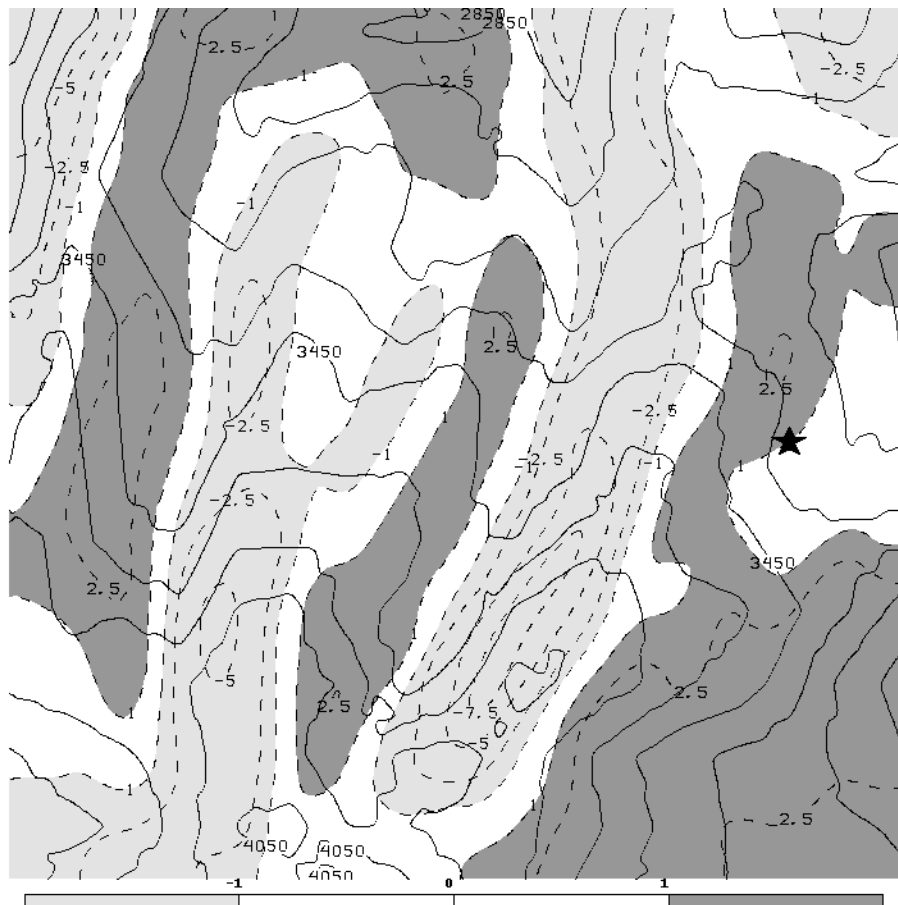
Figure 2.24: 275 hPa vertical velocity (ms^{-1}, dashed, light shading negative, dark shading upward) and surface terrain (m) valid 1507 UTC 9 December 1992 from 71 m NHMASS simulation. Aircraft incident location indicated by star.

CHAPTER 3

INTERACTIONS OF AN UPPER TROUGH AND JET STREAK WITH MOUNTAIN WAVES LEADING TO EXTREME AVIATION TURBULENCE DURING T-REX IOP 6

3.1. Introduction

Clear air turbulence (CAT) is difficult to predict, and often even more difficult to verify. Jet flows over complex terrain are often associated with extreme aviation turbulence (Clark et al. 2000, Kaplan et al. 2006), however such CAT events are often only verified by a handful of pilot reports (PIREPS), or in extreme cases (such as the 9 December 1992 event described by Clark et al. 2000), an incident resulting in damage or injury. Confirming the existence of a climatological signal for severe or extreme stratospheric turbulence is hampered by this relative dearth of direct observations. However, a field experiment conducted in the Owens Valley of California (between the Sierra Nevada and the Inyo/White Mountains) during early 2006 provided a vast array of direct observations of wave-induced turbulent flows at many altitudes over a two-month period, including periods of continuous observation by high-altitude aircraft. The Terrain-Induced Rotor Experiment (T-REX) represented the second phase of a major effort to study rotors, mountain waves, and other atmospheric phenomena in complex terrain; the first phase was the Sierra Rotors Experiment conducted in the same location in 2004. Among the many objectives of this ambitious project was the verification of the numerical modeling of orographic flows designed to improve the mesoscale simulation of complex flows (Grubišić et al. 2004 and Grubišić et al. 2006).

While it should come as no surprise that jet streaks interacting with mountain waves should lead to turbulence, it is hypothesized that a specific upper-level synoptic structure can allow mountain wave activity to trigger particularly violent lower stratospheric CAT, and that this configuration was present during IOP 6. This configuration involved an approaching cyclonic polar jet streak at the base of an upstream trough with associated upward vertical motion and cooling undercutting a subsiding warm layer in the stratosphere resulting in differential subsidence. This vertically confluent flow resulting from differential vorticity advection led to a particularly intense inversion above and distinct from the tropopause. It is just below this stratospheric inversion layer and in the presence of jet-induced shear that the high-frequency gravity waves began to break and possible turbulence occurred.

The challenge confronting the aviation forecaster can be seen by examining the T-REX data. Of the 15 IOPs conducted during the experiment, all involved a cyclonic polar jet (at the base of a trough or cut-off low) intersecting the Sierra Nevada in some manner, yet only IOP 6 was characterized by direct observations of extreme wave breaking in the lower stratosphere by the NSF/NCAR High-performance Instrumented Airborne Platform for Environmental Research (HIAPER) aircraft. Large-amplitude gravity waves were observed in the stratosphere by the research aircraft during IOP 4 and IOP 13 as well, though the flow in those cases was not observed to be as turbulent as during IOP 6 (Doyle et al. 2007). With respect to forecast parameters, a pronounced tropopause or stratospheric inversion alone is not a sufficient condition for turbulence, as several IOPs were observed to exhibit transient inversions above the tropopause but were not reported to have generated stratospheric aviation turbulence (see Chapter 4). The synergistic combination of strong shear, vertically-

varying static stability, and a large-amplitude mountain wave is hypothesized to have created

a particularly favorable environment for aviation turbulence during IOP 6. It is hypothesized

that the synoptic setup involving the jet flow at and above tropopause during IOP 6 allowed

for an unstable layer to develop below 225 hPa, with a strong stable layer above at

approximately 150 hPa in the presence of string wind shear. The tight vertical stability

gradient present allowed the mountain wave to penetrate deep into the stratosphere and to

break just below the stratospheric inversion. The model simulations and direct aircraft

observations showed transient high-frequency wave generation and wave breaking in the

lower stratosphere.

That vertically overlapping and differing jet circulations can lead to extreme

turbulence in the presence of mountain waves is inferred from the literature. Clark et al.

(2000) examined a case of extreme aviation turbulence along the Front Range of the

Colorado Rockies on 9 December 1992 which resulted in severe damage to a DC-8 aircraft

just above tropopause on a day with dozens of turbulence reports. Clearly evident in the data

from that case was an unusually strong inversion in the lower stratosphere trapped between

an approaching polar jet streak with a strong cold layer and departing subtropical jet streak.

Other case studies involving high-altitude aviation turbulence reports, including some

without orographic influence, do often show this complex jet/front structure with a strong

inversion above the tropopause (Kaplan et al. 2005a, 2005b, and 2006 and Koch et al. 2005).

One particularly high-profile aviation accident, the 28 January 1986 Space Shuttle

Challenger explosion, was examined by Uccellini et al. (1986) and exhibited a very similar

structure to IOP 6. Their study showed several layers of subcritical (<.25) Ri trapped

between a cyclonic polar jet streak to the north and an anticyclonic subtropical jet over

Florida, leading them to hypothesize that severe turbulence was quite possible in this region and could conceivably have contributed to the loss of the Shuttle. Therefore it appears evident that there is a climatological signal for severe aviation turbulence associated with vertically differing jet flows over complex terrain, resulting in a strong inversion manifested either as an enhanced tropopause or as a distinct structure in the stratosphere.

3.2. Synoptic Conditions and Observations

IOP 6 was conducted from 2000 UTC 24 March 2006 to 0500 UTC 26 March 2006 and was characterized by a strong upper-level trough which passed north of the T-REX area, as indicated in the NCEP/NCAR North American Regional Reanalysis (NARR) data (Fig. 3.1). During the 33 hour period of the IOP, the axis of the trough and associated jet streak approached and then eventually passed the T-REX experiment site. The core of the polar jet streak was indicated at 250 hPa (Fig. 3.1c-d) and was present at the base of the upper-level trough. Above the 250 hPa polar jet, the character of the flow changed. The 150 hPa jet feature was considerably less cyclonic at 0000 UTC 25 March (Fig. 3.1a) and by 0000 UTC 26 March (Fig. 3.1b) was primarily westerly with very slight anticyclonic curvature over the TREX area, extending as high as 100 hPa. Quasigeostrophic trough dynamics would indicate ascent below 250 hPa associated with increasing cyclonic vorticity advection (CVA) with height and slight descent and adiabatic warming above the trough axis resulting from decreasing CVA with height, leading to vertically confluent flow. Fig. 3.2 depicts a north to south vertical cross-section along the dashed line in Fig. 3.1a in a plane 2.5 degrees longitude upstream of the T-REX area and windward of the Sierra Nevada. At 0000 UTC 25 March 2006 (18 hours prior to the HIAPER arriving on station), a complex jet structure existed with a subtropical jet feature above 150 hPa well to the south and an approaching cyclonic polar

jet feature between 300 hPa and 250 hPa to the north. There was an indication of descending air below an anticyclonic vorticity advection maximum just to the north of the T-REX area and the altitudes at which the HIAPER aircraft would be orbiting. However, the troposphere showed only slight ascent south of the T-REX area, and large-scale descent to the north. By 2100 UTC (during the strong stratospheric gravity wave period), however, the upper edge of the polar jet had core ascended to 250 hPa (Fig. 3.2b). Additionally, a tropopause fold was developing to the north of the jet core. Strong subsidence was apparent above the dyanmic tropopause as CVA decreased sharply with height. Upward vertical motion was evident below the tropopause below associated with the vertically increasing CVA below the jet streak. This vertically convergent flow is hypothesized to have helped create a strong stratospheric inversion as will be seen in later figures.

This jet/front and tropopause structure was also causing a differential thermal advection pattern as subsidence above the polar jet and descending tropopause was increasing the relative strength of the warm layer at 150 hPa as it was undercut by a cold layer below. This differential advection pattern is consistent with a folded tropopause preceding cyclogenesis (Hirschberg and Fritsch 1991), and while not unique to this case, is important in that it is hypothesized to have supported the formation of the strong inversion in the stratosphere. Evidence that this was occurring can be seen in the NARR potential temperature fields. At 150 hPa (Fig. 3.3c-d) a warm ridge remained over the T-REX site, extending southward along the Pacific coast. In contrast, a relatively cold trough extended west-to-east at 250 hPa across the T-REX site (Fig. 3.3e-f). By 0000 UTC 26 March 2006 (Fig. 3.3f) a strong north-south temperature gradient was apparent at 250 hPa along the Sierras. This complex thermal pattern would be indicated by a strong inversion in the

stratosphere as described in the soundings to follow. Above the 150 hPa warm layer, the 100

hPa level was characterized by a complex horizontal temperature gradient over the Owens

Valley, with the 100 hPa temperature decreasing at the T-REX site 3 K in 24 hours (Fig.

3.3a-b). In contrast, θ at 150 hPa increased over the Owens Valley by 12 K in 24 hours.

This rapid increase in θ led to a complex stratification of the 250-100 hPa layer, which is

hypothesized to have played a significant role in establishing the conditions which led to the

violent vertical motions observed and simulated in this case.

Figures 3.4a-b are the soundings from Vandenberg Air Force Base, CA (VBG),

upstream and southwest of the T-REX field experiment site at 0000 UTC 25 March and 0000

UTC 26 March 2006. In particular, one sees a significant development of a complex

stratification above the tropopause (approximately 200 hPa). By 0000 UTC 26 March 2006

there were multiple isothermal layers above the inversion, indicating that the vertical stability

gradients had changed significantly in that layer during the 24-hour period. These two

soundings bracket a period during which the HIAPER Gulfstream V high-altitude research

aircraft encountered extreme wave activity in the vicinity of the 175 hPa inversion in Fig.

3.4b. The 0000 UTC 26 March 2006 profile was characterized by a roughly -50° C warm

layer over a depth of 50 hPa, bracketed above and below by -55° C layers. At Three Rivers,

CA, (upstream of the T-REX site on the windward side of the Sierra Nevada) at 0952 UTC

25 March 2006 an Air Force Research Laboratory radiosonde sounding (Fig. 3.5) depicted

the complex upper-level structure some eight hours prior to the onset of the strongest

turbulence in the stratosphere. The tropopause is seen near 12 km MSL, just above the

maximum wind speed associated with the polar jet. A second, more pronounced inversion

appears between 15 and 17 km MSL, associated with a second wind maximum. Real-time

soundings from Independence, CA were available during this IOP as part of the T-REX research sounding network, and are shown in Fig. 3.6. Of note is the evolution of the inversion at 125 hPa. At 1117 UTC (Fig. 3.6a.) it represented only a +5 K departure from the nearly isothermal layer below it, however by 1701 UTC (Fig. 3.6b, approximately one hour prior to arrival of the HIAPER aircraft on-station) it had strengthened to a +13 K increase over 25 hPa. Also at this time, the layer between this inversion and the tropopause had experienced a decrease in static stability and an increase in directional wind shear. Apparent in both soundings is the difference between wind regimes across the tropopause, with the west-northwesterly component of an anticyclonic jet feature at 150 hPa above the west-southwesterly polar jet flow at 250 hPa.

An example of HIAPER observations of stratospheric gravity-waves is shown in Fig. 3.7. Within a horizontal distance of 10 km on the west slope of the Inyo range, the HIAPER encountered vertical velocities varying between -4 ms^{-1} and +7 ms^{-1} at an altitude of 43 kft (Doyle 2006). Multiple passes in time through this region showed that this feature was near steady-state for a period of more than an hour. Smaller-scale fluctuations were also detected in the wind speed, potential temperature, and vertical velocity fields between 39 and 43 kft (approximately 13.1 km). However, by the HIAPER's exit leg (2242 UTC 25 March 2006), the flow had become more violent and transient (Fig. 3.8). In particular, the vertical motion field indicated the potential for violent fluctuations, most likely due to wave breaking, in which the HIAPER encountered a vertical velocity jump between -5 and +10 ms^{-1} over a horizontal distance of less than one kilometer at a flight level of 45 kft (13.7 km). The aircrew reported "rather strong" turbulence upon encountering this spike (Doyle et al. 2007). Unfortunately, the HIAPER departed the T-REX area immediately afterward. However, the

BAE146 mission reported that around 0000 UTC 26 March 2006, vertical velocities at 35 kft exceeded ± 5 ms^{-1} and that lenticular clouds were visible above that altitude (Brown 2006).

3.3. Methodology

The current case employed the Weather Research and Forecasting (WRF-ARW) Version 2.2, using the Global Forecast System (GFS) 00-hour analyses as initial and lateral boundary conditions to produce a more detailed representation of the environment surrounding the HIAPER observations. The model top was set at 10 hPa with 90 levels distributed linearly. The model was integrated at five grid lengths (18 km, 6 km, 2 km, 667 m, and 222 m) with one-way nesting between domains (Fig. 3.9) with the intent of resolving features across the full spectrum of scales from the synoptic to the lower boundary of the meso-γ. The outer three domains were integrated for a 48-hour period starting at 1200 UTC 24 March 2006, centered over the Owens Valley of California on a 163x163 horizontal grid. The 18 and 6 km domains used the Kain-Fritsch convective parameterization scheme while the remainder used none. The 667 m and 222 m domains were integrated from 1800 UTC 25 March 2006 to 0000 UTC 26 March 2006 on 193x163 grids. All domains used 30 second terrain data. All simulations used the Yonsei University (YSU) boundary layer scheme and a horizontal Smagorinsky first order closure scheme for turbulence. Fig. 3.10 depicts the 2 km WRF-simulated terrain along with the HIAPER GV track and the major geographical features of the T-REX area of operations.

3.4. Model Simulations of mesoscale waves

The WRF model reproduced the polar jet and trough structure at 18 km horizontal resolution quite well in time and space. Comparisons between the 18 km simulation 250 hPa winds and the vertical structure in cross-section from the 2 km simulations (Figures 3.11-3.13) indicate that the nature of the interactions between the 250 hPa cyclonically curved jet streak associated with the large-scale upper-level trough and the mountain wave changed with time as the trough passed over the area. This resulted in multiple mountain-wave regimes, not all of which were conducive to upper-tropospheric and lower stratospheric turbulence. Early in the IOP (24 March 2006), the trough was well off the coast of California, and the mountain wave consisted of a downslope wind/hydraulic jump couplet with little stratospheric penetration (not shown). By 1200 UTC 25 March 2006 (Fig. 3.11), however, the mountain wave was perturbing the isentropic fields as high as 100 hPa. The period from 1800 UTC 25 March 2006 to 0000 UTC 26 March 2006 exhibited the greatest wave activity and potential for turbulence in the lower stratosphere. At 2100 UTC 25 March 2006 (Fig.3.12), the base of the 250 hPa trough was over central California and the model was simulating wave breaking above 100 hPa, with deep lee waves developing over and downstream of the Owens Valley. By 0000 UTC 26 March 2006 (Fig. 3.13), the trough axis was directly over the T-REX site, and wave breaking (at 2 km horizontal grid spacing) extended down to 175 hPa. The lee waves at this point also extended well into the stratosphere. As the trough axis departed to the east, the atmosphere quickly returned to a quiescent condition (not shown), with almost no mountain wave present by 0600 UTC 26 March 2006.

Upon further examination of the cross-sections in Figures 3.11-3.13, it is apparent that by 1200 UTC 25 March 2006 the simulations showed a fairly strong stability gradient at

200 hPa and a minimum of N^2 at 300 hPa. Perturbations in the isentropic field showed

vertical propagation of the main mountain wave well above 100 hPa. A band of low Ri

(<0.5) had developed at 300 hPa (on the lower edge of the polar jet streak), and at 250 hPa,

two local maxima in the horizontal wind appeared roughly 90° out of phase with the vertical

velocity maxima, indicative of the strong standing wave at this time. However, by 2100

UTC (Fig. 3.12), the environment had become more perturbed. The band of minimum static

stability had lifted to 200 hPa, compressing the N^2 gradient above it. A pocket of subcritical

Ri (<0.25) appeared deep into the stratosphere above the main mountain wave, thus

satisfying a necessary condition for shear-induced turbulence (Miles 1961; Howard 1961).

The horizontal velocity fields showed a very regular wave-like pattern at and above

tropopause. The vertical velocity showed a series of lee waves extending from near-surface

to the lower stratosphere. This time period roughly corresponds to HIAPER observations of

intense gravity waves and indications of wave-breaking between 39 kft and 45 kft (roughly

180-160 hPa) (Doyle 2006). By 0000 UTC 26 March 2006 (Fig. 3.13), the simulated

isentropic field was highly distorted, with overturning isentropes indicating wave breaking at

multiple locations between roughly 125 hPa and 70 hPa. These locations corresponded to

pockets of subcritical Ri. The mountain wave was extremely intense at this time, with

vertical velocities exceeding ± 10 ms^{-1}. The polar jet streak at this time was also highly

distorted. Upstream the core had descended to 300 hPa, however by 0000 UTC there were

two horizontal wind maxima exceeding 50 ms^{-1} at 150 hPa associated with the mountain

wave. Unfortunately by this time the HIAPER had departed the area and no direct

observations were available to verify the presence of these features at or above 250 hPa.

The preceding indicates that the shear and static stability fields evolved throughout IOP 6 in such a manner as to maximize the vertically-varying horizontal thermal and velocity discontinuities in the lower stratosphere. The 6 km WRF simulation showed a significant increase in time in the vertical variation of the Scorer parameter (Scorer 1949) given by:

$$l^2 = \frac{N^2}{U^2} - \frac{\left(\partial^2 U / \partial z^2\right)}{U} \qquad (3.1)$$

where N is the Brunt–Väisälä frequency and U is the mean wind. It has been shown that the significant vertical variation (layering) of the Scorer parameter may associated with large-amplitude mountain wave breaking (Durran 1986, 1990) and that large local maxima in the vertical Scorer parameter profile are a preferred region for wave amplification and breaking (Weissbluth and Cotton 1989). Fig. 3.14 shows the 10 to 20 km MSL Scorer parameter profile from the 6 km WRF simulation over the midpoint of the southern leg of the HIAPER racetrack. Of note is the relatively linear profile indicated prior to the start of IOP 6 through 0000 UTC 25 March 2006. By 1200 UTC 25 March, the 16-18 km Scorer profile began to vary greatly. By 0000 UTC 26 March, the model-simulated Scorer parameter spanned two orders of magnitude in less than 1 km of depth. It is theorized that the compression and strengthening of the warm layer in this layer is responsible for the discontinuous stratification indicated by the Scorer profile. It is directly below this layer that high-frequency waves were seen to develop and break at finer model resolution.

3.5. Model simulations of fine-scale non-laminar flows

At scales of 2 km horizontal grid spacing and below, a distinct transition between laminar wave action and turbulent precursor flow becomes apparent in the lower stratosphere. The 2 km WRF simulation hints at such a transition; i.e., the 1800 UTC 175

hPa vertical velocity field (roughly matching the altitude and time of the HIAPER

observations in Fig. 3.7) depicted in Fig. 3.15a shows a fairly smooth, laminar wave pattern.

By 2200 UTC (Fig. 3.14b), higher-frequency waves are seen to appear within the larger

wave. By 2230 UTC 25 March 2006, flow over the T-REX area was significantly perturbed.

Fig. 3.16 from the 667 m simulation shows the 100 hPa and 200 hPa horizontal winds at that

time. Of note is that at 100 hPa a flow reversal was simulated by the model, i.e., at 100 hPa

above an area experiencing a 40 ms^{-1} band of downstream flow. At 100 hPa, the model-

simulated waves amplified to near a breaking state, as evidenced by the pockets of flow

reversal, perhaps allowing the waves to extract energy from the jet environment through

resonant amplification (Clark and Peltier 1984). The two levels depicted bracket the strong

stratospheric inversion seen in several of the observed soundings (Figures 3.4-3.6).

The WRF simulation was able to capture in space and time a particularly strong wave

amplification event recorded by the HIAPER aircraft and described by Doyle (2006) as a

strong turbulent event. Comparing the HIAPER observations (Fig. 3.8) and the WRF 667 m

simulation in the vertical cross-section along the exit leg (Fig. 3.17), at approximately 2240

UTC 25 March 2006, one notes the high-frequency waves and wave-breaking at HIAPER

altitude. The model shows this vertical velocity couplet at roughly 150 hPa at the same point

in the valley that the HIAPER encountered the 15 ms^{-1} vertical velocity jump. These model-

simulated high-frequency waves were transient and appeared to break when viewed in

animation. The large-amplitude mountain wave displayed a horizontal wavelength of 20 km

while at 150 hPa most of the high-frequency waves were on the order of 2-5 km. Vertical

isentropes indicated the potential for wave breaking, leading to violent turbulent eddies.

Again, it is worth noting that this is the layer bracketed by the differing jet and thermal structures discussed in Section 3.2.

Examination of the vertical variation of the Scorer parameter from the 222 hPa simulation showed that at 16 km altitude (above the HIAPER altitude), the vertical gradient increased with time (Fig. 3.18). Between 1900 and 2100 UTC, the Scorer parameter gradient increased only slightly over the T-REX area from below 1×10^{-9} m^{-3} to 2×10^{-9} m^{-3}. However, by 2200 UTC (Fig. 18d), values had increased by two orders of magnitude, exceeding 1×10^{-7} m^{-3} in the center of the Owens Valley. This corresponds with the appearance of transient high-frequency waves at this altitude in the model at this time. The significant increase in the vertical gradient of the Scorer parameter heralds the potential for wave breaking and the onset of aviation turbulence. Further evidence of this breakdown to turbulent flow is seen in Fig. 3.19 which shows the model-simulated 12-18 km vertical cross-section along the HIAPER aircraft track at 2240 UTC 25 March 2006. This stable region represents the compressed warm layer at 150 hPa. Waves appear to be breaking in these regions, as evidenced by overturning and closed isentropes, as well as a model-simulated vertical velocity maximum exceeding +15 ms^{-1} at 15 km MSL. The model depicted amplified, fine scale stratospheric waves in the layer from approximately 13.5 km (near the HIAPER altitude) to 17.5 km. However, the influence of the large-amplitude mountain wave is still visible, with a broad region of vertical motion of order 1 ms^{-1} outside of the wave breaking regions.

Fig. 3.20 shows the perturbation vertical velocity (w') calculated as a departure from a spatial mean value following Lane et al. (2003) valid at 2240 UTC 25 March 2006 13.75 km (approximately the HIAPER altitude). Fig. 3.20 depicts a roughly 33 km by 23 km

subregion of the 222 m domain for clarity. Here the HIAPER track was seen to traverse

perturbations in vertical velocity between +4 and -7 ms^{-1} several times along a distance of

roughly 30 km. Several strong "shafts" of negative w' were apparent even at this altitude;

higher aloft at 16 km some of these negative perturbations exceeded -15 ms^{-1} (not shown).

One possible explanation for these vigorous downdrafts are the so-called "turbulent

downbursts" described in Clark et al. (2000), in which "phasing" occurs between wave

breaking and the descending branch of a horizontal vortex tube (HVT). While the

downbursts themselves are transient in nature, they appeared in these simulations to be

generated over a period of over one hour at the peak of this event. Moreover, the strong

horizontal gradient of vertical velocity seen in Fig. 3.20 would tend to enhance the

overturning associated with shear-induced HVTs. In such a manner, the static stability

gradient would serve to enhance, rather than counter, the shear instability. In addition, the

soundings described in Section 3.2 all depict considerable moisture in the inversion layer,

making a microburst scenario quite feasible. Fig. 3.21 shows the model-derived vertical

temperature and dew point profile for a point along the HIAPER track at 2240 UTC 25

March 2006. The inversion beginning at the HIAPER altitude of 13 km is quite visible,

reaching its apex at 15.5 km. Evidence of vertical circulation and overturning at scales of a

few km is clear in Figures 3.17, 3.18 and 3.20, and tend to support the concept of "phasing"

of wave breaking the inversion base with the descending branches of these circulations below

the inversion. The Clarke et al. (2000) turbulent downburst mechanism may partially explain

the horizontal structure of the features in Fig. 3.20, as some nearly symmetrical up- and

downdrafts appear along with the large-amplitude features associated with the mountain

wave.

It is clear even at 222 m horizontal grid spacing that the synoptic-scale inversion is collocated with the strongest model-simulated turbulent motions. The stable layer was compressed between the large-scale subsidence above the inversion and the combined influence of the mountain wave and upward vertical motion ahead of the cyclonic polar jet streak until the necessary conditions for breakdown to turbulent flow were met. In particular, the development of large regions of subcritical Richardson number and the sudden increase in the vertical variation of the Scorer parameter indicate that this threshold was met in the model fields at approximately 2200 UTC 25 March 2006. In-situ observations by the HIAPER aircraft support this assertion. Observations before 2200 UTC showed strong gravity waves, however only light turbulence (Doyle 2006). By 2200 UTC, violent fluctuations in vertical motion were encountered, culminating with the event recorded during the exit leg at 2242 UTC. The model simulations clearly show this transition at resolutions below 2 km. It is hypothesized that the pre-turbulent environment, characterized by a strong thermal gradient and shear layer, set the stage for violent breakdown to non-laminar flow when acted upon by the mountain wave. The compression of this thermal gradient eventually led to an environment conducive to wave breaking and aviation turbulence at and below the base of the inversion.

3.6. Comparisons with other IOPs

As mentioned in Section 1, two other T-REX IOPs exhibited large-amplitude gravity waves in the lower stratosphere. Both IOP 4 (13-15 March 2006) and IOP 13 (15-17 April 2006) were characterized by vertical velocity perturbations above the tropopause of order 10 ms^{-1} (Doyle et al. 2007). IOP 4, 6, and 13 all involved a stratospheric inversion above the tropopause, and all were characterized by a cyclonic polar jet streak at the base of a trough

upstream of the T-REX area of operations. However, only IOP 6 was associated with direct observations of vertical velocity perturbations inferred to be caused by wave breaking in the stratosphere. An analysis of the potential temperature fields in all three cases (not shown) provides little clue as to the difference between the violent (IOP 6) and non-violent (IOP 4 and 13) cases, as all were characterized by a warm layer near 150 hPa between cold pockets at 100 hPa and 250 hPa, consistent with a deep cyclonic trough and tropopause fold upstream. Thee difference between the cases is hypothesized to lie within the trough structure and inferred vertical motion above the polar jet, and its effect of the relative magnitude of the inversion.

Fig. 3.22 shows the NCAR ISS soundings launched from the T-REX research site during IOP 4. At 2301 UTC 13 March 2006 (Fig. 22a) a -48° C inversion was present near 150 hPa with a lower inversion associated with the tropopause at 200 hPa. A slightly less stable layer was centered at 175 hPa. By 2257 UTC 14 March 2006 (Fig. 3.22b), the temperature at 150 hPa had decreased by 5° C, and the nose of both the inversion and the tropopause had lowered by 150 hPa. The temperature at the tropopause, however, had increased by 5° C, thus reducing the vertical variation of the static stability between 250 hPa and 100 hPa. This is in contrast to IOP 6, during which the vertical variation of the temperature increased with time in the 250 hPa to 100 hPa layer, as evidenced both by the NARR potential temperature fields (Fig. 3.3) and the sounding data (Figures 3.4-3.6).

Fig. 3.22 depicts the winds at 0000 UTC 15 March 2006, during the second HIAPER mission of IOP 4. At this time the HIAPER recorded vertical velocity perturbations of order ±6 ms^{-1} at 13.1 km MSL (Doyle et al. 2007), although these waves were characterized as "smooth (Smith 2006)." IOP 4 resembled IOP 6 at 250 hPa (Fig. 3.23a), as a cyclonically-

curved polar jet streak was located upstream of the T-REX area of operations, causing the 250 hPa flow to be southwesterly over the Owens Valley. This cyclonic southwesterly flow extended to 100 hPa. Contrasting Fig. 3.23 with Fig. 3.1, one sees that during IOP 6, the flow at 100 hPa was westerly to west-northwesterly with very little curvature. The cyclonic southwesterly flow from 250 to 100 hPa during IOP 4 would serve to cool the entire layer, weakening the inversion as seen in Fig. 3.22.

IOP 13 came closest to matching the conditions observed during IOP 6. Examination of the sounding from Independence, CA at 0159 UTC 16 April 2006 (Fig. 3.24a) reveals a weak stratospheric inversion above the tropopause at 150 hPa. Just a few hours prior to this, the HIAPER aircraft was recording wave amplitudes of the order of ±10 ms^{-1} vertical velocity at 11.3 km (Doyle et al. 2007). The HIAPER was airborne again late in the day on 16 April 2006. The 2003 UTC 16 April 2006 sounding from Independence, CA (Fig. 3.24b) showed two inversions above the tropopause. One appeared at 150 hPa and another at 120 hPa, with wind maxima found at 250 hPa and 100 hPa. This profile is strikingly similar to the IOP 6 configuration, particularly with the upper inversion and distinct jet core. Not surprisingly, the HIAPER again encountered wave-induced vertical velocities of ±10 ms^{-1} at 37 kft (Smith 2006). However, like the previous day, these waves were reported to be not as violent as were encountered during IOP 6. Upon examination of both soundings in Fig. 3.24, one sees that the 200 hPa temperature warmed significantly (+10 °C in 18 hours) while the 150 hPa temperature remained relatively constant. A small cold layer developed between 150 hPa and 120 hPa, however overall the 250 hPa to 100 hPa vertical temperature variation decreased significantly with time, unlike that seen in IOP 6. Cyclonic flow through the 250 hPa to 100 hPa layer was again evident in IOP 13 (Fig. 3.25) Throughout the 24-hour period

between 0000 UTC 16 April 2006 and 0000 UTC 17 April 2006, the 250 hPa winds became more southwesterly and cyclonic (Fig. 3.25c-d) as the polar jet streak approached the T-REX area of operations. The 100 hPa flow again remained southwesterly and cyclonic through the period (Fig. 3.25 a-b). The relatively uniform flow through the 250 hPa to 100 hPa prevented a pronounced differential vorticity advection as was seen in IOP 6 thereby reducing the vertical stability gradient hypothesized to be so critical in the generation of the turbulent downbursts seen in the IOP 6 simulations.

Fig. 3.26 is a comparison of soundings from VBG, representative of the upstream conditions of all three IOPs. The upstream location of this site along the California coast ensures that the lower stratospheric structure is independent of significant terrain effects. All three soundings indicate an inversion structure above the tropopause. The inversion is strongest and deepest during IOP 6 (Fig. 3.26b). To confirm this, the inversions appearing near 175 hPa in all three cases were examined. For an air parcel or layer lifted adiabatically from the base of the inversion to the top (as indicated in each sounding by the shaded area), the buoyant force per unit mass to be countered for IOP 4, 6, and 13 would be approximately -0.45 ms^{-2}, -0.6 ms^{-2}, and -0.3 ms^{-2}, respectively. The IOP 6 upstream sounding therefore had approximately 33% more negative buoyancy than the IOP 4 sounding, and roughly 50% more than for IOP 13. Moreover, the lifted layer in IOP 6 would become saturated unlike those for the IOP 4 and 13 soundings. This would tend to support the microburst analogy for the turbulent downbursts simulated by the model.

The differences between T-REX IOP 6 and IOPs 4 and 13 are subtle, while the similarities are many. Because of the extremely transient nature of aviation turbulence, it is unclear whether it may have occurred in IOPs 4 and 13 and was just not sampled by the

aircraft, or if it simply did not occur. Further modeling studies could confirm the potential

for wave breaking and turbulent downburst activity in the other two IOPs. However, the lack

of corroborating observations leaves this question open. Clearly the presence of a

stratospheric inversion supports vertical propagation of mountain waves due to the rapid

increase in static stability with height. All three IOPs examined had a distinct inversion

above the tropopause and all three were characterized by strong gravity waves in the lower

stratosphere. It is hypothesized that the factor which distinguished the more violent observed

motions in IOP 6 from the smoother flows for IOPs 4 and 13 was the configuration of the

vertical motions associated with the curvature of the upstream trough/jet feature and its effect

on the static stability. In IOP 6, the jet and trough structure was such that the differential

CVA associated with the rapid decrease in cyclonic curvature above the jet core and its

associated vertical motion and thermal advection created a warm ridge over a cold layer,

leading to a sharp vertical gradient of static stability as the inversion was compressed and

strengthened between cold air from below and sinking air from above, allowing possible

wave over-reflection and breaking. IOPs 4 and 13, on the other hand, had cyclonic jet

configurations through the depth of the stratosphere that would lead to the maintenance or

weakening of the stratospheric inversion by reducing the vertically differential vorticity

advection, maintaining the large-amplitude gravity waves and thus preventing the breakdown

of the flow to turbulent eddies as a result of descending accelerative flow. The key is likely

to be in the strong subsidence above the inversion in the violent case which would enhance

the compression of the warm layer and increase the differential horizontal warm air

advection. Examination of the 9 December 1992 Colorado Front Range extreme turbulence

case (Ralph et al. 1997, Clark 2000) reveals a similar theme; the directional shear across the

250 hPa (northwesterly) to 100 hPa layer (west-southwesterly) was associated with differential temperature advection, leading to a very pronounced warm layer in the lower stratosphere just above the altitude of the aircraft incident. As in the IOP 6 case, that layer was compressed and eventually violent eddies resulted as the orographically-induced waves broke in that layer.

3.7. Conclusions

T-REX IOP 6 offered a unique opportunity to study stratospheric aviation turbulence. The pre-turbulence environment, characterized by a strong upstream trough with vertically convergent flow which developed a very strong inversion above the tropopause in the presence of shear. While all of the T-REX IOPs involved a mountain wave of some extent, and all involved the polar jet impinging upon the Sierra Nevada, IOP 6 directly recorded the most violent lower stratospheric turbulence of the experiment. This lends credence to the hypothesis that it was this jet and trough structure and its resultant thermal and shear profile resulting from differential subsidence that "primed" the atmosphere for turbulent flow above the tropopause. The key effect that set IOP 6 apart was the extreme discontinuity in the static stability, as manifested by the rapid variation of the Scorer parameter with height (Figures 3.14 and 3.18) associated with the inversion. Model simulations indicated wave breaking at this interface, inferring that descending eddies could be generated in a manner similar to Clark's microburst of turbulence in the 9 December 1992 case study.

From a forecast perspective, one might expect extreme aviation turbulence in the lower stratosphere under similar conditions. Forecasters are already trained to expect the potential for turbulence in the vicinity of jet streaks and with strong flow over complex terrain. A scenario in which a cold layer associated with a cyclonic polar jet feature and deep

trough undercuts a warm layer associated with a large-scale subsidence would tend to develop a strong inversion above or collocated with the tropopause, which could be a climatological signal for where turbulence might be expected. The presence of a vertically-propagating mountain wave makes turbulence in this environment far more likely, consistent with the hypothesis. While this regime is not expected to be commonplace, the literature suggests that it happens often enough to pose a threat to aviation operations in the lower stratosphere.
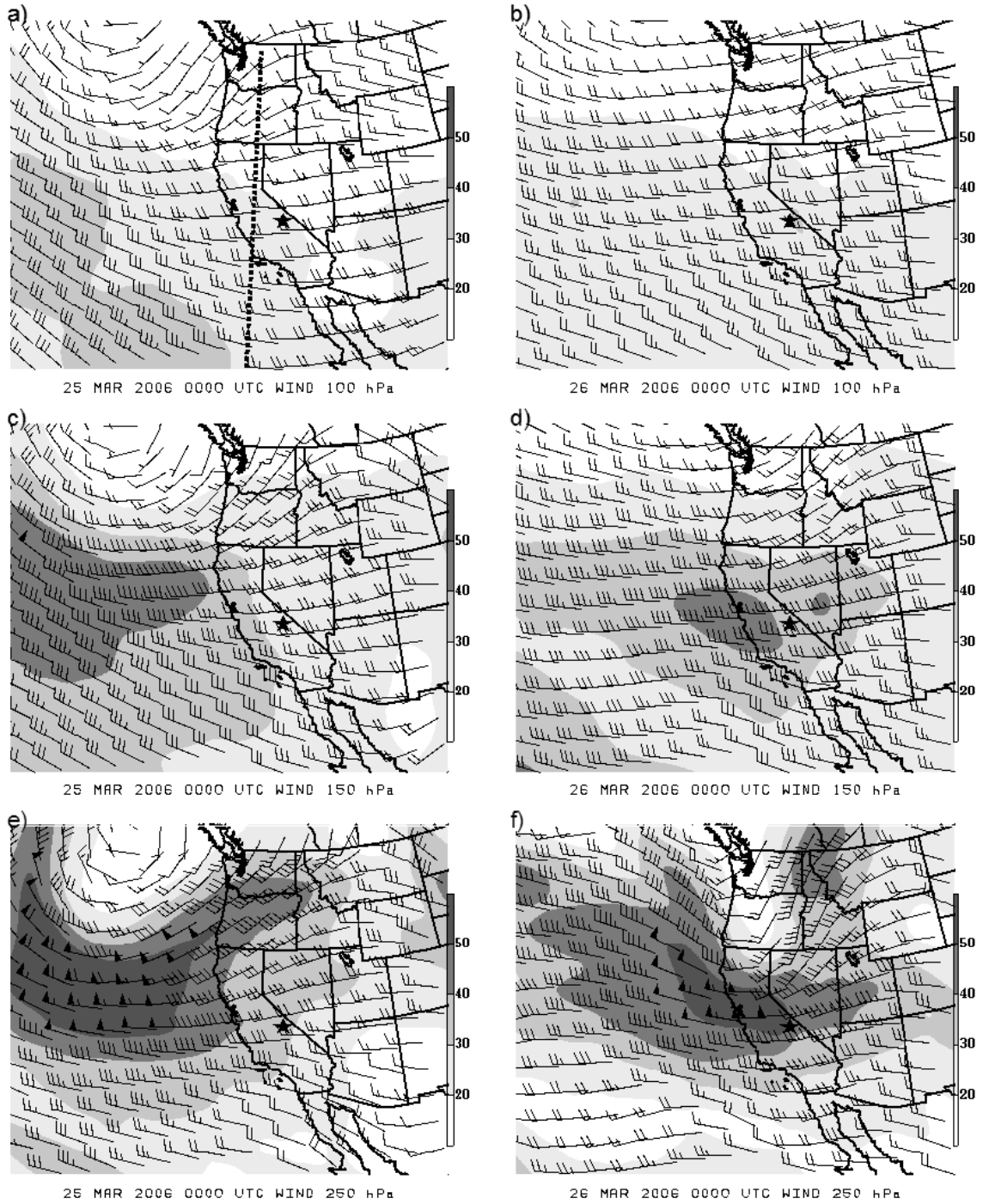
Figure 3.1: Wind speed and wind barbs (ms^{-1}) at (a-b) 100 hPa, (c-d) 150 hPa, and at (e-f) 250 hPa valid 0000 UTC 25 March 2006 (left column) and 0000 UTC 26 March 2006 (right column). Data from NCEP/NCAR North American Regional Reanalysis. Data was smoothed with six passes of a Gaussian filter to eliminate noise after winds were corrected from model-relative to true. The star marks the T-REX field site. The dashed line in (a) depicts the plane of the cross sections in Fig 3.2.
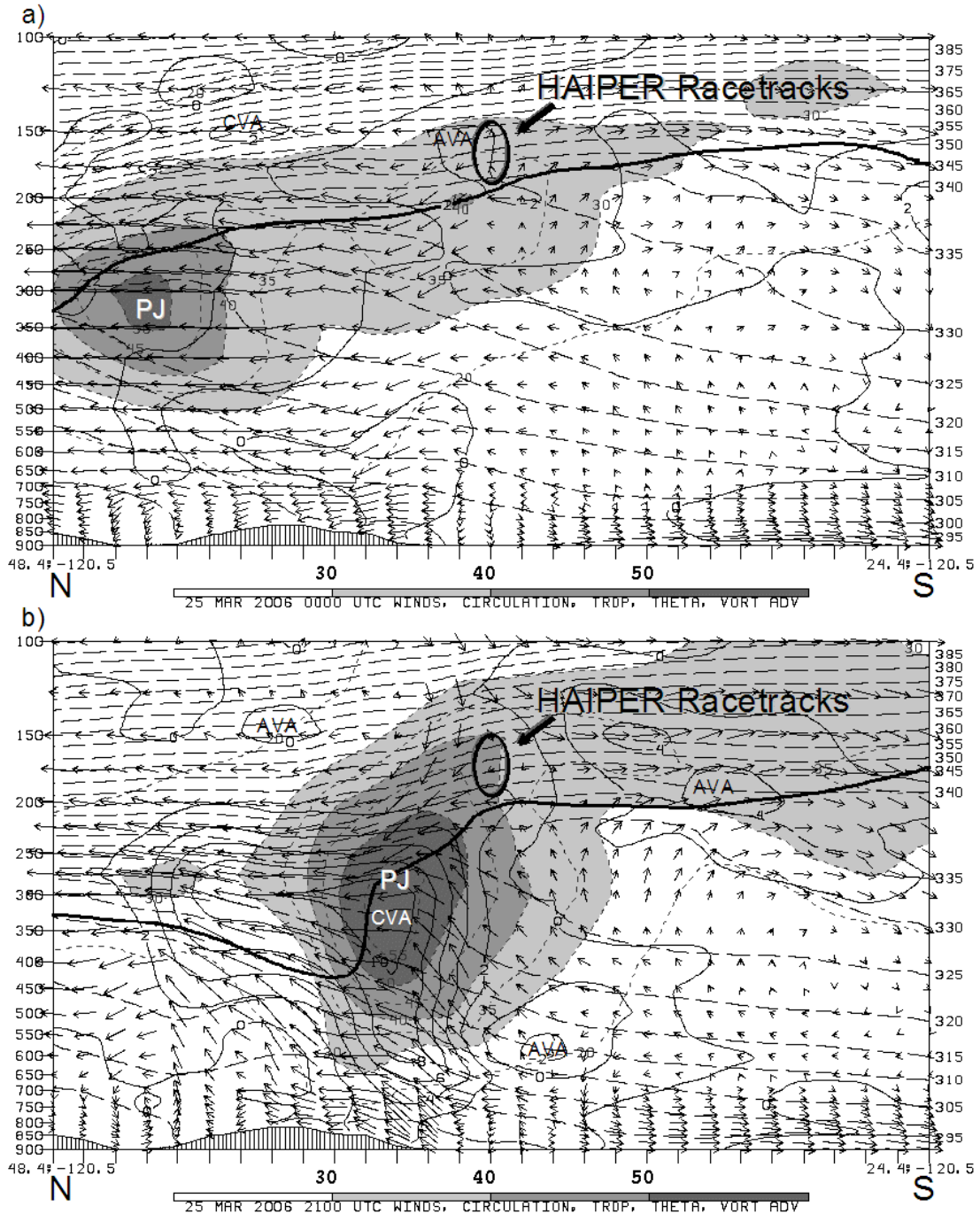
Figure 3.2: North-south vertical cross sections at (a) 0000 UTC and (b) 2100 UTC 25 March 2006 of isotachs (shaded, short dashed contours, ms^{-1}), absolute vorticity advection (solid contours, s^{-2} × 10^{-9}, with local cyclonic vorticity advection maxima labeled CVA and local anticyclonic vorticity maxima labeled AVA), potential temperature (long dashed contours, K), dynamic tropopause (heavy contour, 2 PVU), and circulation vectors of the horizontal wind and ω. Location of HIAPER racetracks after 1800 UTC and polar jet core indicated. Data from NCEP/NCAR North American Regional Reanalysis.

97
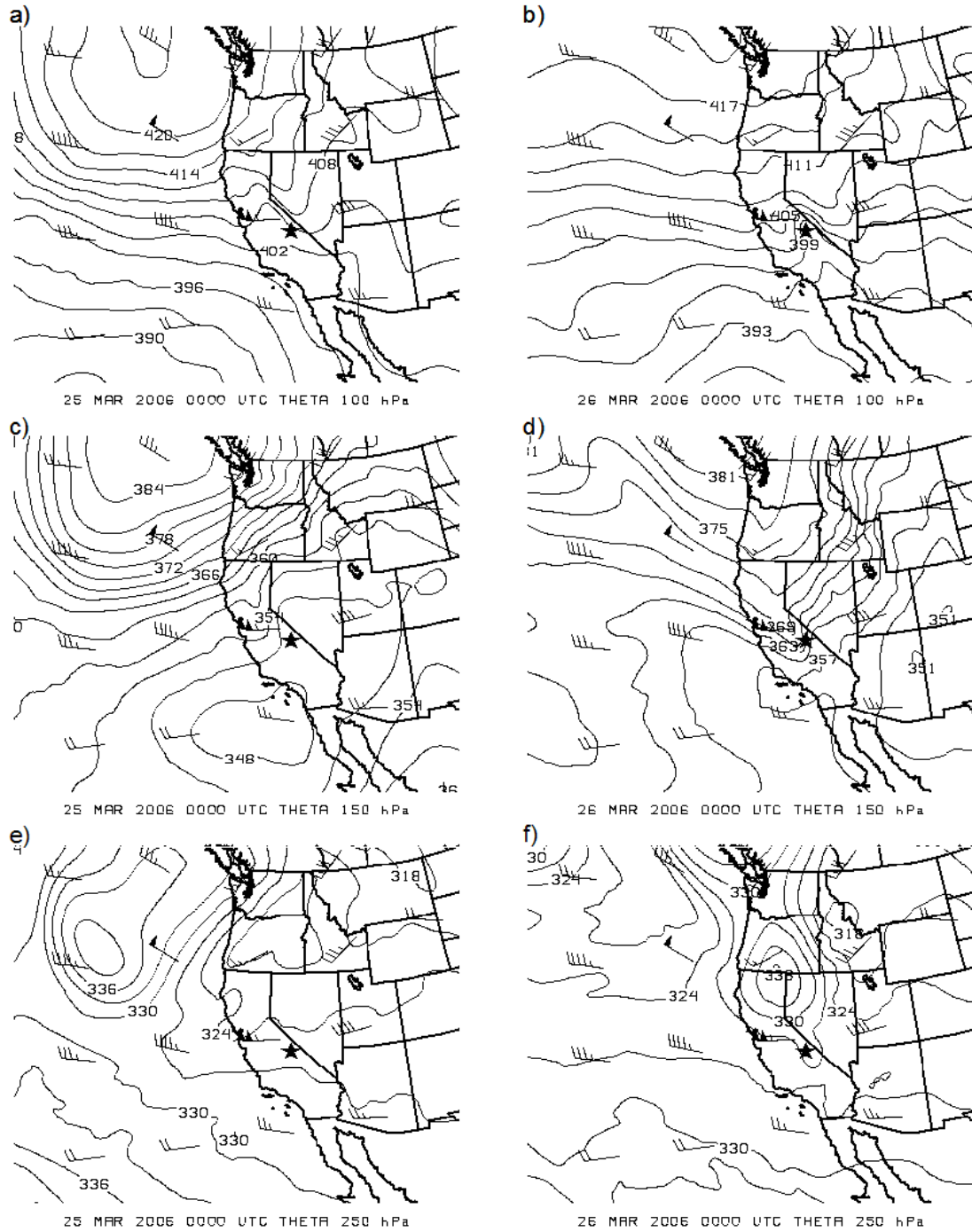
Figure 3.3: Potential temperature (K) and wind barbs (ms^{-1}) at (a-b) 100 hPa , (c-d) 150 hPa, and at (e-f) 250 hPa valid 0000 UTC 25 March 2006 (left column) and 0000 UTC 26 March 2006 (right column). Data from NCEP/NCAR North American Regional Reanalysis. The star marks the T-REX field site.
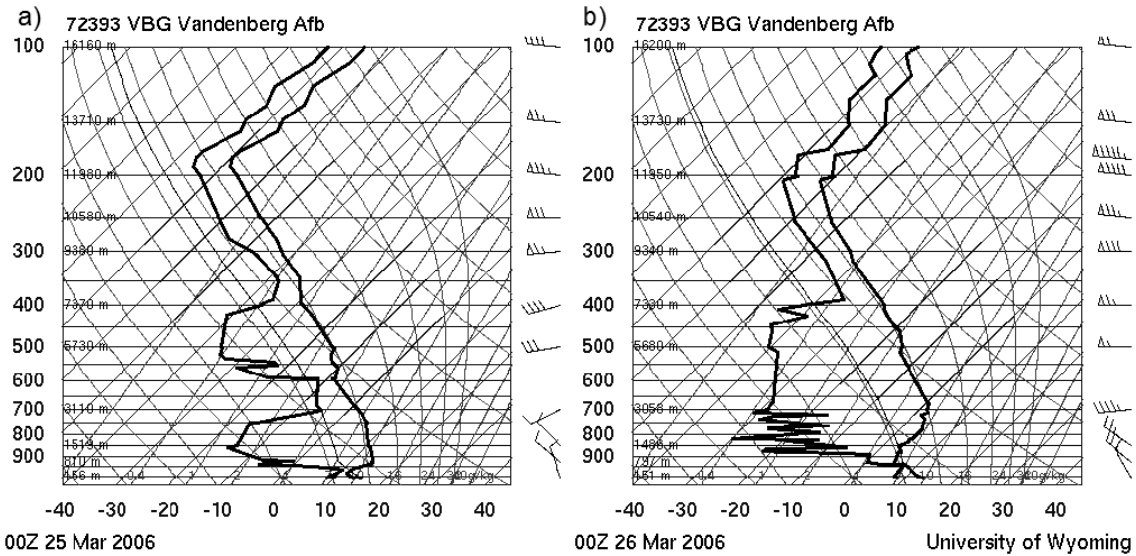
Figure 3.4: Rawinsonde soundings from Vandenberg Air Force Base (VBG) valid (a) 0000 UTC 25 March 2006 and (b) 0000 UTC 26 March 2006. From University of Wyoming.
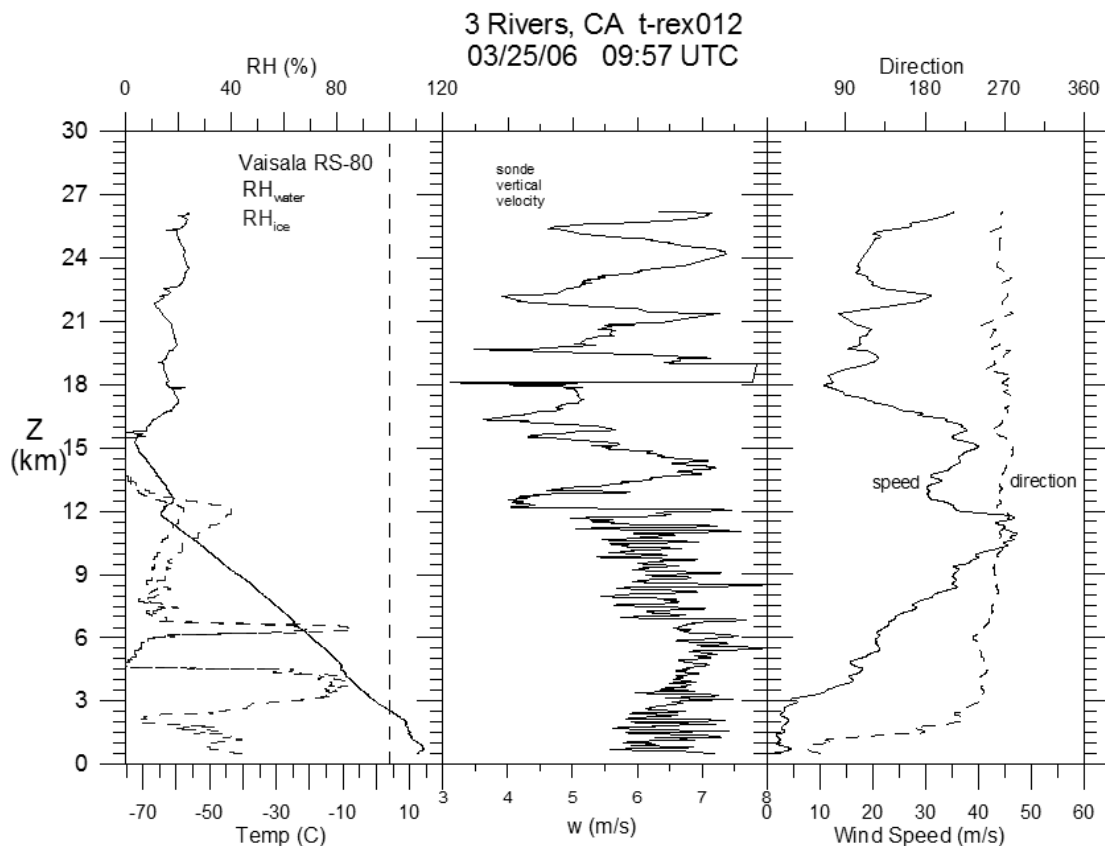
Figure 3.5: Air Force Research Laboratory radiosonde sounding from Three Rivers, CA, launched 0957 UTC 25 March 2006. Left panel is temperature (solid, °) and relative humidity with respect to ice and water (%, dashed). Center panel is vertical velocity (ms^{-1}) and right panel is wind speed (ms^{-1}) and direction. From T-REX field catalog (http://catalog.eol.ucar.edu/trex/).
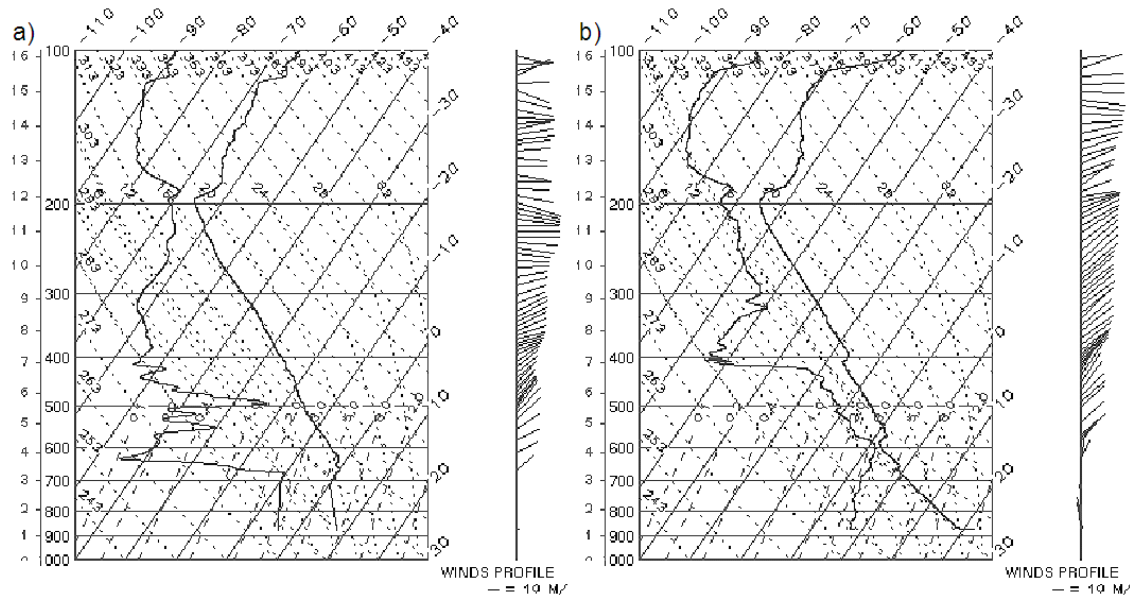
Figure 3.6: NCAR Integrated Sounding System (ISS) soundings from Independence, CA valid (a) 1117 UTC 25 March 2006 and (b) 1701 UTC 25 March 2006. From T-REX field catalog (http://catalog.eol.ucar.edu/trex/).
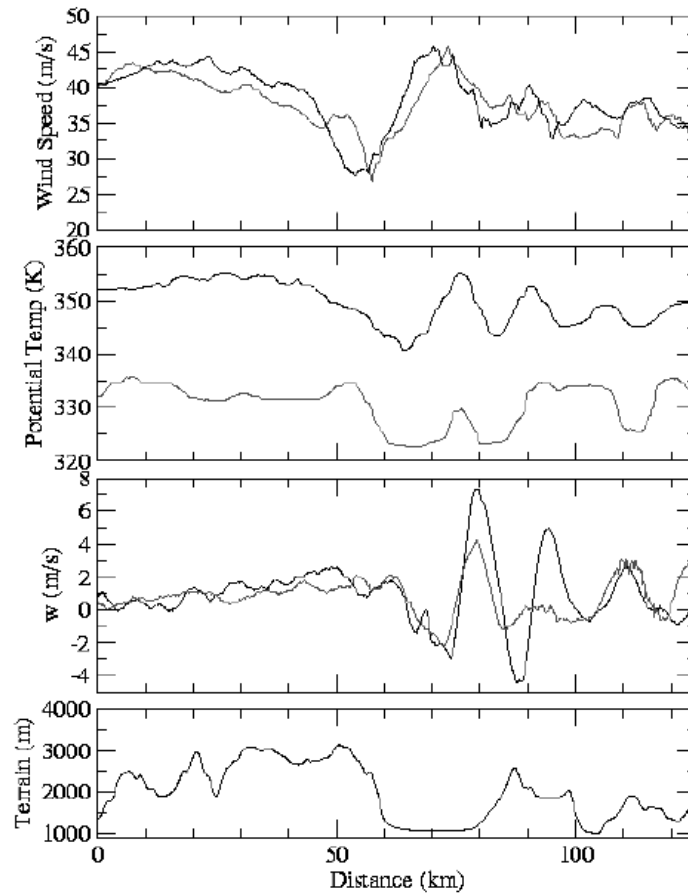
Figure 3.7: HIAPER observations from the southern leg at flight level 43 kft and 39 kft of wind speed (ms^{-1}), potential temperature (K), and vertical velocity (ms^{-1}), with the terrain profile below. These two segments were flown with about a one hour separation period between approximately 1815 UTC and 1915 UTC 25 March 2006 (Doyle, 2006). From T-REX field catalog (http://catalog.eol.ucar.edu/trex/).
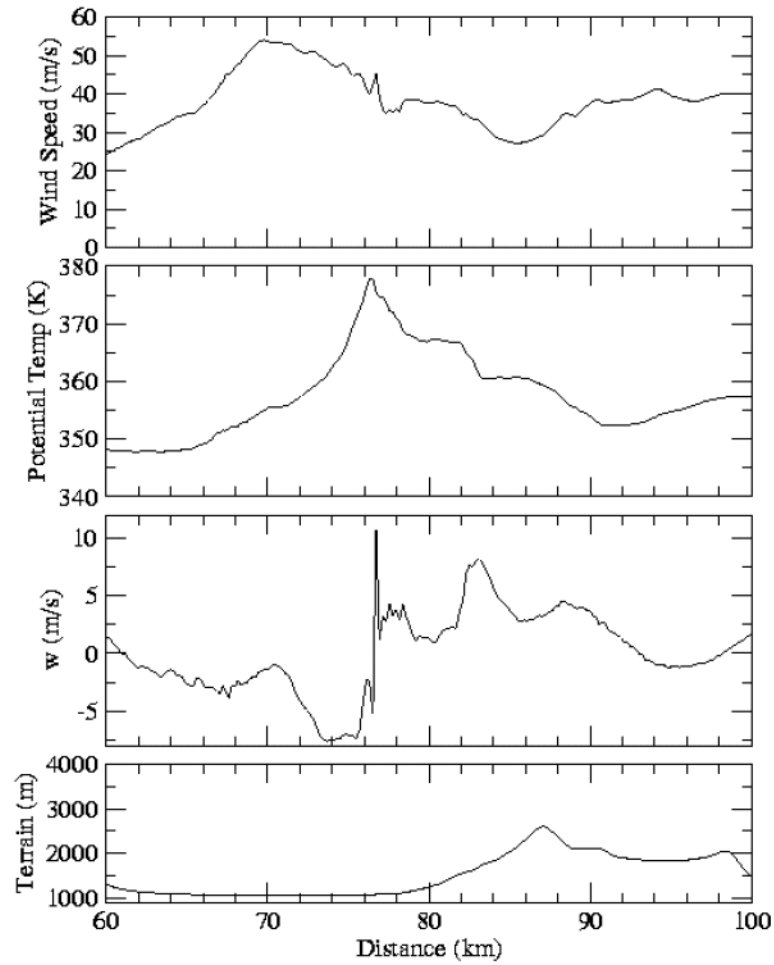
Figure 3.8: Same as in Fig. 3.6, except from the southern segment exit leg, approximately 2242 UTC and 45 kft (Doyle 2006). From T-REX field catalog (http://catalog.eol.ucar.edu/trex/).
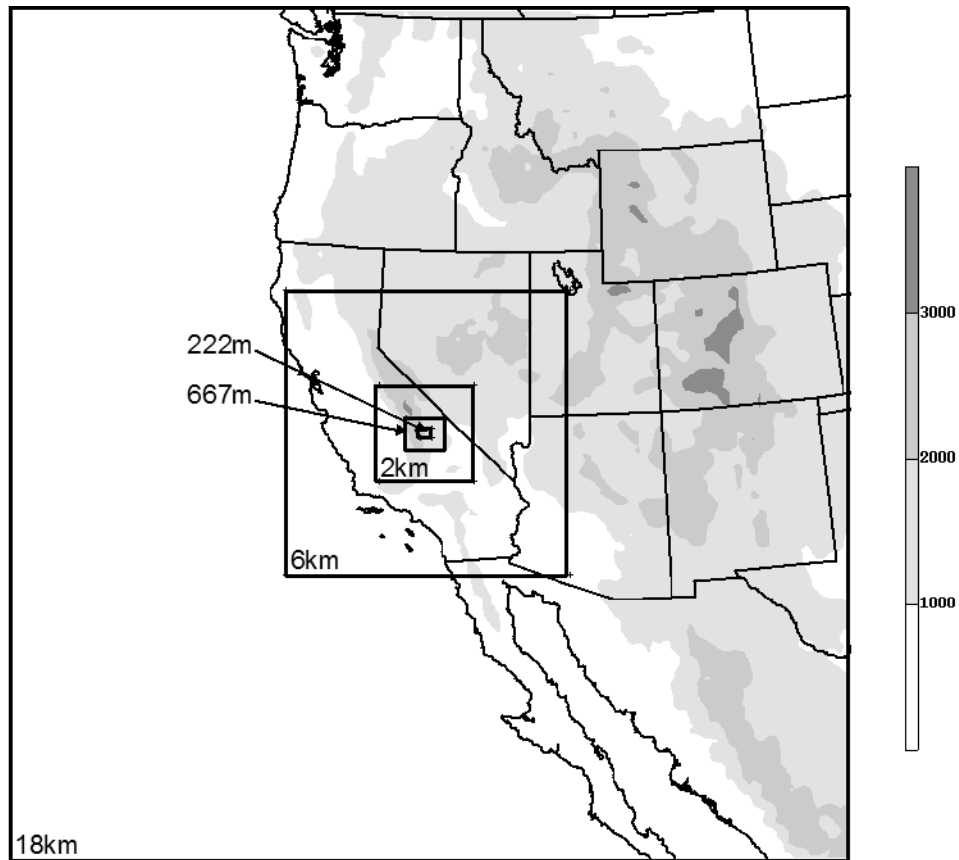
Figure 3.9: WRF/ARW v2.2 numerical simulation nesting strategy. Domains are labeled by horizontal grid spacing. 18 km WRF terrain shaded in meters.
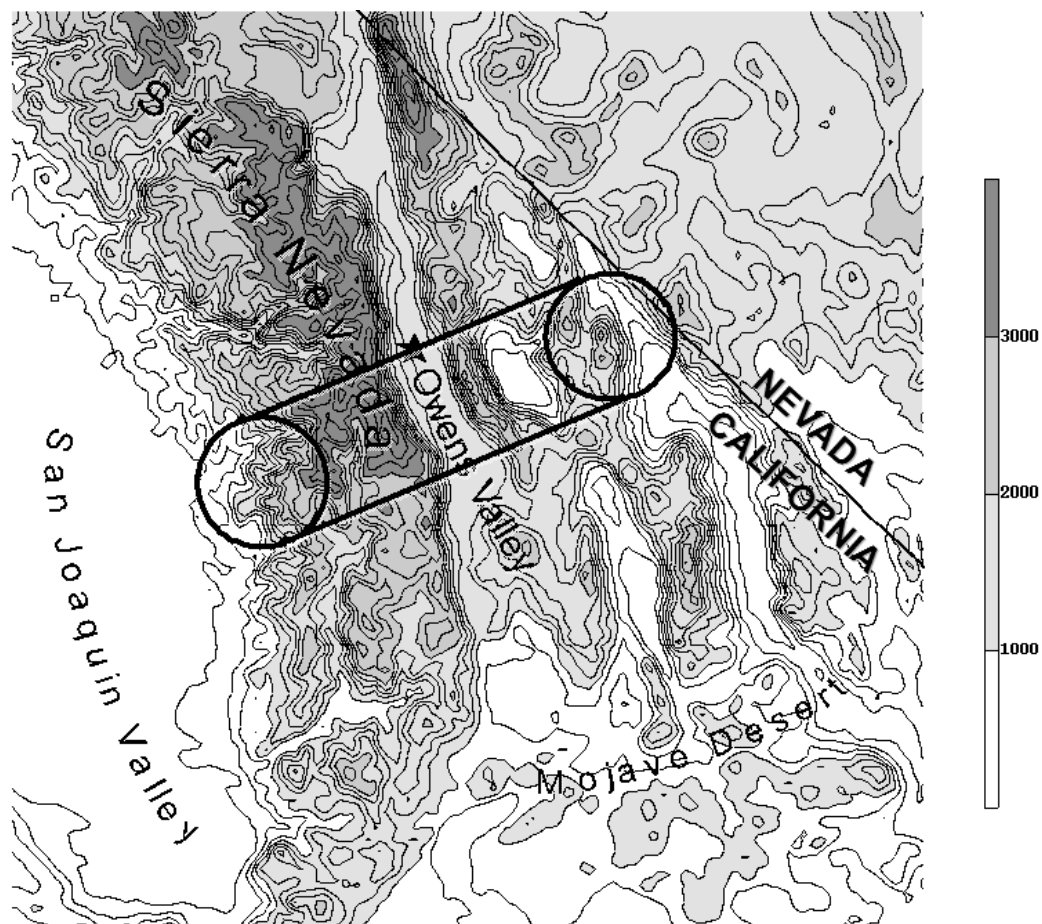
Figure 3.10: Model-simulated terrain in T-REX area (250 m contour, shaded every 1 km) showing Independence, CA (star) and GV HIAPER racetracks for IOP 6 (heavy solid contour; end circles depict turns for altitude changes). From 2 km WRF simulation.
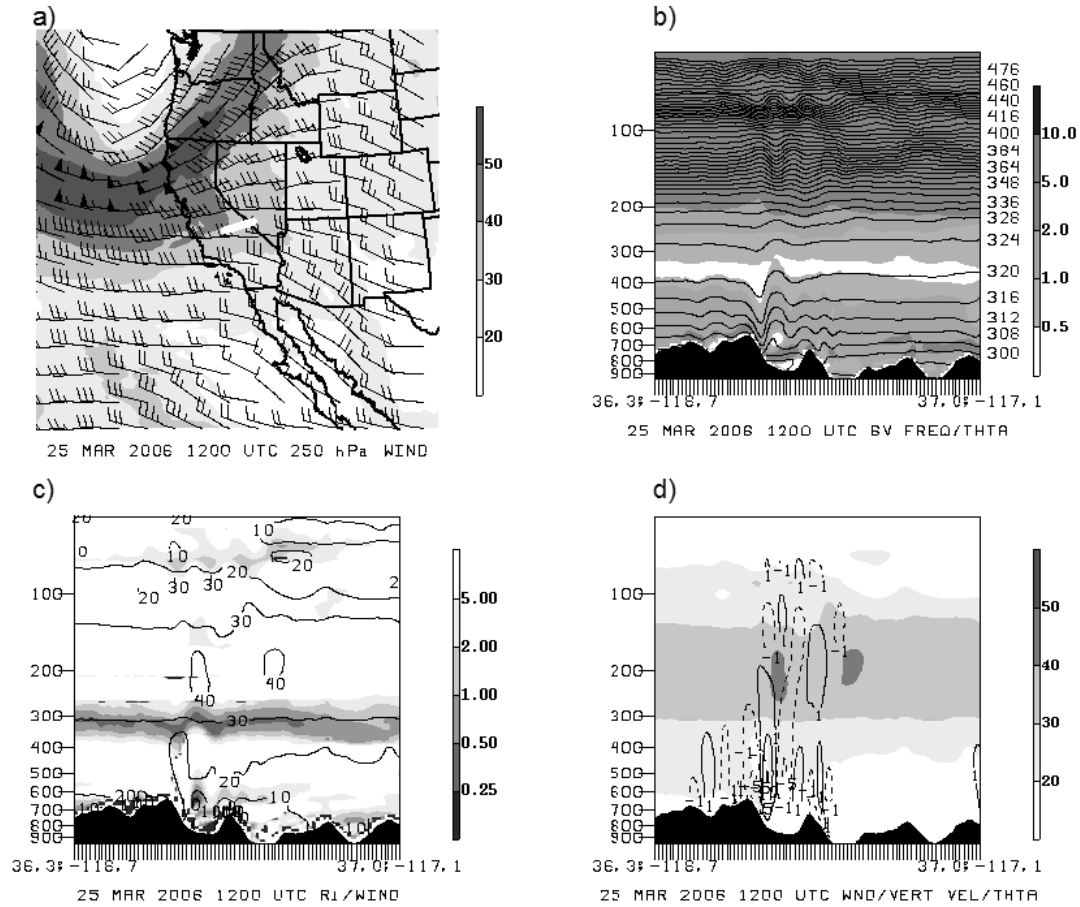
Figure 3.11: (a) Winds (ms^{-1}) at 250 hPa from 18 km WRF simulation. Vertical west-east cross-section of (b) potential temperature (contoured) and N^2 (shaded, s$^{-1} \times 10^{-4}$), (c) Ri (shaded) and wind speed (ms^{-1}, contoured), and (d) wind speed (ms^{-1}, shaded) and vertical velocity (ms^{-1}, contoured, dashed for downward vertical motion), from 2 km WRF simulation valid 1200 UTC 25 March 2006. Cross-sections along the heavy white line in (a). Vertical scale is hPa and horizontal scale is grid spacing (2 km per tick).
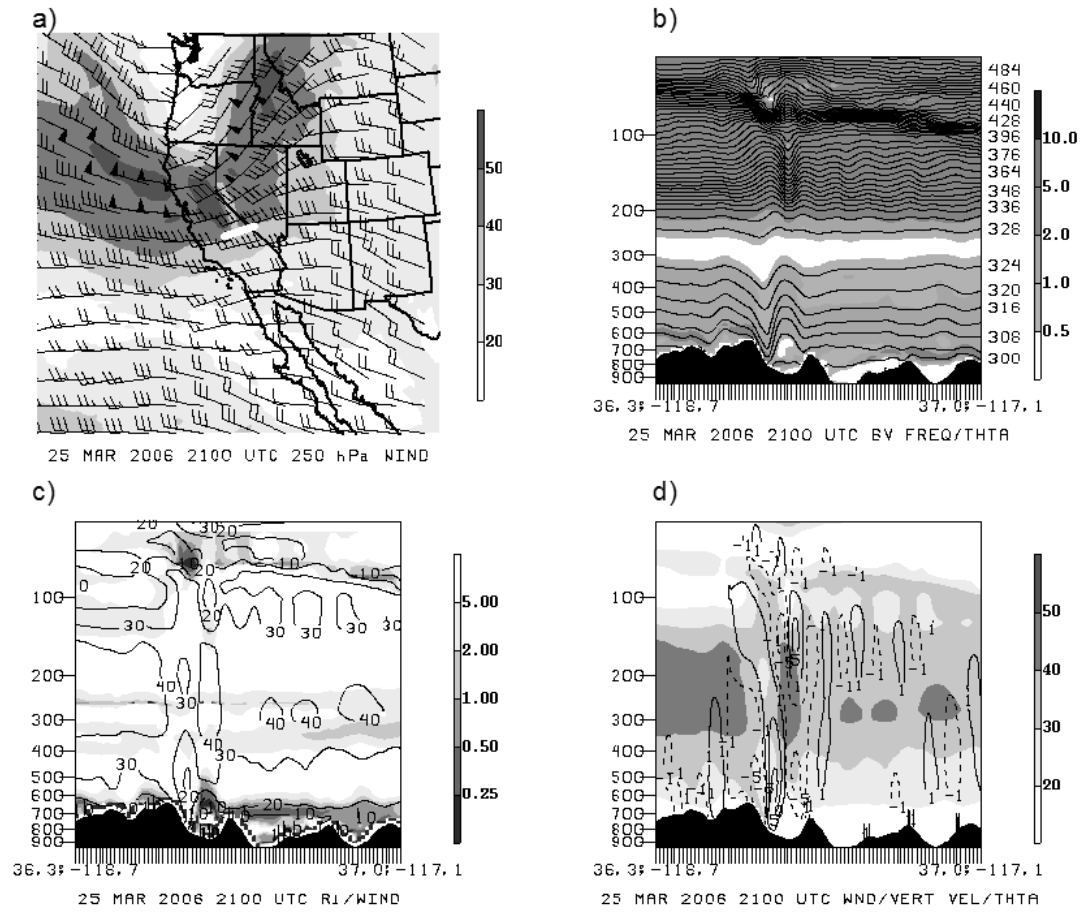
Figure 3.12: Same as Fig. 3.11, valid 2100 UTC 25 March 2006.

a)

26 MAR 2006 0000 UTC 250 hPa WIND

b)

26 MAR 2006 0000 UTC BV FREQ/THTA

c)

26 MAR 2006 0000 UTC Ri/WIND

d)

26 MAR 2006 0000 UTC WND/VERT VEL/THTA
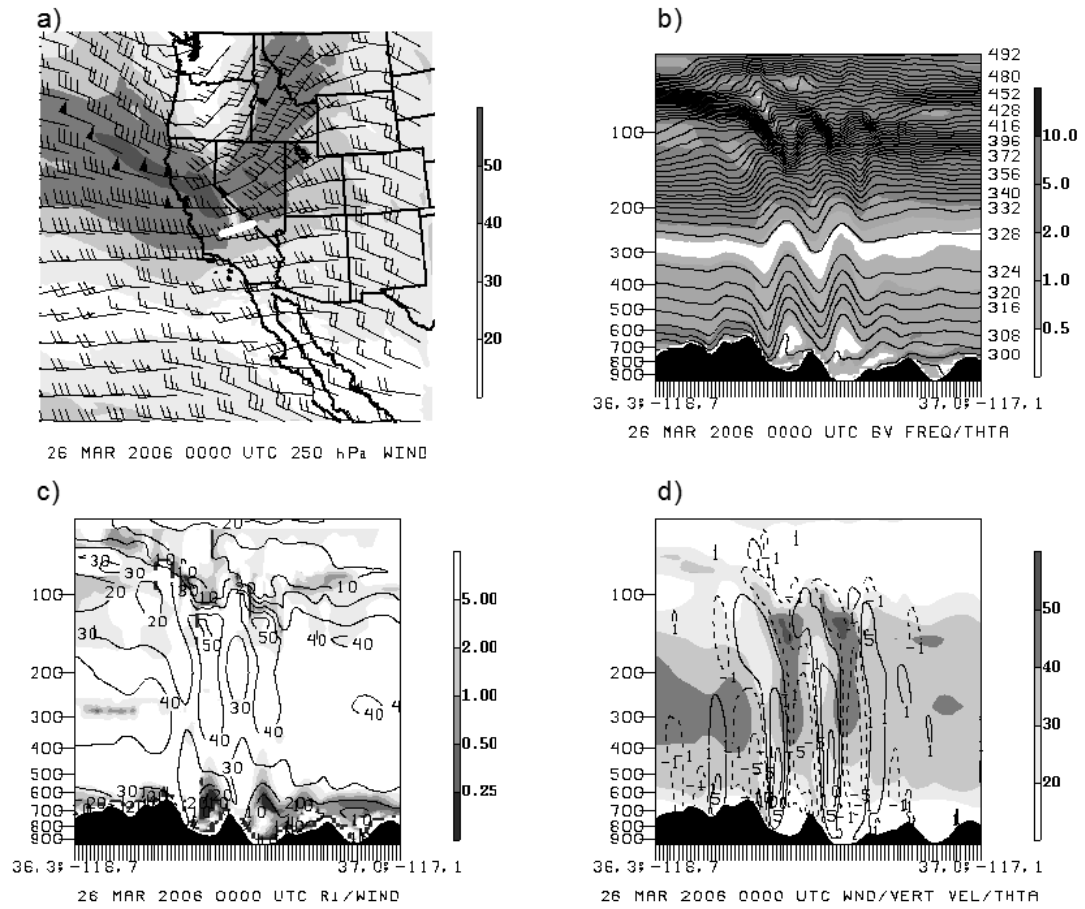
Figure 3.13: Same as Fig. 3.11, valid 0000 UTC 26 March 2006.
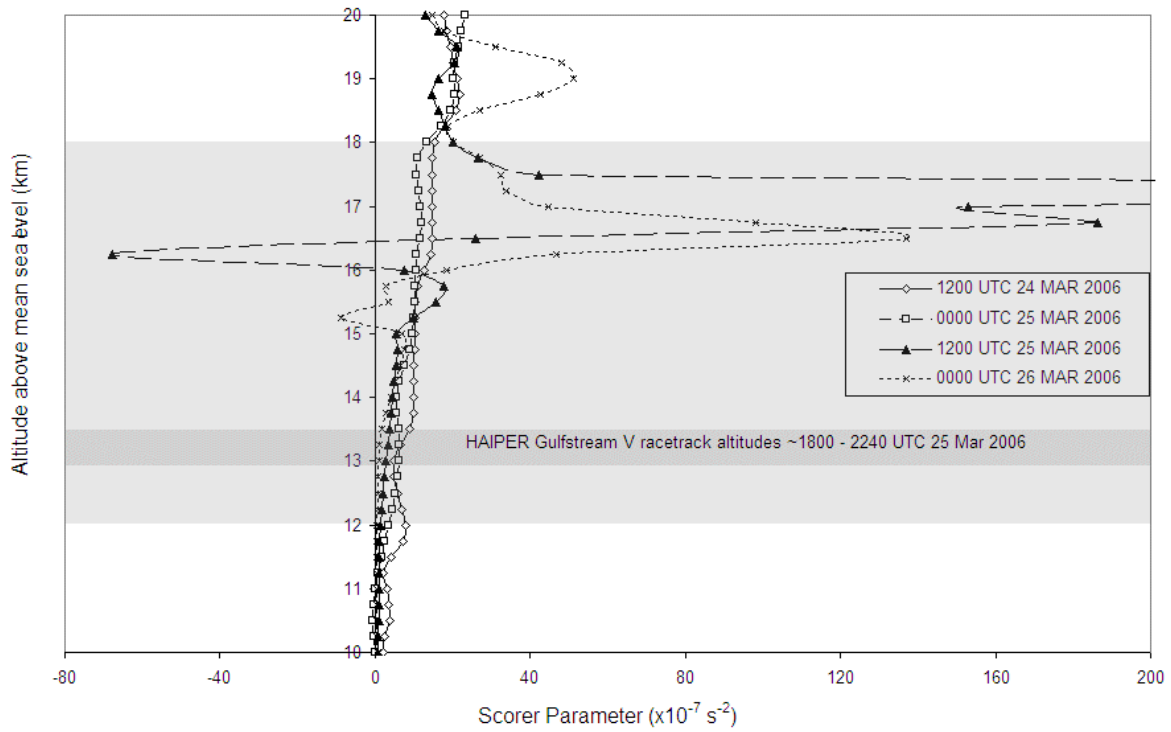
Figure 3.14: Vertical profile of Scorer parameter ($m^{-2} \times 10^{-7}$), above 36.4N, 118.0W, at 1200 UTC 24 March 2006, 0000 UTC and 1200 UTC 25 March 2006, and 0000 UTC 26 March 2006. The shaded area represents the levels at which gravity wave breaking was seen to occur in the model simulations, with the darkest shading representing the overlap of the wave-breaking levels with the HIAPER racetrack altitudes. From 6 km WRF simulation.
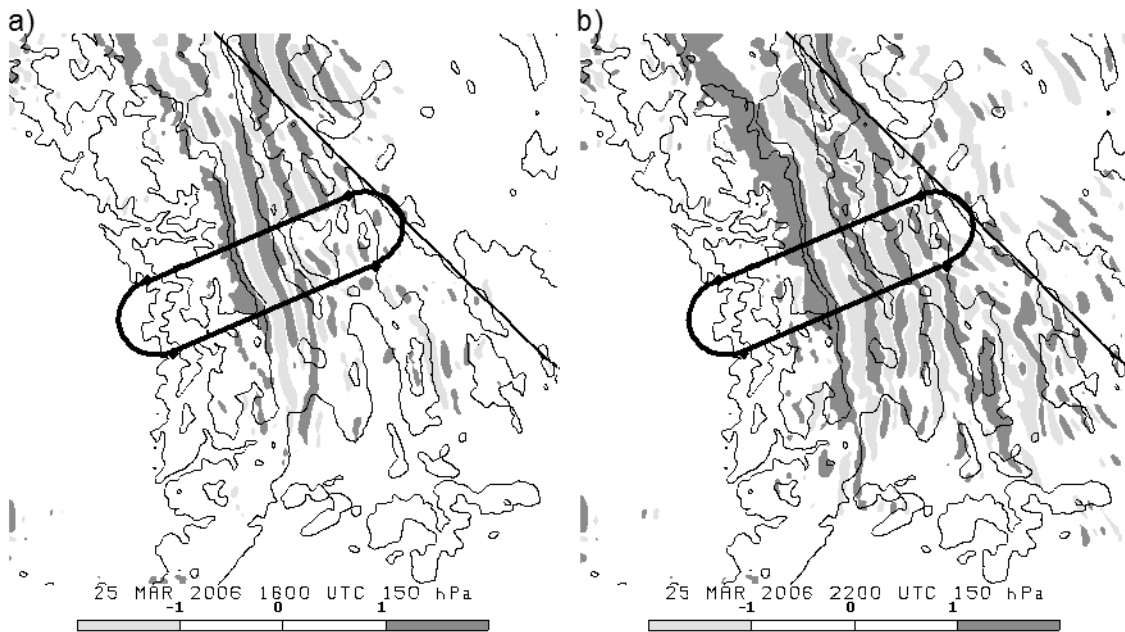
Figure 3.15: Simulated vertical velocity (shaded, ms^{-1}) at 150 hPa (approximate HIAPER exit-leg altitude), HIAPER racetrack (heavy loop), and model terrain (thin contour, 1 km increment) valid (a) 1800 UTC and (b) 2200 UTC 25 March 2006. From 2 km WRF simulation.
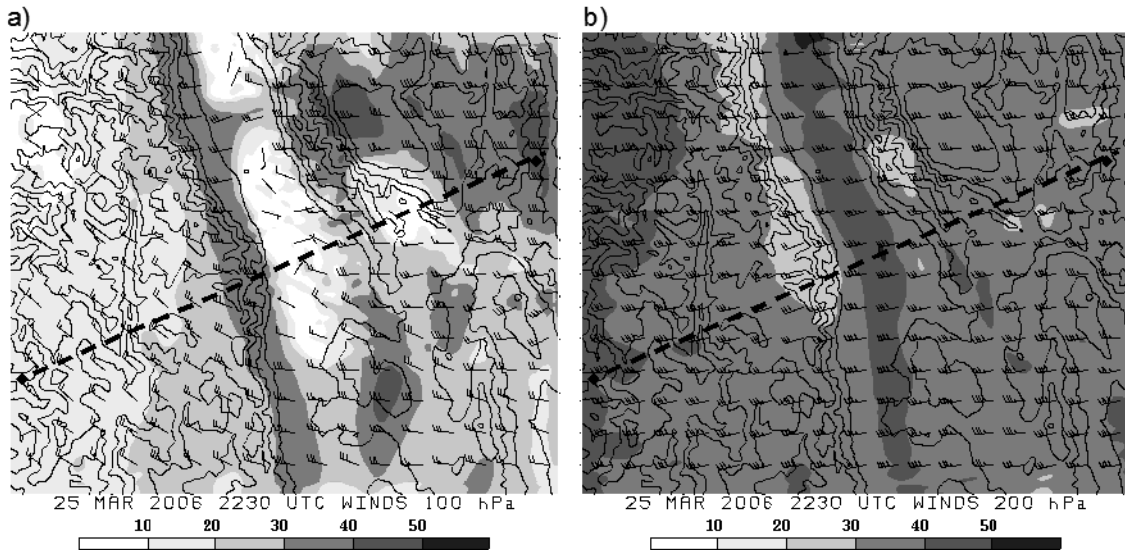
Figure 3.16: Simulated horizontal winds (shaded, ms^{-1}) and wind barbs at (a) 100 hPa and (b) 200 hPa valid 2230 UTC 25 March 2006. Thin contours are terrain height, 500 m increment, and dashed line is HIAPER track, southern leg. From 667 m WRF simulation.

109
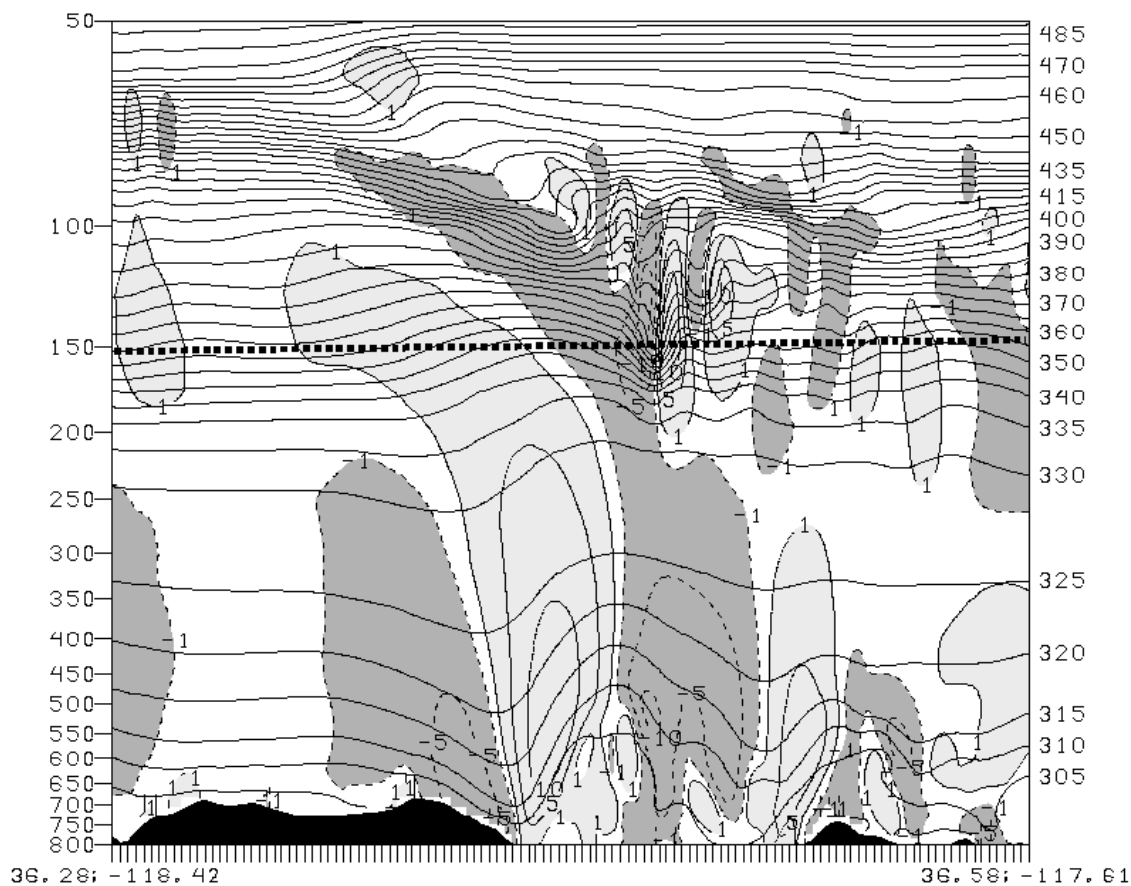
Figure 3.17: West-east vertical 850 to 50 hPa cross-section along HIAPER southern exit leg (dashed line in Fig. 3.15) of vertical velocity (shaded and contoured, , ms^{-1}, dashed contour for downward vertical motion, solid for upward), potential temperature (K, solid contours), and approximate HIAPER altitude (heavy dashed line). Horizontal scale is equal to grid spacing. Valid 2240 UTC 25 March 2006. From 667 m WRF simulation.
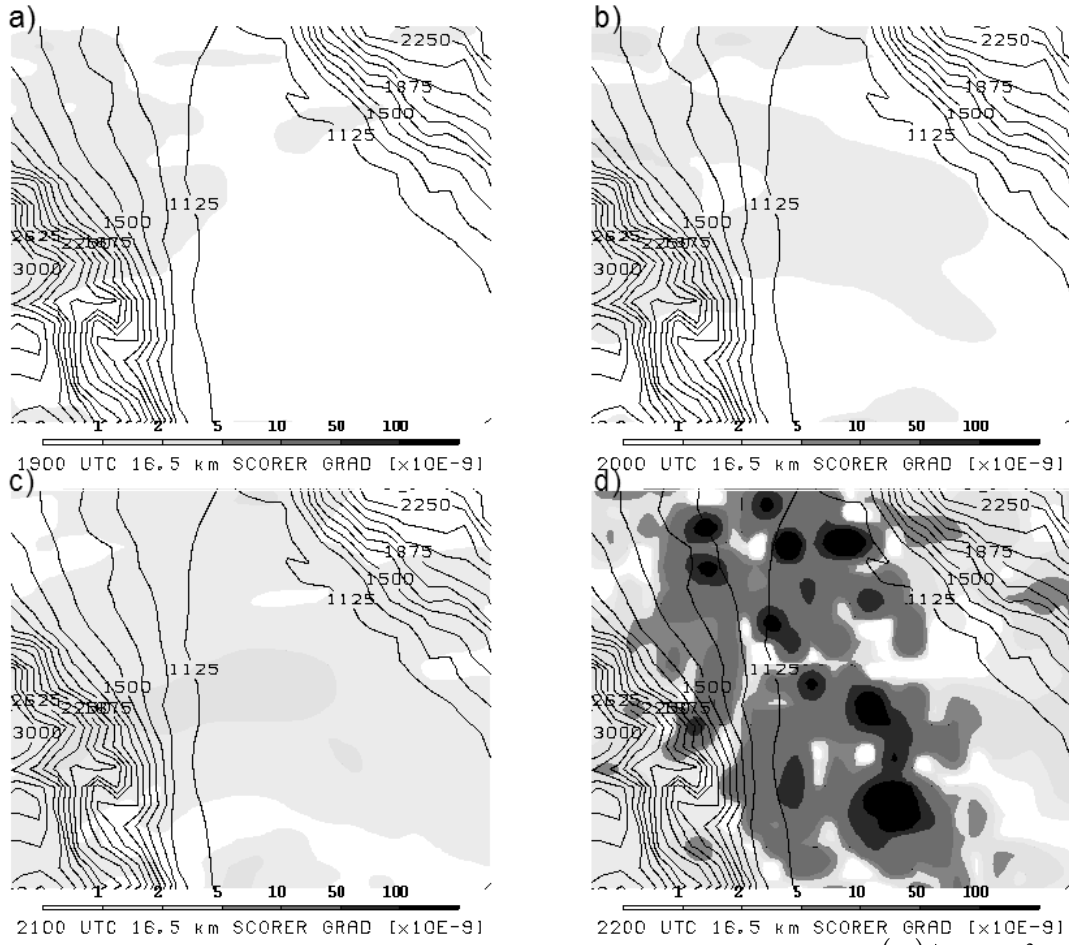
Figure 3.18: Simulated vertical gradient of the Scorer parameter ($\partial(l^2)/\partial z$, m^{-3} × 10^{-9}, shaded) for a portion of the 222 m WRF domain at 16.5 km MSL at (a) 1900 UTC, (b) 2000 UTC, (c) 2100 UTC, and (d) 2200 UTC 25 March 2006.
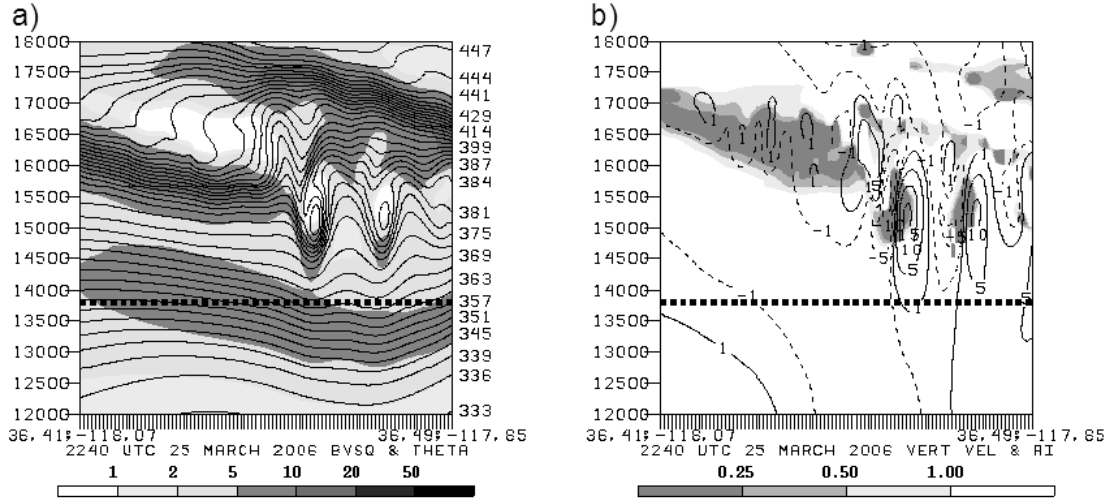
Figure 3.19: West-east vertical 12 to 18 km MSL cross-section along HIAPER southern exit leg (dashed line in Fig. 15) of potential temperature (contoured) and N^2 (shaded, $s^{-1} \times 10^{-4}$) and (b) Ri (shaded) and vertical velocity (ms^{-1}, contoured, dashed contour indicating downward vertical motion), and approximate HIAPER altitude (heavy dashed line). Valid 2240 UTC 25 March 2006. From 222 m WRF simulation.
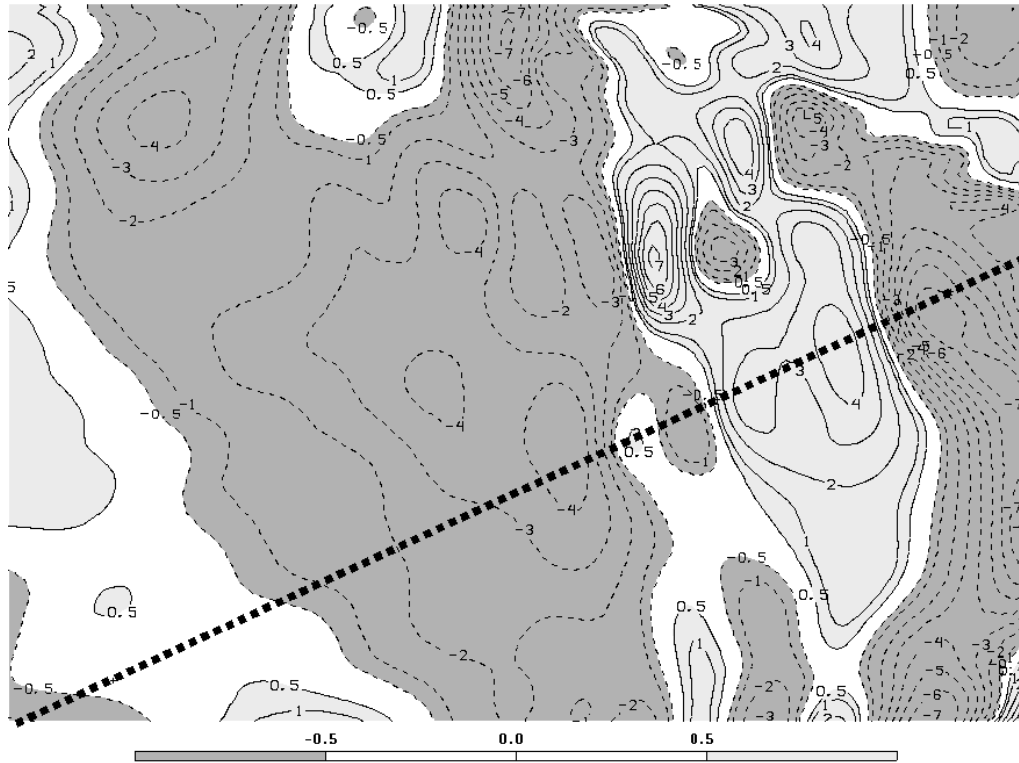
Figure 3.20: w' (ms^{-1}, shaded and contoured, dashed contour indicating downward vertical motion) at 13 km MSL (approximate HIAPER altitude) and HIAPER track (heavy dashed line) at 2240 UTC 25 March 2006. From 222 m WRF simulation.
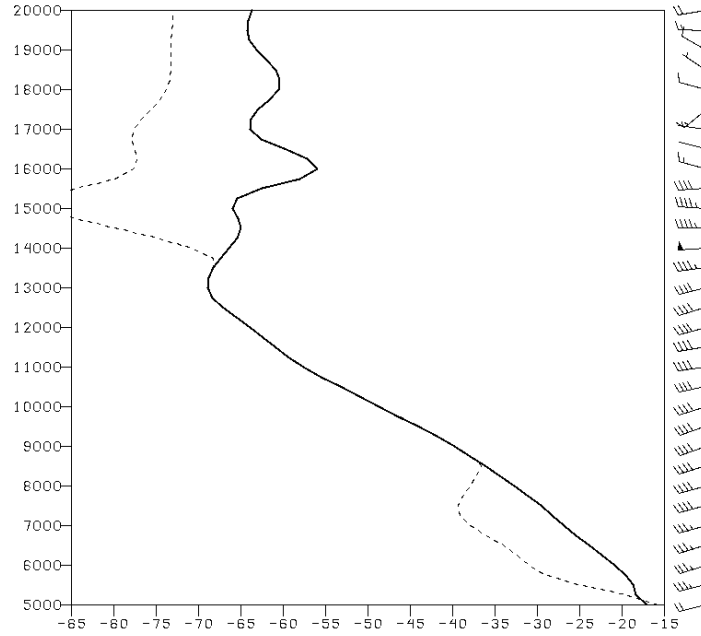
Figure 3.21: Model-derived vertical profile of temperature (°C, solid contour), dew point temperature (°C, dashed contour), and winds (ms^{-1}, barbs), valid 2240 UTC 25 March 2006 for a grid point along the southern HIAPER track. From 222 m WRF simulation.
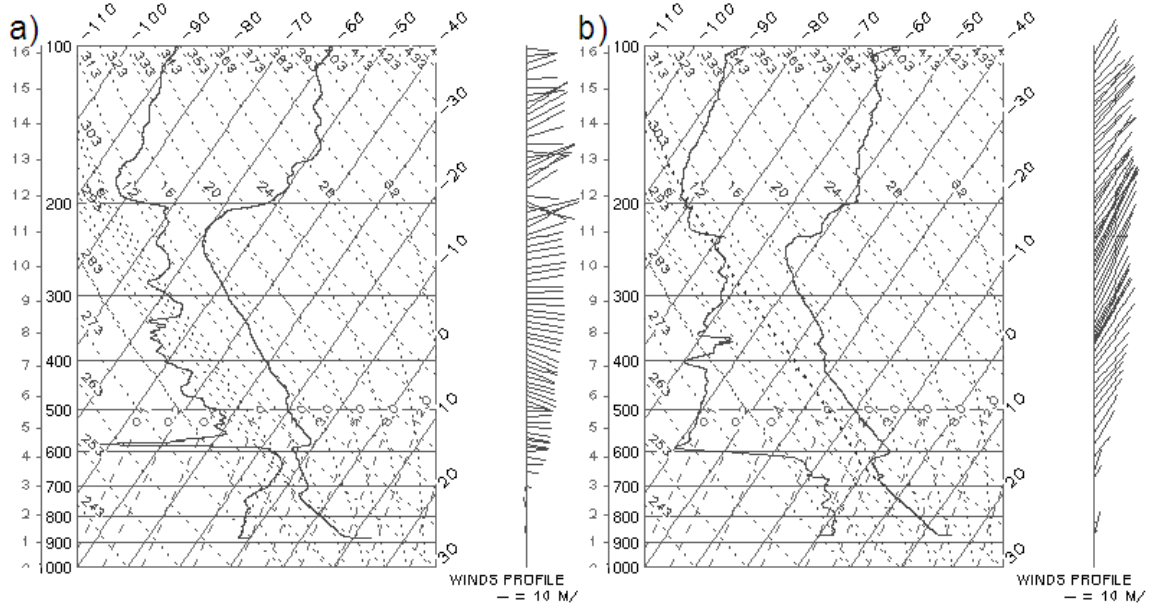
Figure 3.22: NCAR Integrated Sounding System (ISS) soundings from Independence, CA launched (a) 2301 UTC 13 March 2006 and (b) 2257 UTC 14 March 2006 (IOP 4). From T-REX field catalog (http://catalog.eol.ucar.edu/trex/).
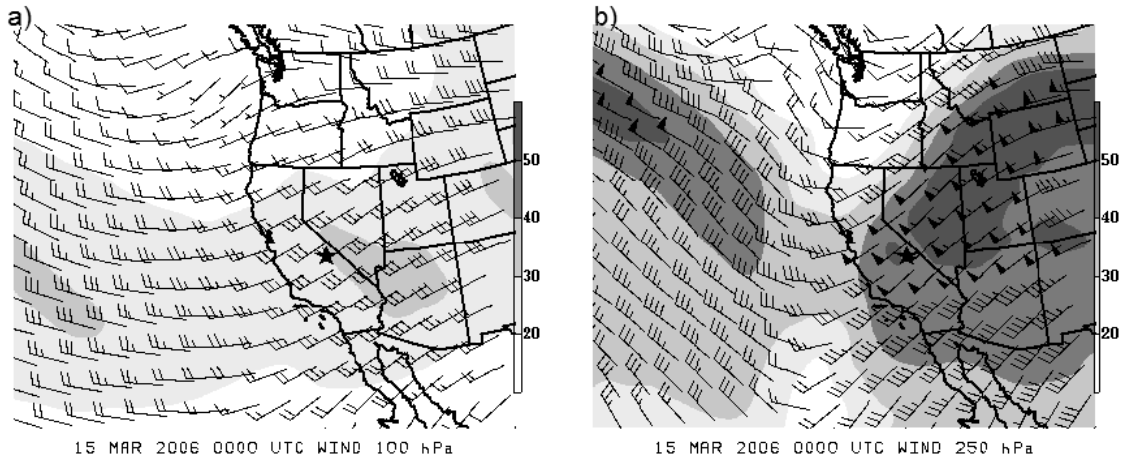
Figure 3.23: Wind speed and wind barbs (ms^{-1}) at (a) 100 hPa and (b) 250 hPa valid 0000 UTC 15 March 2006 (IOP 4). Data from NCEP/NCAR North American Regional Reanalysis. Data was smoothed with six passes of a Gaussian filter to eliminate noise after winds were corrected from model-relative to true. The star marks the T-REX field site.
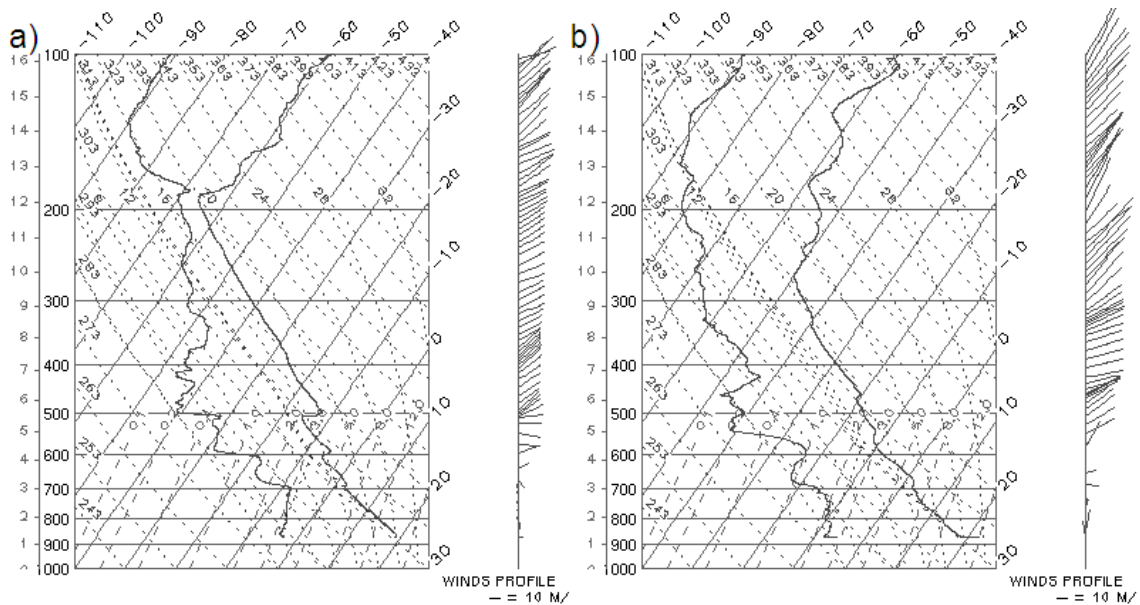
Figure 3.24: NCAR Integrated Sounding System (ISS) soundings from Independence, CA launched (a) 0159 UTC and (b) 2003 UTC 16 April 2006 (IOP 13). From T-REX field catalog (http://catalog.eol.ucar.edu/trex/).

114
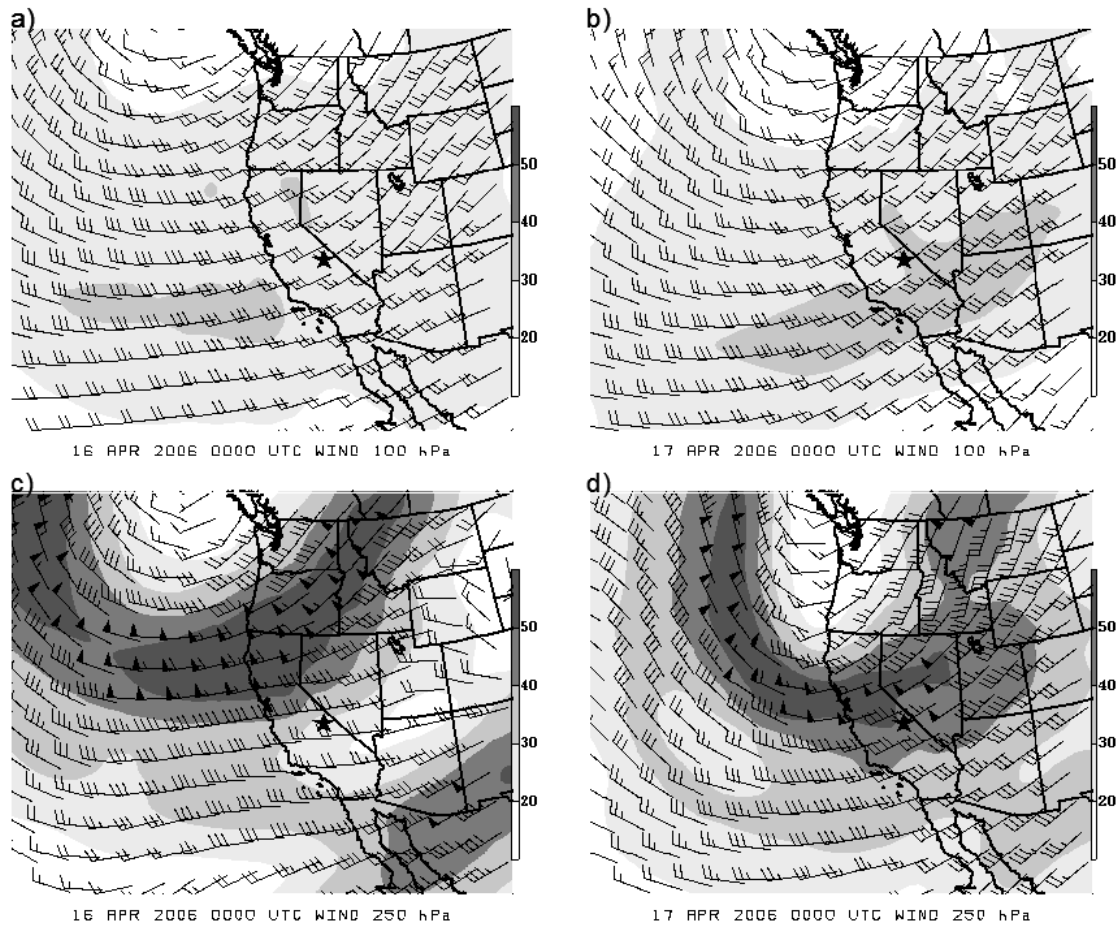
Figure 3.25: Wind speed and wind barbs (ms^{-1}) at (a-b) 100 hPa and at (c-d) 250 hPa valid 0000 UTC 16 April 2006 (left column) and 0000 UTC 17 April 2006 (right column). Data from NCEP/NCAR North American Regional Reanalysis. Data was smoothed with six passes of a Gaussian filter to eliminate noise after winds were corrected from model-relative to true. The star marks the T-REX field site.
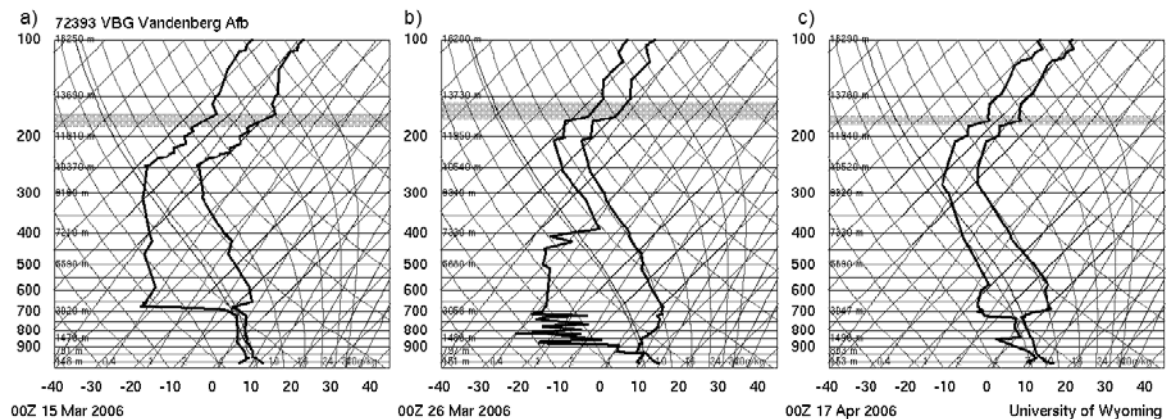
Figure 3.26: 0000 UTC radwinsonde soundings from Vandenberg Air Force Base, CA (VBG) from (a) 15 March 2006 (IOP 4) (b) 26 March 2006 (IOP 6) and (c) 17 April 2006 (IOP 13). Shaded area depicts depth over which parcels lifted for buoyancy calculation. Wind profiles eliminated for clarity. From University of Wyoming.

115

CHAPTER 4

**IDEALIZED 2-DIMENSIONAL SIMULATIONS OF JET/MOUNTAIN WAVE
INTERACTIONS WITH VARYING WIND AND TEMPERATURE PROFILES**

4.1. Introduction

Case studies involving real data, while critical to our understanding of the dynamics

of lower stratospheric aviation turbulence, can be limiting simply because of the relative

scarcity of observations, which in turn is a function of the transient nature of turbulence. One

of the major limiting factors in the real data cases (Chapters 2 and 3) was that the data used

to initialize the models (global reanalysis, GFS, etc.) had very limited vertical resolution and

so was insufficient to capture the full magnitude of the stratospheric gradients of static

stability and shear hypothesized to be so critical in these cases. Idealized simulations, on the

other hand, allow for easy modification of the initial and boundary conditions to any

resolution the user desires. To that end a series of 2-dimenional simulations were conducted

using the full atmospheric profiles of wind, temperature, and moisture from the two previous

case studies (the 9 December 1992 Colorado DC-8 incident and the T-REX IOP 6 case) over

idealized terrain, roughly matching the corresponding terrain profiles for each case. The

expected result was a series of simulations with initial and boundary conditions that were

truly representative of the thermal and momentum structures of the real atmosphere in the

previous two chapters.

The hypothesis is that the combination of a strong inversion above the tropopause

bracketed by distinct jet features governs the intensity of the stratospheric turbulence. The

hypothesized role of the mountain wave is to provide a continuous buoyancy perturbation to

this stable layer. In turn the stable layer allows for the mountain wave to amplify and

eventually break. While Chapters 2 and 3 dealt in part with the synoptic conditions which

lead to the stable layer in the stratosphere (specifically anticyclonic flow above and cyclonic flow below leading to a compressed warm layer in between), in these simulations that process is pre-supposed. The objective for the idealized simulations was instead to quantify the degree to which the strength of the inversion and the wind structures affect the intensity of the potential for aviation turbulence. In order to accomplish this objective, two approaches were used. For the 9 December 1992 Colorado cases, the 1200 UTC Denver (DEN) sounding from 9 December was used as the basis for all simulations, with the control simulation using the unmodified sounding and terrain. By modifying individual components of the sounding such as the 200 hPa inversion strength, the vertical wind profile, the static stability through the depth of the troposphere, and even the terrain, these simulations were conducted to isolate those parameters that had the greatest effect on both the flow response and the model-parameterized TKE. Additionally, three fine resolution simulations were integrated using modified DEN soundings to determine at higher resolution the effect of the inversion strength on the model production of TKE.

For the T-REX case, a different approach was taken. The "control simulation" used the Vandenberg AFB (VBG) sounding at 0000 UTC 26 March 2006 (corresponding to IOP 6), but rather than modify this sounding and/or the terrain, simulations were instead initialized using representative VBG soundings from five other IOPs. Two of these other IOPs were 4 and 13 (discussed in Chapter 3) which also were characterized by large-amplitude stratospheric gravity waves, and the remaining three IOPs (1, 8, and 14) were cases with relatively weak stratospheric gravity waves. In these cases the mountain waves were either trapped below the tropopause or weak overall. The purpose of these simulations was to establish the differences in upper-level wind and temperature structures between those

IOPs that were observed to have strong stratospheric gravity waves (and the potential for CAT) and those that did not, within the context of the hypothesized paradigm for jet streak/mountain wave interaction.

4.2. Methodology

The idealized simulations all use the Weather Research and Analysis/Advanced Research WRF (WRF/ARW) Version 2.2 NWP model as described in Chapter 1. The module used for these simulations was the em_hill2d_x (Eulerian mass 2-dimenional hill, with the horizontal plain in the x direction) module. This module requires an input sounding which includes the vertical temperature, winds, and moisture profile as initial conditions. The domain was periodic in y and open in x. The terrain was modified in the model source code, and changes to the terrain required re-compilation of the model code. All domains had 90 vertical levels, distributed linearly with a model top at 30 km (roughly 10 hPa), giving an average vertical grid length of 0.33 km. The model used an absorbing upper boundary condition in the top 15 km with a damping coefficient of 0.003 in order to reduce reflection of gravity waves. All simulations were integrated for four hours and model fields were output every five minutes. No microphysical parameterization was used. The model output was visualized using the Grid Analysis and Display System (GrADS).

The simulations used a 1.5-dgree TKE closure scheme for turbulence. The equation governing the prognostic TKE scheme in the WRF/ARW v2.2 diffusion module (Skamarock et al. 2007) is given by:

$$\frac{\partial}{\partial t}(\mu_d e) + (\nabla \bullet \vec{V}_\eta) = \mu_d (shear\ production + buoyancy + dissipation) \qquad (4.1)$$

In Eq. (4.1), the μ_d represents the mass of dry air in the column and $\left(\nabla \bullet \vec{V}_\eta\right)$ represents divergence on the model's hydrostatic-pressure terrain-following vertical coordinate surfaces. The two production terms are given by:

$$shear\ production = K_h D_{11}^2 + K_h D_{22}^2 + K_v D_{33}^2 + \overline{K_h D_{12}^2}^{xy} + \overline{K_v D_{13}^2}^{x\eta} + \overline{K_v D_{12}^2}^{y\eta} \qquad (4.2)$$

and:

$$buoyancy = -K_v N^2 \qquad (4.3)$$

where D_{11}, D_{22}, etc. represent the components of the stress tensor (see Skamarock et al. 2007 for more details) and K_h and K_v are the horizontal and vertical eddy viscosities, respectively. These are calculated dynamically:

$$K_{h,v} = C_k l_{h,v} \sqrt{e} \qquad (4.4)$$

where C_k is a constant ($0.15 < C_k < 0.25$). The user is given the option to choose a critical length which drives the calculation of length scales $l_{h,v}$. If no critical length is chosen, the model defaults to a length scale longer than the grid spacing, setting both horizontal and vertical length scales ($l_{h,v}$) equal to $\sqrt[3]{dx\,dy\,dz}$. The result of this formulation is that $K_h = K_v$ which is undesirable (typically $K_h > K_v$). For this study, the critical length scale was chosen to always be $dx - 0.1$ so that the alternate $l_{h,v}$ calculation would be used by the model. In the alternate formulation, $l_h = \sqrt{dx\,dy}$ and:

$$l_v = \min\left[dz, 0.76\sqrt{e}/N\right] \qquad \qquad \text{for } N^2 > 0 \qquad (4.5)$$

$$l_v = dz \qquad \qquad \text{for } N^2 \leq 0 \qquad (4.6)$$

which, when used in Eq. (4.4), gives the desired result of $K_h > K_v$.

In order to examine the relative contributions of the shear and buoyancy terms to the overall model TKE, the stress tensors and eddy viscosities were extracted from the model output for the fine-resolution Colorado simulations and the T-REX cases. The WRF model diffusion module code differs slightly from (4.2) in that the variance deformation terms are multiplied by 0.5 and the covariance deformation terms are computed as an average of the four surrounding deformation tensors. This code was replicated to reproduce the model shear and buoyancy production/destruction terms as they were not available as output via the model registry. To check the validity of these results, an alternate form of TKE calculation was also used. This form follows Eq. (1.10):

$$shear\ production = K_v \left[\left(\frac{\partial U}{\partial z} \right)^2 + \left(\frac{\partial V}{\partial z} \right)^2 \right] \tag{4.7}$$

In order to reconcile the scales and units with Eq. (4.7), the buoyancy and shear TKE production arrays calculated following the model code (Equations 4.1-4.3) were divided by μ_d. Overall, the magnitudes and distributions of the shear production terms calculated by both methods (Equations 4.2 and 4.7) were similar, although some subtle differences were seen. Both will be examined in the following sections. However, it is noted that shear production calculated from (4.7) may not be consistent with overall total kinetic energy of both wave and turbulent motions because the model uses (4.2) for shear production. Although the simulations are two-dimensional, for all simulations, the horizontal wind field includes both the u and v components. Gradient Ri was calculated using the model output N^2 and the square of both the U and V shear. A vertical centered difference over 500 m was used to calculate vertical shears.

It is worth noting that there are several sources of error in these simulations, all of which are necessary to simplify the problem and isolate specific aspects of the flow response. One such issue is that the upstream boundary conditions remain steady-state throughout the simulation time, in clear contrast to real-world conditions. The input profiles used in these simulations are from nearby rawinsonde soundings (with GFS analysis data above to complete the boundary conditions to 30 km AGL) that may not have been truly representative of the profile immediately upstream of the mountain. Additionally, no attempt was made to enforce geostrophic balance on the modified soundings in the Colorado cases, a point which would have been moot given the lack of a Coriolis parameter in the two-dimensional simulations. In spite of these potentially large sources of error, the results of the simulations were predictable within the context of the hypothesis.

4.3. 9 December 1992 Colorado Coarse Resolution Simulations

A total of 14 simulations were conducted relating to the 9 December 1992 Colorado aviation turbulence case (Table 4.1). Most of these simulations involved using a Gaussian bell-shaped mountain with a height of 2 km and a half-width of 10 km, approximating the Colorado Front Range (Doyle 1999). The first seven simulations used a 2 km horizontal grid spacing on a domain that was 200 grid cells in x by 3 grid cells in y, and varied the input sounding profile. The control simulation used the 1200 UTC 9 December DEN sounding temperatures and winds as shown in Fig. 4.1. The other six simulations in this group used a modified version of this sounding as seen in Fig. 4.2 and described in Table 4.1. These modifications included changing the strength of the 200 hPa inversion, changing the wind profile, and cases with an isothermal layer in the stratosphere. DEN is 1625 m above mean sea level (MSL), and at 1200 UTC on 9 December, the surface pressure was 829 hPa. For

the purposes of these simulations, the 0 km level in the model was set at 829 hPa, and the heights of the pressure levels indicated in Fig. 2.3, were reduced by 1625 m. This placed the aircraft incident altitude, (9.7 MSL) at approximately 8 km AGL (above ground level). The tropopause in the control simulation was at 8.7 km AGL and 200 hPa inversion was at 10 km AGL.

Because the simulations began from a uniform, quiescent state, considerable time was required for model spin-up. Fig. 4.3 shows the evolution of the vertical velocity and potential temperature fields for the control simulation. Although the downslope wind/hydraulic jump couplet develops rather quickly in the lower troposphere, one sees that even at t = 90 min (Fig. 4.3b), the isentropes have only begun to become perturbed in the stable layer. By t = 180 minutes (Fig. 4.3c) a fully-developed stationary mountain wave, repeating in the vertical (~ 6 km vertical wavelength) is present, with steeply tilted isentropes at and above 8 km and vertical velocities reaching ±5 ms^{-1}. Also present is a second wave downstream of the hydraulic jump. This wave is seen to have propagated approximately 20 km downstream by t = 240 min (Fig. 4.3d). The downstream propagating wave is a feature that appears in all simulations with a 200 hPa inversion present.

At the end of simulation time (t =-240 min, Fig. 4.4), the control simulation output bore a remarkable resemblance to the NHMASS full-terrain real data simulations described in Chapter 2. Specifically, in the 8 km to 10 km AGL layer, a strong horizontal gradient of vertical velocity was present directly in the lee of the mountain (in excess of ±5 ms^{-1} over a distance of a few km) associated with a hydraulic jump, with nearly vertical isentropes, indicating strong gravity wave action. Additionally, this region was characterized by a strong gradient of static stability, Ri < 0.25, and an area of model-parameterized TKE 5-7

$m^2 s^{-2}$ in the 7 to 9 km AGL layer, indicating strong potential for turbulent flow near the aircraft incident location. Additionally, a strong overturning wave at 14 km was producing model TKE exceeding 10 $m^2 s^{-2}$. That the idealized terrain simulation produced a very similar flow to what was modeled and observed in the real data case indicates the robustness of the hypothesis, i.e., the sensitivity of the flow at and above the tropopause is to the thermal and wind structure rather than the specific terrain gradients.

It was hypothesized that by increasing the strength of the 200 hPa inversion by approximately 8.9 K and shifting the profile above by an equal amount, the potential for turbulence in the vicinity of the inversion would increase. The PCM simulation showed the maximum magnitude and distribution of TKE below the inversion at 215 minutes into the simulation, after which time the mountain wave had propagated slightly upstream. Fig. 4.5 supports the hypothesis that the stronger inversion would increase the aviation turbulence potential, as the (t =-215 min) PCM isentropic fields are severely deformed in the vertical with horizontal wavelengths varying from a few km to 10 km. The primary standing wave shows even stronger w values, in excess of ± 10 ms^{-1}. When viewed in animation, the isentropes are seen to overturn, indicating wave breaking. The vertical velocity field is more chaotic, with rapidly varying values in the horizontal. This would tend to support the generation of HVTs such as were found in the Clark et al. (2000) simulations. The static stability also varies by two orders of magnitude between 8 km and 10 km AGL, with a region of $N^2 < 0$ within the breaking wave, indicating static instability. From 6 km to 10 km AGL the Ri varies considerably as well, with the dominant feature being a deep layer of subcritical Ri in the mountain wave, extending from 5 to 9 km. In conjunction with the low Ri pocket, an area of TKE with a maximum greater than 10 $m^2 s^{-2}$ is also found within the breaking

wave. As expected, the flow is more turbulent near the tropopause in the stronger inversion case than in the control simulation. Interestingly, the second TKE feature at 14 km AGL reached an earlier (t = 195 min) maximum of 10 m^2s^{-2} (not shown), which was comparable to that in the CC case. However, once the large standing wave began to break in the PCM case, the TKE values dropped rapidly at 14 km AGL, perhaps indicating that much of the wave energy has been over-reflected in the wave breaking region below the inversion and so less energy has penetrated deep into the stratosphere.

In a similar fashion, it was hypothesized that weakening the 200 hPa inversion would decrease the intensity of the turbulence near the aircraft's flight level. Fig. 4.6 depicts the (t = 240 min) fields from the PCW simulation. The PCW case clearly shows a reduced response. The standing wave still dominates the flow, but w is less than ±5 ms^{-1}. The Ri field associated with the 8-10 km wave feature directly in the lee has only a small region of subcritical Ri, and the flow remains statically stable throughout. The feature at 14 km AGL is associated with significant TKE > 6 m^2s^{-2}, but near the aircraft incident level (8 km AGL), the TKE was found to be significantly lower than either the CC or PCM case. The greater TKE values at 14 km suggest that less energy was reflected near the tropopause than in the PCM case. By weakening the inversion, however, the potential for turbulent flow was significantly reduced throughout the depth of the model atmosphere.

Two more simulations were conducted involving modifications to the input thermal profile at 2 km grid spacing. The PCS simulation (Fig.4.7a) used the US Standard Atmosphere profile. Interestingly, it produced the highest TKE values, with broad regions of TKE > 10 m^2s^{-2} both in downslope wind and in a large region between 12 and 14 km AGL. This result can be understood by comparing the CC sounding (Fig. 4.1) with the PCS

sounding (Fig. 4.2d) The CC sounding is nearly dry adiabatic throughout the troposphere, whereas the PCS sounding has steadily increasing static stability with height, the latter being more favorable for vertical wave propagation and amplification. Of course, the Standard Atmosphere is a conceptual model, and would not be in anything resembling geostrophic balance with the 1200 UTC 9 December DEN winds. The PCS model solution is therefore likely unphysical, however is shown here simply for comparison. The PCI simulation has the 9 December DEN temperature up to the tropopause at 202 hPa and is isothermal above. Fig. 4.7b shows the PCI model TKE field at $t = 240$ min, and shows very little turbulence, as expected, with none present near 10 km (where the inversion layer would otherwise be).

The other two simulations with fixed terrain but modified soundings tested the sensitivity of the response to the wind profile while setting the temperature profile equal to the 1200 UTC 9 December DEN sounding. The PCU simulation had a uniform wind field ($u = 30$ ms^{-1}, $v = 0$). As a result, no significant areas of Ri < 0.25 occur in the simulation (not shown), and model TKE is everywhere < 1 m^{2}s^{-2} (Fig. 4.8a). Clearly the shear present in the control simulation is critical in setting the stage for turbulence; mountain wave perturbations of the stable layer appear to be insufficient to generate turbulence in the absence of shear. The PCNS simulation represents perhaps a more physical case, removing the westerly upper jet feature, hypothesized to be a remnant of a departing subtropical jet streak in Chapter 2. The winds were fixed from the northwest and tapered in speed with height. The purpose of this simulation was to test the hypothesis that the superposition of the jets helps to organize the downscale energy cascade to turbulence. Fig.4.8b shows that while some TKE is generated in the same locations as in the CC simulation, the PCNS case clearly has significantly reduced TKE generation, with a maximum of 2 m^{2}s^{-2} at 9 km AGL. While the

overlapping jets are hypothesized in Chapter 2 to establish and compress the stable layer, in this case the stable layer is already established at t = 0. Therefore the role of the second jet feature in the idealized case is to increase the shear, as the PCNS case shows higher Ri values (not shown) above the inversion when compared to the CC case. Two additional simulations were performed (not shown) in order to isolate the individual contributions by the change in wind direction and the removal of the wind speed maximum toward the overall reduction of TKE in the PCNS simulation. The greatest reduction of model-parameterized TKE was associated with the simulation which held the wind direction northwesterly but kept the original (CC) speed profile, suggesting that the anticyclonic curvature of the jet feature above the strong inversion in the 1200 UTC 9 December 1992 DEN sounding is perhaps more critical than the magnitude of the jet feature for the Colorado simulations.

The vertical Scorer parameter (Eq. 1.3) profiles for all of the soundings used in the Colorado cases for which the vertical profile was modified are shown in Fig. 4.9. The most dramatic vertical variation of l^2 occurs at and above the 10 km AGL inversion in most cases. The difference in magnitude of l^2 between the CC (black), PCM (red), and PCW (green) at 10 km is as expected, with the PCM simulation having the highest value (4×10^{-6} m^{-2}) followed by CC and PCW, respectively. Because the weaker inversion profile was tapered back to match the control simulation sounding immediately above the inversion, it results in a more stable layer centered at 11.5 km AGL compared to the PCM and CC profiles, resulting in half the magnitude of l^2 for the PCW simulation. The PCI simulation matches the CC l^2 profile in the lower troposphere as expected with less variation in l^2 above the tropopause. Because the PCS simulation had little variability in static stability, the majority of the l^2 variations are likely due to wind shear. Changes to the wind profile also have a

profound effect on the l^2 profile, as evidenced by the PCU simulation. In this case the winds were uniform with no shear, so the resultant l^2 profile varies the least of all the cases. The largest magnitude of l^2 for the PCU simulation is (2×10^{-6} m^{-2}) at the inversion nose, or 66% of the CC simulation magnitude. Above 14 km AGL, the PCU l^2 profile is again flatter, with magnitudes equaling roughly 25% of the corresponding CC values, suggesting that shear accounts for the majority of the l^2 variation at these altitudes. Lastly, the PCNS l^2 profile follows the CC profile reasonably well below 14 km, above which the subtropical jet feature and its associated shear had been removed, thus decreasing both the magnitude and the variability of l^2 relative to the CC case. Overall it can be said with confidence that changes in both shear and static stability in these simulations have an impact on the resultant Scorer parameter magnitude and variation. In these simulations, the dominant component (shear or stability) is height-dependent. It appears based primarily on the PCU and PCNS simulations that at most altitudes, shear dominated the l^2 profile, with static stability dominating in the 10-14 km AGL layers (i.e., the level of the strong inversion).

Four simulations were conducted to examine the effect of mountain height on the response near the tropopause. Not surprisingly, the flat terrain case showed no response at all; with no source of buoyancy perturbation to trigger turbulence in the 8-10 km layer, the flow remained laminar and steady-state (Fig.4.10a) . The TCS simulation (h = 1 km, Fig. 4.10b) reduced the strength of the mountain wave response and resultant TKE by approximately ½ compared to the CC simulation. By increasing the mountain height by 1 km in the TCH simulation (Fig. 4.10c), the TKE produced at 14 km AGL increased to > 10 m^{2}s^{-2} over a slightly broader area than in the CC case. However, little TKE was generated at or just below the stable layer compared to the CC case. The vertical wavelength in this case

appears longer in response to the higher mountain, with the result that the maximum

buoyancy perturbation may not be at the optimum level (i.e., the base of the inversion) to

extract energy from the base state. Lastly, the TCW simulation (Fig. 4.10d) added twice the

mountain half-width, and showed a similarly reduced response compared to the CC

simulation. At least in the Colorado turbulence case, the approximate dimensions of the

Front Range appear to be optimized relative to the 1200 UTC 9 December DEN sounding.

4.4. 9 December 1992 Colorado Fine Resolution Simulations

The remaining 9 December 1992 Colorado simulations were conducted using a 0.5

km horizontal grid spacing. The purpose of these finer-resolution simulations was to provide

greater insight into the vertical structure of turbulence resulting from the interactions of the

mountain wave with the jet and upper front structure. At 0.5 km horizontal and 0.333 km

vertical grid spacing, the model was still not directly simulating turbulent eddies, however

was able to capture the high-frequency gravity wave features with wavelengths on the order

of a few km. In order to examine the TKE budget, the model-parameterized turbulence was

output from the diffusion module. In addition, the buoyancy and shear production terms

from the TKE tendency equation were calculated following Section 4.2.

The fine control simulation (CCF) used the 1200 UTC Denver sounding while the

PCMF and PCWF soundings used the stronger and weaker inversion soundings, respectively.

All three simulations generated a downstream propagating wave at inversion level in addition

to the expected stationary wave, just as in the 2 km simulations. This suggests dynamic

similarity between the two sets of simulations. However, the downstream wave propagates

faster in the 0.5 km simulation and a stream of lee waves develops downstream of the peak in

all three cases. Fig. 4.11 shows the evolution of the mountain wave and vertical velocity

fields (as in Fig. 4.3) for the CCF case. Of note, by t = 180 min (Fig. 4.11c), the aforementioned lee waves develop, and by t = 240 min (Fig. 4.11d), they extend from the base of the inversion layer well into the stratosphere, with a horizontal wavelength of order ~8km. At the end of the simulation, a very strong mountain wave is present in the CCF case, showing steeply tilted isentropes, the "dead region" from Smith's (1985) hydraulic theory, and a downslope wind/hydraulic jump couplet with vertical velocities approaching ± 10 ms^{-1}. Fig. 4.12 shows the vertical velocity and potential temperature fields for the PCMF and PCWF cases at t = 240 min. There are some very clear differences between three cases, although the PCMF simulation (Fig.4.12a) resembles the CCF simulation (Fig. 4.11d) more closely than does the PCWF simulation (4.12b) with respect to the presence of high-frequency waves. The mountain wave in the PCMF case shows a slight upstream propagation in animation (as did the PCM case), while the PCWF wave is stationary. This is not unexpected given the static stability profiles (for the $8 - 10$ km layer $\partial(N^2)/\partial z$, PCMF > CCF > PCWF) since the dispersion relation governing the tilt of the phase lines from the vertical is a function of the static stability (Durran 1990). Also of note is that the horizontal wavelength of the higher frequency lee waves in the PCMF case is approximately 6-7 km, while in the PCWF case they have an approximate wavelength of 11 km.

Fig. 4.13 shows the vertical cross-section of Ri and N^2 and of model-parameterized TKE at the time of maximum TKE generation above 6 km (chosen subjectively as the output time depicting the largest areal extent of the highest contoured value present in the simulation). For CCF and PCWF (Fig. 4.13a,b and Fig.4.13e,f, respectively), maximum TKE generation occurred at the end of the simulation. For the PCMF simulation, the maximum generation of TKE occurred at t = 205 min; after that time the wave had

propagated upstream of the mountain peak and the maximum TKE value had diminished by over 60% by the end of the simulation (t = 240 min). As hypothesized, the stronger the inversion, the greater the vertical variation of the static stability (depicted in Fig.4.13a,c,f) in that layer. As a result, the PCMF and CCF simulations showed persistent TKE features above and below the inversion just downstream of the mountain peak between 10 and 12 km (Fig.4.13b,d). The PCWF simulation (Fig.4.13f) did generate a very weak region of TKE (< 1 m^2s^{-2}) in the same layer downstream of the peak, however does not show the region of large TKE associated with the wave breaking in the CCF and PCMF simulations. The maximum TKE generated by any of the simulations occurred in the CCF case (Fig. 4.13b) with a maximum greater than 20 m^2s^{-2} at 6 km, but embedded in a column of TKE exceeding 6 m^2s^{-2} extending through 9.5 km. For these simulations, the comparable location for the 9 December aircraft incident would have been at approximately 8 km immediately downstream of the peak, well within the deep column of high TKE generation in the CCF and PCMF simulations. This region corresponds directly to the region of subcritical Ri and negative static stability (Fig.4.13a).

The mechanical shear production of TKE using Eq. (4.2) and (4.7) is shown in Fig. 4.14 for the same times as depicted in Fig. 4.13. It is worth noting that the initial and boundary conditions of all three cases used the identical shear profile. In all the simulations, both calculations of shear production compared favorably. A potential source of slight disparity between the two depictions of shear production of TKE stems from the fact that the model-parameterized shear production occurs within the diffusion module on the raw model fields, whereas Eq. (4.7) uses shear calculated from the model output velocities that have already been smoothed through the model diffusion process. The CCF simulation (Fig.

4.14a-b) had the greatest shear production of the three cases, with the model-parameterized shear production extending from 5 to 9.5 km MSL. The alternate shear production is somewhat reduced, however it still shows a feature at 9.5 km. In both calculations the maximum shear production is occurring at the base of the breaking wave near 6 km. The maximum PCMF shear production magnitude and distribution (t = 205 min, Fig. 4.14c-d) closely resembles that of the CCF simulation except for a reduced shear production signature above 14 km, suggesting perhaps that less wave energy was able to penetrate the stronger inversion. In Fig. 14e-f, however, virtually no shear TKE production appears in the vicinity of the inversion in the PCWF simulation, with only the 14 km AGL feature present.

The buoyant production of TKE is seen in Fig.4.15 for all three cases. In Fig.4.15a (CCF case), a region of positive buoyant production (corresponding to the region of absolute static instability) appears in the wave breaking region. This region appears in both the CCF (Fig. 4.15a) and PCMF (Fig. 4.15b) cases, however is clearly absent in the PCWF (Fig. 4.15c) simulation. The amount of positive buoyant TKE production is slightly reduced in the PCMF simulation, presumably because the strengthened inversion inhibits the de-stabilization in the wave-breaking region. However, this condition may also be related to the upstream propagation of the wave away from the buoyancy source in the lee of the peak. Negative buoyant TKE production occurs over a broader area in the PCMF simulation, suggesting the role of negative buoyancy in the turbulent downburst in Chapter 2 is dependent upon the inversion strength.

In summary, the CCF simulation generated the most TKE of all the simulations and the PCWF case generated relatively little. As expected, the CCF simulation matched the actual conditions of the 9 December Colorado turbulence case reasonably well, producing

significant TKE and violent vertical motions at both the altitude and horizontal position of the DC-8 incident. It can be inferred that the strength of the inversion at the tropopause has a significant impact in the generation and distribution of TKE in both the upper troposphere and lower stratosphere, with increasing inversion strength allowing for greater TKE aloft with a fixed shear profile. Apparently, however, there is a finite limit to which the inversion strength can increase TKE in a steady-state flow, because upstream propagation (such as occurred in the PCMF case) can separate the mountain wave from the buoyancy source, i.e., the mountain itself.

4.5. Idealized T-REX simulations and comparisons between IOPs

During T-REX, virtually all of the IOPs involved a cyclonically curved polar jet streak associated with an upstream longwave trough. However, the wave response to the flow over the Owens Valley differed greatly from one IOP to the next, with some IOPs exhibiting very strong stratospheric gravity waves, others with low-level rotors and trapped lee waves, and still others with almost no flow response at all, suggesting that there was more governing the flow regime and the potential for stratospheric gravity waves and aviation turbulence than simply the cyclonic polar jet streak and upstream trough. Several questions naturally follow: What were the differences between those cases observed to be associated with strong stratospheric gravity waves and those that were not? What were the similarities between cases that did have strong stratospheric gravity waves? Which thermal and wind profiles had the greatest potential for stratospheric aviation turbulence and which effects dominated?

To answer these questions, six idealized simulations were conducted for which the model terrain was modified to approximate the Owens Valley of California. These

simulations were conducted on a grid of $200 \times 3 \times 90$ grid cells. The terrain profile is show

in Fig. 4.16a. The Sierra Nevada range was represented with a height of 3.6 km and a half

width of 40 km to the west, and 5 km to the east with the Inyo/White range represented by a

height of 2.6 km and a half-width of 5 km following Hertenstein and Kuettner (2003) and

Koch et al. (2006). Fig.4.16b shows the actual terrain for the Owens Valley for comparison.

The Owens Valley floor was chosen as the zero elevation for the simulations. Model output

fields were calculated in the same manner as for the 9 December 1992 Colorado idealized

cases.

The choice of T-REX IOPs was described in Section 4.1 and is further explained in

Table 4.2. Essentially IOP 6 was used as a "control run" because it involved direct

observation of stratospheric turbulence by an aircraft and could be compared to real-data

simulations in Chapter 3. The other two stratospheric wave IOPs described in Section 3.6

were also simulated. Three cases in which the turbulence was confined primarily to the

lower troposphere were chosen for the sake of comparison. At least one case, IOP1, did

entail observations of stratospheric gravity waves; however they were relatively weak and

laminar. In addition, IOP14 had virtually no wave response at all in spite of a strong jet

structure and static stability gradients in the vertical.

Fig.4.17 shows the input soundings used for the six IOPs simulated, with Fig.4.17a-c

depicting the stronger stratospheric wave cases and Fig. 4.17d-f showing the cases with a

relatively weaker to non-existent stratospheric signal. All soundings were from Vandenberg

AFB, CA, and were chosen from a time closest to when the HIAPER (see Chapter 3) aircraft

was active, or if it was not used, closest to the middle of the IOP.

The evolution of the vertical velocity and isentropic fields in the idealized T-REX IOP 6 mountain wave is shown in Fig. 4.18. The idealized terrain, coupled with the steady-state boundary forcing, has clearly exaggerated the non-linear response in the model, as vertical velocities by t =90 min (Fig. 4.18b) have exceeded +25 ms^{-1} in the lee of the Inyo range and by t = 180 min (Fig. 4.18c) fully-enclosed isentropes are seen from the surface to 14 km AGL. Time-lapse animation of this case clearly shows the development of deep rotors being shed downstream. Nevertheless, the presence of overturning and enclosed isentropes is indicative of wave-breaking in the 10 to 14 km layer in which the HIAPER was flying when it encountered such an event during the actual IOP 6. More evidence of the potential for turbulence due to wave breaking is shown in Fig. 4.19, which shows the *u*-component of the horizontal wind for the IOP 6 simulation. At initialization time (Fig.4.19a), jet maxima at 9.5 km AGL and 12 km AGL are apparent. Fig. 4.19b shows the development of a downslope wind in the lee of the Sierra by t = 90 min, with several regions of flow reversal in the stratosphere. The flow is reversed at over 30 ms^{-1} upstream (representing a difference of over 70 ms^{-1} from the base state flow) between 8 and 12 km AGL at t = 180 and 240 min (Fig. 19c,d). Such a wave-induced flow reversal represents a critical level which would support resonant amplification of the mountain wave (Clark and Peltier 1984).

Fig. 4.20 shows the model stability fields and parameterized TKE at various points in the simulation (t = 90, 135, and 220 min). The stratospheric response to the mountain wave and stacked jet regime is the extreme vertical variation of static and shear stability (Fig.4.20a,c,d), with what is essentially the de-stratification of the atmosphere between 10 and 20 km AGL. Subcritical Ri and negative N^2 accompany the regions of enclosed isentropes and reversed flow in Fig. 4.19. Again, while the response appears to be greatly

exaggerated, the overall vertical variation of Ri and N^2 is reminiscent of the high-resolution real data WRF simulation of this case (Fig. 3.18). The transient nature of these stratospheric wave-breaking features and their associated turbulence is evident in Fig. 4.20b,d,f, as pockets of TKE exceeding 50 m^2s^{-2} are seen to appear briefly and are swept downstream. By t = 240 min, a deep layer of > 50 m^2s^{-2} TKE values appear along the dividing streamline (see Section 1.2.1) above the lee of the Sierras, extending from 10 km down to 5 km AGL.

The model-parameterized TKE is shown for all six IOPs in Fig.4 21 at the time each individual simulation showed the broadest region of the maximum TKE contour achieved during the simulation. This subjective time is labeled, as in Section 4.4, as the time of maximum TKE. The three strong stratospheric wave cases (Fig. 4.21a-c) show very similar responses, with deep rotors and strong TKE above 12 km. The IOP4 simulation produced the majority of its TKE between 14 and 18 km (Fig. 21a). The most significant isentropic deformation by the mountain wave appears in IOP13 (Fig. 4.21c), which is consistent with the description of the actual IOP13 as having the strongest stratospheric gravity waves (Doyle et al. 2007). The maximum TKE, however, was generated in IOP 6 (Fig. 4.21b), which is also the only IOP with direct observations to verify turbulence from wave-breaking. The IOP1 and IOP8 (Fig. 4.21d,e) simulations still produced significant stratospheric waves (including some overturning isentropes indicating wave breaking), however the parameterized TKE values were at least 30 m^2s^{-2} less than in the stronger cases. They were, interestingly, of comparable magnitude to the TKE generated in the Colorado fine-resolution simulations, further suggesting that the idealized terrain profile in the T-REX simulation has had the effect of exaggerating the flow response. The IOP 14 simulation, as the null case (Fig.4.21f), shows virtually no TKE and only minor perturbations to the isentropic fields.

The reason for this is apparent in Fig. 4.17f, as the tropospheric flow (which launches the mountain wave) is aligned nearly parallel to the north-south ridges.

Fig. 4.22, shear production at the time of maximum TKE for the three stronger IOPs, shows some minor differences in the distribution between the two calculations as described in Section 4.4. In particular, the model-parameterized shear production covers a broader area in these cases, suggesting that the alternate calculation is missing some of the weaker shear TKE production. Again, this is likely due to the influence of diffusion on the model output velocity fields having reduced the shear. The highest mechanical shear production above the boundary layer is found to occur in the region where the isentropes are most dense and tilted in the vertical, along the lower boundary of the wave-breaking regions. This observation holds for the weaker cases as well (Fig. 4.23). Fig. 4.24 indicates that buoyant production of TKE in the stratosphere is significantly greater in the strong stratospheric wave cases (Fig. 4.24a-c). These cases are associated, as in Fig. 4.17a-c, with stronger vertical variation of static stability in the lower stratosphere and stronger jet flow. Regions of positive buoyant production are associated with wave breaking above the tropopause, and with the ascending branches of the tropospheric rotors. In Fig. 4.24d-f, only IOP 8 shows significant buoyant production in the stratosphere near the enclosed 335 K isentrope (Fig. 4.24e).

Figures 4.25 and 4.26 compare the vertical profiles of momentum and stability with the vertical profile of maximum TKE generated during each simulation in the 10 to 20 km AGL layer. In Fig. 4.25, IOP13 shows the greatest variation of shear, while IOP 6 clearly shows the largest vertical variation of static stability. IOP 6 generated the maximum TKE, over 25% more than that produced by the next strongest case (IOP13). In Fig. 4.26, IOP8 and IOP14 depict strong vertical variation of N^2, however little shear and weak flow overall.

TKE values were more than 80% less than in other IOPs. Fig. 4.26c is interesting because it depicts a vertical stability and shear profile comparable to the strong cases in Fig. 4.25, yet produced virtually no TKE. This is the result of the winds being nearly parallel to the terrain barrier in the troposphere, inhibiting mountain wave generation. Thus it is clear that the thermal and shear profiles in the stratosphere may prime the atmosphere for turbulence however are not always sufficient to generate significant turbulence without a local buoyancy source such as a mountain wave.

Table 4.3 presents a summary for the T-REX simulations and the factors that most directly affect the generation of turbulence in the 10-20 km layer. Not surprisingly, the angle of incidence of the winds to the terrain barrier plays a major role in determining the amount of model-parameterized TKE produced. The 4 to 20 km initial mean wind was examined because the winds at ridge-top level (in these cases, 3.6 km) strongly influenced the generation of the mountain wave. The winds in IOP 6 were almost normal to the terrain and also exhibited the strongest mean flow overall. In contrast, the mean wind in IOP14 was over 55° from normal and had the weakest flow overall. IOP 6 also shows the largest value of $\left|\partial\left(N^2\right)/\partial z\right|$ in the 10 to 20 km layer. At 6.2×10^{-5} $m^{-1}s^{-2}$ corresponding to the maximum TKE simulated (107.3 $m^{-2}s^{-2}$), this is nearly a full order of magnitude greater than four of the other IOPs, indicating that stratospheric turbulence is significantly influenced by the variation of the static stability in the vertical. IOP14 also showed significant variation in N^2; however, absent a significant cross-barrier component to the flow, no significant turbulence was generated by the model. Interestingly, the magnitude of the shear did not seem to play as significant a role as one might expect in these simulations, as the maximum speed shear values were comparable for all cases. In fact, IOP1 showed the strongest 10-20 km shear

value, yet produced the third lowest model-parameterized maximum TKE. However, for the three strong cases, there was both directional and speed shear present throughout the 10-20 km AGL layer, whereas in the weaker cases it tended to be primarily speed or directional shear. Also, for IOP 8 and IOP 14, most of the shear was present below 15 km. Of these six cases, IOP 6 seemed to be uniquely structured to maximize TKE generated by the model (107.3 m^2s^{-2}) through the combination of strong ridge-normal flow at all levels, a particularly intense cyclonic jet streak, and a strong stratospheric inversion leading to large vertical gradients of static stability. However, Fig. 4.3 illustrates that the similarities between these cases are many, and the differences not particularly profound. The magnitude of the ridge-normal component of the mean tropospheric wind is critical as would be expected. Far more challenging to observe and forecast accurately are the inversion strength and the magnitude and distribution of shear above the polar jet streak, all of which were shown to affect the potential for aviation turbulence.

4.6. Conclusions

The idealized simulations examined the effects of wind and temperature profiles in the stratosphere on flow over topography representing the 9 December Colorado and TREX IOP 6 cases. The Colorado control simulation produced significant turbulence in a location comparable to the 9 December DC-8 incident. In the Colorado case, it was found that strengthening the inversion near the tropopause did increase the potential for aviation turbulence near the tropopause and into the lower stratosphere. Weakening the inversion had the expected result of decreasing the potential for turbulence in the lower stratosphere. At finer resolutions, however, the mountain waves began to propagate upstream in the stronger inversion case, reducing the model TKE generation after peaking at 205 minutes into the

simulation. Buoyancy alone was insufficient in these cases to trigger significant turbulence, as reduction of the initial shear prevented the shearing instability necessary to support turbulence. Changing the terrain also influenced the response, with taller terrain creating a longer vertical wavelength not resonant with the inversion, and shorter terrain generating a weaker mountain wave. IOP 6 was the strongest of the T-REX simulations in terms of model TKE, and was the only IOP during T-REX characterized by an aircraft observation of wave-breaking. IOP 6 appeared most favorable for turbulence due to its strong cross-barrier flow and significant vertical variation of static stability. IOP14 was the weakest case due to the winds being nearly ridge-parallel.

While the previous chapters have dealt with the manner in which the jet/front system creates a favorable environment for turbulence in the presence of the mountain wave, the current chapter examined the influence of that jet-induced wind and temperature profile on the evolution of the mountain wave and ensuing turbulence. These sensitivity studies illustrate the extreme sensitivity of the flow response and potential for aviation turbulence to the upstream conditions, thus emphasizing the enormous forecast challenge presented by such situations. It was found that the stratospheric inversion strength was critical to the generation of model TKE and the potential for aviation turbulence. While extremely stable conditions are normally expected to suppress turbulence, the enhanced vertical gradient of static stability appeared to serve as a critical level, forcing wave breaking directly below. This was especially true for the Colorado simulations in which the inversion was strengthened. However, as both the Colorado and T-REX simulations showed, a stratospheric inversion alone was not a sufficient condition for strong aviation turbulence. The presence of strong jet flow and shear above 200 hPa, especially as seen in IOPs 6 and 13

and in the Colorado simulations, was required to maintain the shearing instability and associated low Ri necessary for wave breaking to occur well into the stratosphere. What was established, through sensitivity testing and comparisons, is a regime for extreme aviation turbulence from near tropopause into the lower stratosphere characterized by strong, highly sheared jet flow bracketing a strong inversion above the tropopause. This structure is then perturbed by mountain waves and eventually allows for wave breaking to occur. Clearly the jet/front system and mountain waves work synergistically to govern the generation of turbulence in the lower stratosphere, consistent with the overall hypothesis for this dissertation.

Table 4.1: Idealized WRF simulations for 9 December 1992 Colorado case. Horizontal grid spacing (dx), mountain height (hm), and mountain half-width (xa) shown for each simulation.

Simulation	Description	dx	hm	xa
CC	Control run (DEN sounding temps/winds)	2 km	2 km	10 km
PCM	Stronger inversion (+~8.9K) /DEN winds	2 km	2 km	10 km
PCW	Weaker inversion (-~7K)/DEN winds	2 km	2 km	10 km
PCI	Isothermal above tropopause/DEN winds	2 km	2 km	10 km
PCS	US standard atmosphere/DEN winds	2 km	2 km	10 km
PCU	Uniform winds (30 kts westerly)/DEN temps	2 km	2 km	10 km
PCNS	No subtropical jet feature/DEN temps	2 km	2 km	10 km
TCF	Flat terrain (DEN winds/temps)	2 km	0 km	N/A
TCS	Half mountain height (DEN winds/temps)	2 km	1 km	10 km
TCH	1.5x mountain height (DEN winds/temps)	2 km	3 km	10 km
TCW	Twice mountain width (DEN winds/temps)	2 km	2 km	20 km
CCF	Control run finer resolution (DEN winds/temps)	0.5 km	2 km	10 km
PCMF	Stronger inversion finer resolution (DEN winds)	0.5 km	2 km	10 km
PCWF	Weaker inversion finer resolution (DEN winds)	0.5 km	2 km	10 km

Table 4.2: Idealized T-REX simulation IOPs, date/time group for initialization sounding from Vandenberg AFB, CA (VBG), and description of IOP from T-REX catalog (http://catalog.eol.ucar.edu/trex/).

IOP	DTG	Description of T-REX Observed Regime
1	0000UTC 3 Mar 2006	Moderate waves and a rotor within Owens Valley with the late afternoon amplitude maximum.
4	0000 UTC 15 Mar 2006	Trapped lee wave/rotor event transitioning to moderate stratospheric gravity waves
6	0000 UTC 26 Mar 2006	Large-amplitude trapped-lee waves w/ rotor, moderate amplitude waves aloft, & possible wave breaking in stratosphere
8	0000 UTC 1 Apr 2006	Weak coupled mountain wave-rotor-boundary layer system
13	0000 UTC 17 Apr 2006	Strong downslope wind event in lee of Sierra crest with rotors & strong gravity waves in lower stratosphere
14	1200 UTC 21 Apr 2006	Moderate southerly flow nearly parallel to the Sierra crest and weak gravity waves

Table 4.3: 4 to 20 km layer sounding-derived mean wind angle from normal to model terrain and mean wind speed, 10 to 20 km maximum vertical variation of N^2, maximum wind speed shear, and maximum model-parameterized TKE for all simulation times by IOP.

IOP	4-20 km mean wind departure from ridge-normal (°)	4-20 km mean wind speed (ms^{-1})	10-20 km max $\left|\partial\left(N^2\right)/\partial z\right|$ (m^{-1}s^{-2})	10-20 km max speed shear (s^{-1})	10-20 km max TKE (m^{2}s^{-2})
1	37.4	30.5	6.5×10^{-6}	6.5×10^{-2}	20.6
4	27.9	34.2	8.2×10^{-6}	1.1×10^{-2}	53.2
6	3.4	36.3	6.2×10^{-5}	3.8×10^{-2}	107.3
8	38.1	27.0	8.8×10^{-6}	1.9×10^{-2}	20.1
13	27.6	34.3	9.0×10^{-6}	2.4×10^{-2}	83.1
14	55.3	26.3	1.0×10^{-5}	1.4×10^{-2}	0.04
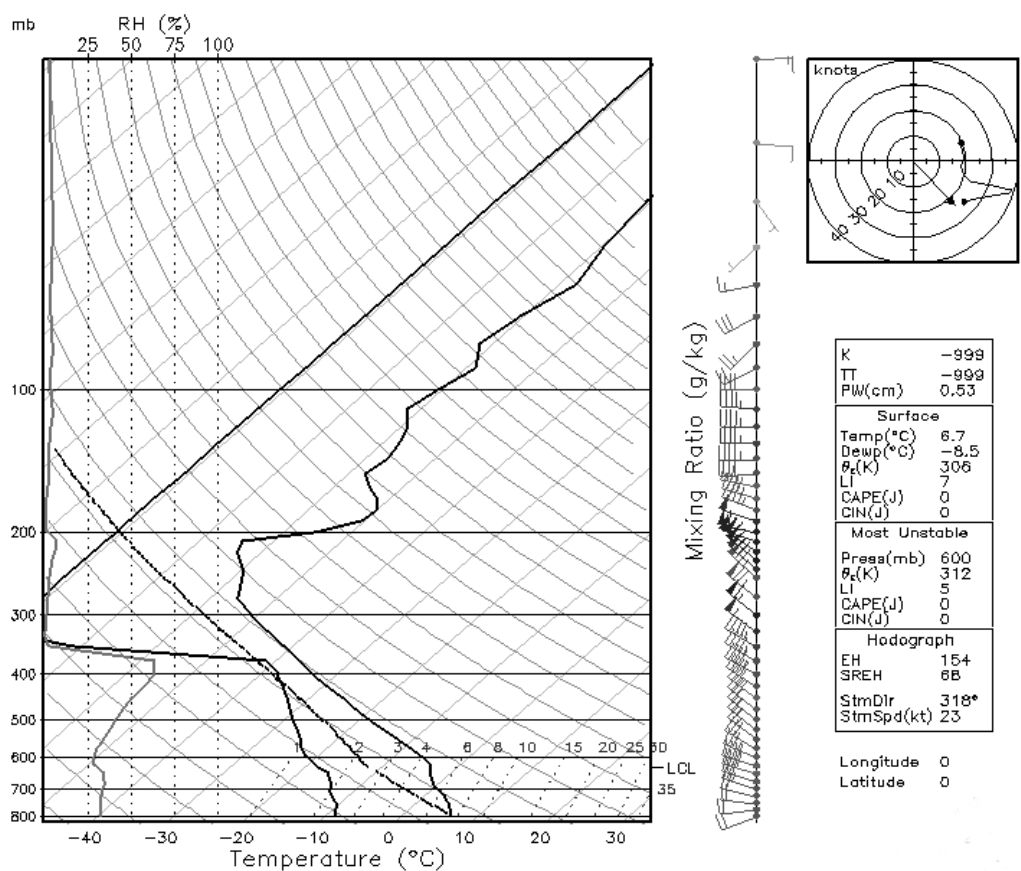
Figure 4.1: Initialization sounding from 9 December 1992 Colorado control idealized simulation (CC). Data from 1200 UTC 9 December 1992 DEN sounding.
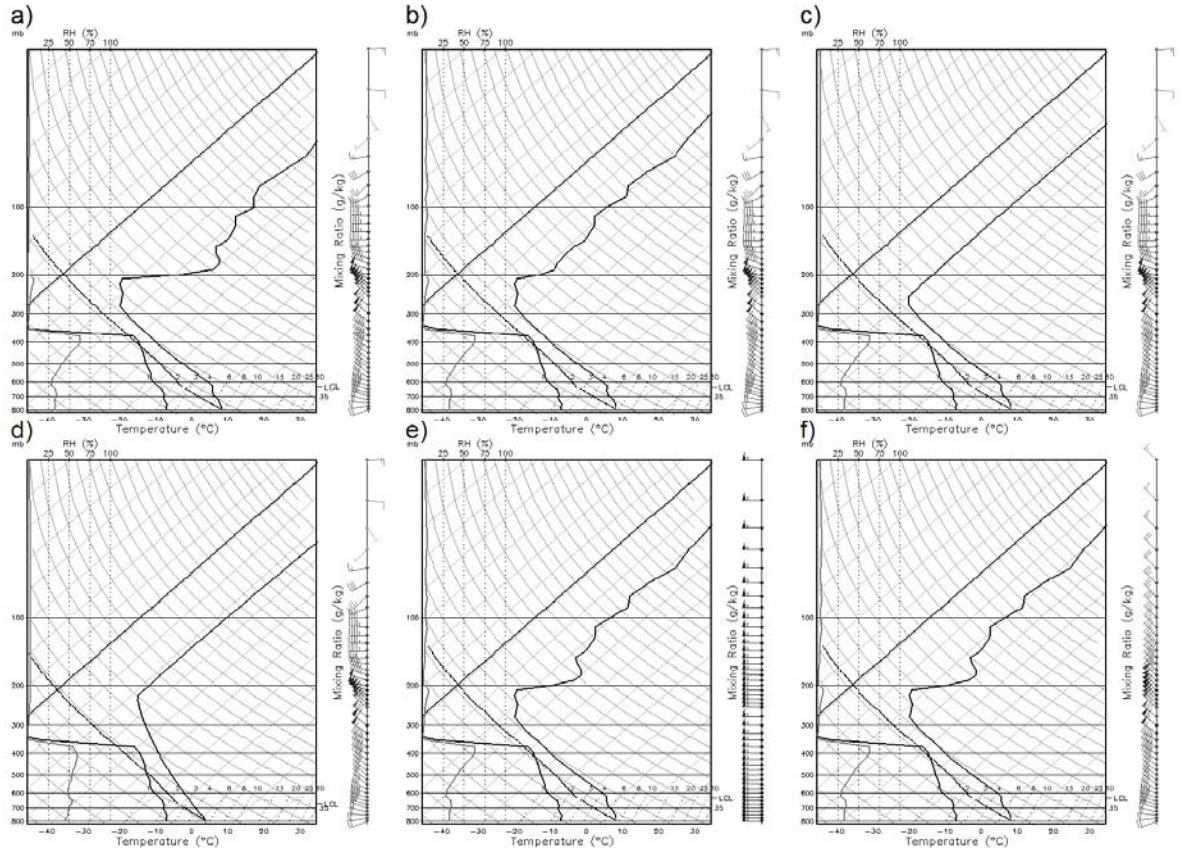
Figure 4.2: Initialization soundings of temperature, dew point, and winds for simulations (a) PCM, (b) PCW, (c) PCI, (d) PCS, (e) PCU, and (f) PCNS. Simulation designations described in Table 4.1
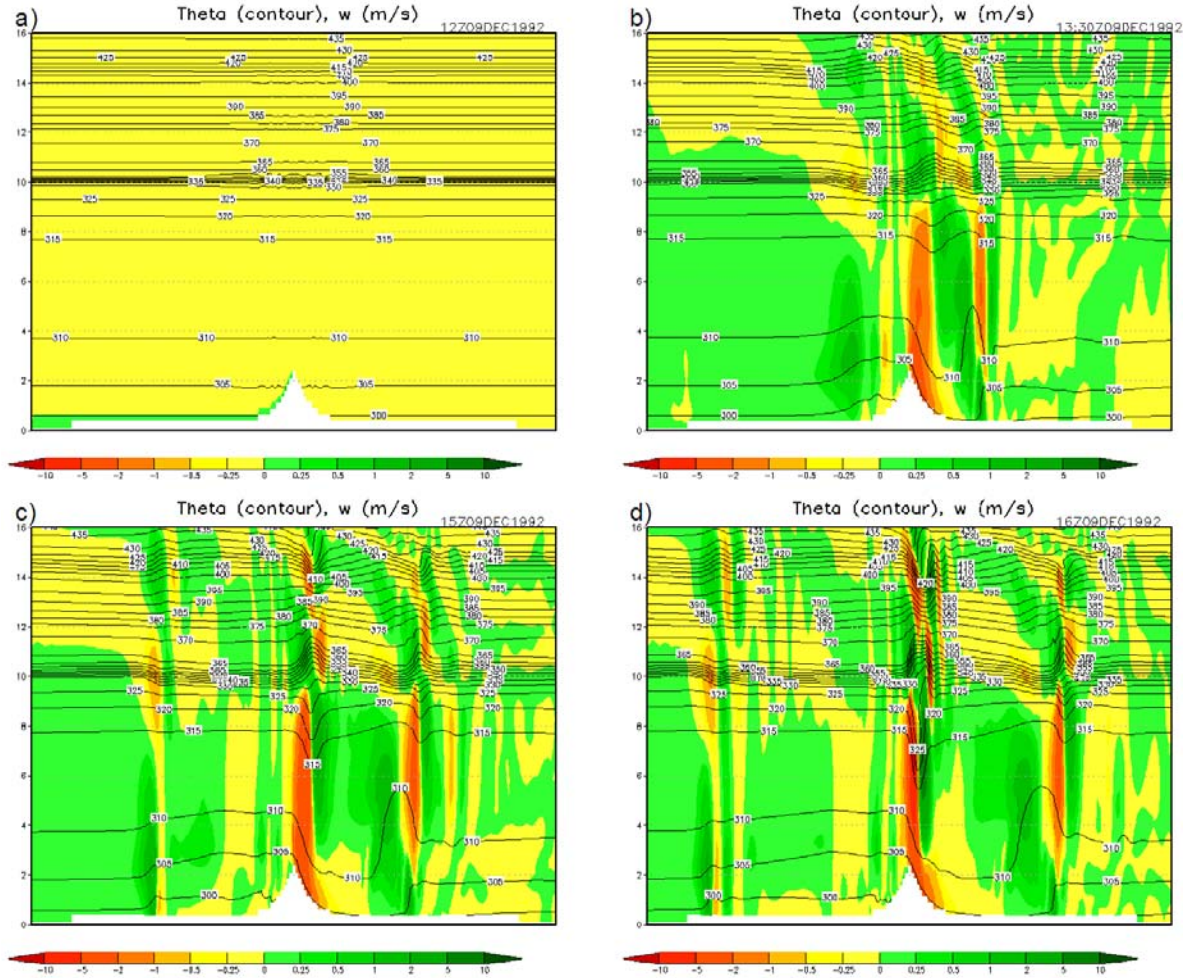
Figure 4.3: Time lapse vertical cross-section of vertical velocity (shaded, ms^{-1}) and potential temperature (K, contour) at time = (a) 0 min, (b) 90 min, (c) 180 min, and (d) 240 min for 2 km Colorado control simulation (CC). Vertical scale is km, and horizontal domain width is 400 km, with mountain centered at x = 200 km.
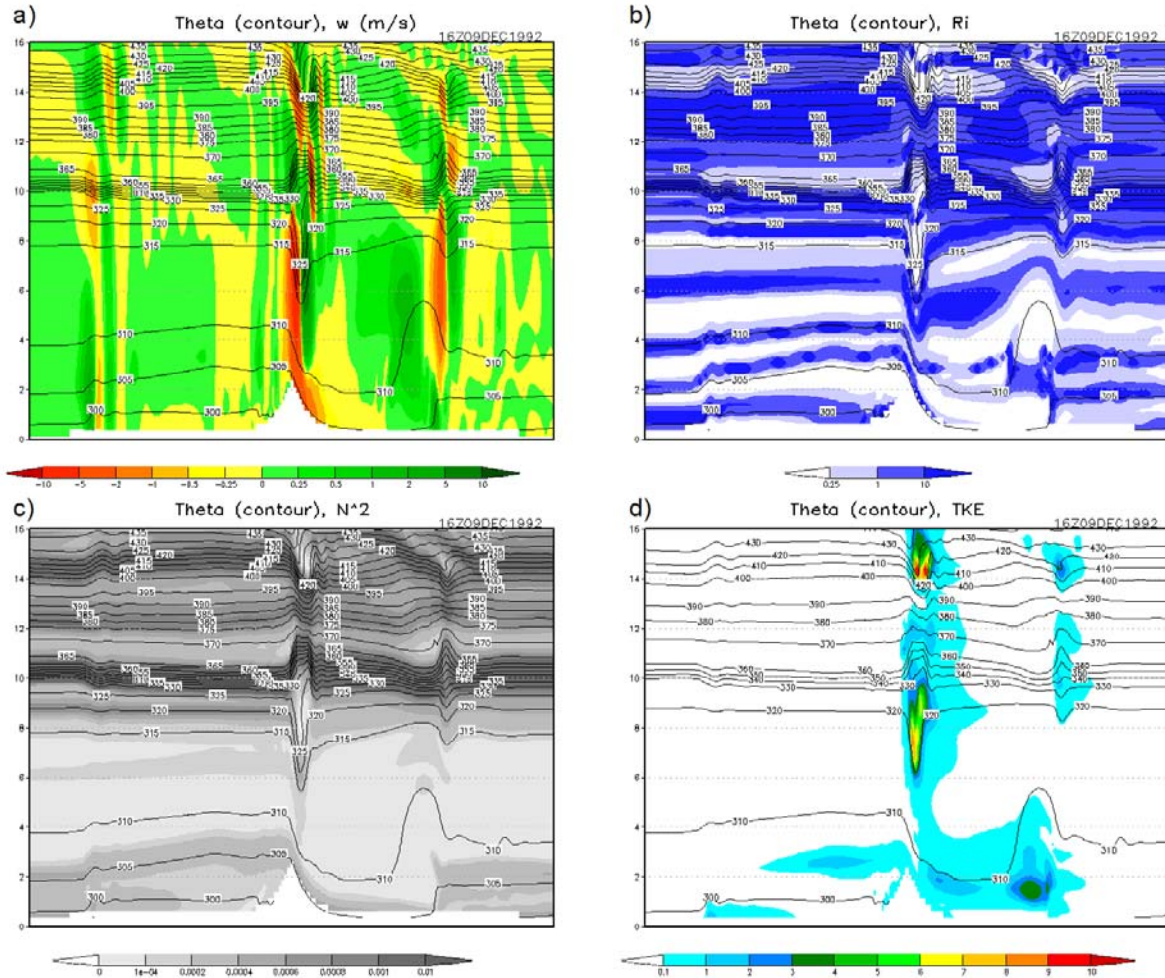
Figure 4.4: 2 km Colorado control simulation (CC) output at t = 240 min. Fields shown are (a) vertical velocity (shaded, ms^{-1}), (b) gradient Richardson number (white means $Ri < Ri_c$), (c) Brunt-Väisälä frequency squared (shaded, s^{-2}, darker shading indicates increased static stability), and (d) model-parameterized TKE (shaded, m^{2}s^{-2}). In all panels, solid contours are of potential temperature (K), with 5 K interval for (a)-(c), and 10 K contour for (d) for clarity.
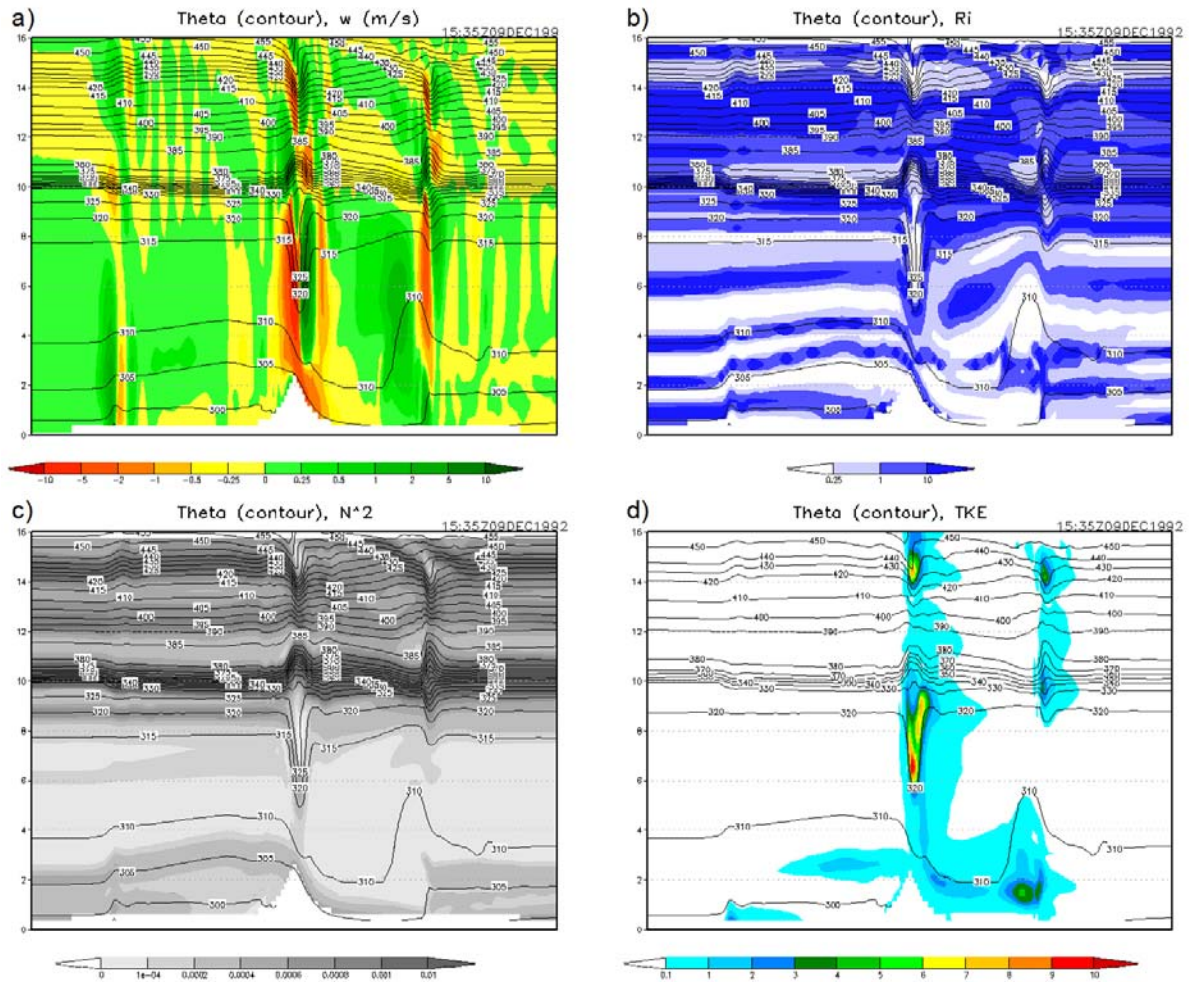
Figure 4.5: Same as Fig. 4.4, except for the 2 km stronger inversion simulation (PCM).
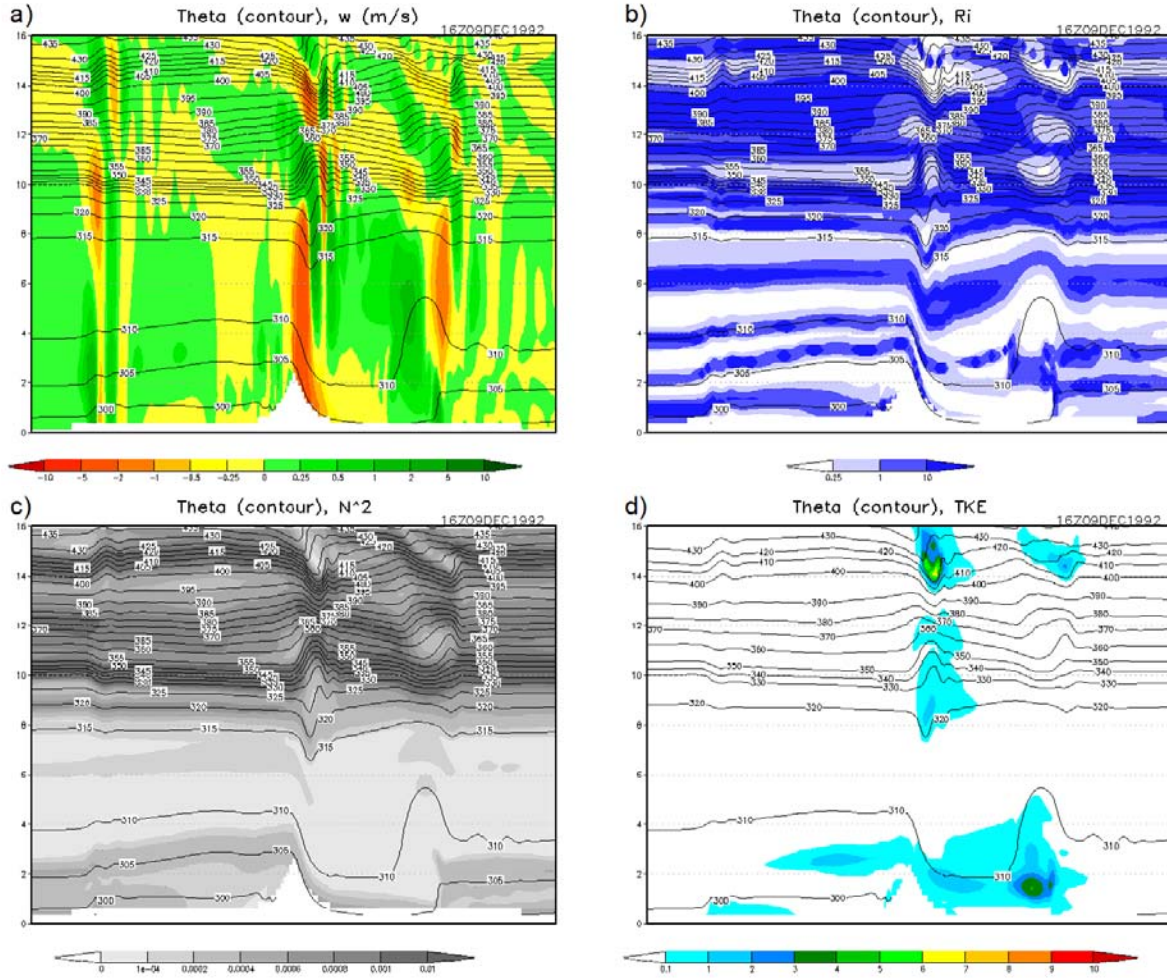
Figure 4.6: Same as Fig. 4.4, except for the 2 km weaker inversion simulation (PCW).
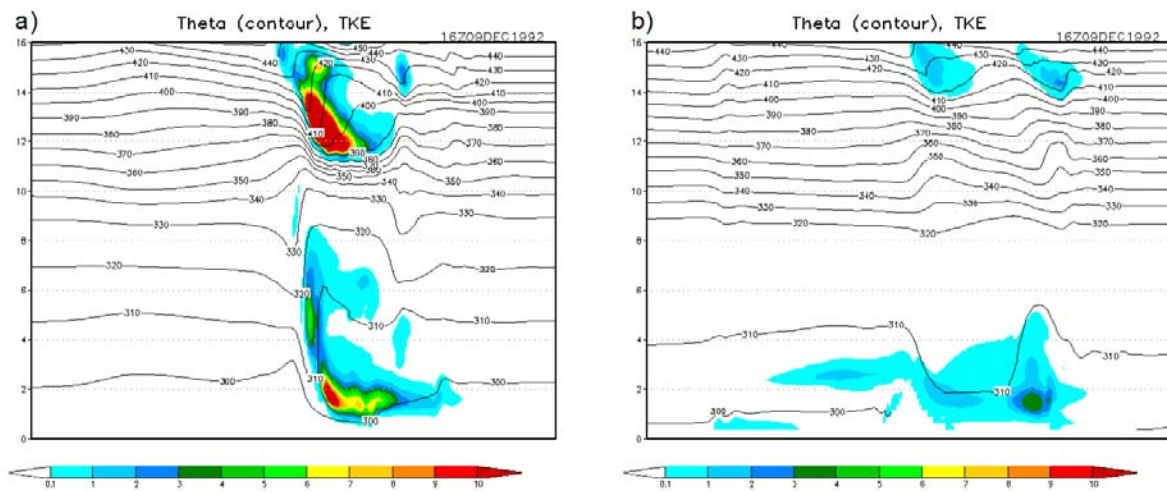
Figure 4.7: Model parameterized TKE (shaded, $m^2 s^{-2}$) and potential temperature (contoured, K) at t = 240 min for (a) PCS and (b) PCI simulations.
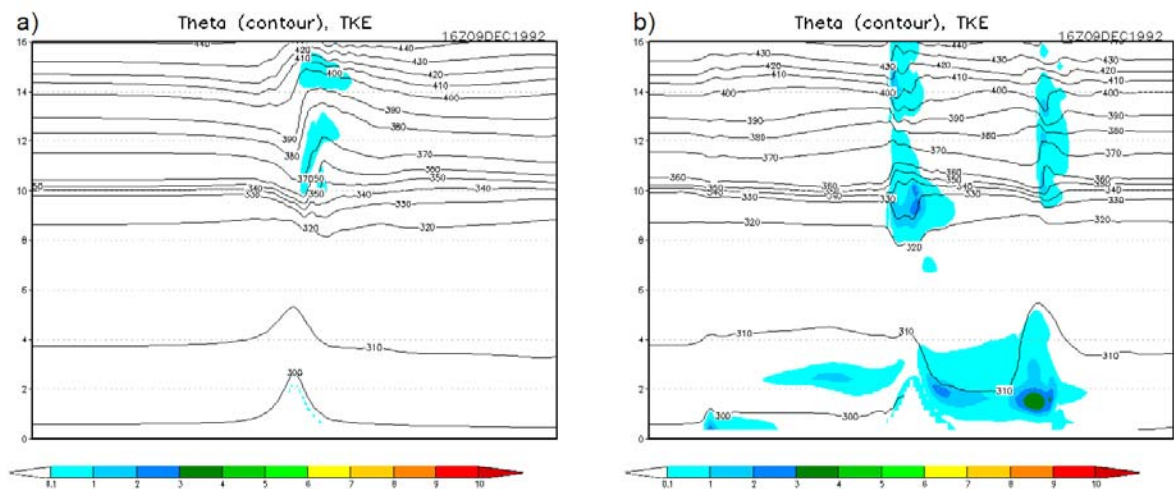
Figure 4.8: Same as Fig. 4.7, except for (a) PCU and (b) PCNS simulations.
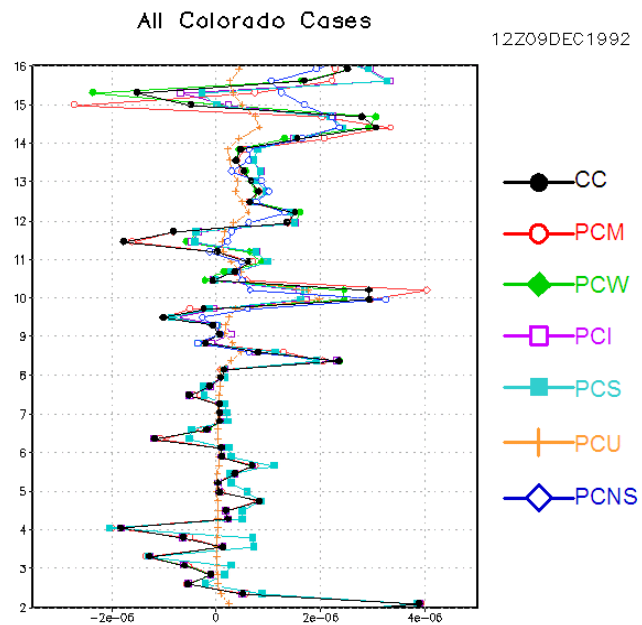
Figure 4.9: Scorer parameter (m^{-2}) in the 2 to 16 km AGL layer associated with the upstream boundary conditions for all 9 December 1992 Colorado simulations as indicated.
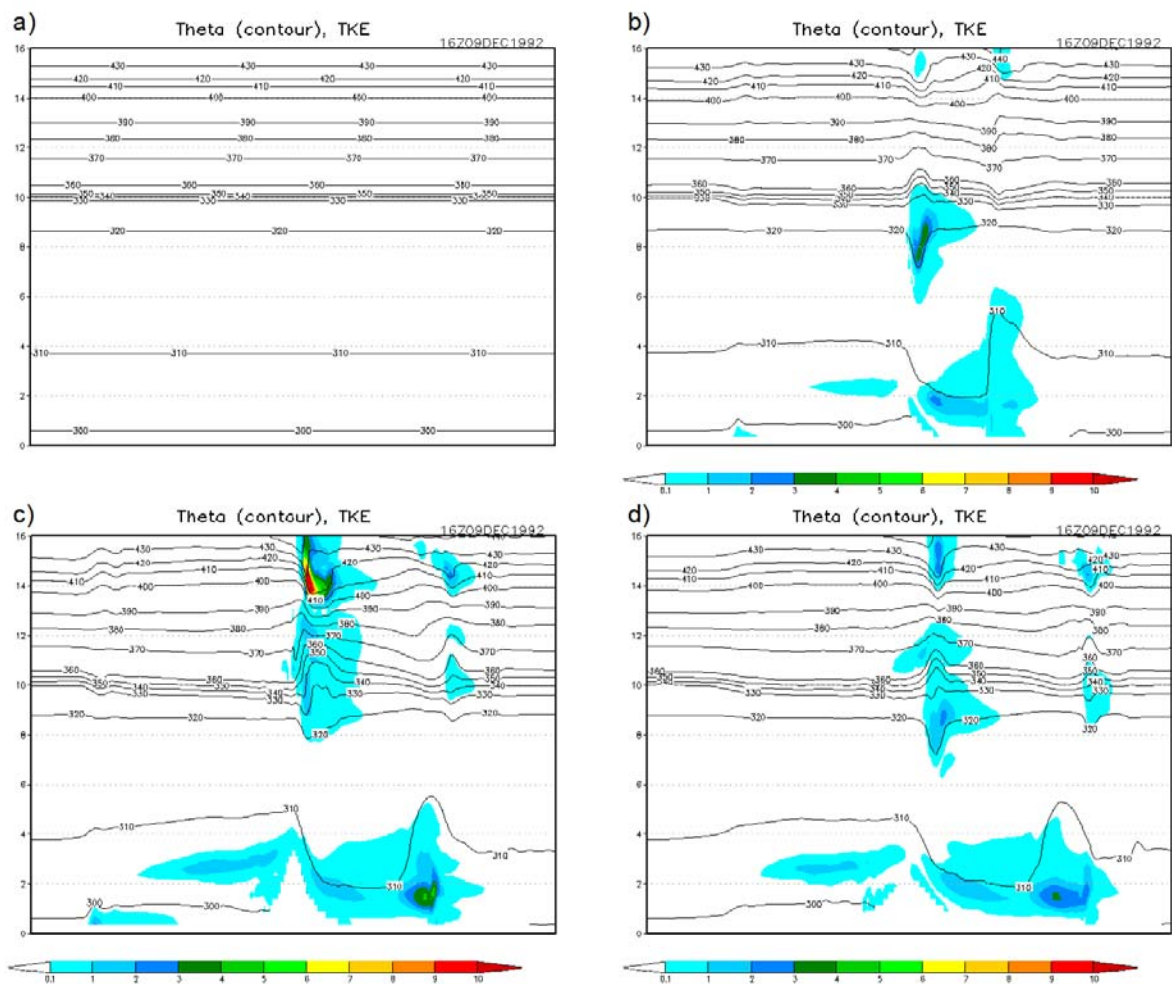
Figure 4.10: Same as Fig. 4.7, except for (a) TCF, (b) TCS, (c) TCH, and (d) TCW simulations.

150
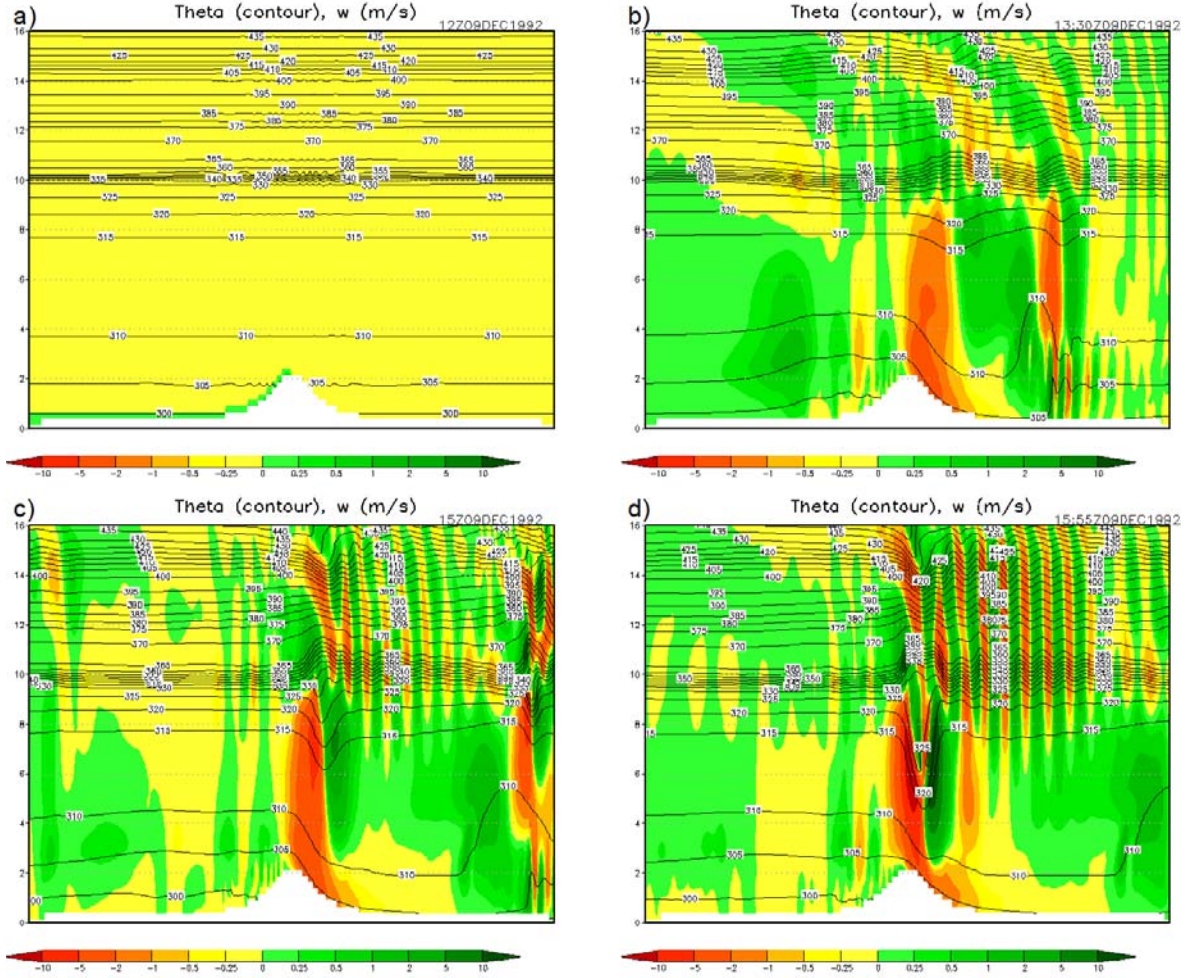
Figure 4.11: Same as Fig. 4.3, however for CCF (0.5 km control simulation) and horizontal domain width is 200 km, with mountain centered at x = 100 km.
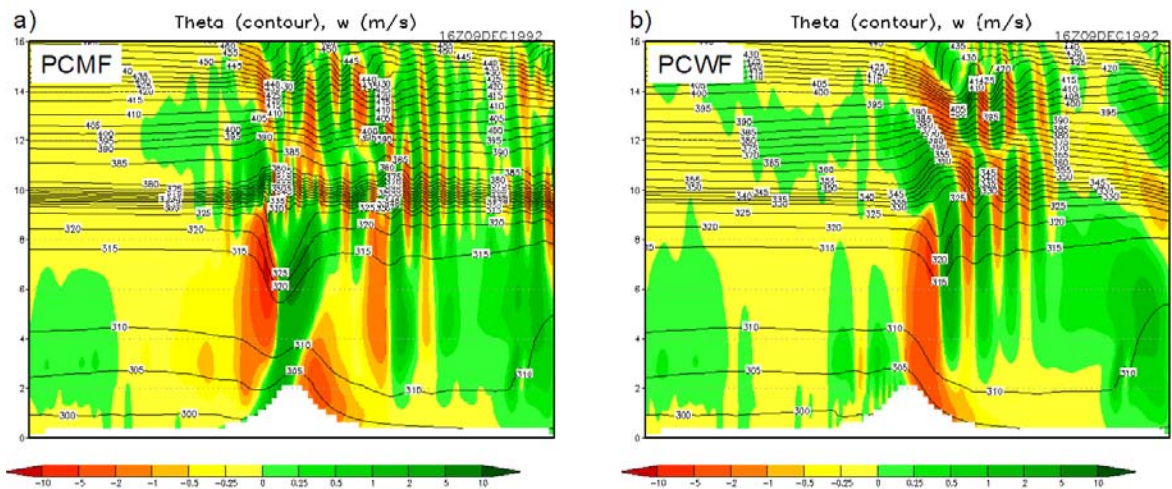
Figure 4.12: Vertical velocity (shaded, ms^{-1}) and potential temperature (K, contoured every 5 K) at t = 240 min for (a) PCMF and (b) PCWF simulations.
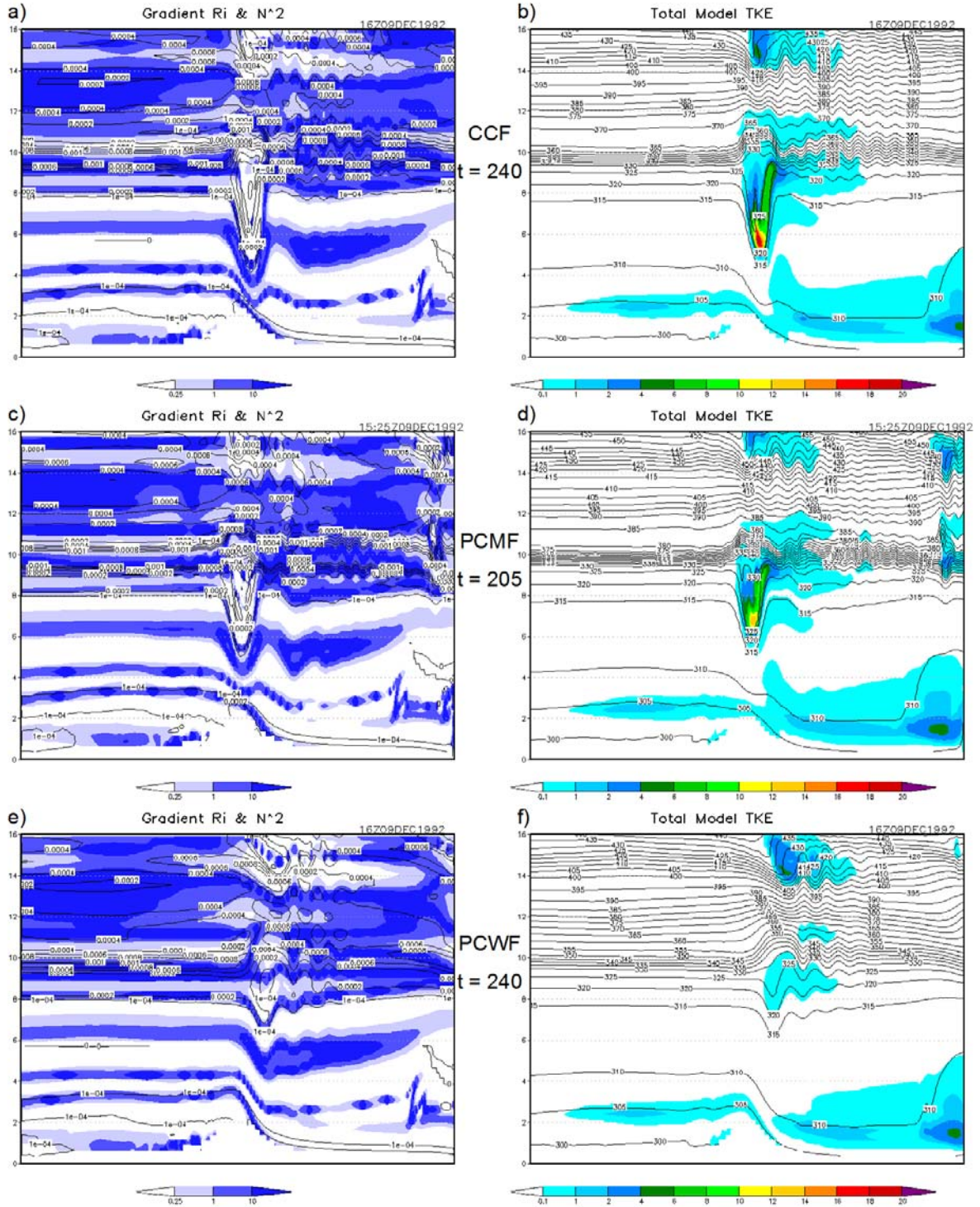
Figure 4.13: Gradient Richardson number (shaded) and Brunt-Väisälä frequency squared (contoured, s^{-2}) on left, model-parameterized TKE (shaded, m^2s^{-2}) and potential temperature (contoured, K) on right. Output shown at time of maximum TKE for (a-b) CCF (240 min), (c-d) PCMF (205 min), and (e-f) PCWF (240 min) simulations.
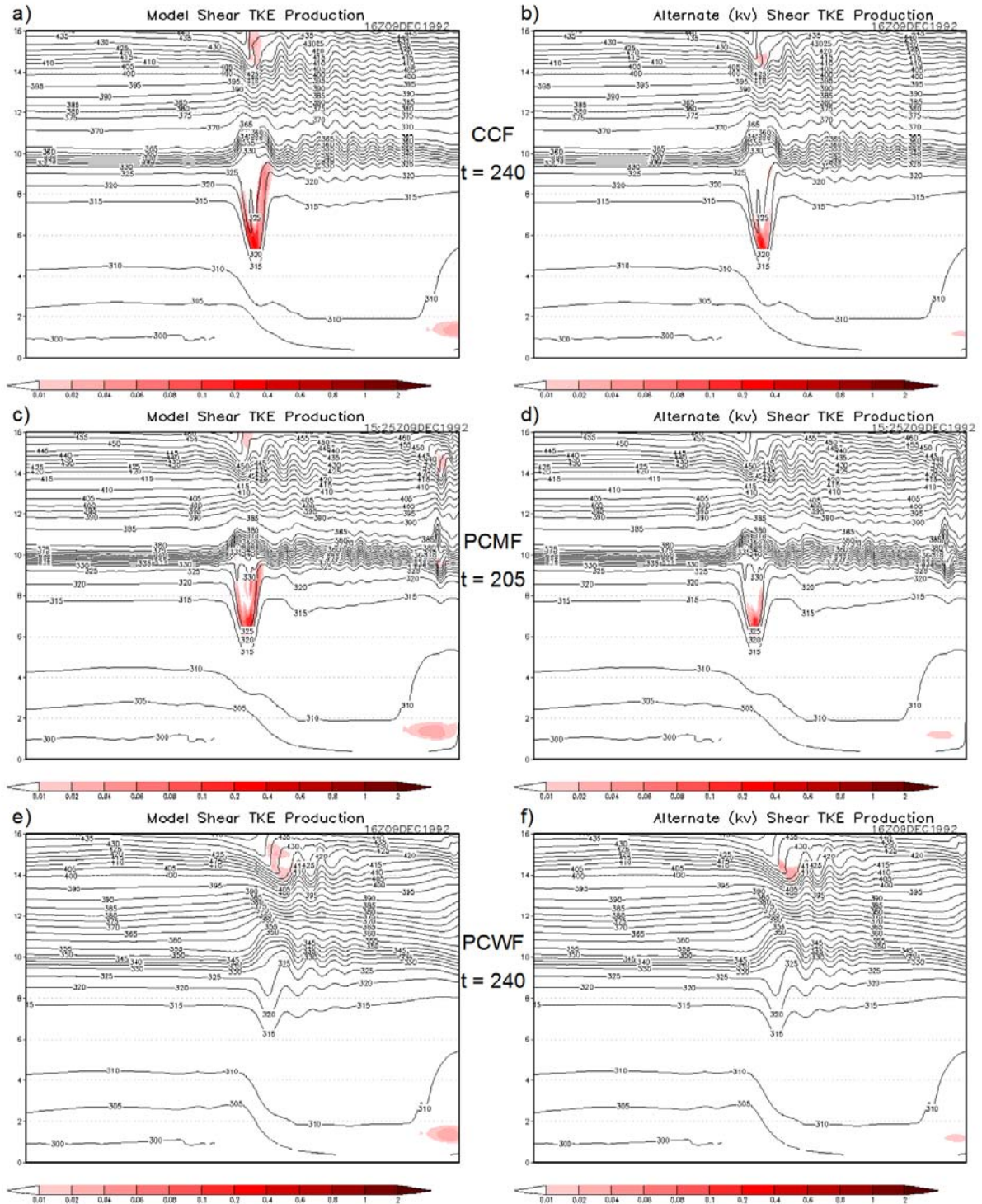
Figure 4.14: Model-parameterized mechanical shear TKE production (left, shaded, m^2s^{-3}) from Eq. (4.2) and alternate mechanical shear TKE production (right, shaded, m^2s^{-3}) from Eq. (4.7). Output shown at time of maximum TKE for (a-b) CCF (240 min), (c-d) PCMF (205 min), and (e-f) PCWF (240 min) simulations.
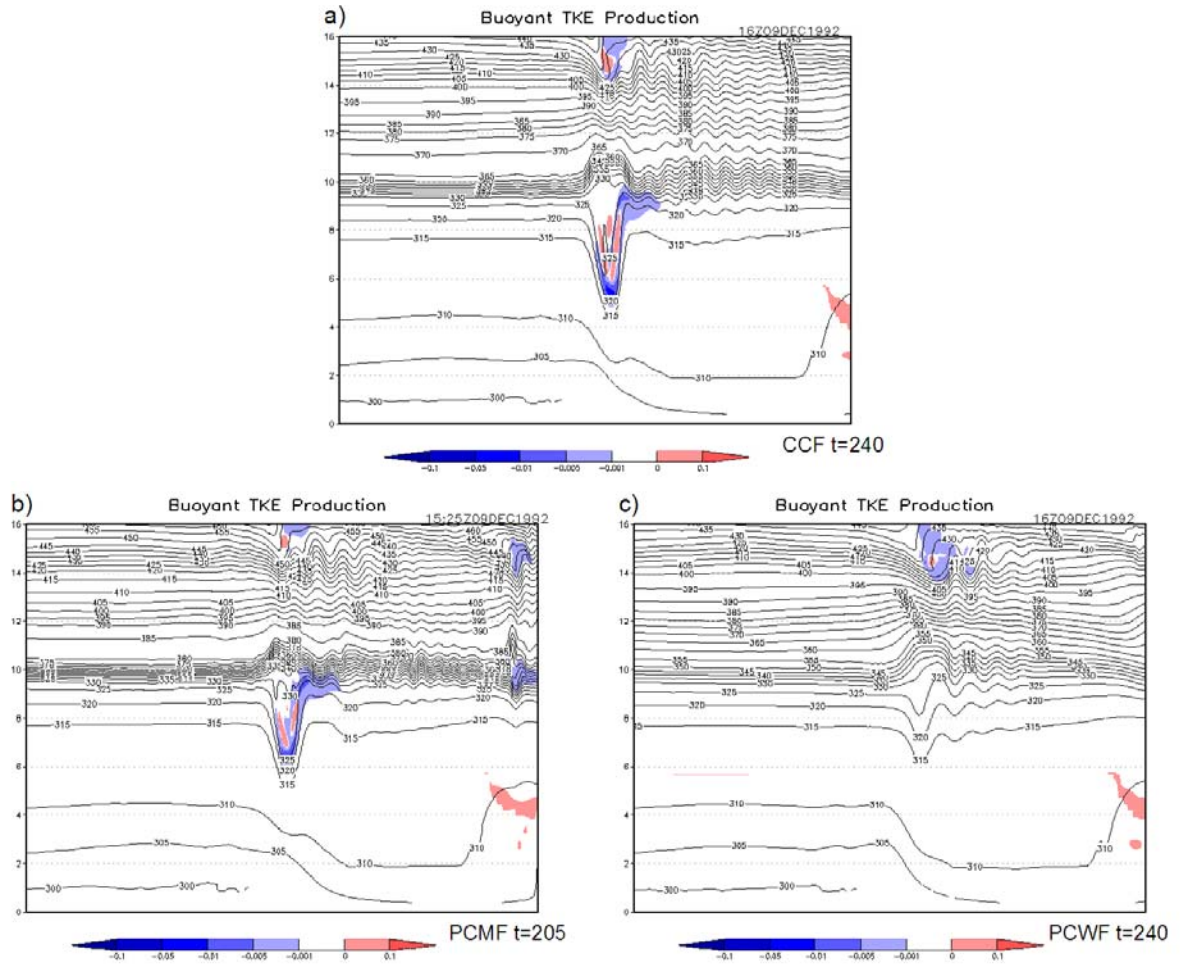
Figure 4.15: Buoyant production of TKE (shaded, m^{2}s^{-3}) from Eq. (4.3) for (a) CCF (240 min), (b) PCMF (205 min), and (c) PCWF (240 min) simulations.
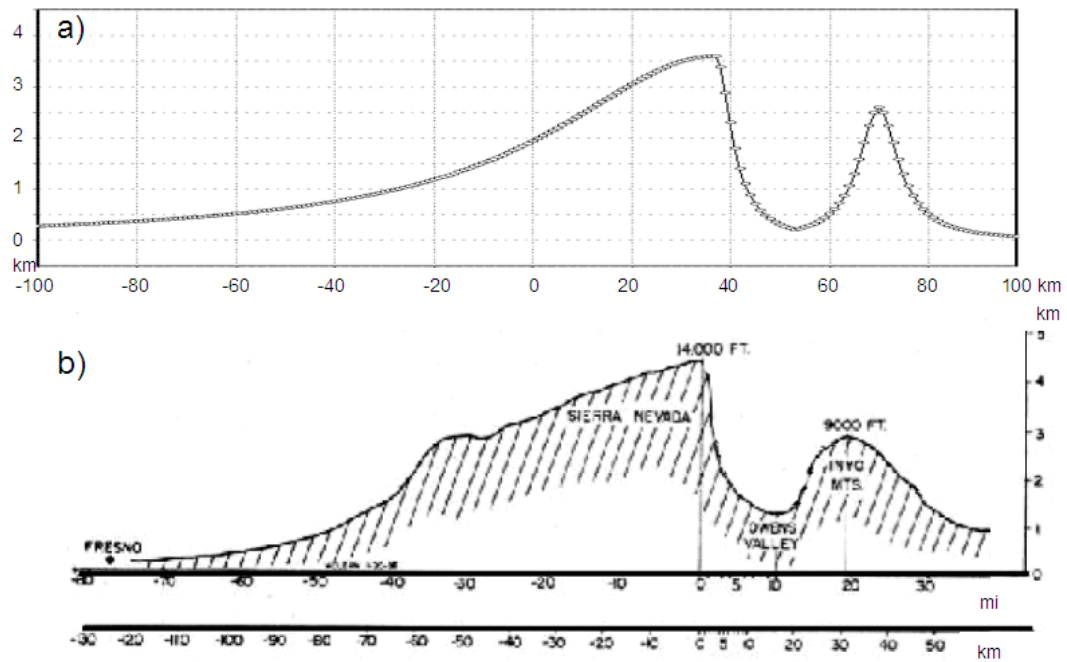
Figure 4.16: Terrain profile (a) from 1 km idealized simulations and (b) actual profile of Owens Valley from Grubišić et al. (2007). The following cross-sections depict only the right half of the domain shown in (a), from x = 0 to x = 100 km.
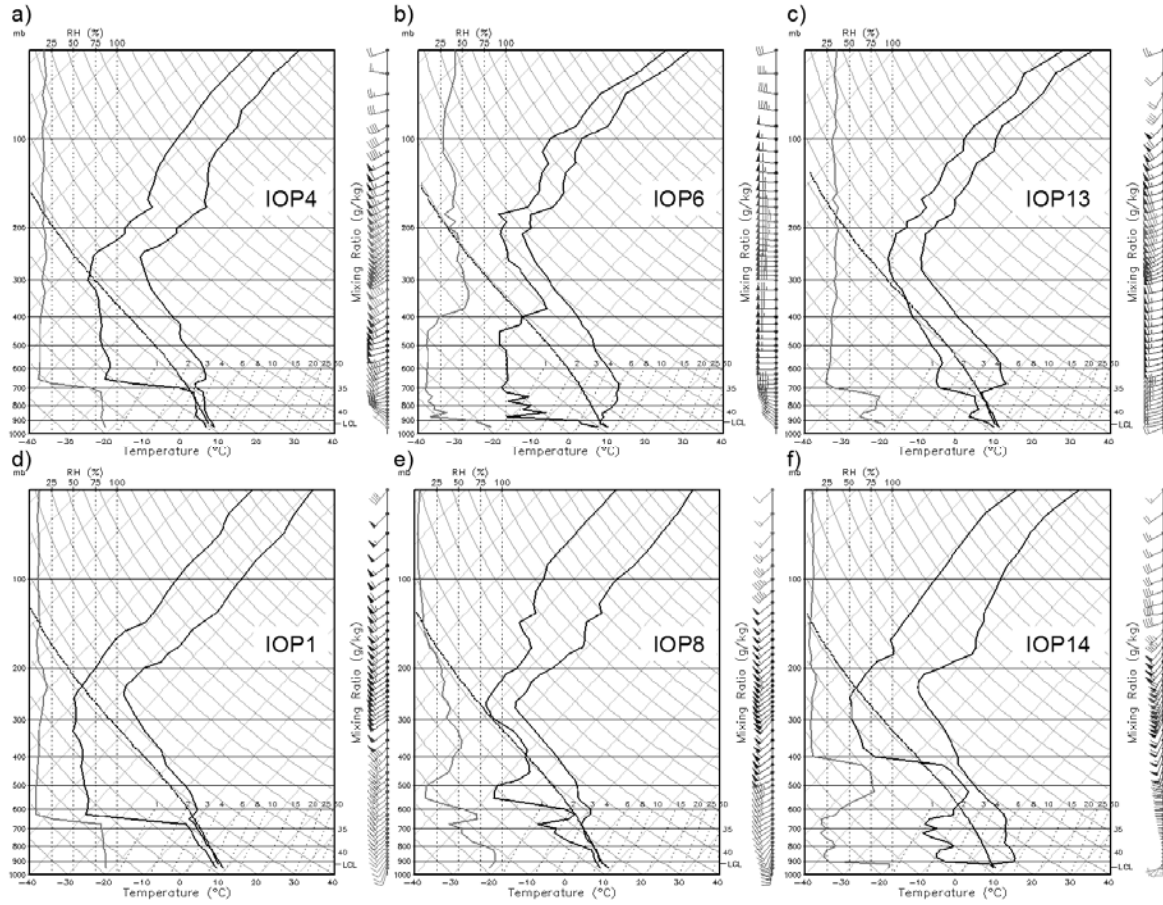
Figure 4.17: Initialization soundings from Vandenberg AFB, CA, for three T-REX IOPs with strong stratospheric wave activity (a-c) and relatively weak stratospheric wave activity (d-f). Date/time groups for the soundings are shown in Table 4.2.
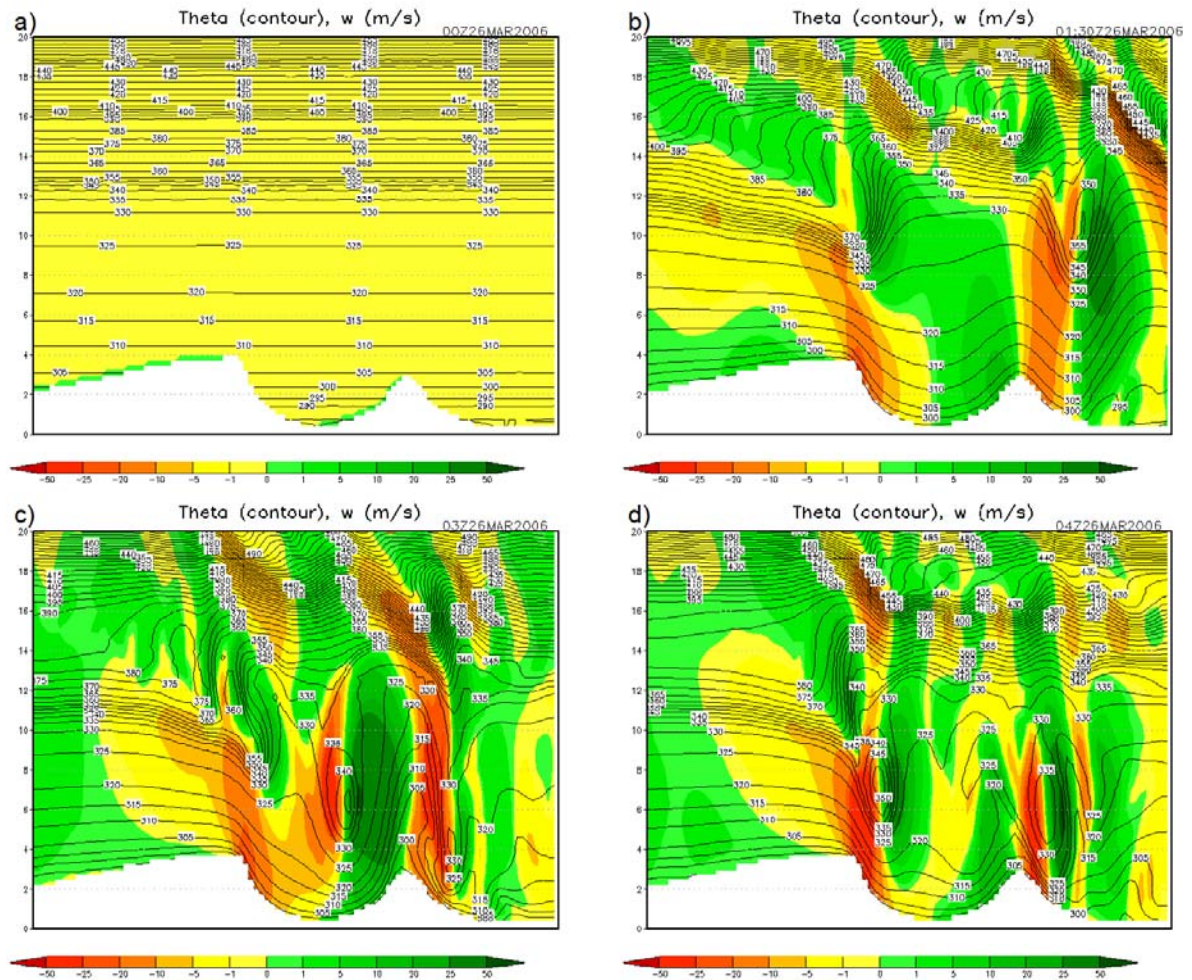
Figure 4.18: Time lapse vertical cross-section (right half of domain) of vertical velocity (shaded, ms^{-1}) and potential temperature (K, contour) at time = (a) 0 min, (b) 90 min, (c) 180 min, and (d) 240 min for 1 km IOP 6 simulation. Vertical scale is km, and horizontal domain width is 100 km.
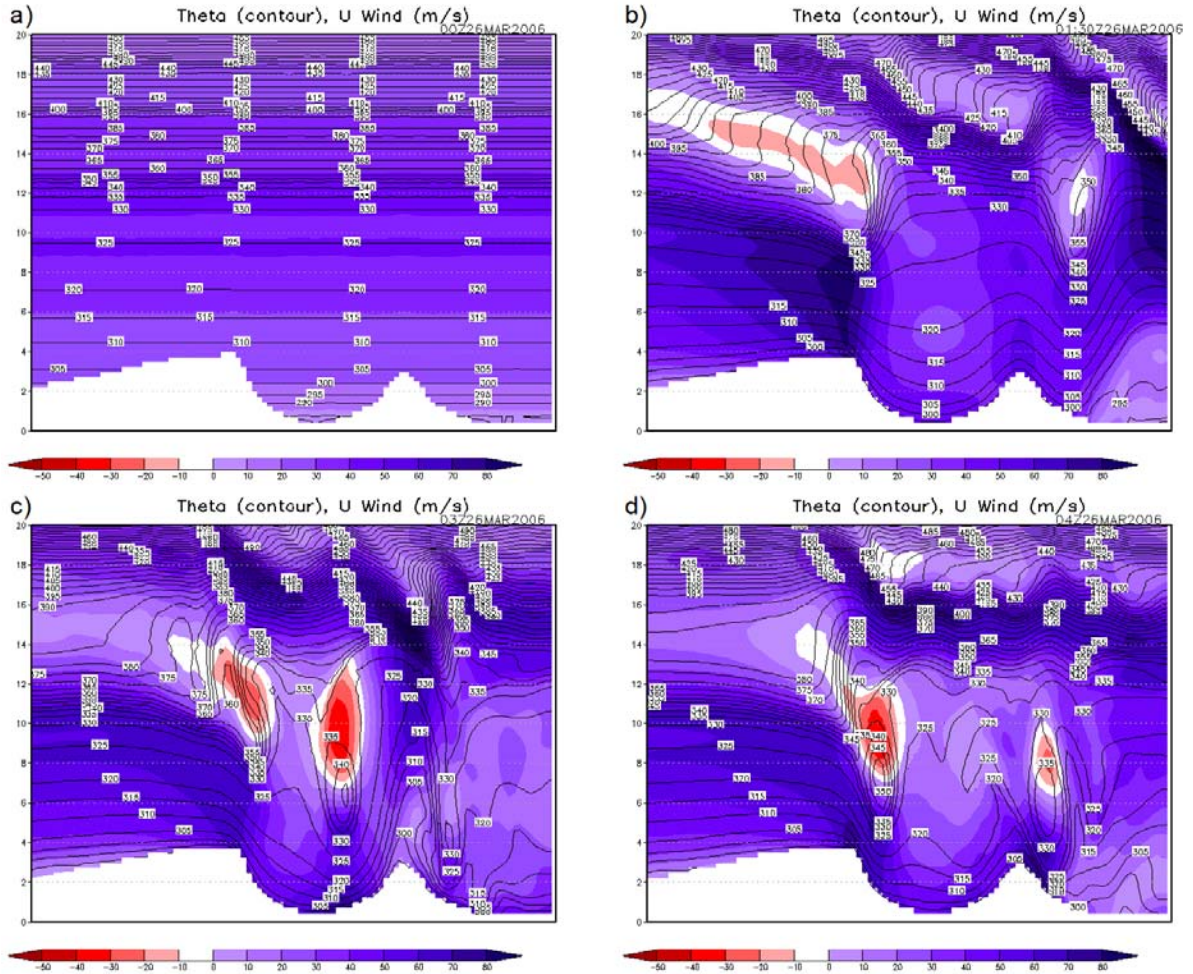
Figure 4.19: Time lapse vertical cross-section of *u* component of wind (shaded, ms^{-1}) and potential temperature (K, contour) at time = (a) 0 min, (b) 90 min, (c) 180 min, and (d) 240 min for 1 km IOP 6 simulation. Red shading indicates reversed flow.
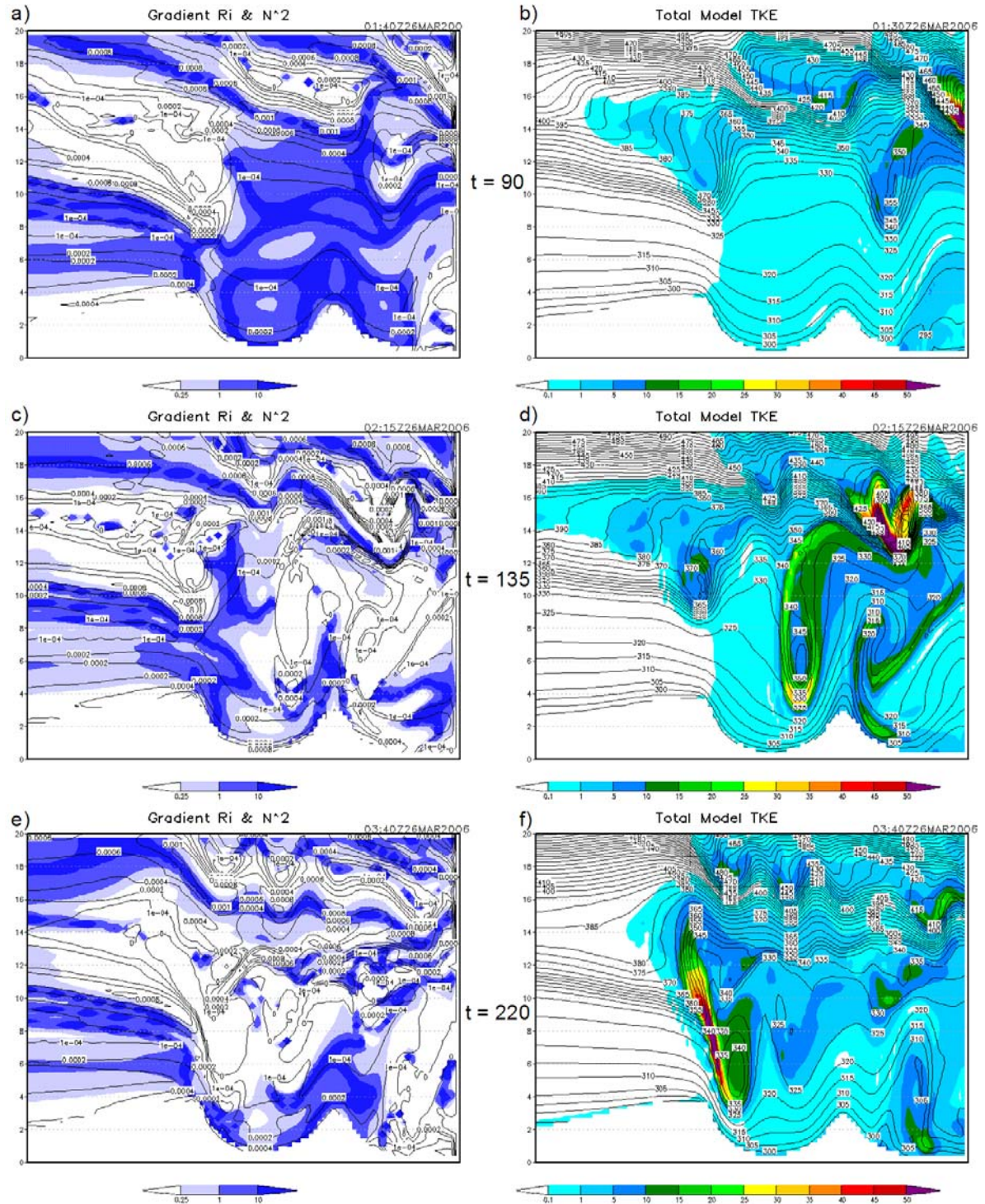
Figure 4.20: IOP 6 gradient Richardson number (shaded) and Brunt-Väisälä frequency squared (contoured, s^{-2}) on left, model-parameterized TKE (shaded, m^{2}s^{-2}) and potential temperature (contoured, K) on right. Output shown at t = (a) 90 min, (b) 135 min, and (c) 220 min.
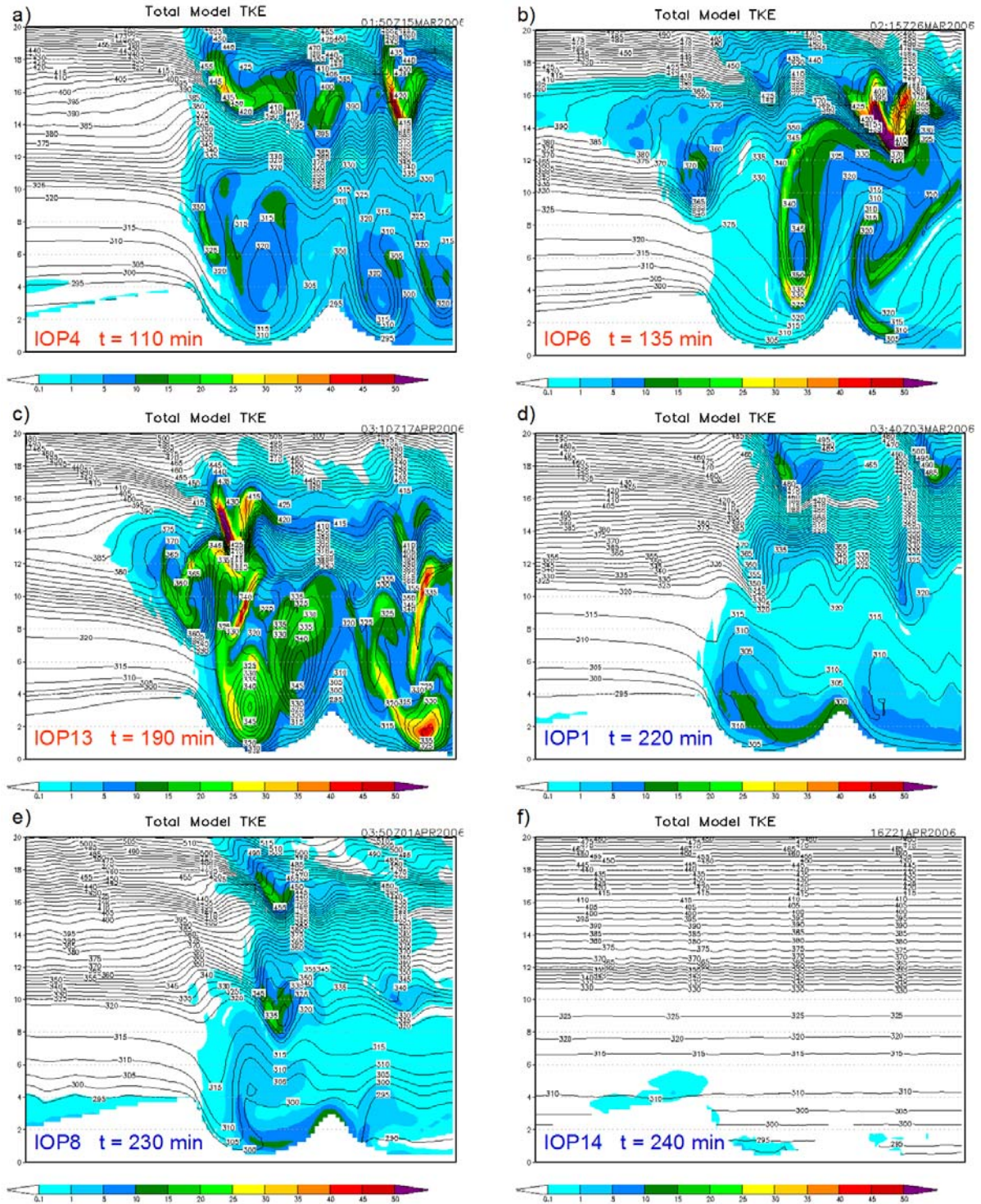
Figure 4.21: Model-parameterized TKE (shaded, $m^2 s^{-2}$) and potential temperature (contoured, K) for the IOPs and times indicated (representing the time of maximum TKE above the tropopause). Red text in the caption denotes strong stratospheric wave IOPs and red text denotes weaker stratospheric wave IOPs.
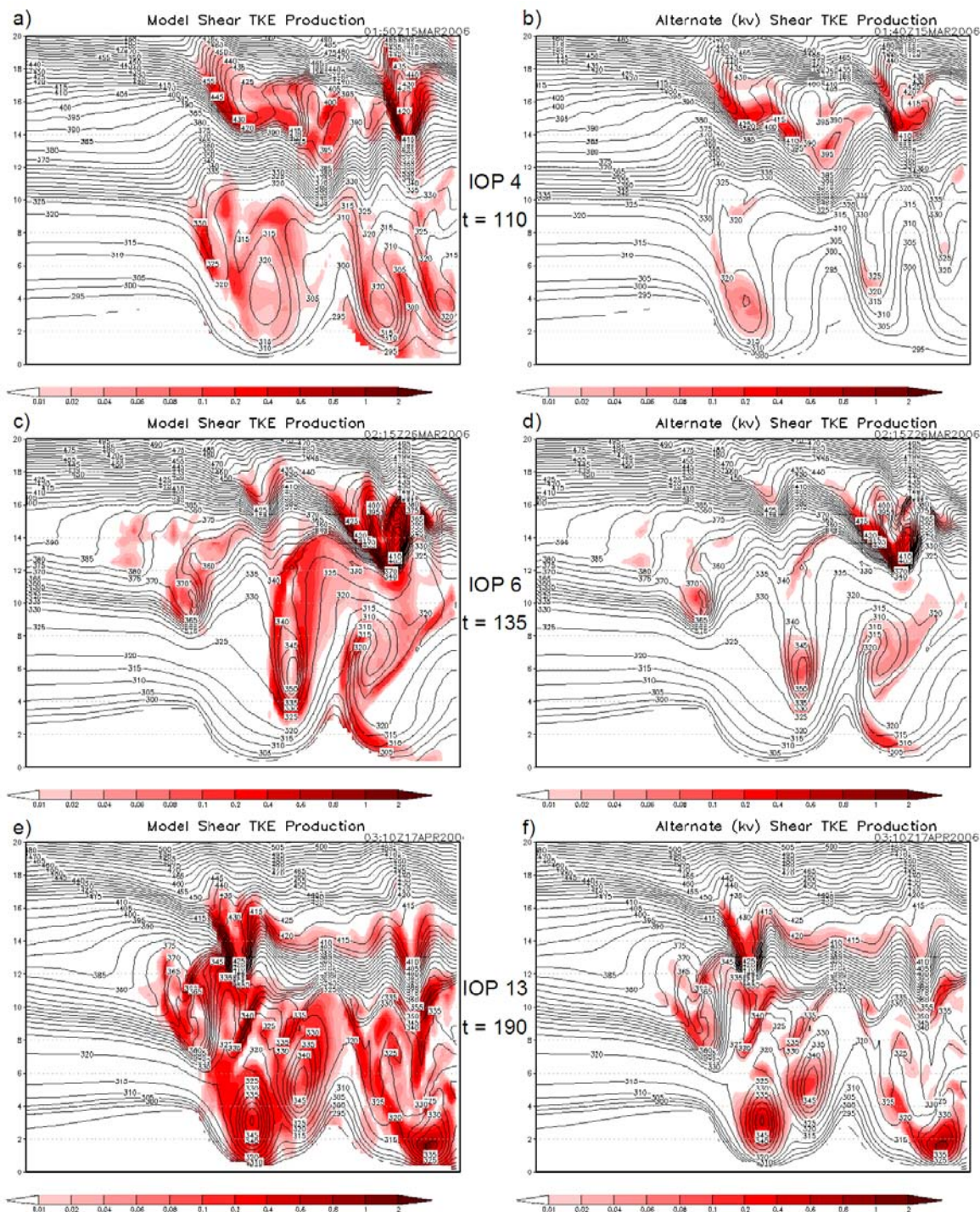
Figure 4.22: Model-parameterized mechanical shear TKE production (left, shaded, m^2s^{-3}) from Eq. (4.2) and alternate mechanical shear TKE production (right, shaded, m^2s^{-3}) from Eq. (4.7). Output shown at time of maximum stratospheric TKE for the three strong stratospheric wave cases.
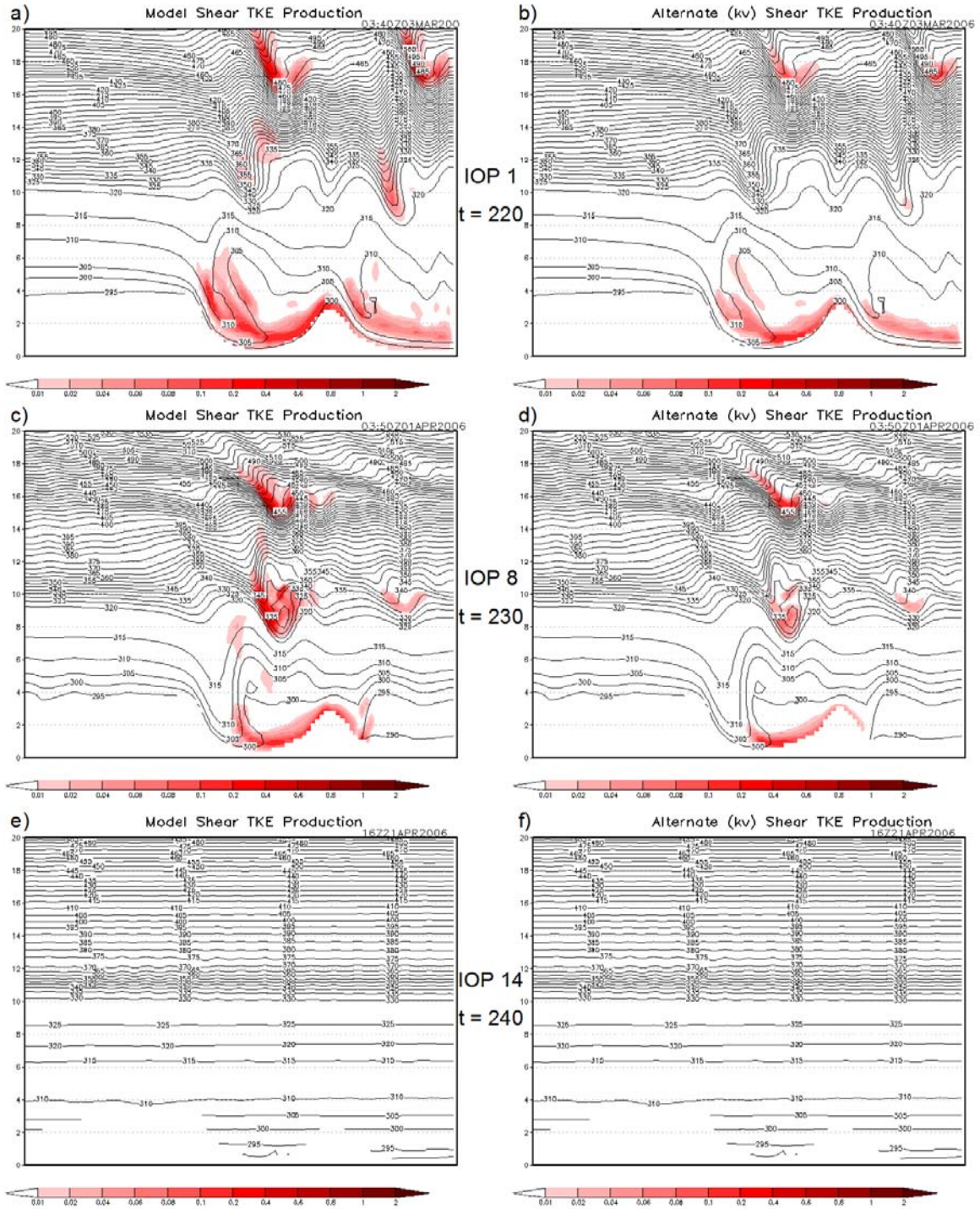
Figure 4.23: Model-parameterized mechanical shear TKE production (left, shaded, m^2s^{-3}) from Eq. (4.2) and alternate mechanical shear TKE production (right, shaded, m^2s^{-3}) from Eq. (4.7). Output shown at time of maximum stratospheric TKE for the three weak stratospheric wave cases.
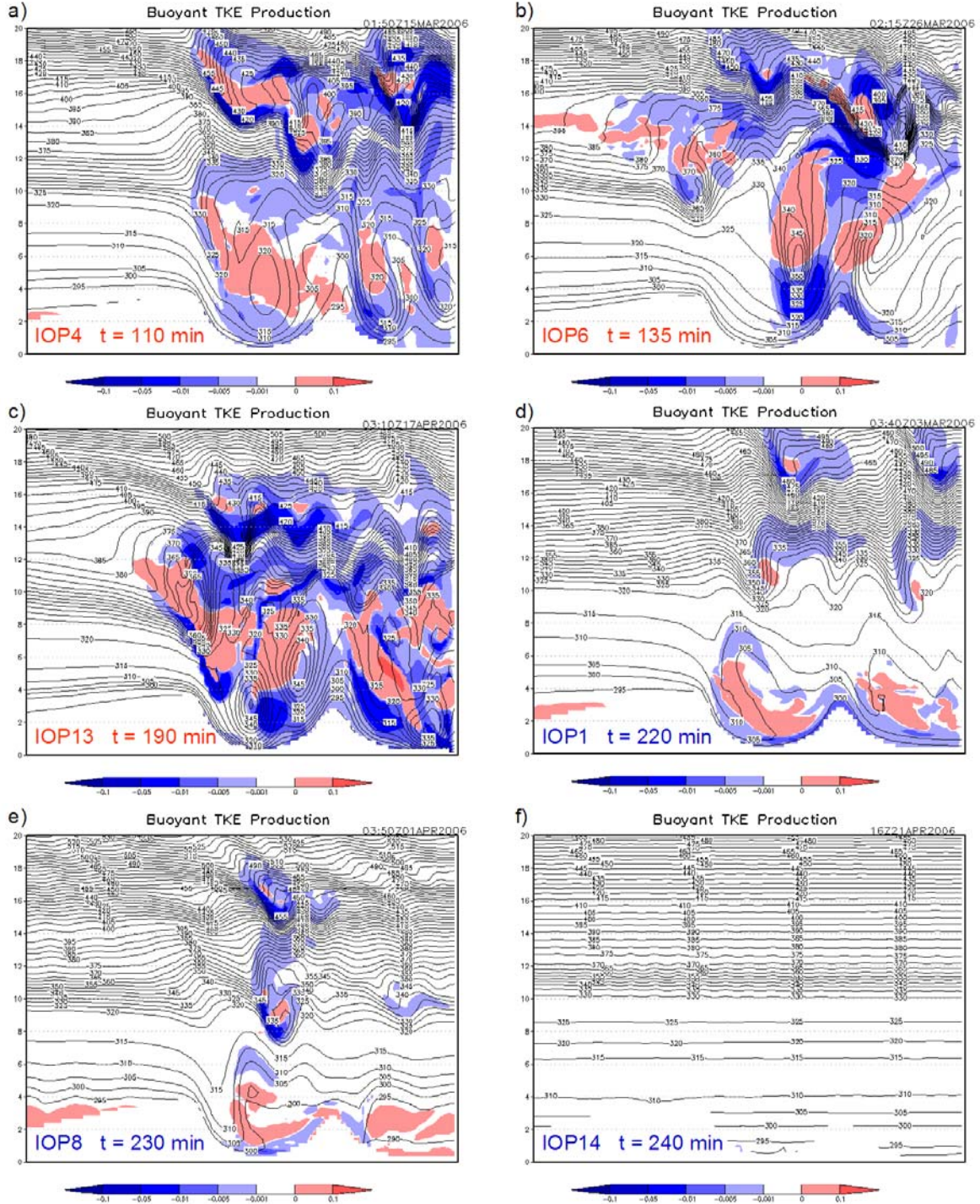
Figure 4.24: Model-parameterized buoyant TKE production (shaded, m^2s^{-3}) from Eq. (4.3) and potential temperature (contoured, K) for the IOPs and times indicated (representing the time of maximum TKE above the tropopause). Red text in the caption denotes strong stratospheric wave IOPs and red text denotes weaker stratospheric wave IOPs.
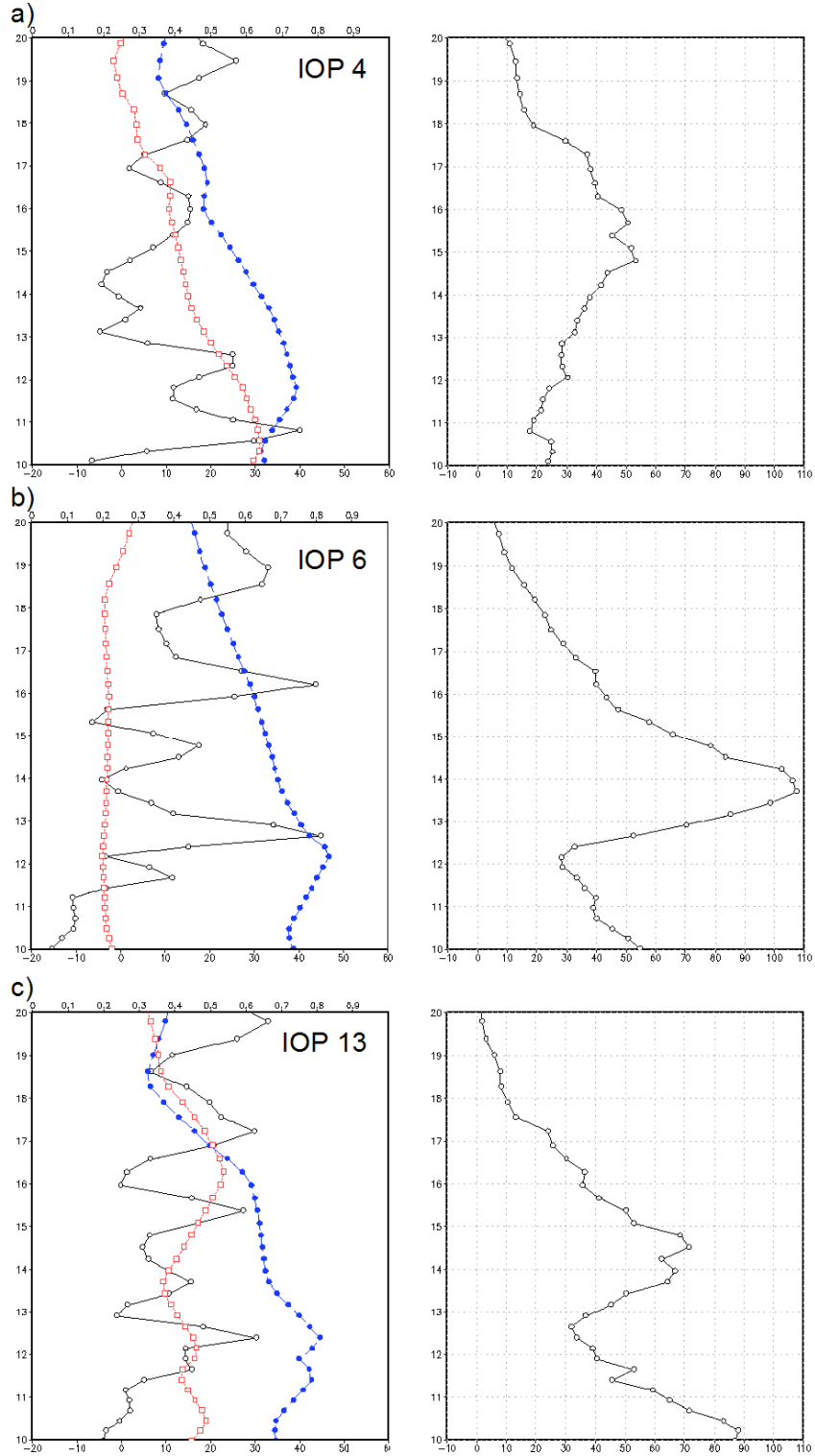
Figure 4.25: Vertical profile of initialization N^2 (black, x values on upper axis, $s^{-2} \times 10^{-4}$), u (blue, lower x axis, ms^{-1}), and v (red, ms^{-1}) on left, and all-time maximum TKE (m^2s^{-2}) in the 10-20 km layer for the right half of the domain for IOPs (a) 4, (b) 6, and (c) 13 (cases with strong stratospheric wave action).
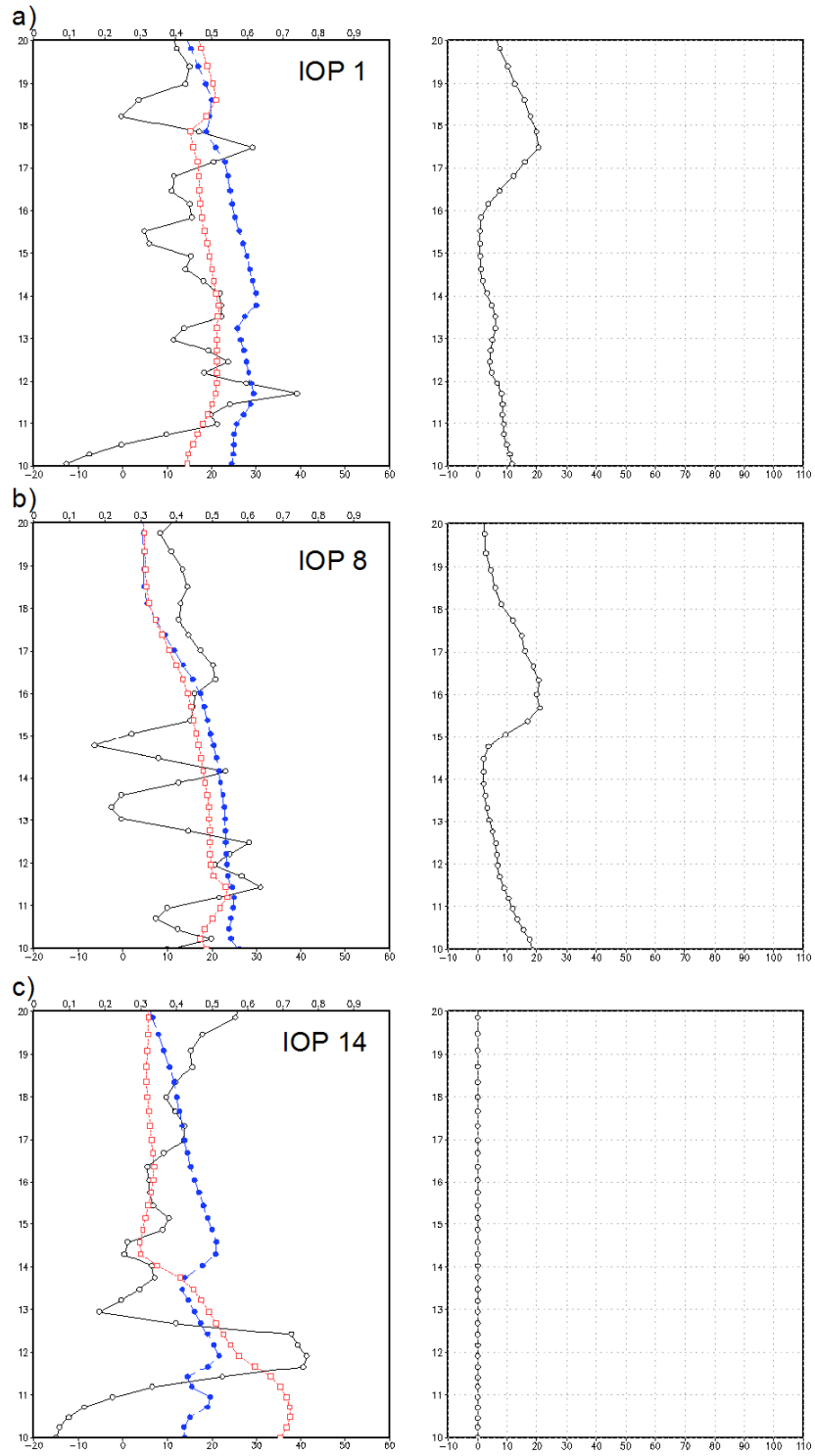
Figure 4.26: Same as Fig. 4.24 except for IOPs (a) 1, (b) 4, and (c) 14 (cases with relatively weak stratospheric wave action).

CHAPTER 5

CONCLUSIONS

5.1. Summary

This dissertation tested a hypothesis that certain configurations of upper-level circulations leading to vertically confluent flow can create a particularly favorable thermal and shear profile for the generation of upper tropospheric and lower stratospheric aviation turbulence when acted upon by a mountain wave. This structure is characterized either by differing jet flows bracketing a strong inversion at or above tropopause or through differential vertical motions ahead of a strong upper-level trough and is a favored region for wave breaking. To that end, two cases of extreme aviation turbulence in the vicinity of the tropopause were examined from a multi-scale perspective using both observed data sets and numerical models. Additionally, a series of idealized simulations were conducted for the purposes of testing the sensitivity of the flow response to the various components of the hypothesized structure.

On 9 December 1992, a DC-8 was severely damaged while attempting to cross the Front Range near the tropopause on a day that was characterized by a vigorous 250 hPa polar jet streak diving down into Colorado from the northwest. At the same time, an anticyclonic subtropical jet feature at 150 hPa had recently departed the area (Figures 2.5 and 2.6), leaving the upper fronts aligned in the vertical and causing a significant inversion to develop above an unstable layer at 200 hPa, (Fig. 2.3). Numerical simulations of the case indicated that the compression of the stable layer above 200 hPa and de-stabilization below generated strong vertical gradients of static stability which, in turn, led to intense buoyancy-driven vertical

166

circulations as the mountain wave provided a continuous source of strong buoyancy perturbations to the thermal fields (Figures 2.16-2.19). These vertical circulations increased the horizontal shear which, in conjunction with the pre-existing horizontal shear, encouraged the downscale organization of small, violent eddies (such as HVTs, Fig. 2.21). The model simulations showed evidence of a possible turbulent downburst of the type discussed in Clark et al. (2000) (Fig. 2.24).

During the Terrain-Induced Rotor Simulation (T-REX) IOP 6, a high-altitude research aircraft encountered a violent updraft/downdraft couplet while crossing the Owens Valley in the lower stratosphere (Fig. 3.7). The research crew attributed this turbulent event to wave-breaking (Doyle 2006). The synoptic conditions during IOP 6 featured a strong upper-level trough and associated 250 hPa cyclonic polar jet streak crossing the Sierra Nevada, with curvature-induced subsidence above 150 hPa and inversions near 175 hPa and 100 hPa. A series of nested-grid simulations of the case was able to reproduce in time and space the wave breaking associated with the aircraft observation of turbulence (Figures 3.17 and 3.19). Buoyancy was found to play a significant role in the generation of violent eddy motions in the stratosphere as the mountain wave perturbed the jet/front system. The vertical variation of the Scorer parameter in the lower stratosphere (Figures 3.14 and 3.18) indicated both shear and static stability gradients conducive to the generation of violent eddies, which in turn can cause aviation turbulence such as was detected by the HIAPER. The strength of the stratospheric inversion was found to be greater in the IOP 6 case than in the two other T-REX IOPs characterized by a strong stratospheric wave signal (Fig. 3.26).

A series of two-dimensional idealized simulations was conducted to test the role of the stratospheric thermal and wind structure on the evolution of mountain-wave induced

167

turbulence. Model-parameterized TKE was examined in all cases, and the strength of the

lower stratospheric inversion at or above the tropopause was found to significantly affect the

generation of TKE by the model. In the Colorado case, the control simulation representing

the conditions on 9 December 1992 produced the most model-parameterized TKE at finer

resolution (0.5 km grid length, Fig. 4.13), while at the coarse resolution (2 km grid length)

the stronger inversion case generated the most model-parameterized TKE (Fig. 4.5). In all of

the Colorado cases, it was clear that the inversion strength was important, however not

surprisingly, strong shear was still required to generate turbulence. For the T-REX

simulations, three cases with strong stratospheric gravity waves were compared to three cases

with weaker stratospheric waves. All simulations seemed to generate an exaggerated

response compared to actual observations and real-data simulations of the cases

(http://catalog.eol.ucar.edu/trex/). However, the simulations did produce the relative

responses to one another, i.e., IOP 6 had the most model-parameterized TKE while IOP14

had virtually no response (Fig. 4.21). It was found that the vertical variation of static

stability coupled with strong terrain-normal flow maximized the model generation of TKE

(Table 4.3). These findings support the hypothesis stated in Chapter 1.

In summary, this research strongly indicates that a regime for extreme mountain-

induced turbulence likely exists when vertically intersecting jet/front circulations or trough-

induced vertical motions are such that a strong cold layer develops below a warm layer in the

stratosphere, creating a very strong inversion directly above or associated with the

tropopause. While the presence of differential thermal advection is not an uncommon

occurrence in the presence of strong cyclonic curvature aloft (Hirschberg and Fritsch 1991),

the combination of the inversion, the jet-induced shear, and the mountain wave result in

strong vertical discontinuities which then set the stage for a downscale cascade of kinetic energy. The mountain wave compresses and perturbs the inversion layer, the base of which becomes the focus for wave amplification and breaking as well as strong horizontal vortices. The kinetic energy is eventually transferred to violent turbulent eddies capable of damaging an aircraft. Fig. 5.1 is a flow chart describing a likely series of events which summarizes the findings of key processes resulting in violent aviation turbulence. This process is shown as a conceptual model in Fig. 5.2. This research suggests that the process shown in Fig. 5.2 can be the result of more than one precursor condition, as the differential subsidence indicated can be associated with both vertically-intersecting ageostrophic jet circulations or via the differential advection of cyclonic vorticity advection associated with strong upstream troughing. The presence of a jet feature in this process is also critical to providing adequate shear.

5.2. Future Work

As with all aspects of turbulence research, a significant limitation of this project stems from the small sample set of cases. Future work on this problem should involve additional cases involving documented aircraft encounters with upper-level CAT. Such research should examine the synoptic precursors as well as the fine-scale motions leading to CAT. Additional fine-scale numerical simulations should also be conducted to further refine the downscale energy cascade process at the mesoscale. More idealized simulations may also prove enlightening, especially at much finer resolution. To this end, a WRF idealized 2-dimensional simulation was attempted using a grid cell size of $50 \times 50 \times 50$ m to approach LES, however the simulations generated spurious standing waves on the upstream boundary.

LES simulations of lower stratospheric CAT over topography will need a more robust LES model with a terrain-following vertical coordinate.

Although not discussed in this dissertation, a large part of the research conducted in support of this project involved testing an automatic grid nesting algorithm for operational NWP models. The premise behind this idea is that using certain thresholds for parameters that indicate the potential for aviation turbulence (such as the NCSU1 Turbulence Index) the model would automatically trigger a finer-resolution inner domain once that threshold was exceeded on the parent domain. This would continue to finer and finer resolutions until the CAT motions would be partially resolved. The computational expense of this scheme makes full application in real-time several years away. However in the meantime, more testing can be conducted to perfect the thresholds. Additionally, many of the turbulence parameters used operationally are very small numbers that are the product of perturbations (again, such as NCSU1). This makes "portability" between models problematic, as was seen in testing of the NCSU1 index against the Colorado case; NCSU1 values near the incident location differed by two orders of magnitude between NHMASS and WRF/ARW simulations using the same configuration. It would be useful to derive a turbulence parameter that will capture the mesoscale precursors to CAT such as NCSU1, however of order 1 and/or non-dimensional.

Another area of research that was not investigated as part of this dissertation but that may have an impact on the development of upper tropospheric and lower stratospheric mountain-wave induced aviation turbulence are moisture effects. As was seen in the 9 December 1992 case, the model produced a saturated layer above the inversion. Sensitivity testing involving the model microphysical parameterization may yield some insight into the

effects of moisture on the evolution of the aviation turbulence. Durran and Klemp (1982, 1983) found that the addition of low-level moisture in numerical simulations had a profound effect on the structure of both trapped and vertically-propagating mountain waves. It would be useful to examine whether there is a stratospheric analog for the jet streak/mountain wave interaction case. The addition of moisture can inhibit wave breaking as simulated by Weissbluth and Cotton (1989). However, the majority of the study in this area has been confined to the troposphere. While by definition CAT occurs outside of cloud, satellite imagery of the 9 December 1992 case (Clark et al. 2000) as well as many of the T-REX cases indicate some clouds present near the tropopause, leading to further questions as to the role of moisture at high altitude.

Lastly, as this research indicates that more than one regime may lead to the favorable vertical shear and static stability gradients that appear to be critical to the formation of mountain-induced stratospheric turbulence, additional research into other possible synoptic precursors is warranted. One aspect not fully explored in the present dissertation is the relative role of the curvature associated with the trough with respect to the 250 hPa jet streak in the T-REX IOP 6 case. Dissecting the Q-vector into its along- and cross-isentropic components should help illuminate which aspect of the T-REX IOP 6 configuration contributed the most to the vertical confluence which created the inversion. Additionally, a Rossby analysis would be necessary to confirm the applicability of QG theory to these cases. Further case studies would be ideal to validate both the upstream trough and the vertically stacked jet structure as causal mechanisms, and may perhaps indicate yet another synoptic situation that might lead to similar vertical confluence at or above the tropopause.

The problem of aviation turbulence forecasting will continue to vex civil and military aviators as long as aviation operations are conducted above complex terrain at high altitude. Therefore, further research on this subject will be of great importance to flight safety. It is hoped that the work contained herein will serve to advance the science of aviation turbulence forecasting by providing a useful conceptual model, and that aviators and their craft may be made safer through its use.
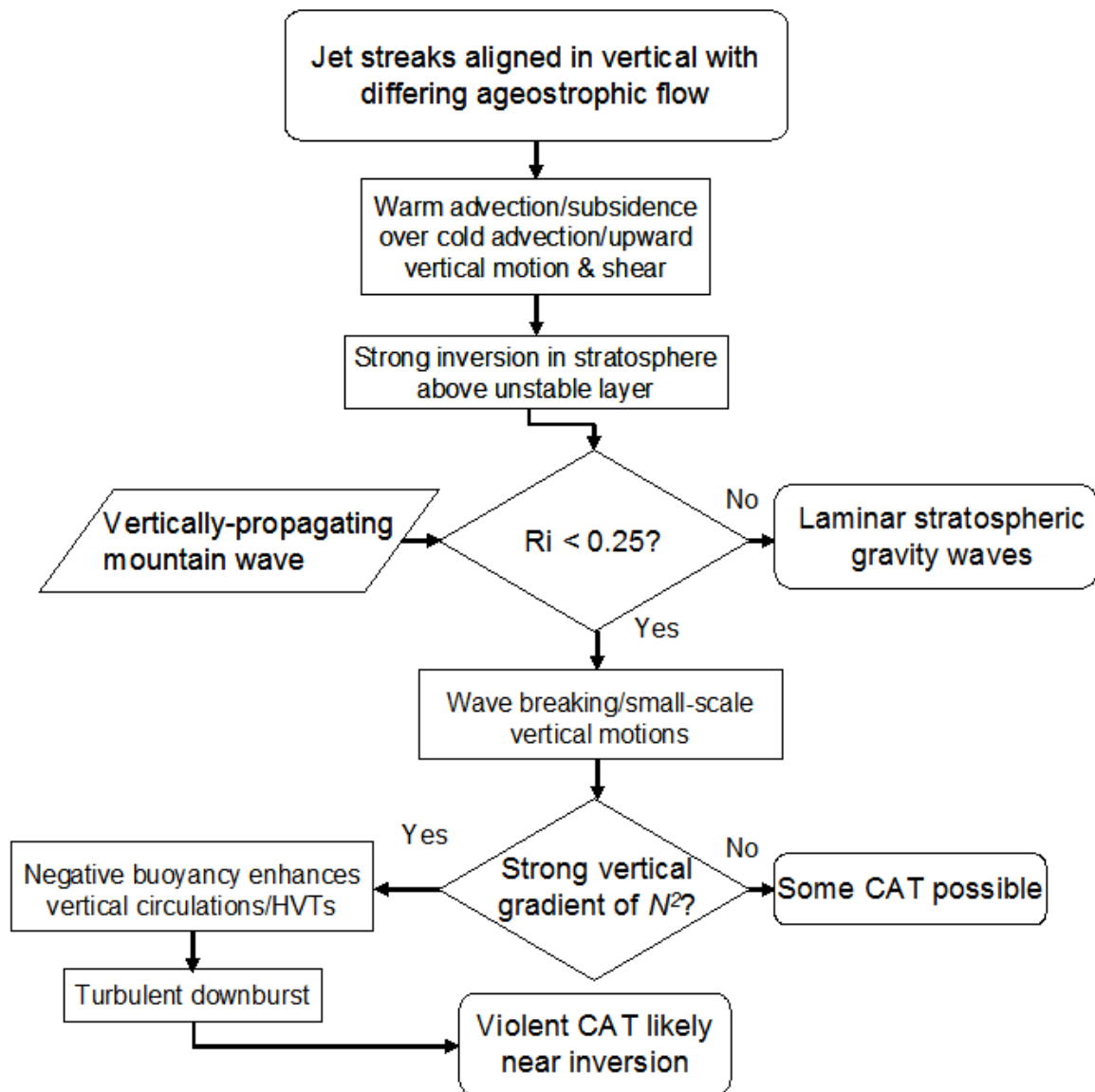
Figure 5.1: Hypothesized sequence of events leading to violent lower stratospheric clear air turbulence in a regime characterized by vertically stacked jet/front systems perturbed by mountain wave activity.
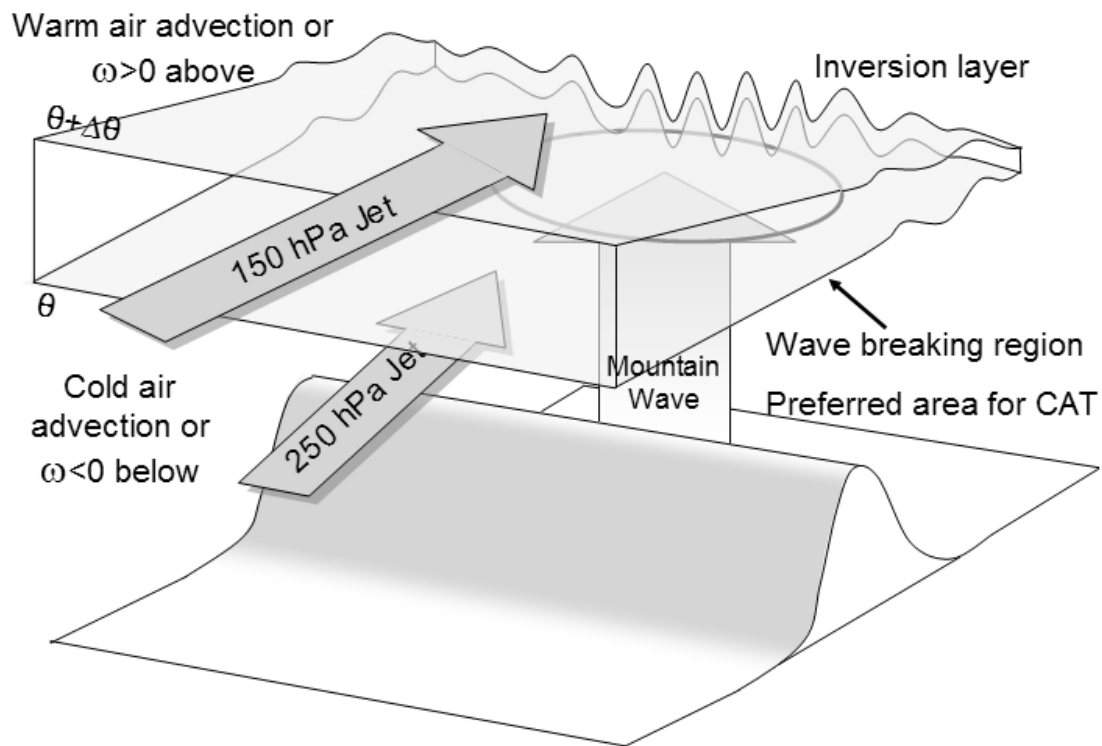
Figure 5.2: Conceptual model of the regime for extreme turbulence associated with vertically-intersecting jet/front systems and mountain waves. In this optimal configuration, the upper jet feature is associated with warm advection and/or subsidence and the lower jet feature is associated with cold advection or upward motion. The result is a compressed inversion layer at or above tropopause. This layer is significantly perturbed by the mountain wave. The base of the inversion is the focus for significant aviation turbulence as gravity waves break and horizontal vortices develop in response to 3-dimenisonal gradients in shear and stability.

REFERENCES

Arya, S. P., 2001: Introduction to *Micrometeorology*. Academic Press, 420 pp.

Bedard, A., F. Canavero, and F. Einaudi, 1986: Atmospheric gravity waves and aircraft turbulence encounters. *J. Atmos. Sci.*, **43**, 2838–2844.

Bosart, L. F., 1970: Mid-tropospheric frontogenesis. *Quart. J. Roy. Meteor. Soc.,* **96,** 442–471.

Brown, P., 2006: Flight report from T-REX BA146 mission B181 on March 25, 2006. Available at http://catalog.eol.ucar.edu/trex/.

Carney, T.Q., A. J. Bedard Jr., J. M. Brown, J. McGinley, T. Lindholm, M.J. Kraus, 1988: Hazardous mountain winds and their visual indicators. US Dept of Transportation, FAA, Washington, D.C. Publication AC 00-57.

Clark, T. L., and W. Peltier, 1984: Critical Level Reflection and the Resonant Growth of Nonlinear Mountain Waves. *J. Atmos. Sci.*, **41**, 3122–3134.

_____, and W. D. Hall, 1991: Multi-domain simulations of the time dependent Navier Stokes equations: Benchmark error analyses of some nesting procedures. *J. Comput. Phys.,* **92,** 456–481.

_____, W. D. Hall, R. M. Kerr, D. Middleton, L. Radke, F. M. Ralph, P. J. Neiman, and D. Levinson, 2000: Origins of aircraft-damaging clear-air turbulence during the 1992 Colorado downslope windstorm: numerical simulations and comparison with observations. *J. Atmos. Sci.*, **57**, 1105-1131.

Conaty, A.L., J.C. Jusem, L. Takacs, D. Keyser, and R. Atlas, 2001: The structure and evolution of extratropical cyclones, fronts, jet streams, and the tropopause in the GEOS General Circulation Model. *Bull. Amer. Meteor. Soc.*, **82**, 1853–1867.

Deardorff, J.W., 1970: Convective velocity and temperature scales for the unstable planetary boundary layer and for rayleigh convection. J. Atmos. Sci., **27**, 1211–1213.

_____., 1972: Parameterization of the planetary boundary layer for use in general circulation modelshttp://ams.allenpress.com/perlserv/?request=cite-builder&doi=10.1175%2F1520-0493%281972%29100%3C0093%3APOTPBL%3E2.3.CO%3B2 - n1#n1. Mon. Wea. Rev., **100**, 93–106.

Doyle, J.D., D.R. Durran, C. Chen, B.A. Colle, M. Georgelin, V. Grubisic, W.R. Hsu, C.Y. Huang, D. Landau, Y.L. Lin, G.S. Poulos, W.Y. Sun, D.B. Weber, M.G. Wurtele, and M.

Xue, 2000: An intercomparison of model-predicted wave breaking for the 11 January 1972 Boulder windstorm. *Mon. Wea. Rev.*, **128**, 901–914.

_____., and D. R. Durran, 2002: The dynamics of mountain-wave-induced rotors. *J. Atmos. Sci.*, 59, 186–201.

_____, 2006. Flight report from T-REX GV mission RF05 on March 25, 2006. Available at http://catalog.eol.ucar.edu/trex/.

_____, R. B. Smith, W. A. Cooper, V. Grubišić, J. Jensen, Q. F. Jiang,2007: Three-dimensional characteristics of mountain waves generated by the Sierra Nevada. Preprints, *12th Conf. on Mesoscale Processes.* Waterville Valley, NH, Amer. Meteor. Soc.

Durran, D. R., and J.B. Klemp, 1982: The Effects of Moisture on Trapped Mountain Lee Waves. *J. Atmos. Sci.*, **39**, 2490–2506.

_____, and J.B. Klemp, 1983: A Compressible Model for the Simulation of Moist Mountain Waves. *Mon. Wea. Rev.*, **111**, 2341–2361.

_____, 1986: Another Look at Downslope Windstorms. Part I: The Development of Anal_ogs to Supercritical Flow in an Infinitely Deep, Continuously Stratified Fluid. *J. Atmos. Sci.*, **43**, 2527–2543.

_____, 1990: Mountain waves and downslope winds. *In*: Atmospheric Processes over Complex Terrain. W. Blumen, (Ed), *Meteorol. Monogr. Am. Meteorol. Soc*. **23 (45)**: 59–81.

Glickman, T. S., Ed., 2000: *Glossary of Meteorology (2nd ed.)*. Amer. Meteor. Soc., 855 pp.

Grubišić, V., J. D. Doyle, J. Kuettner, G. S. Poulos, and C. D. Whiteman, 2004: Terrain-induced Rotor Experiment (T-REX) overview document and experiment design. 72 pp. Available at http://www.eol.ucar.edu/projects/trex/documents/

_____, L. Armi, J. P. Kuettner, S. J. Haimov, L. Oolman, R. R. Damiani, and B. J. Billings, 2006: Atmospheric rotors: Aircraft in situ and cloud radar measurements in T-REX. Preprints, *12th Mountain Meteor. Conf.*, Santa Fe, Amer. Meteor. Soc.

Hirschberg, P.A., and J.M. Fritsch, 1991: Tropopause Undulations and the Development of Extratropical Cyclones. Part I. Overview and Observations from a Cyclone Event. *Mon. Wea. Rev.*, **119**, 496–517.

Holton, J. R., 2004: *An Introduction to Dynamic Meteorology, 4th ed.* Academic Press, 535 pp.

Howard, L. N., 1961: Note on a paper of John W. Miles. *J. Fluid Mech.,* **101,** 509–512.

Huppert, H. E., and J. W. Miles, 1969: Lee waves in a stratified flow. Part 3: Semi-elliptical obstacles. *J. Fluid Mech.,* **35,** 481–496.

Kaplan, M. L. and V. M. Karyampudi, 1992.: Meso-beta scale numerical simulations of terrain-drag induced along-stream circulations. Part I: Midtropospheric frontogenesis. *Meteorol. Atmos. Phys.*, **49**, 133-156.

_____, Y.-L. Lin, J. J. Charney, K. D. Pfeiffer, D. B. Ensley, D. S. DeCroix, and R. P. Weglarz, 2000: A terminal area PBL prediction system at Dallas-Fort Worth and its application in simulating diurnal PBL jets. *Bull. Amer. Meteor. Soc.*, **81**, 2179-2204.

_____ A. W. Huffman, K. M. Lux, J. D. Cetola, J. J. Charney, A. J. Riordan, Y.-L. Lin and K. T. Waight III, 2005a: Characterizing the severe turbulence environments associated with commercial aviation accidents. Part 1: A 44 case study synoptic observational analysis. *Meteorol. Atmos. Phys.*, **88**, 129-152.

_____, A. W. Huffman, K. M. Lux, J. D. Cetola, J. J. Charney, A. J. Riordan Y. L. Lin, and K. T. Waight III, 2005b: Characterizing the severe turbulence environments associated with commercial aviation accidents. Part 2: Hydrostatic nesoscale numerical simulations of supergradient wind flow and streamwise ageostrophic frontongenesis. *Meterol. Atmos. Phys.*, **88**, 153-173.

_____ J. J. Charney, K. T. Waight III, K. M. Lux, J. D. Cetola, A. W. Huffman, A. J. Riordan, S. D. Slusser, M. T. Kiefer, P. S. Suffern and Y.-L. Lin, 2006: Characterizing the severe turbulence environments associated with commercial aviation accidents. A real-time turbulence model (RTTM) designed for the operational prediction of hazardous aviation turbulence environments. *Meteorol. Atmos. Phys.*, **94**, 235-270.

Keyser, D.A., and D.R. Johnson, 1984: Effects of diabatic heating on the ageostrophic circulation of an upper tropospheric jet streak. *Mon. Wea. Rev.*, **112**, 1709–1724.

_____, and M. Shapiro, 1986: A Review of the Structure and Dynamics of Upper-Level Frontal Zones. *Mon. Wea. Rev.*, **114**, 452–499.

Klemp, J., and D. Lilly, 1975: The dynamics of wave-induced downslope winds. *J. Atmos. Sci.*, **32**, 320–339.

Koch, S.E., M. desJardins, and P.J. Kocin, 1983: An interactive barnes objective map analysis scheme for use with satellite and conventional data. *J. Appl. Meteor.*, **22**, 1487–1503.

_____, B. D. Jamison, C. Lu, T. L. Smith, E. I. Tollerud, C. Girz, N. Wang, T. P. Lane, M. A. Shapiro, D. D. Parrish, and O. R. Cooper, 2005: Turbulence and gravity waves within an upper-level front. *J. Atmos. Sci.*, 62, 3885-3908.

_____, L. R. Bernardet, B. D. Jamison, and J. M. Brown, 2006: Modeling of mountain waves in T-REX. Preprints, *12th Mountain Meteor. Conf.*, Santa Fe, Amer. Meteor. Soc.

Kolmogorov, A.N., 1941: Local structure of turbulence in an incompressible fluid at very high Reynolds numbers. *Dokl. Akad. Nauk. SSSR*, **30**, 299-303.

Krishnamurti, T.N., 1961: The subtropical jet stream of winter. *J. Atmos. Sci.*, **18**, 172–191.

Kuettner, J. P., 1959: The rotor flow in the lee of mountains. GRD Research Notes, No. 6, AFCRCTN-58-626, ASTIA Document No. AD-208862, pp. 20.

_____, R.F. Hertenstein, 2003: Simulations of rotors using steep lee-slope topography. Preprints, *10th Mountain Meteor. Conf.,* Park City, Amer. Met. Soc., 2003.

Lackmann, G.M., D. Keyser, and L.F. Bosart, 1997: A characteristic life cycle of upper-tropospheric cyclogenetic precursors during the Experiment on Rapidly Intensifying Cyclones over the Atlantic (ERICA) . *Mon. Wea. Rev.*, **125**, 2729–2758.

Lane,T. P., R. D. Sharman, T. L. Clark, H.-M. Hsu, 2003: An investigation of turbulence generation mechanisms above deep convection. *J. Atmos. Sci.,* 60, 1297-1321.

Laprise, R., and W.R. Peltier, 1989: The structure and energetics of transient eddies in a numerical simulation of breaking mountain waves. *J. Atmos. Sci.*, **46**, 565–585.

Lilly, D., 1978: A severe downslope windstorm and aircraft turbulence event induced by a mountain wave. *J. Atmos. Sci.*, **35**, 59–77.

Lin, Y. L., 2007: *Mesoscale Dynamics*, Cambridge University Press, 632 pp.

_____, and T.A. Wang, 1996: FRlow regimes and transient dynamics of two-dimensional stratified flow over an isolated mountain ridge. *J. Atmos. Sci.*, **53**, 139–158.

_____, C. J. Ringley, D. R. Vollmer, P. S. Suffern, Z. G. Brown, M. T. Kiefer, M. K. Kaplan, and K. T. Waight III, 2006: The development of a stratospheric real-time turbulence modeling system; Scientific and technical report for year #2. AFRL/FA8718-04-C-0011, 86 pp.

Mattocks, C., and R. Bleck, 1986: Jet streak dynamics and geostrophic adjustment processes during the initial stages of lee cyclogenesis. *Mon. Wea. Rev.*, **114**, 2033–2056.

McComb, W. D., 1990: *The physics of fluid turbulence.* Oxford University Press, 600 pp.

Miles, J. W., 1961: On the stability of heterogeneous shear flow. *J. Fluid Mech.,* **10,** 496–508.

Miller, J.E., 1948: On the concept of frontogenesis. *J. Atmos. Sci.*, **5**, 169–171.

Moin P. and K. Mahesh, 1998: Direct numerical simulation: A tool in turbulence research. *Annu. Rev. Fluid Mech.*, **30**, 539-578.

Moore, J. T., and G. E. Vanknowe, 1992: The effect of jet-streak curvature on kinematic fields. *Mon. Wea. Rev.*, **120**, 2429–2441

Namias, J., and P.F. Clapp, 1949: Confluence theory of the high tropospheric jet stream. *J. Atmos. Sci.*, **6**, 330–336.

Obukhov, A. M., 1941: Spectral energy distribution in turbulent flow, *Izv. Aka. Nauk SSSR* **5**, 453–566.

Pope, S. B., 2000: *Turbulent Flows.* Cambridge University Press, 806 pp.

Queney, P., 1948: The problem of airflow over mountains: A summary of theoretical results. *Bull. Amer. Meteor. Soc.*, **29**, 19-26.

Ralph, F. M., P. J. Neiman, and D. Levinson, 1997: Lidar observations of a breaking mountain wave associated with extreme turbulence. *Geophys. Res. Lett.*, **24,** 663-666.

Reed, R.J., and F. Sanders, 1953: An investigation of the development of a mid-tropospheric frontal zone and its associated vorticity field. *J. Atmos. Sci.*, **10**, 338–349.

_____, 1955: A study of a characteristic tpye of upper-level frontogenesis. *J. Atmos. Sci.*, **12**, 226–237.

Reiter, E.R., and A. Nania, 1964: Jet-stream structure and clear-air turbulence (CAT). *J. Appl. Meteor.*, **3**, 247–260.

Sawyer, J. S., 1956: The vertical circulation at meteorological fronts and its relation to frontogenesis. *Proc. Roy. Soc. London,* **234A,** 346–362.

Scinocca, J. F. and W. R. Peltier, 1993: The instability of Long's stationary solution and the evolution toward severe downslope windstorm flow. Part I: Nested grid numerical simulations. *J. Atmos. Sci.*, **50**, 2245-2263.

Scorer, R. S., 1949: Theory of waves in the lee of mountains. *Quart. J. Roy. Meteor. Soc.*, **75**, 41-56.

Shapiro, M. A., 1970: On the applicability of the geostrophic approximation to upper-level frontal-scale motions. *J. Atmos. Sci.*, **27**, 408–420.

_____, 1976: The role of turbulent heat flux in the generation of potential vorticity in the vicinity of upper-level jet stream systems. *Mon. Wea. Rev.*, **104**, 892–906.

_____, 1978: Further evidence of the mesoscale and turbulent structure of upper level jet stream–frontal zone systems. *Mon. Wea. Rev.*, **106**, 1100–1111.

_____, 1981: Frontogenesis and geostrophically forced secondary circulations in the vicinity of jet stream-frontal zone systems. *J. Atmos. Sci.*, **38**, 954–973.

_____ and P. Kennedy, 1981: Research aircraft measurements of jet stream geostrophic and ageostrophic winds. *J. Atmos. Sci.*, **38**, 2642–2652.

Sharman, R., C. Tebaldi, G. Wiener, and J. Wolff, 2006: An integrated approach to mid- and upper-level turbulence forecasting. *Wea. Forecasting*, **21**, 268–287.

Skamarock, W. C., J. B. Klemp, J. Dudhia, D. O. Gill, D. M. Barker, W. Wang and J. G. Powers, 2007: A description of the Advanced Research WRF Version 2, 100 pp, NCAR Tech. Note NCAR/TN–468+STR

Smagorinsky, J., 1963: General circulation experiments with the primitive equations. *Mon. Wea. Rev.*, **91**, 99–164.

Smith, R. B., 1985: On severe downslope winds. *J. Atmos. Sci.*, **42**, 2597-2603.

_____, 2006. Mission summary for T-REX IOP 13. Available at http://catalog.eol.ucar.edu/trex/.

Stull, Roland B., 1988: *An Introduction to Boundary Layer Meteorology*. Kluwer Academic Press: 639 pp.

Swanson, K.L., 2001: Upper-tropospheric potential vorticity fluctuations and the dynamical relevance of the time mean. *J. Atmos. Sci.*, **58**, 1815–1826.

Taylor, G.I., 1938: The spectrum of turbulence. *Proc. Roy. Soc. London,* **A164**, 476-490.

Therry, G., and P. Lacarrere, 1983: Improving the eddy kinetic energy model for planetary boundary layer description. *Bound.-Layer Meteor.,* **25,** 63–88.

Uccellini, L.W., and D.R. Johnson, 1979: The coupling of upper and lower tropospheric jet streaks and implications for the development of severe convective storms. *Mon. Wea. Rev.*, **107**, 682–703.

_____, K. F. Brill, R. A. Petersen, D. Keyser, R. Aune, P. J. Kocin, M. des Jardins, 1986: A report on the upper-level wind conditions preceding and during the Shuttle Challenger (STS 51L) explosion. *Bull. Amer. Meteor. Soc.*, **67,** 1248-1265.

Wakimoto, R.M., 1985: Forecasting dry microburst activity over the high plains. *Mon. Wea. Rev.*, **113**, 1131–1143.

Weissbluth, M.J., and W.R. Cotton, 1989: Radiative and Nonlinear Influences on Orographic Gravity Wave Drag. *Mon. Wea. Rev.*, **117**, 2518–2534.

APPENDIX A

COMPARISON BETWEEN SMOOTH-TERRAIN AND FULL-TERRAIN SIMULATIONS OF THE 9 DECEMBER 1992 COLORADO SEVERE TURBULENCE EVENT

A.1. Introduction

In the 9 December 1992 Colorado case (Chapter 2), it was hypothesized that the mountain wave served as a source of buoyancy perturbations to the pre-turbulence environment established by the overlapping jet regime. That pre-turbulence environment consisted of a strong stratospheric inversion and shear layer at 200 hPa, below which developed an unstable layer. To quantify the effect of the mountain wave on the resultant turbulence required removal of the mountain wave which was accomplished by smoothing the terrain and significantly reducing the terrain gradients. The expected result was a smooth jet streak, similar to the standard model (Keyser and Shapiro 1986), with none of the wavelike perturbations seen in the full terrain case. Also expected was a significant reduction in the amount of turbulence near the accident location as compared to the full-terrain simulations.

A.2. Methodology

Using the same configuration of the NHMASS model described in Section 2.3, a separate set of smoothed terrain experiment simulations were conducted in which a 9-point smoother was run over the terrain 1000 times during pre-processing in order to significantly reduce the terrain gradients. The advantage to this method over removing the terrain entirely was that there was no need to arbitrarily bogus the atmosphere in the regions where the mountains were eliminated. There remained some elevation differences across each domain,

however the slope was so slight as to eliminate high-frequency orographic waves. An 18 km simulation was run in this manner from the same initial and boundary conditions as the control 18 km run. The 18 km smooth-terrain fields were then used as initial and boundary conditions for a 6 km smooth-terrain simulation, and likewise, the 6 km fields initialized a 2 km smooth-terrain simulation.

A.3. Comparisons between full-terrain and smoothed-terrain simulations

Fig. A.1 is similar to Fig. 2.10 in that it depicts 1000, 1500, and 2000 UTC 9 December 1992 along-flow vertical cross-sections of the jet streak, however from the 6 km smooth-terrain NHMASS simulation. The most striking feature, beyond the smoothed terrain, is the lack of meso-γ wave-like structures evident in the Clark et al. (2000) results or our full-terrain simulations. Notice that the dynamic tropopause is relatively smooth and level as well. What slight wave-like structures that existed above the jet in the smoothed case are relatively large scale and most likely a vestige of the boundary conditions for the 18 km simulation, which did include the mountain and the mountain wave. Nevertheless, as one might expect, the jet streak transited smoothly through the area with very little perturbation. Fig. A.2 shows the same along-flow vertical cross-section as Fig. 2.11, however now depicts the vertical profile of stability (N^2 and Ri) and velocity divergence for the smooth-terrain case at 1000 and 1500 UTC (near accident time). Of note, the static stability still increased with height above 225 hPa, with the unstable layer present at 250 hPa. The area of lower Ri in the mid-troposphere was still present in the smooth case, however exhibited no wave-like perturbations. Interestingly, the low Ri feature directly below 200 hPa in the smooth case appeared more intense than the full-terrain simulation shown in Fig. 2.11. It is possible that the shear in this case is actually stronger than in the full-terrain simulations because of a

tighter, smoother gradient of isotachs (since there are no buoyant perturbations to mix the momentum vertically as in the full-terrain case), thus reducing Ri. The presence of low Ri is a necessary, however not sufficient, condition for shear-induced turbulence. Clearly the mountain wave in the full-terrain case is the source of the perturbations which then trigger the downscale cascade of kinetic energy.

The west-east vertical cross section in Fig. A.3 shows none of the horizontal accelerations in Fig. 2.12, as well as no downward trajectory for the jet core as was seen in the full-terrain simulations. Fig. A.4 is a cross-flow vertical cross-section of the circulation around the jet axis near the accident location. All show very little in the way of wave-like perturbations, and very little vertical motion. Comparing Fig. A.4 with Fig. 2.14, the smooth-terrain case shows a lack of complex vertical circulations of the sort hypothesized to lead to the formation of the unstable layer and turbulent downburst described in Section 2.5.

The NCSU1 Turbulence Index (described in Section 1.2.4) is used as an indicator of the potential for aviation turbulence in that it can identify those regions where the mesoscale structure is characterized by instabilities that may lead to small-scale violent turbulent eddies. Fig. 28 shows the 1500 UTC 200 hPa (225 to 175 hPa layer) NCSU1 fields from both 6 km NHMASS simulations. It becomes quite clear that the full-terrain case shows far more potential for aviation turbulence than does the smooth terrain case by several orders of magnitude. This implies that the terrain gradients lead to the velocity perturbations which help to organize the circulations leading to the downscale cascade of kinetic energy. The smooth-terrain case shows little such instability, in spite of the low Ri depicted in Fig. A.2, similar in magnitude to that in Fig. 2.11. Therefore the gradient of vorticity and momentum advection must dominate the NCSU1 signal in the full-terrain case; likely resulting from the

velocity perturbations caused by the mountain wave as well as the vertical circulations across the spectrum of scales. The Scorer parameter and vertical Scorer parameter gradient fields in Fig. A.6 also show that the vertical variation of static stability and shear are intensified in the presence of the mountain wave-induced perturbations. While the meso-α static stability structure is hypothesized to be governed by the jet/front system and attendant ageostrophic circulations, the meso-γ scale thermal and momentum structures will be impacted significantly due to the convergence/divergence associated with the mountain wave, thus increasing both l^2 and $\partial(l^2)/\partial z$ in the full-terrain case.

Again, one of the important aspects of the hypothesis regarding the pre-turbulence environment is that the jet/front system provided a favorable environment for the generation and downscale-organization of mountain-induced turbulent eddies. The pockets of Ri <1 in Fig. A.2 indicate that even in the smooth-terrain case, there was a pre-existing shear and static stability structure favorable for turbulence. On 9 December, observations indicated that the upper-level fronts associated with the two distinct jet regimes bracketing the 250-150 hPa layer were aligned in the vertical, with the colder air at 250 hPa outdistancing the front at 150 hPa. To examine this in detail, plots were generated showing GEMPAK-derived frontogenesis, given by (GEMPAK/N-AWIPS User's Guide, available at http://www.unidata.ucar.edu/software/gempak/help_and_documentation/manual/):

$$FRNT = \left(\frac{1}{2}(1.08 \times 10^{-4})(10^{-5})|\nabla_H \theta| \right)\left(DEF * \cos(2\beta) - (\nabla \bullet \vec{V}) \right) \qquad (A.1)$$

where:

$$\beta = \sin^{-1} \left(\frac{\left(-\cos\delta \frac{\partial\theta}{\partial x} - \sin\delta \frac{\partial\theta}{\partial y} \right)}{|\nabla_H \theta|} \right) \qquad (A.2)$$

and:

$$\delta = \frac{1}{2} \tan^{-1} \frac{shearing\ deformation}{stretching\ deformation} \qquad (A.3)$$

These plots are shown in Figures A.7 and A.8, which depict the evolution of the frontogenesis fields at 200 hPa and 250 hPa for the full-terrain simulation and smooth-terrain simulations, respectively. For clarity, the contour values for Fig. A.8 were multiplied by 10. It is clear that a major contribution to the frontogenesis is the tilting and deformation of the isentropic surfaces by the mountain waves in the full-terrain case since the values in the full-terrain case exceed the smooth-terrain values by an order of magnitude. Nevertheless, some indication of a frontal boundary at both 250 and 200 hPa is present in the smooth-terrain case, with the 250 hPa frontal boundary over western Kansas at 1500 UTC slightly outpacing the 200 hPa boundary at the eastern Colorado border. This supports the hypothesis that the cold air undercutting the warmer air at 200 hPa leading to the significant vertical discontinuity in static stability was a result of the upper jet/front structure rather than a response to the mountain wave.

A.4. Conclusions

The smooth-terrain NHMASS simulations on the Colorado 9 December turbulence case produced the expect result in that the strong vertical circulations present in the full-terrain case were not seen. The pre-turbulence structure, characterized by a strong thermal inversion at 200 hPa with an unstable cold layer below with associated strong gradients in

static stability and low Richardson number, had a similar appearance in both cases. Indicators for the potential for strong turbulent motions such as the vertical gradient of the Scorer parameter and NCSU1 Turbulence Index showed the smooth-terrain case to be considerably less conducive for aviation turbulence. Both sets of simulations indicated that the jet/front system was responsible for setting the stage for the downscale cascade of kinetic energy. However, both sets of simulations also indicate that the mountain wave, forced by sharp terrain gradients, is responsible for the buoyancy perturbation which then allows the extraction of energy from the base state by the higher-frequency waves, and so on down to turbulent motions on the aircraft scale.
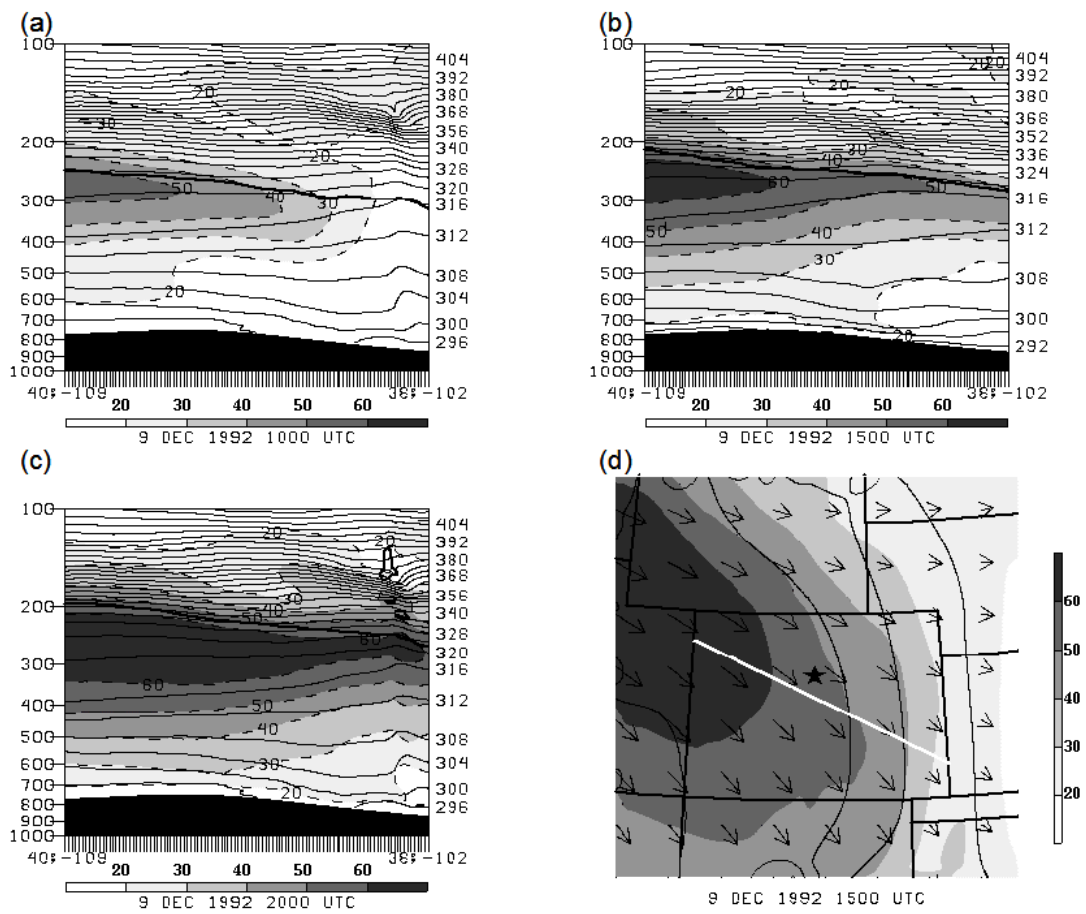
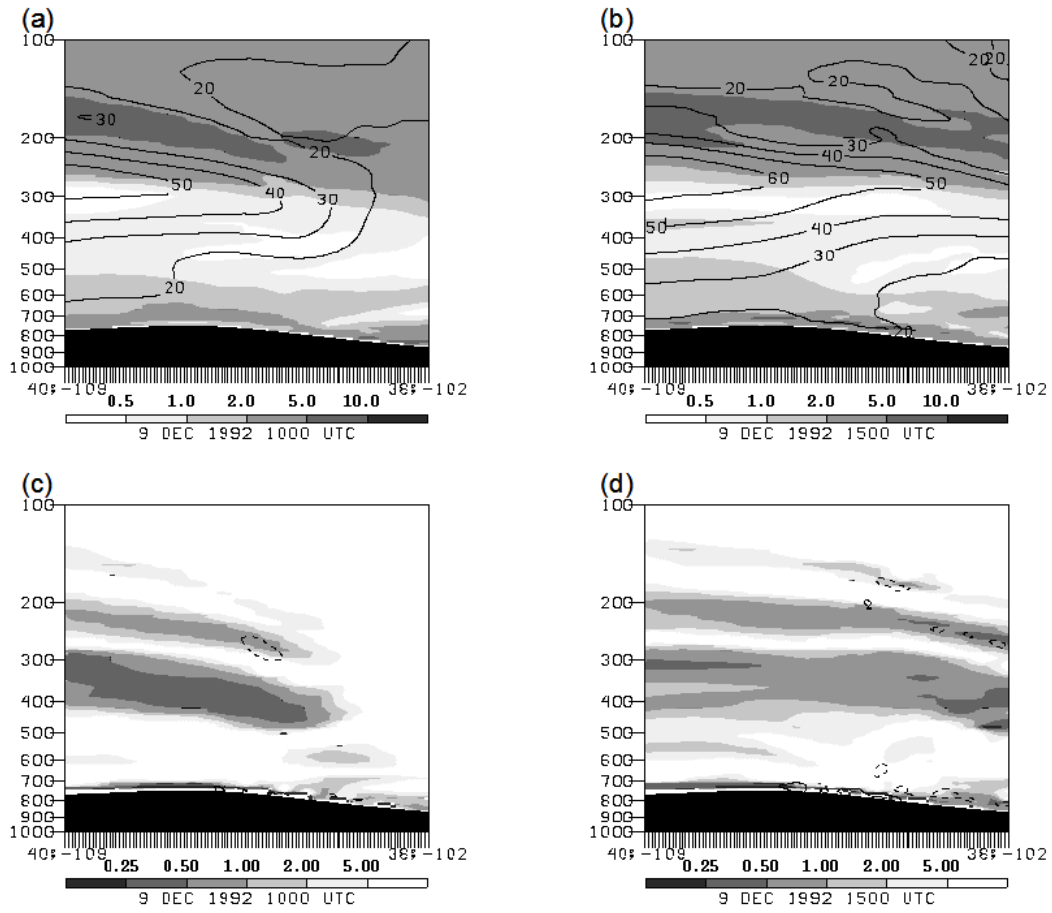Figure A.1: Same as Fig.2. 10, except from 6 km smooth-terrain NHMASS simulation.

Figure A.2: Same as Fig. 2.11, except from 6 km smooth-terrain NHMASS simulation.
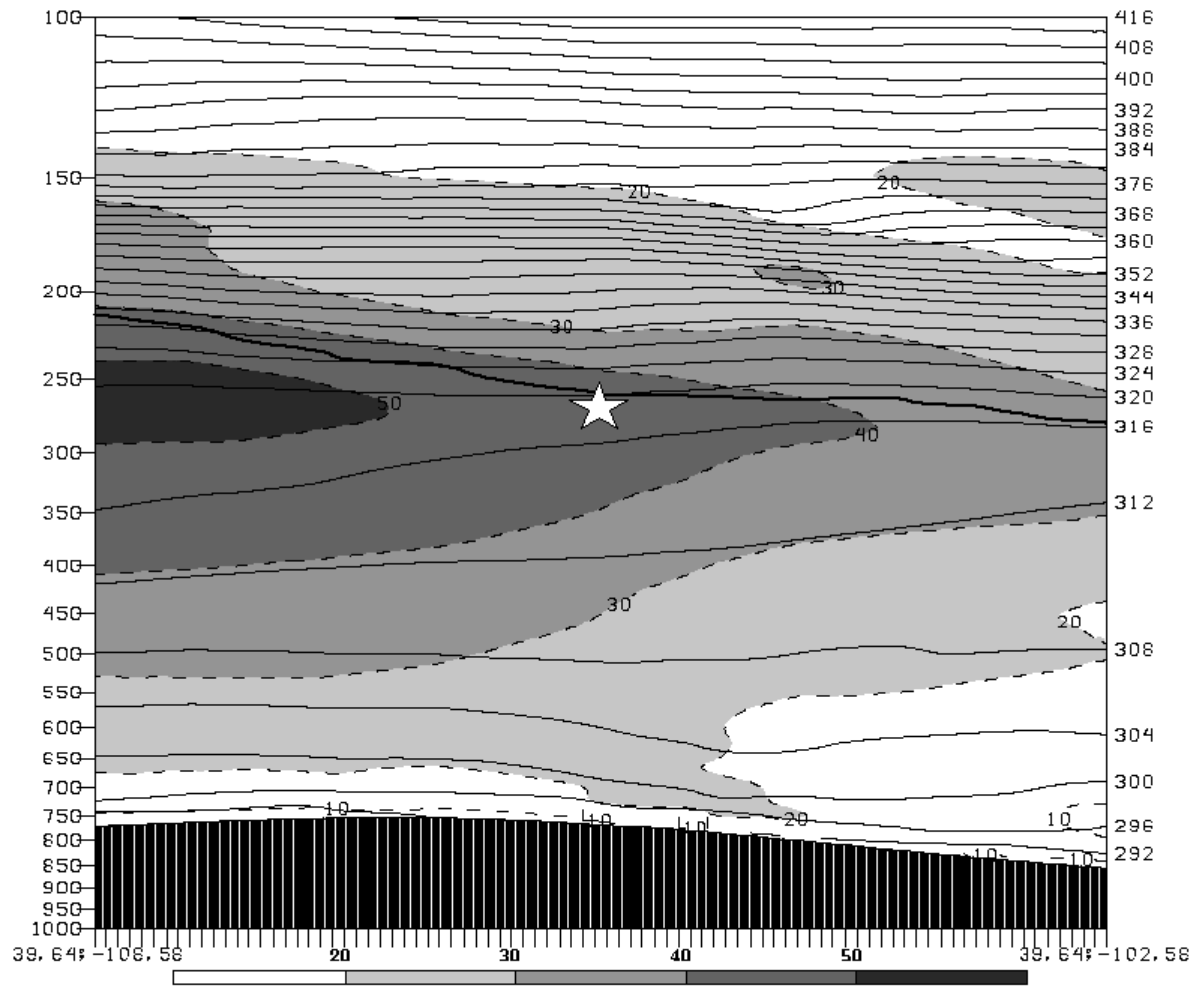
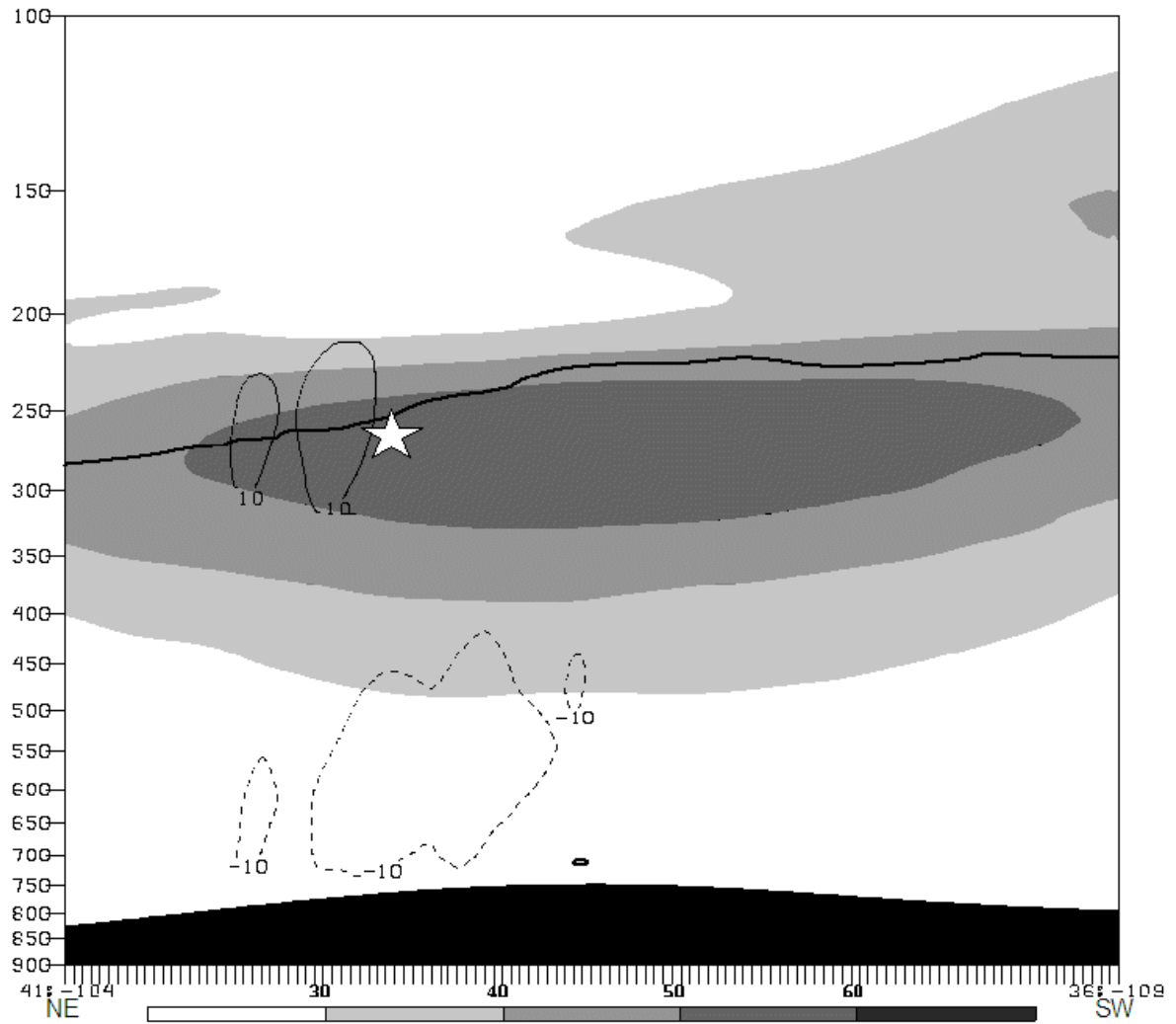Figure A.3: Same as Fig. 2.12, except from 6 km smooth-terrain NHMASS simulation.

Figure A.4: Same as Fig. 2.14, except from 6 km smooth-terrain NHMASS simulation.
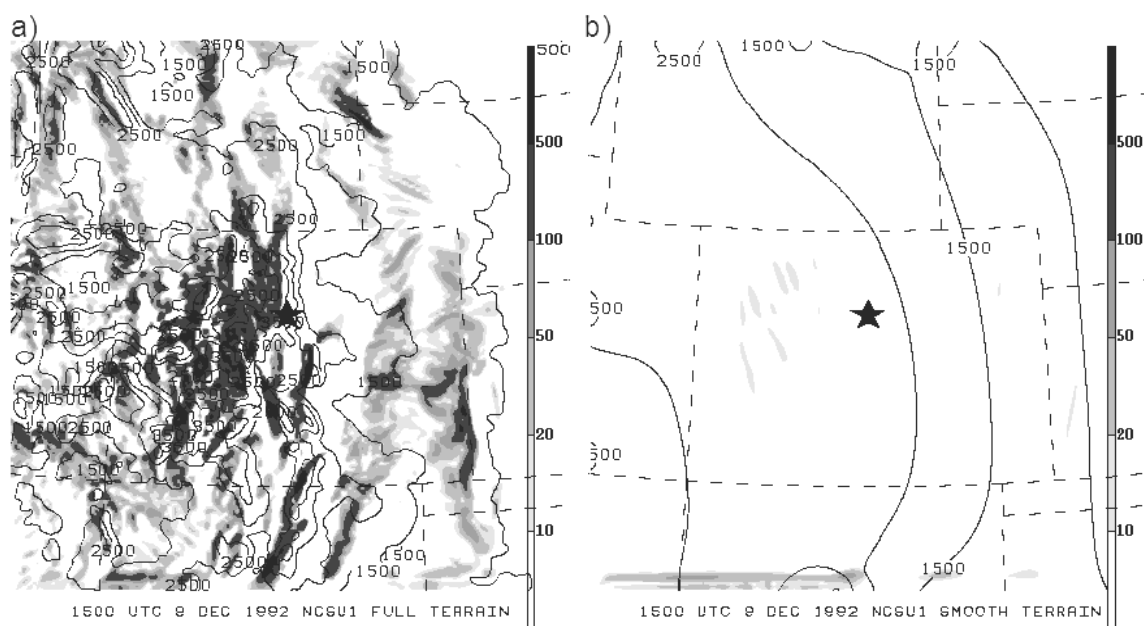
Figure A.5: 225-175 hPa layer NCSU1 Turbulence Index ($s^{-3} \times 10^{-14}$) valid 1500 UTC 9 December 1992 from (a) full-terrain and (b) smooth-terrain 6 km NHMASS simulations. Terrain contours in meters. Aircraft incident location marked by star.
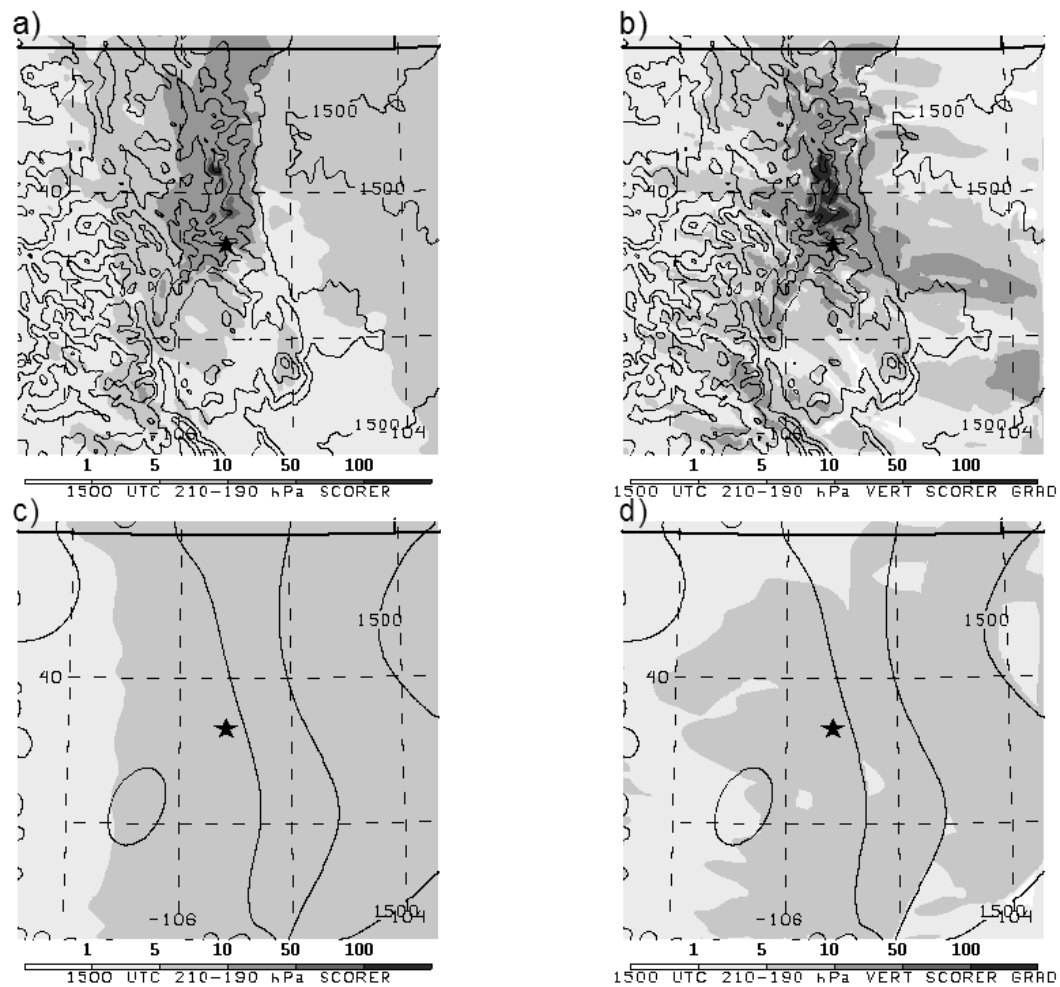
Figure A.6: 210-190 hPa layer (a,c) l^2 (shaded, $\text{m}^{-2} \times 10^{-7}$) and $\partial\!\left(l^2\right)\!/\partial z$ ($\text{m}^{-3} \times 10^{-10}$) valid 1500 UTC 9 December 1992 for the full-terrain (a,b) and smooth terrain (c,d) 2km NHMASS simulations. Terrain contours every 500 m. Aircraft incident location marked by star.

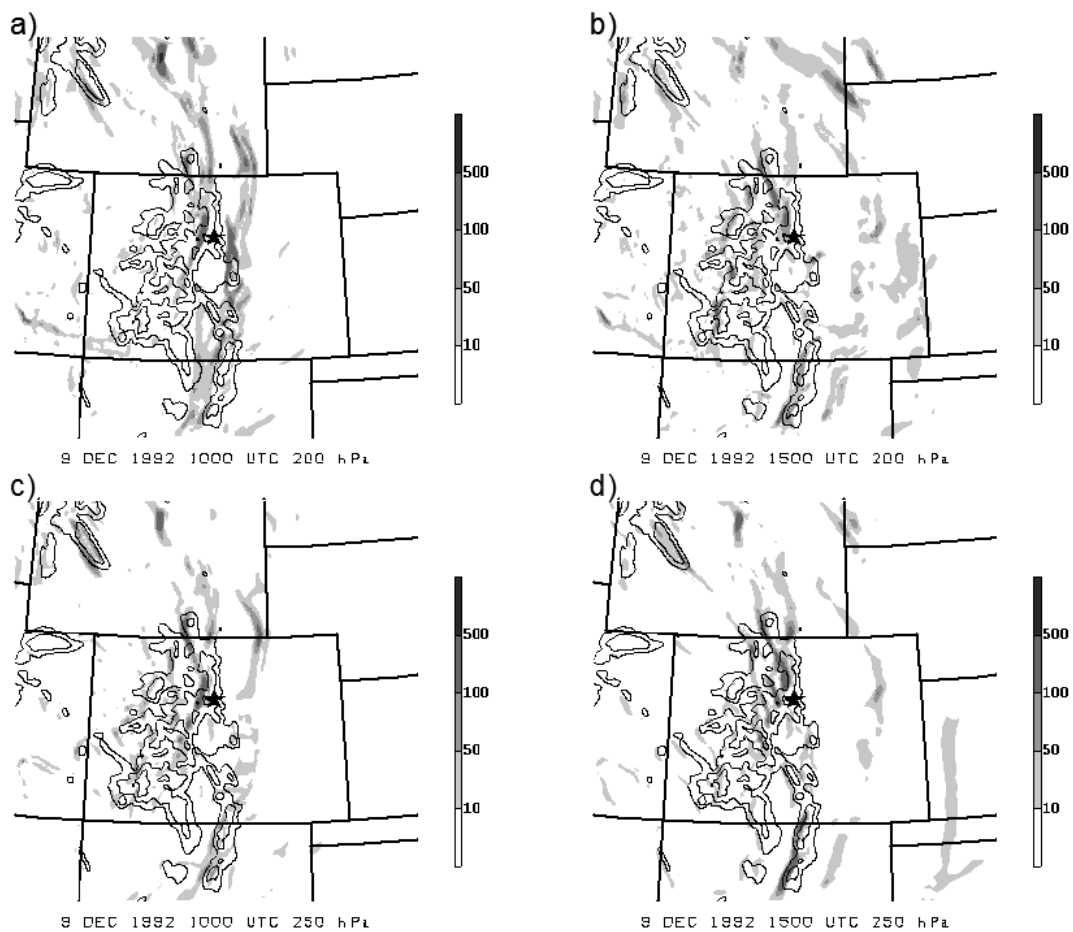Figure A.7: Simulated 200 hPa GEMPAK-derived horizontal frontogenesis function (K 100 km^{-1} 3hr^{-1}, shaded) at (a) 1000 UTC and (b) 1500 UTC and at 250 hPa at (c) 1000 UTC and (d) 1500 UTC 9 December 1992. Terrain contours at 2.5,3, and 3.5 km. From 6 km NHMASS full-terrain simulation. Aircraft accident location denoted by star.
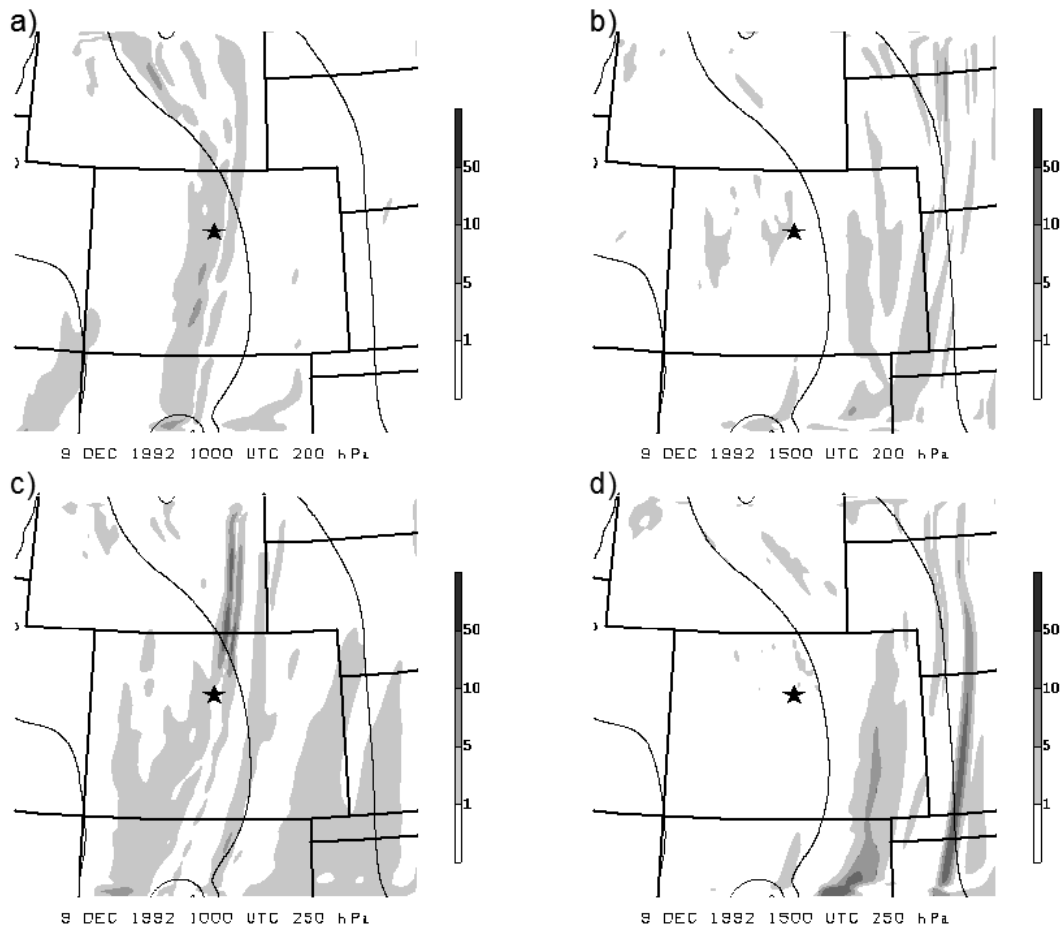
Figure A.8: Same as Fig. A.7 except from 6 km NHMASS smooth-terrain simulation. Also the contour levels are reduced by a factor of 10.

APPENDIX B

STRATOSPHERIC NON-HYDROSTATIC MESOSCALE ATMOSPHERIC SIMULATION SYSTEM VERSION 6.4

Table B.1. STRATONHMASS (Version 6.4)

Initialization
• 3-D multivariate OI procedure used to blend a first guess fields (e.g. previous MASS simulation, NCEP model output, archived Reanalysis data) with observations from a variety of sensing systems (e.g. surface, rawinsonde) • Global databases of terrain height, land cover/land use, vegetation index, sea surface temperature, soil texture, snow cover, soil moisture, subsurface temperature, and sea ice
Numerical Techniques
• Option of hydrostatic or non-hydrostatic primitive equations in terrain-following (σ_p) vertical coordinate with 4th-order accurate finite differencing • MPDATA positive definite advection scheme • Option of one-way or two-way interactive nesting, with arbitrary coarse/fine grid spacing ratio and unrestricted number of nested domains for one-way nesting
Boundary Layer/ Surface Physics
• 1.5 order Turbulence Kinetic Energy (TKE) parameterization with surface layer based on similarity theory formulation • Surface energy budget with option of isothermal or non-isothermal soil-vegetation canopy formulations and heterogeneous subgrid scale areas • Surface hydrology includes budget equations for three moisture reservoirs (cover layer, shallow and deep soil layers) and snow cover which incorporates the effects of accumulation, settling, melting and sublimation
Moisture Physics
• Option of diagnostic or three prognostic schemes with varying levels of sophistication. Prognostic equations for cloud water, cloud ice, rain water, snow and hail using a bulk microphysics parameterization • Option of Kuo-type cumulus parameterization with moist downdraft physics, Fritsch-Chappell scheme, Kain-Fritsch scheme or Grell scheme
Radiation
• Longwave and shortwave radiation parameterized in surface energy budget and in the free atmosphere. Interaction with atmospheric water vapor, liquid/frozen water, and parameterized sub-grid clouds

APPENDIX C

WEATHER RESEARCH AND FORECASTING MODEL ADVANCED RESEARCH WRF VERSION 2.2

Table C.1. WRF/ARW (Version 2.2)

Model Solver
- Fully compressible nonhydrostatic equations with hydrostatic option
- Complete Coriolis and curvature terms
- Two-way nesting with multiple nests and nest levels
- One-way nesting
- Experimental moving nest
- Mass-based terrain following coordinate
- Vertical grid-spacing can vary with height
- Map-scale factors for conformal projections:
-- Polar stereographic
-- Lambert-conformal
-- Mercator
- Arakawa C-grid staggering
- Runge-Kutta 2nd and 3rd order timestep options
- Scalar-conserving flux form for prognostic variables
- 2nd to 6th order advection options (horizontal and vertical)
- Time-split small step for acoustic and gravity-wave modes:
-- Small step horizontally explicit, vertically implicit
-- Divergence damping option and vertical time off-centering
-- External-mode filtering option
Lateral Boundary Conditions
- Idealized cases: periodic, symmetric, and open radiative
- Real cases: specified with relaxation zone
- Upper boundary absorbing layer option
- Positive definite advection scheme for scalars (microphysics species, and TKE) (new in V2.2)
- SST and greenness fraction update during long simulations
- Two-way and one-way nesting
Moisture Physics
- Microphysics
-- Kessler
-- WRF Single Moment (WSM) 3, 5 and 6 class
-- Lin et al.
-- Eta Ferrier
-- Thompson (a new version in V2.2)
- Cumulus Parameterization
-- Kain-Fritsch with shallow convection
-- Betts-Miller-Janjic
-- Grell-Devenyi ensemble

Table C.1 (cont.). WRF/ARW (Version 2.2)

Physics Options

- Planetary boundary layer
  -- Yonsei University (S. Korea)
  -- Mellor-Yamada-Janjic
  -- MRF
- Surface layer
  -- Similarity theory MM5
  -- Eta or MYJ
- Land-surface
  -- Slab soil model (5-layer thermal diffusion)
  -- Noah land-surface model
  -- Urban canopy model (works with Noah LSM, new in V2.2)
  -- RUC LSM
- Longwave radiation
  -- RRTM
  -- CAM
- Shortwave radiation
  -- simple MM5 scheme
  -- Goddard
  -- CAM
- Sub-grid turbulence
  -- constant K diffusion
  -- 2-D Smagorinsky
  -- Predicted TKE
- Land-use categories determine surface properties
- Analysis nudging (3 D only) (new in V2.2)
- Observation nudging (new in V2.2)

Inputs for WRF Initialization
- Idealized: several cases set up, both 2D and 3D - Real-data using Standard Initialization (SI) conversion from Grib files
I/O Options
- NetCDF, most common. Work with all supported graphics. - PHDF5 (Kent Yang, University of Illinois) - GriB 1 (Todd Hutchinson, WSI) - GriB 2(Todd Hutchinson, WSI) (new in V2.2) - Binary - Parallel netCDF (Argnnon National Lab, experimental only)